



BERGISCHE  
UNIVERSITÄT  
WUPPERTAL

FACHBEREICH C  
FACHGRUPPE PHYSIK

---

INCLUSIVE AND DIFFERENTIAL  
CROSS-SECTION MEASUREMENTS OF  
 $t$ -CHANNEL SINGLE TOP-QUARK  
PRODUCTION AT  $\sqrt{s} = 7$  TeV  
WITH THE ATLAS DETECTOR

---

Dissertation

VON

Dipl.-Phys. Anne Kathrin Becker

aus Haan

*Eingereicht am 13. August 2014*

CERN-THESIS-2014-325  
16/01/2015



Referent: Prof. Dr. Wolfgang Wagner, Fachbereich C - Experimentelle Teilchenphysik, Bergische Universität Wuppertal (DE)

Korreferent: Dr. Tancredi Carli, CERN, Genf (CH)

Tag der mündlichen Prüfung: 16. Januar 2015

# Introduction

Mankind has always asked questions about the composition of matter and the origin of the universe. Already in the 5th century BC Democritus and Leukippus developed the idea of atomism, a theory that hypothesizes that the universe is made up of indivisible particles, that move continually in otherwise empty space. Over the centuries scientists probed small scales to find the indivisible elementary particles, that make up the universe. Today, elementary particle physics is able to investigate experimentally what matter is made of, which elementary particles exist, and how they interact with each other. Improved understanding of the structure of matter allows to draw conclusions regarding the beginning of the universe.

To study subatomic particles of a size below  $10^{-17}$  m, particles like protons or electrons are brought to collision using particle accelerators. The spacial resolution at which the structure of matter can be probed is proportional to the inverse of the energy in these collisions. Thus, with higher collision energy the frontier of particle physics is pushed towards smaller dimensions. Currently, the most powerful man-made particle accelerator is the Large Hadron Collider (LHC) at the European Organization for Nuclear Research (CERN). It is a circular collider with a circumference of 27 km, that is designed to accelerate protons up to a center-of-mass energy of  $\sqrt{s} = 14$  TeV. Four particle detectors are located at the four collision points along the ring to measure the collision remnants and reconstruct the event as detailed and precise as possible. One of these four detectors is the ATLAS (A Toroidal LHC ApparatuS) experiment, a multipurpose detector of 46 m in length, 25 m in diameter and a weight of 7000 metric tons. This large detector is used to measure precisely the properties of known particles and to search for new particles.

All current experimental observations in particles physics, all particles and their interactions are described in a relativistic quantum field theory, the Standard Model of Elementary Particle Physics (SM). It was developed in the 1960s and 1970s and includes all known elementary matter particles. In the SM, the matter particles are six leptons and six quarks, that make up three particle generations combining two leptons and two quarks each. Currently, four fundamental forces are known in physics, and three of these forces are incorporated in the SM. The electromagnetic, strong and weak force are mediated by the exchange of force particles. There are a few observations from astrophysics and astroparticle physics, that are not explained by the SM and hint to the fact, that the SM is not complete. One missing part is a consistent description of the fourth fundamental force, gravitation, within the SM. Also experimental data shows, that neutrinos are not massless, as they are in the SM, and that about 27% of the energy in the universe is dark matter which is

not described at all by the SM. Furthermore, the stable universe consists to current knowledge completely of matter, stemming from a large asymmetry between matter and antimatter. While matter and antimatter are not completely symmetric in the SM due to a violation of the combined charge conjugation and parity symmetry ( $\mathcal{CP}$ ), the resulting asymmetry is not sizable enough to describe the matter-antimatter asymmetry in the universe. The  $\mathcal{CP}$  violation of quarks in the SM is expressed in the quark mixing matrix, called CKM matrix, that describes the coupling of the quarks to each other.

A good approach to further study the SM and search for deviations from current knowledge is the study of the heaviest quark in the SM, the top quark. It was discovered in 1995 in proton-antiproton ( $p\bar{p}$ ) collisions at the Tevatron accelerator located at the Fermi National Accelerator Laboratory, USA, by the CDF and DØ experiments [1, 2]. With a mass of  $m_t = 173.34 \pm 0.27 \pm 0.71$  GeV [3] it is almost as heavy as a gold atom and about 40 times heavier than the next heaviest quark, the bottom quark. The top quark is the only quark, that decays via the weak interaction, before getting confined in a bound state via the strong force, resulting in a very small lifetime of  $\tau = 5 \times 10^{-25}$  s. Thus, it is possible to study the top quark as a “quasi”-free quark.

At the LHC top quarks are mainly produced in pairs via the strong interaction, but top quarks can also be produced singly via the weak interaction. At leading order there are three different single top-quark production-modes, the  $t$ -channel production in which a space-like  $W$  boson is exchanged between a light quark and a bottom quark, the  $s$ -channel production where a time-like  $W$  boson is exchanged, and the  $Wt$ -channel production where the top quark is produced in association with a  $W$  boson. Electroweak single top-quark production was first observed in 2009 at the Tevatron accelerator by the CDF and DØ experiments [4, 5] in the combined  $s$ - and  $t$ -channel production. The production rate of single top-quarks is a factor of 30 larger at the LHC with a center-of-mass energy of at  $\sqrt{s} = 7$  TeV than at the Tevatron. Thus, it is possible to perform precise cross-section measurements and detailed studies of the characteristics of singly produced top quarks, including effects in production and decay of the top quark. The unitary, three-dimensional CKM matrix of the SM predicts, that single top-quarks are almost exclusively produced via the  $Wtb$  vertex. Therefore, the cross section of single top-quark production is directly proportional to  $|V_{tb}|^2$ .

The single top-quark production mode with the highest cross-section at the LHC is the production via the  $t$ -channel. The production cross-section of a process depends on the probability of the presence of the initial quarks having sufficient momentum in the proton. This is described by parton distributions functions (PDF). As  $t$ -channel single top-quark production requires a bottom quark in the initial state, the process is one of the few processes sensitive to the  $b$ -quark PDF. By measuring the  $t$ -channel single top-quark production separately for top-quarks and top-antiquarks, the cross-section ratio of top-quark and top-antiquark production is sensitive to the ratio of the up-quark PDF over the down-quark PDF.

The aim of this thesis is to study  $t$ -channel single top-quark production in detail by measuring the top-quark cross section  $\sigma(tq)$ , the top-antiquark cross section  $\sigma(\bar{t}q)$ ,

---

and their ratio,  $R_t \equiv \sigma(tq)/\sigma(\bar{t}q)$ , as well as the inclusive cross section  $\sigma(tq + \bar{t}q)$ . The value of the CKM matrix element  $|V_{tb}|$  is extracted. In addition, differential cross sections are measured as a function of the transverse momentum of the top-(anti)quark and as a function of the absolute value of its rapidity, respectively. These differential measurements are done for the first time and allow for tests of the different theoretical predictions. All measurements use an integrated luminosity of  $4.59 \text{ fb}^{-1}$  of  $pp$  collision data at  $\sqrt{s} = 7 \text{ TeV}$ , that were recorded by the ATLAS detector in 2011.

The experimental signature of single top-quark candidate events is characterized by the decay products of the top-quark. Only the leptonic final state of the  $W$  boson originating from the top-quark decay is reconstructed in the  $e\nu$  or  $\mu\nu$  decay mode. Fully-hadronic final states are not considered due to the large multijet background at the LHC. The selected data have some acceptance to  $W \rightarrow \tau\nu$  decays, if the  $\tau$  lepton decays subsequently leptonically. Thus, the observable final state of the signal process is given by one charged lepton (electron or muon), high missing transverse momentum, and two or three hadronic jets with high transverse momentum. The acceptance for  $t$ -channel single top-quark events is dominated by the 2-jet signature, where one jet is a  $b$ -quark jet, while the second jet is a light-quark jet. A significant fraction of single top-quark events is also present in the 3-jet channel.

The biggest challenge in this analysis is the distinction between the signal process and background processes, that also include on-shell  $W$ -boson production. To explore kinematic differences between signal and background processes, event models are constructed deploying simulation techniques. Using the event models, several observables discriminating between signal and background events are combined by a neural network to one discriminant. The cross-section measurements are based on a simultaneous fit to these discriminants. To measure the differential cross sections, a sample enriched in  $t$ -channel single top-quark events is obtained by cutting on the neural network discriminant in the 2-jet signal region. The differential distributions are then extracted using an iterative Bayesian method.



# Contents

<b>1</b>	<b>Theory</b>	<b>1</b>
1.1	The Standard Model of Elementary Particle Physics . . . . .	1
1.1.1	Matter particles and their interactions . . . . .	1
1.1.2	Charged-current weak interaction . . . . .	4
1.1.3	Unification to electroweak interaction and mass of particles . .	6
1.1.4	The SM and beyond . . . . .	7
1.1.5	Predictions by the SM . . . . .	8
1.1.6	Determination of PDFs . . . . .	10
1.2	The top quark . . . . .	14
1.2.1	Production via the strong interaction . . . . .	15
1.2.2	Electroweak production . . . . .	16
1.3	$t$ -channel single top-quark production . . . . .	18
1.3.1	Characteristics of the production process . . . . .	19
1.3.2	The CKM element $ V_{tb} $ . . . . .	22
1.3.3	Kinematic properties and polarization of the top quark . . . .	24
1.3.4	Sensitivity to physics beyond the SM . . . . .	25
<b>2</b>	<b>The ATLAS detector at the LHC</b>	<b>29</b>
2.1	The LHC . . . . .	29
2.2	The ATLAS experiment . . . . .	32
2.2.1	The ATLAS coordinate system . . . . .	33
2.2.2	The Inner Detector . . . . .	35
2.2.3	Calorimeters . . . . .	37
2.2.4	The Muon System . . . . .	39
2.2.5	Luminosity detectors . . . . .	40
2.2.6	Trigger system . . . . .	41
2.3	The 2011 dataset . . . . .	41
<b>3</b>	<b>Event generation and reconstruction</b>	<b>45</b>
3.1	Event generation . . . . .	45
3.1.1	Monte-Carlo generators . . . . .	47
3.1.2	Detector simulation . . . . .	49
3.2	Event reconstruction . . . . .	49
3.2.1	Tracks of charged particles . . . . .	49
3.2.2	Primary vertex . . . . .	50

3.2.3	Electrons . . . . .	51
3.2.4	Muons . . . . .	53
3.2.5	Jets . . . . .	54
3.2.6	Missing transverse momentum . . . . .	62
3.2.7	Top quarks . . . . .	63
<b>4</b>	<b>Signal extraction</b>	<b>65</b>
4.1	Modeling of signal and background processes . . . . .	65
4.1.1	Signal modeling . . . . .	65
4.1.2	Background modeling . . . . .	70
4.2	Event selection . . . . .	77
4.2.1	Selection cuts . . . . .	77
4.2.2	Normalization of the multijet background . . . . .	80
4.2.3	Event yield . . . . .	82
4.3	Event classification . . . . .	84
4.3.1	Neural networks . . . . .	84
4.3.2	Input variables . . . . .	86
4.3.3	Trained neural networks . . . . .	104
<b>5</b>	<b>Inclusive cross-section and <math>R_t</math> measurements</b>	<b>109</b>
5.1	Statistical methods . . . . .	109
5.1.1	Binned maximum-likelihood fit-method . . . . .	109
5.1.2	Frequentist estimation of uncertainties . . . . .	111
5.2	Binned maximum-likelihood fit to the NN discriminants . . . . .	111
5.3	Systematic uncertainties . . . . .	125
5.3.1	Sources of systematic uncertainties . . . . .	125
5.3.2	Evaluation of the uncertainties . . . . .	131
5.4	Results . . . . .	138
5.4.1	Inclusive cross-section measurements . . . . .	139
5.4.2	Measurement of the cross-section ratio $R_t$ . . . . .	140
5.4.3	Cross-section dependence on the top-quark mass . . . . .	141
5.4.4	$ V_{tb} $ extraction . . . . .	142
<b>6</b>	<b>Differential cross-section measurements</b>	<b>145</b>
6.1	High-purity region . . . . .	145
6.1.1	Measured distributions . . . . .	147
6.2	Extraction of differential cross sections . . . . .	150
6.2.1	Unfolding methods . . . . .	154
6.2.2	Tests of the unfolding process . . . . .	156
6.2.3	Evaluation of uncertainties . . . . .	156
6.3	Results . . . . .	161
<b>7</b>	<b>Conclusion</b>	<b>167</b>
<b>A</b>	<b>Additional material to Chapter 5</b>	<b>171</b>
A.1	Acceptance uncertainties . . . . .	171

---

<b>B Additional material to Chapter 6</b>	<b>179</b>
B.1 Selection efficiency in the HPR . . . . .	179
B.2 Detailed list of uncertainties . . . . .	180
B.3 Correlation matrices . . . . .	188
<b>List of Figures</b>	<b>191</b>
<b>List of Tables</b>	<b>194</b>
<b>Bibliography</b>	<b>196</b>



# Chapter 1

## Theory

In this chapter the theoretical basis of particle physics, particularly the production and properties of the top quark, is discussed. The current knowledge of the fundamental particles and their interactions at scales of about 1 fm and below is formulated in the Standard Model of Elementary Particle Physics. After a brief introduction of the SM the characteristics of top quarks and their production are explained. The main focus is on single top-quark production, and the relevance of top quarks concerning searches for new phenomena in particle physics is discussed.

### 1.1 The Standard Model of Elementary Particle Physics

The SM is a relativistic quantum field theory [6–10] and has been in place since 1968. It provides a highly successful description of fundamental particles and their interactions on microcosmic scales and is able to provide precise predictions for the outcome of particle collisions. But there are also strong arguments for an extension of this description, e.g. neutrino masses, baryon asymmetry in the universe and dark matter, as well as conceptual issues indicating, that the SM is embedded in a more fundamental theory. In this section particles and interactions as well as selected fundamental concepts of the SM are introduced. A complete description of the SM can be found elsewhere, e.g. in Ref. [11].

#### 1.1.1 Matter particles and their interactions

All known fundamental particles are classified as either fermions, particles with half-integer spin, or bosons, particles with integer spin. In the SM all matter and their interactions are described with three kinds of elementary particles: leptons, quarks and gauge bosons. Leptons and quarks are spin-1/2 fermions and form together the building blocks of matter. They occur in three generations, where the lightest particles are found in the first generation and the heaviest in the third generation. Particles of the first generation form the stable matter in the universe, while particles of the higher generations are unstable with the exception of the neutrinos. Each

generation contains an electrically charged lepton, an electrically neutral neutrino, an up-type quark and a down-type quark with electric charges,  $Q = +2/3$  and  $Q = -1/3$ , respectively. The type of the leptons or quarks is called “flavor”. An overview of the elementary fermions and their properties is given in Table 1.1.

**Table 1.1:** Flavor, electric charge  $Q$ , and mass of elementary fermions taken from Ref. [12], except for the mass of the top quark, that is taken from Ref. [3].

Generation	Flavor	Quarks		Leptons		
		$Q$	Mass	Flavor	$Q$	Mass
I	up $u$	+2/3	1.8 – 3.0 MeV	electron $e^-$	-1	0.511 MeV
	down $d$	-1/3	4.5 – 5.5 MeV	$e$ neutrino $\nu_e$	0	< 2 eV
II	charm $c$	+2/3	1.275 GeV	muon $\mu^-$	-1	105.66 MeV
	strange $s$	-1/3	90 – 100 MeV	$\mu$ neutrino $\nu_\mu$	0	< 0.19 MeV
III	top $t$	+2/3	173.34 GeV	tau $\tau^-$	-1	1776.82 MeV
	bottom $b$	-1/3	4.18 GeV	$\tau$ neutrino $\nu_\tau$	0	< 18.2 MeV

In total, the SM comprises six leptons and six quarks in the SM. Each elementary fermion has an antiparticle, a particle with the same mass, but opposite quantum numbers, e.g. electric charge and color charge.

Apart from its electric charge each quark carries one of three different color charges: red, green and blue. Antiquarks carry the corresponding anticolors. So far, isolated color-charged particles have not been observed. This phenomenon is called quark confinement. Therefore, quarks are only observed in form of color-neutral objects, called hadrons. Hadrons can either be mesons, quark-antiquark pairs, baryons, combinations of three quarks, or antibaryons, combinations of three antiquarks. An example for a meson is the positively charged pion consisting of an up-quark and a down-antiquark. The positively charged proton is a baryon consisting of two up-quarks and one down-quark with different colors.

Interactions between elementary particles are incorporated in so called gauge theories, quantum field theories which are invariant under certain symmetry transformations. Noether’s theorem states, that each law of conservation is equivalent to a symmetry. Therefore, an interaction can be described via gauge theories based on a symmetry group. Massless gauge fields are introduced to describe interactions acting on a conserved quantity. The gauge fields are incorporated in the SM by demanding the Lagrangian density for a gauge theory to be invariant under its local gauge transformation. The force associated with such a gauge field is mediated by spin-1 gauge bosons. With this mechanism the electromagnetic, the strong, and the weak interaction are included in the SM. In the following the properties of those interactions are described. Figure 1.1 illustrates the possible interactions for all particle types. In addition, the interaction via the Higgs boson is shown, that will be introduced later.

The electromagnetic interaction is formulated by quantum electrodynamics (QED), that is based on the symmetry group  $U(1)_Q$ . The mediator of the interaction is the

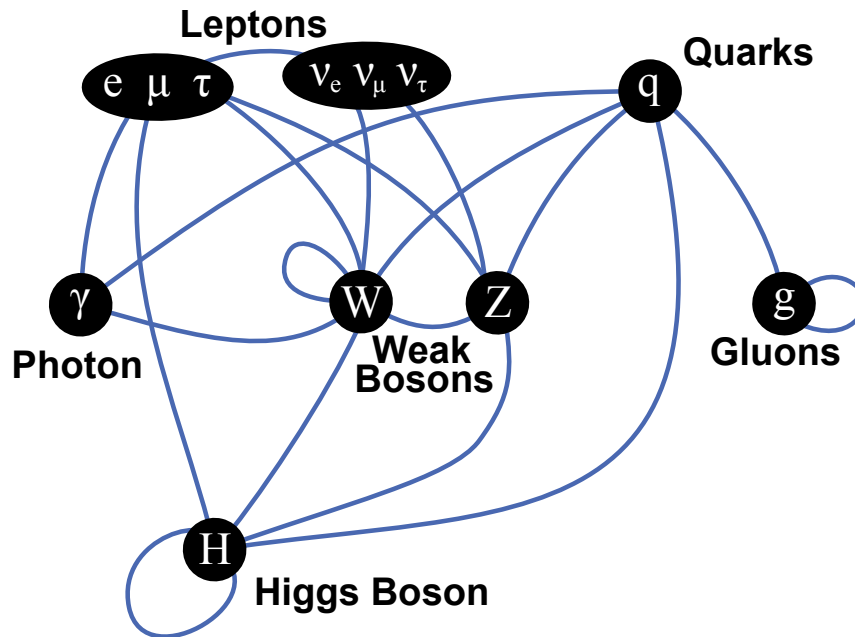


**Figure 1.1:** Graphic showing all fundamental particles and interactions described in the SM. The couplings between particles are denoted by the blue lines. The electromagnetic interaction is mediated by the photon and couples to all charged particles. Gluons carry the strong force between color charged particles, while the weak force is mediated by the  $W$  and  $Z$  bosons. The Higgs boson couples to all massive particles. The graphic is taken from Ref. [13].

massless photon  $\gamma$ , that couples only to particles carrying an electric charge  $Q$ , including all quarks, charged leptons and charged gauge bosons. As the photon itself does not carry an electric charge, a self-coupling of the photon is not possible. Because there is no direct self-interaction of the photon and because the photon is massless, the range of the electromagnetic interaction is infinite, and isolated charged particles exist. The strength of the electromagnetic coupling depends on the energy scale of the interaction.

The strong interaction is described by quantum chromodynamics (QCD), that is based on the symmetry group  $SU(3)_C$ . The mediators of the strong force are the gluons ( $g$ ). Gluons are massless, electrically neutral and exist in eight different color states. They couple to color charged particles, that include all quarks, antiquarks and the gluons themselves. Thus, self-interaction of gluons is possible. The size of the coupling  $\alpha_S$  depends strongly on the exchanged momentum during an interaction. In general, it is possible to calculate strongly interacting processes via perturbation theory [14, 15]. Due to the strong “running” of  $\alpha_S$ , this calculation is not possible for low energy interactions. At large distances (size of the proton and larger)  $\alpha_S$  is large. Therefore a calculation of strong physics processes is in general not possible via perturbation theory. But at smaller distances (corresponding to high energetic QCD processes)  $\alpha_S$  is small and thus, a perturbative calculation of QCD physics processes is possible. This phenomenon is called “asymptotic freedom” and was discovered by Wilczek, Gross and Politzer in 1973 [14, 15].

The weak interaction is described by the  $SU(2)_L$  symmetry group. There are three mediators of the weak interaction: two electrically charged  $W$  bosons and one electrically neutral  $Z$  boson. They couple to particles carrying a weak isospin  $T$ . All elementary fermions carry a weak isospin of  $1/2$  for up-type quarks and neutrinos or  $-1/2$  for down-type quarks and charged leptons. Thus, the weak interaction is the only interaction, that acts on all elementary fermions. The coupling strength of the weak interaction is small compared to that of the other interactions because its mediator bosons have a large mass. Thus, the interaction is called “weak”. The masses of the mediator bosons of  $m_W = 80.385 \pm 0.015$  GeV [12] in case of the  $W$  bosons and  $m_Z = 91.1876 \pm 0.0021$  GeV [12] in case of the  $Z$  boson are not described by the gauge theory, as massive gauge fields violate the gauge invariance of the SM.

Two types of interactions are possible in the weak interaction: a charged current interaction, that changes the flavor of the interacting particle, mediated by the electrically-charged  $W$  boson with an electric charge of  $Q = \pm 1$ , and a neutral current interaction mediated by the electrically neutral  $Z$  boson. The neutral current interferes with the electromagnetic interaction when coupling to charged leptons and quarks. The only pure neutral current process is the scattering of neutrinos because neutrinos are not able to interact via the electromagnetic interaction due to their electrical neutrality. In the SM flavor-changing neutral-current interaction vertices are forbidden. The charged current weak interaction is described in more detail in the next section.

### 1.1.2 Charged-current weak interaction

The charged-current weak interaction is discussed here in detail because top quarks decay via the charged-current weak interaction. One of its striking characteristics is the violation of parity. Parity corresponds to the mirror symmetry and is a transformation under which the electromagnetic and strong interactions are invariant. In 1956 experimental evidence showed, that parity is violated in the charged weak interaction [16]. Mathematically the parity violation is formulated by the weak vertex factor using Dirac matrices:

$$-\frac{ig_w}{2\sqrt{2}}\gamma^\mu(1 - \gamma^5) \quad (1.1)$$

where  $g_w$  is the weak coupling constant and  $\gamma^\mu$ ,  $\gamma^5$  are Dirac matrices with  $\mu \in \{0, 1, 2, 3\}$ . Here  $\gamma^\mu$  represents a vector coupling, while  $\gamma^\mu\gamma^5$  represents an axial vector coupling. Because an axial vector is a vector whose reflection also includes a sign flip, the appearance of an axial vector already is bound to violate parity. Due to the  $(\gamma^\mu - \gamma^\mu\gamma^5)$  term, the coupling of the charged weak interaction is called ‘ $V-A$ ’ coupling (vector minus axial vector).

From a physical point of view the ‘ $V-A$ ’ structure of the coupling can be interpreted, such that the charged weak interaction only acts on left-handed particles and right-handed antiparticles. The property of “handedness” of spin-1/2 fermions is called helicity and explained in Fig. 1.2. Right-handedness corresponds to parallel spin and momentum directions, while left-handedness is the case of antiparallel spin and momentum. For massless particles the helicity is Lorentz invariant, as it

is impossible to reverse the direction of motion by changing the rest frames. Therefore, helicity is a fundamental property of massless particles. However, for massive particles the Lorentz invariant property is the chirality, while the helicity depends on the reference frame.

Another characteristic of the charged-current interaction is, that the  $W$  boson couples to a superposition of the physical down-type quarks, that were introduced above. For example, the superposition  $d' = \cos \theta_C \cdot d + \sin \theta_C \cdot s$  couples via a  $W$  boson to the  $u$  quark. Therefore, two possible interactions are observed in an experiment: the interaction via the  $Wud$  vertex and the interaction via the  $Wus$  vertex as shown in Fig. 1.3. The first two generations are connected by the Cabibbo angle [17],  $\theta_C = 13.02^\circ$  [12], that is multiplied to the weak coupling vertex, e.g. in Fig. 1.3(a)  $-\frac{ig_w}{2\sqrt{2}}\gamma^\mu(1 - \gamma^5)\cos\theta_C$ . The superposition concept is further formulated in the GIM mechanism [18], that introduces it as a new state of quarks for the weak interaction: the weak eigenstate, also called Cabibbo-rotated state, that is connected to the physical quark eigenstate by a unitary rotation matrix with the angle  $\theta_C$ .

Kobayashi and Maskawa extended the GIM mechanism to describe the weak eigenstates of all three generations with the CKM matrix [19]:

$$\begin{pmatrix} d' \\ s' \\ b' \end{pmatrix} = \begin{pmatrix} V_{ud} & V_{us} & V_{ub} \\ V_{cd} & V_{cs} & V_{cb} \\ V_{td} & V_{ts} & V_{tb} \end{pmatrix} \begin{pmatrix} d \\ s \\ b \end{pmatrix} \quad (1.2)$$

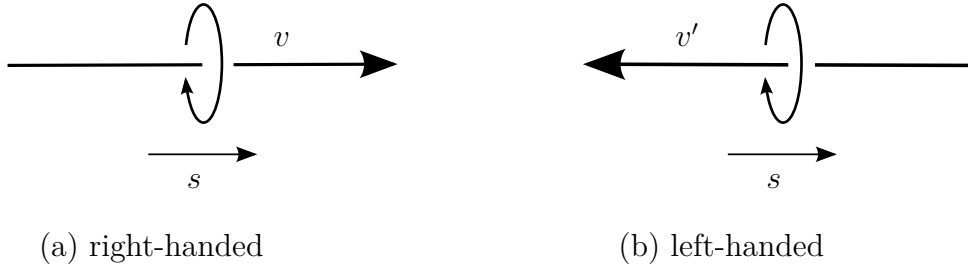


**Figure 1.2:** Handedness. In (a) the spin and the velocity are parallel (right-handed); in (b) they are antiparallel (left-handed).

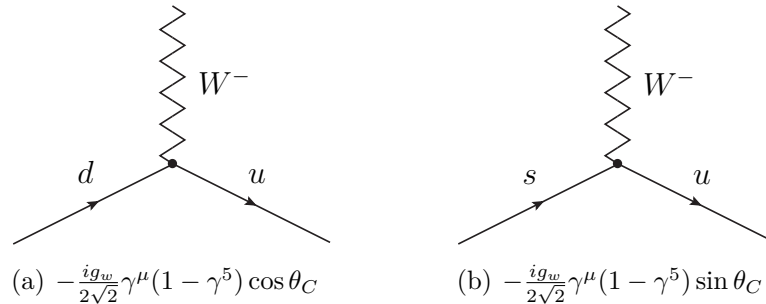


**Figure 1.3:** Cross-generational coupling to the  $W$  boson. In (a) the coupling of the  $W$  boson within the first generation is shown. As  $\theta_C$  is rather small, this coupling is favored. In (b) the mixing between the first and second generation at the  $W$  vertex is shown. It carries a factor of  $\sin \theta_C$ .

where  $d'$  is a mixed state of  $d$ -,  $s$ -, and  $b$ -quarks where the mixing is defined by  $V_{ud}$ ,  $V_{us}$ , and  $V_{ub}$ . The charged-current weak vertex factor for the up-type quark  $i$  and the down-type quark  $j$  can now be written as:

$$-\frac{ig_w}{2\sqrt{2}}\gamma^\mu(1-\gamma^5)\cdot|V_{ij}|. \quad (1.3)$$

There are nine (complex) elements in the CKM matrix. But the number of free parameters is reduced to three angles  $\theta_1$ ,  $\theta_2$ ,  $\theta_3$ , and one phase  $\delta$  because the matrix is unitary in the SM. Thus, the matrix can be written as:

$$\begin{pmatrix} d' \\ s' \\ b' \end{pmatrix} = \begin{pmatrix} c_1 & -s_1c_c & -s_1s_3 \\ s_1c_2 & c_1c_2c_3 - s_2s_3e^{i\delta} & c_1c_2s_3 - s_2c_3e^{i\delta} \\ s_1s_2 & c_1s_2c_3 - c_2s_3e^{i\delta} & c_1s_2s_3 - c_2c_3e^{i\delta} \end{pmatrix} \begin{pmatrix} d \\ s \\ b \end{pmatrix}, \quad (1.4)$$

where  $c_i = \cos \theta_i$  and  $s_i = \sin \theta_i$  for  $i = 1, 2, 3$ . Other than this, the SM gives no insight on the matrix elements of the CKM matrix. To determine them, they must be measured experimentally. The CKM matrix also incorporates the phenomena of  $\mathcal{CP}$  violation via the complex phase  $\delta$ .

Apart from being not invariant under parity transformation ( $\mathcal{P}$ ), that transforms a physical process to its mirror image, and analogously under charge conjugation ( $\mathcal{C}$ ), that transforms particles in the respective antiparticles, the charged weak interaction is also not  $\mathcal{CP}$  invariant. A violation in  $\mathcal{CP}$  corresponds to a different behavior of particles with respect to antiparticles. The observed amount of  $\mathcal{CP}$ -violating weak processes is a small effect.  $\mathcal{CP}$ -violation in weak processes was first observed in neutral kaon decays [20], when a small number of long-lived  $K^0$  decayed into  $\pi^{+(0)}\pi^{-(0)}$  instead of  $\pi^0\pi^{+(0)}\pi^{-(0)}$ .

### 1.1.3 Unification to electroweak interaction and mass of particles

The unification of the electromagnetic and the weak interaction is formulated in the Glashow-Weinberg-Salam (GWS) model [6–8]. Its great advantage is the formulation of the weak coupling as a function of two fundamental parameters, the weak mixing angle  $\theta_W$ , and the electromagnetic coupling. Here, the electroweak interaction is described by the gauge group  $SU(2)_L \times U(1)_Y$ . The gauge group  $SU(2)_L$  has three gauge bosons,  $W^{1,2,3}$ , and the conserved quantity of the interaction is the weak isospin  $T$ . The  $U(1)_Y$  has the gauge boson  $B$  and the conserved quantity is the weak hypercharge  $Y = 2(Q - T_3)$ . One difficulty remains in the GWS model. All of the gauge bosons described above have to be massless for the interaction to be invariant under the symmetry transformation of the gauge group. Mass terms for the gauge bosons are not invariant under local gauge transformations.

The masses of the weak gauge bosons are generated in the SM by the Brout-Englert-Higgs (BEH) mechanism [21, 22] using the concept of spontaneous symmetry breaking. The symmetry of a Lagrangian density based on a specific gauge group is spontaneously broken if the ground state is not invariant under the corresponding

gauge transformation of the group. In the BEH mechanism, this is realized by adding a doublet of complex scalar fields with a non-zero vacuum expectation value to the Lagrangian density. Via interaction with the BEH fields the masses of the  $W$  and  $Z$  bosons are generated and a massive Higgs boson  $H$  appears. Hereby, the observable gauge bosons of the weak and electromagnetic interactions  $W$ ,  $Z$ , and  $\gamma$  are linear combinations of  $W^{1,2,3}$  and  $B$ . The existence of the Higgs boson was experimentally verified in 2012 [23, 24] at the LHC and its mass is measured to be  $125.35 \pm 0.41$  GeV [25]. The BEH mechanism is further used to explain the fermion masses in the SM. Here, the fermions acquire a mass by coupling to the Higgs boson via a gauge invariant Yukawa coupling term for each fermion in the Lagrangian density. Therefore, the coupling strength is proportional to the mass of the fermion. Thus, the coupling of the Higgs boson to the top quark is the largest coupling to a fermion. The SM does not predict the sizes of the Yukawa couplings. They are free parameters in the theory and need to be measured.

### 1.1.4 The SM and beyond

The SM is made up of QCD describing the strong interaction, the electroweak theory describing the weak and electromagnetic interactions, and the BEH mechanism describing the mass generation. Thus, the SM has a total of 18 free input parameters, that are necessary for all three sectors. These free parameters are:

- nine Yukawa couplings, one for each massive fermion (all quarks, electron, muon, and tau)
- three CKM mixing angles and one CKM  $\mathcal{CP}$  violating phase
- three coupling constants for the strong, weak, and electromagnetic interactions
- the Higgs-boson mass and the BEH vacuum expectation value.

So far all parameters apart from the  $\mathcal{CP}$  phase are determined from measurements. In addition, seven free parameters have to be added to the list of free parameters due to the non-zero neutrino masses and the phenomenon of neutrino oscillation. The high number of arbitrary parameters asks for a more unified theory where some of these parameters are predicted. Also, there is no explanation to the differences in size for the different fermion masses.

Following the electroweak unification a unified description of all three fundamental interactions in one interaction is desirable. It is possible, that there is a higher scale where all coupling constants have the same size. Thus, the strong, weak, and electromagnetic interactions could be described as one interaction in a Grand Unified Theory (GUT). This theory is one possible extension of the SM taking place at the GUT scale,  $\Lambda_{\text{GUT}}$ . Other possible extensions include e.g. the symmetrization of the fermion and boson sector (called Supersymmetry).

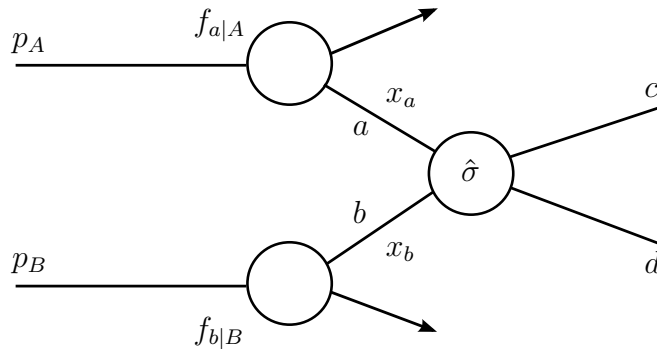


**Figure 1.4:** Sketch of the QCD-improved parton model showing the factorization of the cross section in a hard scattering parton-level cross section and parton distribution functions. The style of the sketch is taken from Ref. [26].

### 1.1.5 Predictions by the SM

The data analyzed in this thesis stem from  $pp$  collisions. To perform measurements or to search for physics beyond the SM, it is crucial to predict the outcome of the  $pp$  collisions according to the SM. The outcome is the number of expected events,  $\nu$ , in a certain final state  $X$ . Predictions of the final state can be divided in two parts: the probability per unit area for a SM particle  $q$  to be produced in the collision, that is described by the cross section  $\sigma$  of a process, and the probability in units of energy for a particle to decay to lighter particles, called decay width  $\Gamma$ . As several final states are possible for the decay of an unstable particle,  $\Gamma_{\text{tot}} = \sum_{i=1}^n \Gamma_i$  gives the total decay width for all possible decays  $n$ . The branching ratio for a certain decay  $i$  is defined as  $\mathcal{B}_i = \frac{\Gamma_i}{\Gamma_{\text{tot}}}$ . With these ingredients  $\nu$  is given by:

$$\nu = \mathcal{L}_{\text{int}} \cdot \sigma(pp \rightarrow q) \cdot \mathcal{B}(q \rightarrow X) \quad (1.5)$$

where  $\mathcal{L}_{\text{int}}$  is the integrated luminosity, corresponding to the total number of particles passing per unit area.

The cross section of a process in  $pp$  collisions at a center-of-mass energy of  $\sqrt{s}$  also has to be predicted by the SM. One difficulty arises from the fact, that the proton is a composite particle. In a collision of protons, constituents of the proton, called partons, interact. The proton is a hadron consisting of the so-called valence quarks ( $uud$ ), that are bound together by gluons. Additionally, there are quark-antiquark pairs, called sea quarks, inside the proton. The theoretical model to describe  $pp$  collisions is the QCD-improved parton model. Here, high-energy protons  $A$  and  $B$  are regarded as a composition of quasi-free quarks and gluons which share the proton momentum  $p_A$  and  $p_B$ , respectively. The interacting parton  $a$  has an initial momentum  $p_a = x_a p_A$  where  $x_a$  is the momentum fraction of the parton with respect to the momentum of the proton  $A$ . The parton  $b$  is treated analogously.

The cross-section calculation is then based on the factorization theorem [27], that states, that the description of  $pp$  collisions can be separated into a hard-scattering partonic cross section,  $\hat{\sigma}_{ab \rightarrow cd}$ , and the probability density to find the partons  $a$  and  $b$  with the respective momentum fractions  $x_a$  and  $x_b$  in the protons. The separation

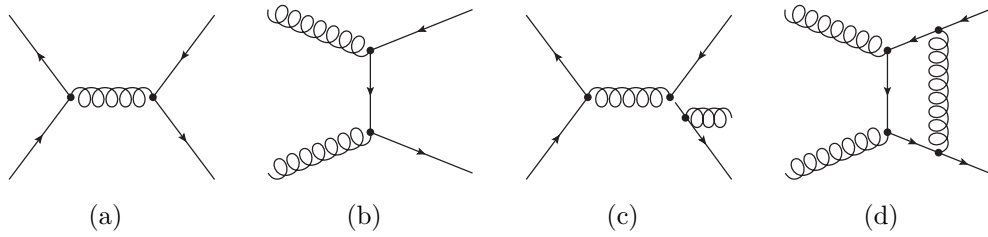


**Figure 1.5:** Panels (a) and (b) show examples for LO QCD Feynman diagrams, while Panels (c) and (d) show examples for NLO QCD Feynman diagrams. The curly lines represent gluons and the straight lines quarks.

of the problem is done at the factorization scale  $\mu_f$  and is depicted in Fig. 1.4. Thus, the cross section with a final state  $cd$  is expressed in the following way:

$$\sigma(AB \rightarrow cd) = \sum_{a,b} \int dx_a dx_b f_{a|A}(x_a, \mu_f^2) f_{b|B}(x_b, \mu_f^2) \cdot \hat{\sigma}_{ab \rightarrow cd}(\hat{s}, \mu_f^2) \quad (1.6)$$

where  $f_{a|A}$  and  $f_{b|B}$  are the two parton distribution functions (PDFs). A PDF corresponds to the probability density to observe parton  $a$  with a momentum fraction  $x_a$ . The determination of PDFs is discussed in the following section.  $\hat{s}$  denotes the center-of-mass energy squared of the colliding partons where  $\hat{s} = x_a x_b (p_A + p_B)^2$ . In case of symmetric colliders  $\hat{s}$  is given by  $\hat{s} = 4x_a x_b p^2 = x_a x_b s$  due to  $p_A = p_B = p$ . The sum in Equation 1.6 runs over all pairs of light partons ( $a, b$ ) contributing to the process.

The partonic cross section  $\hat{\sigma}_{ab \rightarrow cd}$  only involves high-momentum transfer and can be calculated with perturbative QCD. Here, the available phase space and the matrix element  $\mathcal{M}$  of the process need to be taken into account. The matrix element (ME) contains the dynamical information of a process. To determine  $\mathcal{M}$ , the relevant Feynman diagrams [28] are evaluated for the interaction in question up to a certain order of the perturbative series in  $\alpha_S$ . A Feynman diagram represents a contribution to the ME  $\mathcal{M}$  of a transition of an initial quantum state to a final quantum state. This is described in detail elsewhere, e.g. [11]. The main contribution to an interaction stems from the leading-order (LO) diagrams, corresponding to the order of  $\alpha_S^2$ . Higher order corrections are not only important for the precision and stability of the calculation, but also new physical effects can appear at higher orders. For some processes next-to-leading order (NLO) or even next-to-next-to-leading order (NNLO) calculations are available. In Fig. 1.5 examples are shown for LO and NLO Feynman diagrams.

Once the ME is determined, it is integrated over the phase space. In higher-order calculations the integration of the matrix element yields terms, that are divergent. In order to obtain a finite expression for  $\mathcal{M}$ , the divergences are removed by a renormalization procedure, using an arbitrary energy scale, the renormalization scale  $\mu_r$ . The most commonly used renormalization scheme is the  $\overline{\text{MS}}$  scheme, that is introduced in Ref. [29]. Since both, the factorization scale and the renormalization scale, are arbitrary parameters, they are often chosen to be of the same value  $\mu =$

$\mu_f = \mu_r$ . If a complete perturbation series would be performed, the prediction for the cross sections would be independent of the scale choice. Since all calculations are performed at finite order, the dependence of the result on the scale choice is one of the uncertainties of the predictions.

### 1.1.6 Determination of PDFs

The PDFs of the proton,  $f_{a|A}(x_a, Q^2)$ , cannot be calculated perturbatively, but their evolution with the scale,  $Q^2$ , is calculable. The dependence of the PDFs on the scale  $Q$  is expressed by the QCD evolution equations [30–32]:

$$Q^2 \frac{d}{dQ^2} f_a(x, Q^2) = \sum_b \int_x^1 \frac{d\zeta}{\zeta} \mathcal{P}_{ab}\left(\frac{x}{\zeta}, \alpha_s(Q^2)\right) f_b(\zeta, Q^2) \quad (1.7)$$

where  $f_a$  is the PDF of parton  $a$  and  $\mathcal{P}_{ab}$  are the splitting functions. These QCD evolution equations are also called Dokshitzer-Gribov-Lipatov-Altarelli-Parisi (DGLAP) equations. The splitting functions  $\mathcal{P}_{ab}$  can be interpreted in LO as the probability, that an initial parton  $b$  with momentum fraction  $\zeta$  emits a parton  $a$  with momentum fraction  $x$ . The different splitting functions are explained graphically in Fig. 1.6. The splitting functions can be calculated using perturbative QCD in a power series of  $\alpha_s(Q^2)$  and are available up to NNLO in  $\alpha_s$ .

The  $x$  dependence of the PDFs is determined using experimental data. This is done in two steps. First, the PDFs are parameterized at a starting scale  $Q_0$  using smooth functions of  $x$  with a limited number of parameters, typically 10-20.

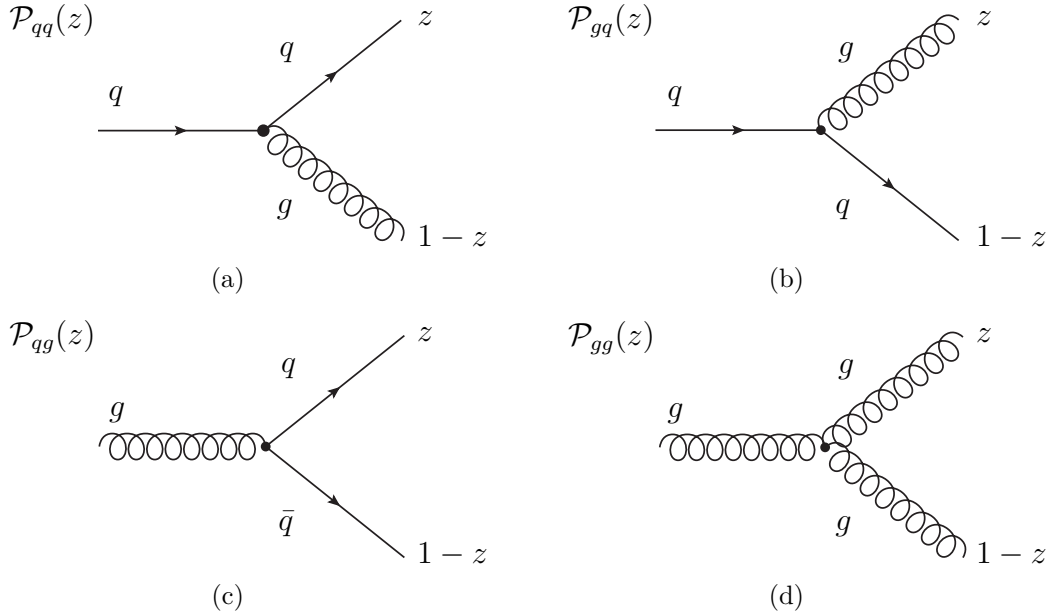


**Figure 1.6:** The DGLAP splitting functions  $\mathcal{P}_{ab}$  where  $b$  is the initial parton with momentum fraction  $\zeta$  and  $a$  the parton after the splitting with momentum fraction  $x$ . The variable  $z$  is defined as  $z = x/\zeta$ . The representative LO Feynman diagrams are shown for each splitting. This sketch is taken from Ref. [26].

Then, the distributions are evolved with the DGLAP equations to obtain values for  $f_a(x, Q^2)$  in the kinematic regions of the experimental data. These PDFs are used to retrieve parameterized predictions for the measured quantities. The predictions are then fitted globally with a  $\chi^2$  fit to the different data points, that are distributed in the  $x$ - $Q^2$  kinematic plane.

A large number of experimental datasets are included in the fits which have sensitivity to the different quark flavors. These datasets are typically from deep inelastic scattering experiments, where electrons, positrons, muons, or neutrinos collide with nucleons in fixed target experiments, and from electron/positron-proton collision data, that was recorded at the  $ep$  storage ring HERA (Hadron-electron ring accelerator). Recent PDF fits also include results from  $p\bar{p}$  collision data at the Tevatron as well as first results from  $pp$  collisions at the LHC. Figure 1.7 shows the coverage of experimental data used to determine PDFs in the  $x$ - $Q^2$  kinematic plane. Furthermore, the kinematic plane of the  $pp$  collision data of the LHC is shown. It can be seen, that in large ranges of the LHC data no previous experimental data is able to provide the PDFs. Here, results from the LHC experiments can provide new insights on the structure of the proton.

In the global fit up to 11 different PDFs are distinguished for each of the 10 quark flavors ( $u, \bar{u}, d, \bar{d}, c, \bar{c}, s, \bar{s}, b, \bar{b}$ ) and the gluon. Here, the top-quark PDFs are set to zero because of the large rest-mass of the top quark. The inclusion of heavy flavor PDFs ( $c, \bar{c}, b, \bar{b}$ ) is not trivial because the DGLAP evolution equations as described above are only valid for massless quarks. To include heavy quark production in the PDFs, several approaches are used by the different PDF fits:

- FFNS (fixed flavor-number scheme): Here, the number of quark flavor  $n_f$  is fixed independent of the scale  $Q^2$ . Heavy quarks, that are not included in  $n_f$ , are only produced in the final state via gluon fusion or gluon splitting. Thus, the mass of the heavy quark is taken into account. The FFNS gives reliable results for scales smaller or equal the masses of the heavy flavor quarks. At large  $Q^2$ ,  $\ln(Q^2/m_{c(b)}^2)$  terms appear, that require large correction terms.
- ZM-VFNS (zero-mass variable flavor-number scheme): In the ZM-VFNS, the heavy quarks are treated as massless partons. Here, the number of active partons  $n_f$  changes depending on the chosen scale  $Q^2$ . If  $Q^2 < m_c$ ,  $n_f$  is set to three. If  $m_c \leq Q^2 < m_b$ ,  $n_f$  is set to four. If  $m_b \leq Q^2$ ,  $n_f$  is set to five. In this treatment, the DGLAP evolution can be performed for all quark flavors and reliable results are achieved for large  $Q^2$ . But the results are not reliable for small  $Q^2$  because the masses of the heavy flavor quarks are ignored.
- VFNS (variable flavor-number scheme): The VFNS combines the FFNS and the ZM-VFNS by interpolating between the FFNS approach at low  $Q^2$  and the ZM-VFNS at large  $Q^2$ .

There are various groups, that provide sets of PDFs using similar fitting methods and similar input measurement data. Recent LO, NLO, and NNLO fits are provided by the CT10 [35], GJR08 [36], ABM11 [37], and MSTW2008 [38] groups. The HERAPDF [34] group constrains their input data mainly to data from experiments

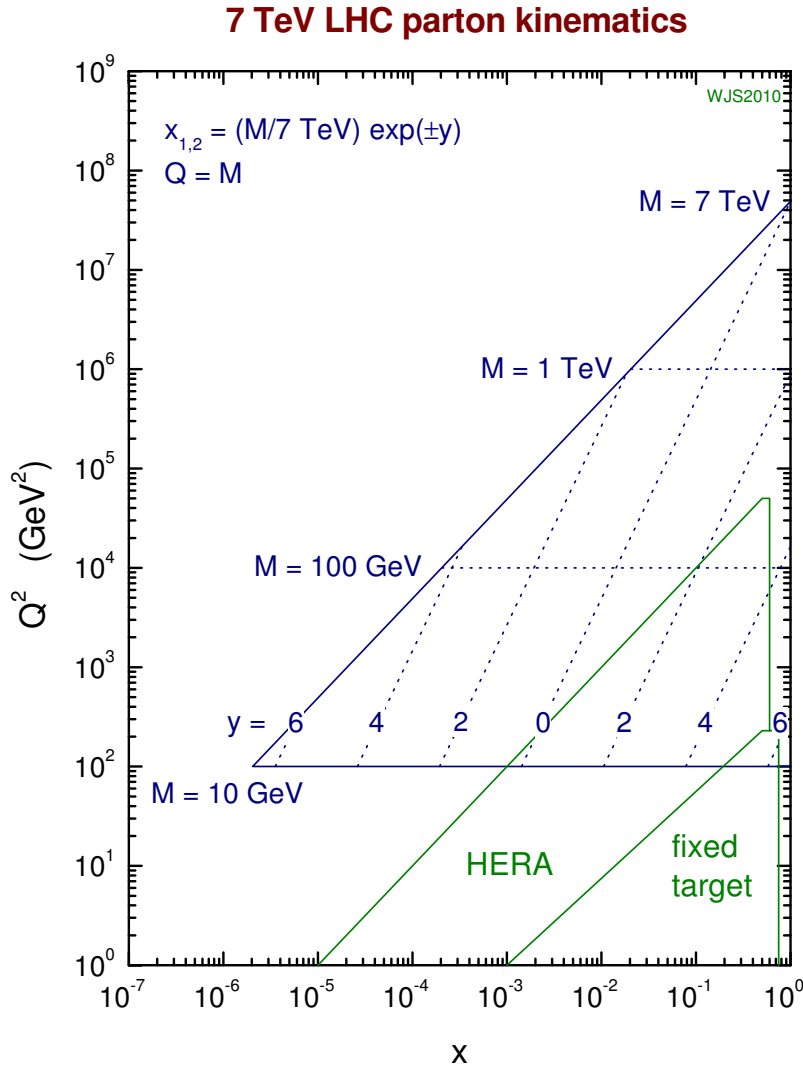
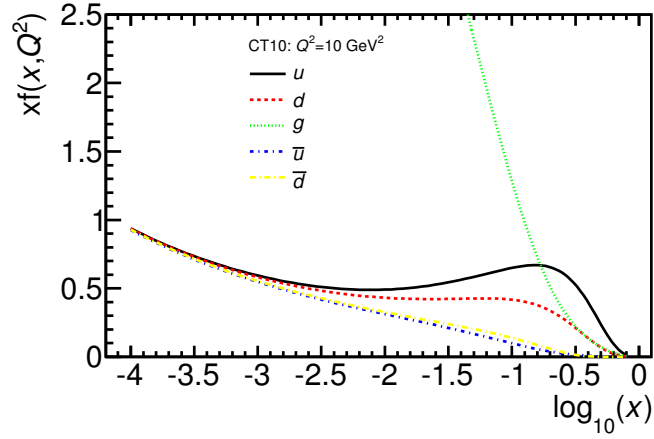
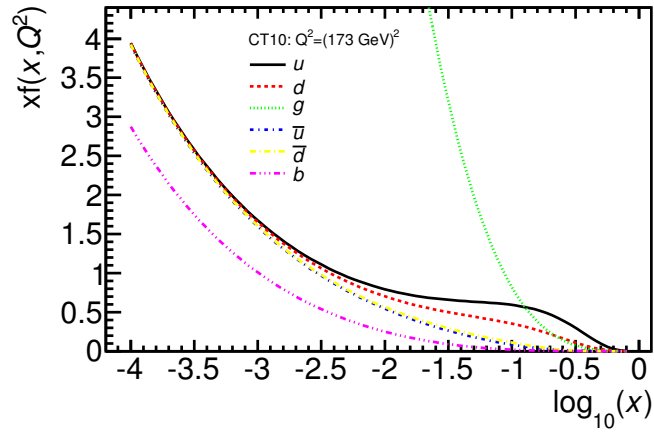


**Figure 1.7:** The approximate sensitive region to PDFs is shown in the parton  $x$ - $Q^2$  kinematic plane for data from the LHC at  $\sqrt{s} = 7$  TeV, along with the regions, where pre-LHC measurements either constrain or are expected to constrain PDFs [33].

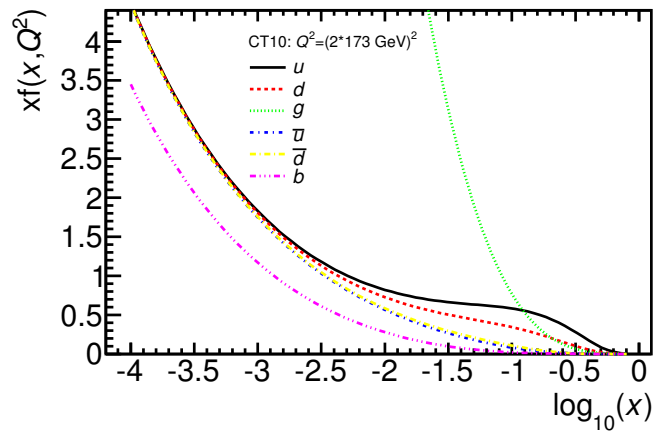
at the HERA collider. The NNPDF [39, 40] group applies a neural network approach to determine PDFs with unbiased parameterization assumptions. All groups deliver PDFs for all different quark flavors and the gluon in a proton. The PDFs provided by the different groups differ in the data used, the value of  $\alpha_S$ , and the values of quark masses. In Table 1.2 the datasets, that are used by the various PDF groups, are listed. The CT10, MSTW2008, GJR08 and NNPDF PDF groups provide PDFs in the FFNS with three, four, or five flavors or in the VFNS. The HERAPDF PDF group provides PDF sets only in the VFNS, while the ABM11 group provides PDFs only in the FFNS with three, four, or five flavors. Figure 1.8 shows an example for the PDFs of the proton using the CT10 PDF set at three different  $Q^2$  values. The valence-quark fraction is visible in the bumps of the  $u$ - and  $d$ -quark PDFs at high values of  $x$ . Valence quarks carry most of the momentum of a proton. Gluons dominate at large  $Q^2$ , especially for small values of  $x$ .



(a)



(b)



(c)

**Figure 1.8:** The CT10 parton distribution functions [35] for up quarks (black), down quarks (red), gluons (green), up antiquarks (blue), down antiquarks (yellow), and bottom quarks (pink) at (a)  $Q^2 = 10 \text{ GeV}^2$ , (b)  $Q^2 = (173 \text{ GeV})^2$  for single top-quark production, and at (c)  $Q^2 = (2 \cdot 173 \text{ GeV})^2$  for top-quark pair production.

**Table 1.2:** List of the used PDFs. The NLO PDF set is used from all mentioned PDFs. HERA I corresponds to HERA DIS data from 1992 to 2000 and HERA II from 2002 to 2007 [34]. Fixed target corresponds to fixed target DIS and DY data.

PDF set	$\alpha_S$	Used data
CT10	0.118	HERA (I & II), fixed target, Tevatron W,Z & jets
ABM11	0.109	HERA (II), fixed target
MSTW2008	0.120	HERA (I), fixed target, Tevatron W,Z & jets
NNPDF 2.3	0.119	HERA (II), fixed target, Tevatron/LHC W,Z & jets
GJR08	0.115	HERA (II), fixed target, Tevatron jets
HERAPDF 1.5	0.118	HERA (I & II)

## 1.2 The top quark

The top quark is the heaviest fundamental particle known so far. It was discovered in 1995 in  $p\bar{p}$  collisions at a center-of mass energy of  $\sqrt{s} = 1.8$  TeV at the Tevatron accelerator located at the Fermi National Accelerator Laboratory, USA, by the CDF and DØ experiments [1, 2]. The existence of the top quark was already predicted by the SM in 1977, when the  $b$  quark was discovered at Fermilab [41]. Therefore, the discovery of a top quark was a great success for the SM. Only the top quark mass and the relevant CKM matrix elements  $V_{td}$ ,  $V_{ts}$ , and  $V_{tb}$  are not predicted by the SM and need to be measured.

The mass of the top quark is measured to be  $m_t = 173.34 \pm 0.27 \pm 0.71$  GeV [3], combining the results of the CDF and DØ experiments at the Tevatron and the ATLAS and CMS experiments at the LHC. Thus, the top quark is almost as heavy as a gold atom and about 40 times heavier than the  $b$  quark. Due to the large mass the decay width of the top quark  $\Gamma_t \propto m_t^3/m_W^3$  [42] is also very large with  $\Gamma_t = 2.0_{-0.6}^{+0.7}$  GeV [12], resulting into a short life time  $\tau \approx 3 \times 10^{-25}$  s. The typical strong interaction time scale to form hadronic states,  $\Lambda_{\text{QCD}}^{-1} \sim 10^{-23}$  s [43], is much larger than the lifetime of the top quark. Thus, the top quark is the only quark, that decays before forming hadrons, making it a quasi-free quark. Therefore, precise predictions of the top quark properties can be made using perturbation theory. By measuring top-quark properties it is possible to perform precise tests of the SM and to search for physics beyond the SM.

The predicted decay of the top quark is determined by the CKM matrix elements  $V_{td}$ ,  $V_{ts}$ , and  $V_{tb}$ , as can be observed in Equation 1.3. In the SM, unitarity of the three-generation CKM matrix is assumed. Therefore, the matrix elements  $V_{td}$ ,  $V_{ts}$ , and  $V_{tb}$  can be determined indirectly from measurements of other CKM matrix elements. The 90% C.L. for these CKM matrix elements are [12]:

$$\begin{aligned}
 |V_{td}| &= 0.00836 & - & 0.00896, \\
 |V_{ts}| &= 0.0399 & - & 0.0415, \\
 |V_{tb}| &= 0.999100 & - & 0.999167.
 \end{aligned}$$

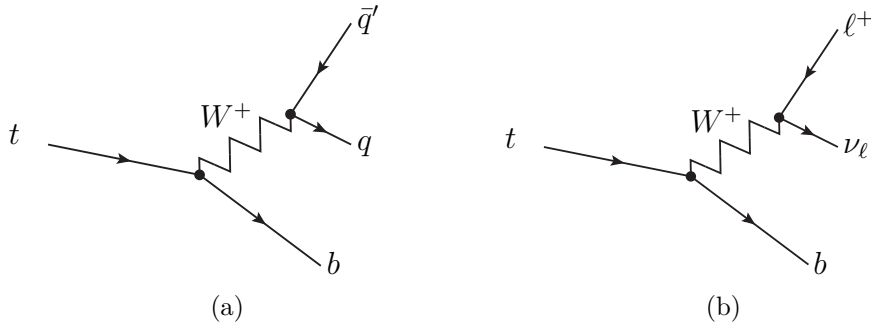


**Figure 1.9:** The decay of a top quark into a  $W$  boson and a  $b$  quark. In Panel (a) the hadronic decay of the  $W$  boson into a quark-antiquark pair is shown. The leptonic decay of the  $W$  boson into a charged lepton and its corresponding lepton neutrino is illustrated in Panel (b).

Thus,  $|V_{tb}|$  is close to one, and the top quark almost exclusively decays into a  $W$  boson and a  $b$  quark with  $\mathcal{B}(t \rightarrow Wb) \approx 100\%$ . Decays of the top quark into  $d$  or  $s$  quarks are suppressed due to the small values for  $|V_{td}|$  and  $|V_{ts}|$ . A direct measurement of the CKM matrix element  $|V_{tb}|$  without assuming unitarity is one of the topics of this thesis and will be introduced later.

The possible final states of top-quark production are determined by the possible decay modes of the  $W$  boson: the hadronic decay mode  $W \rightarrow q\bar{q}$  and the leptonic decay mode  $W \rightarrow \ell\nu$  where  $\ell$  depicts all lepton flavors  $e$ ,  $\mu$ , and  $\tau$ . The decay chains of the top quark are shown in Figure 1.9. The hadronic decay mode has a branching ratio of 67.6% and the leptonic decay mode a ratio of 32.4%, respectively.

### 1.2.1 Production via the strong interaction

At hadron colliders top quarks are mainly produced in top-quark and top-antiquark pairs ( $t\bar{t}$ ) via the strong interaction. There are two possible initial states at LO for the  $t\bar{t}$  production: gluon-gluon fusion ( $gg$ ) and quark-antiquark annihilation ( $q\bar{q}$ ). The corresponding LO Feynman diagrams for this process are shown in Figure 1.10. For the gluon fusion process, there are three possible diagrams (Fig. 1.10(a), 1.10(b), and 1.10(c)), while the  $q\bar{q}$  annihilation is depicted in Fig. 1.10(d). To produce a  $t\bar{t}$  pair, the partonic center-of-mass energy squared must be at least  $\hat{s} \geq 4m_t^2$ . Using  $\hat{s} = x_a x_b s$ , the average momentum fraction  $x$  of the interacting partons  $a$  and  $b$  is approximately  $x \approx 2m_t/\sqrt{s}$  corresponding to  $x = 0.050$  at the LHC with  $\sqrt{s} = 7$  TeV. Comparing the PDFs at this scale and momentum fraction in Figure 1.8(c), it can be seen, that the gluon distribution increases more steeply towards low  $x$  than the quark distributions and contributes most at  $x = 0.050$  ( $\log(x) = -1.3$ ). The contribution of antiquarks on the other hand is very small. Therefore, the  $t\bar{t}$  production via gluon fusion dominates at the LHC.

The  $t\bar{t}$  production cross section was recently calculated at NNLO precision with the top++2.0 [44–49] program using the MSTW2008 NNLO PDF set [50]. In addition, the result is improved with the resummation of large logarithmic terms due to soft-gluon radiation at next-to-next-to-leading logarithm (NNLL) accuracy. The  $t\bar{t}$

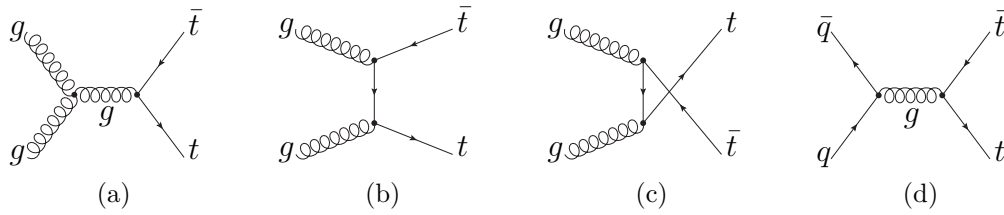


**Figure 1.10:** Top-quark pair production via the strong interaction at hadron colliders at leading order. Panels (a) to (c) show the Feynman diagrams of  $t\bar{t}$  production via gluon fusion. The production via quark-antiquark annihilation is depicted in Panel (d).

cross section for  $pp$  collisions at a centre-of-mass energy of  $\sqrt{s} = 7$  TeV is:

$$\sigma^{\text{NNLO+NNLL}}(t\bar{t}) = 177.31_{-5.99}^{+4.56} (\text{scale})_{-5.24}^{+5.45} (m_t) \pm 9.02 (\text{PDF} + \alpha_S) \text{ pb}$$

for a top-quark mass of 172.5 GeV. The PDF and  $\alpha_S$  uncertainties are calculated using the PDF4LHC prescription [51] with the MSTW2008 68% CL NNLO, CT10 NNLO [52] and NNPDF2.3 NNLO 5 flav. FFNS PDF sets. The scale uncertainty is evaluated by varying  $\mu_r$  and  $\mu_f$  independently by a factor of 2 and 0.5.

$t\bar{t}$  production is experimentally studied in three different decay modes: The  $W$  bosons of both top-quark decays can decay hadronically. This is called the fully-hadronic channel and occurs with a probability of 45.7%. If one of the  $W$  bosons decays leptonically, this is called the semi-leptonic channel and has a probability of 43.8%. The di-lepton channel specifies the case, where both  $W$  bosons decay leptonically. This channel has the lowest probability with 10.5%, but it has a clean final state. Amongst other measurements, the  $t\bar{t}$  production cross section was measured by the ATLAS collaboration at the LHC with  $\sqrt{s} = 7$  TeV in the di-leptonic channel to be  $\sigma(t\bar{t}) = 182.9 \pm 3.1$  (stat.)  $\pm 4.2$  (syst.)  $\pm 3.6$  (lum.)  $\pm 3.3$  (LHC beam) pb using a data sample corresponding to an integrated luminosity of  $4.6 \text{ fb}^{-1}$  [53]. The measurement is consistent with the NNLO+NNLL calculation quoted above.

## 1.2.2 Electroweak production

Top quarks can also be produced singly via the weak interaction involving the  $Wtb$  vertex. In 2009 the Tevatron experiments CDF and DØ measured singly produced top quarks for the first time [4, 5]. There are three possible production modes in the SM which are characterized by the virtuality of the  $W$  boson with a four-momentum  $q$  in the production.

- $t$ -channel or  $tq/\bar{t}q$ : A space-like  $W$  boson ( $q^2 \leq 0 \text{ GeV}^2$ ) interacts with a  $b$  quark in the proton sea, thus producing a top quark, see Fig. 1.11(a). The  $t$ -channel is also referred to as  $W$ -gluon fusion because the  $b$  quark arises from the gluon splitting into  $b\bar{b}$ , see Fig. 1.11(b). If the chosen PDF set provides a  $b$ -quark PDF, the calculation is performed following the Feynman diagram in Fig. 1.11(a) and is called 5-flavor scheme (5FS). A calculation with the gluon in the initial state as shown in Fig. 1.11(b) based on a PDF set without a  $b$ -quark PDF is called 4-flavor scheme (4FS). In the 4FS the  $b$ -quark is treated

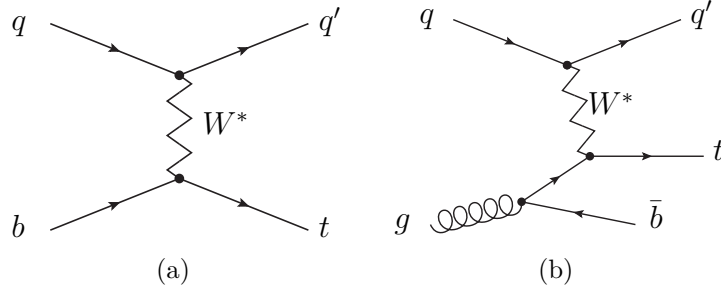


**Figure 1.11:** Electroweak single top-quark production in the  $t$ -channel at hadron colliders. The LO Feynman diagram is shown for the (a) 5-flavor scheme and (b) 4-flavor scheme.

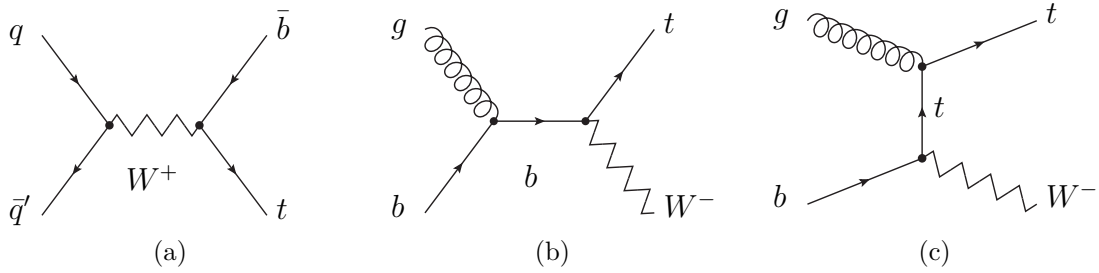


**Figure 1.12:** Representative LO Feynman diagrams of the electroweak single top-quark production at hadron colliders in the (a)  $s$ -channel and in the  $Wt$ -channel ((b) and (c)).

as a massive quark in the matrix element. The  $t$ -channel production mode is the dominant source of single top-quarks at the LHC.

- $s$ -channel or  $t\bar{b}/\bar{t}b$ : This production mode is of a Drell-Yan type where a quark and an antiquark annihilate to a time-like  $W$  boson with  $q^2 \geq (m_t + m_b)^2$ . It is depicted in Fig. 1.12(a).
- $Wt$ -channel: The top quark is produced in association with a real  $W$  boson ( $q^2 = M_W^2$ ), as shown in Fig. 1.12(b) and Fig. 1.12(c). One of the initial quarks is a  $b$ -quark from the parton sea inside the proton. The calculation can be done in the 4FS or the 5FS depending on the chosen PDF set. At LHC energies the  $Wt$  production supersedes the  $s$ -channel production.

All single top-quark production cross sections are proportional to  $|V_{tb}|^2$  (compare Equation 1.3). Therefore, the cross sections have a direct sensitivity to  $|V_{tb}|$  which is one of the free parameters of the SM.

For all production modes calculations exist at NLO+NNLL accuracy. The  $t$ -channel single top-quark production cross section was calculated in Ref. [54] using the 5FS and the MSTW2008 NNLO PDF set. Here, the renormalization  $\mu_r$  and factorization scale  $\mu_f$  are set to  $m_t$ . The inclusive cross sections for the top quark and the top antiquark for  $m_t = 172.5$  GeV in  $pp$  collisions with  $\sqrt{s} = 7$  TeV correspond to:

$$\begin{aligned}\sigma^{\text{NLO+NNLL}}(tq) &= 41.9^{+1.6}_{-0.2}(\text{scale}) \pm 0.8(\text{PDF}) \text{ pb} \quad \text{and} \\ \sigma^{\text{NLO+NNLL}}(\bar{t}q) &= 22.7 \pm 0.5(\text{scale})^{+0.7}_{-0.9}(\text{PDF}) \text{ pb}.\end{aligned}$$

The theoretical uncertainties arise from the dependence on the scale as well as from PDF uncertainties. The scale uncertainty is estimated by varying the scale by a factor of two between  $m_t/2$  and  $2m_t$ . The PDF uncertainty at 90% confidence level (CL) provided by the MSTW group is used as PDF uncertainty. Recently, first NNLO corrections to the  $t$ -channel single top-quark productions were provided [55]. The results show, that the NNLO corrections to the NLO+NNLL results are expected to be small. The  $t$ -channel single top-quark production has already been measured by the ATLAS collaboration in 2011 using  $1 \text{ fb}^{-1}$  of LHC  $pp$  collision data at  $\sqrt{s} = 7 \text{ TeV}$  [56]. The result of  $\sigma(tq + \bar{t}q) = 83 \pm 4(\text{stat.})_{-19}^{+20}(\text{syst}) \text{ pb}$  is in good agreement with the NLO+NNLL prediction.

The  $s$ -channel single top-quark production cross section is calculated at NLO+NNLL precision using the MSTW2008 NNLO PDF set. Again, the scales are set to  $m_t$ . The results for  $m_t = 172.5 \text{ GeV}$  at  $\sqrt{s} = 7 \text{ TeV}$  are [57]:

$$\begin{aligned}\sigma^{\text{NLO+NNLL}}(t\bar{b}) &= 3.19 \pm 0.06(\text{scale})_{-0.10}^{+0.13}(\text{PDF}) \text{ pb} \quad \text{and} \\ \sigma^{\text{NLO+NNLL}}(\bar{t}b) &= 1.44 \pm 0.01(\text{scale})_{-0.04}^{+0.03}(\text{PDF}) \text{ pb}.\end{aligned}$$

The uncertainties are evaluated following the prescription above. Due to the small cross section,  $s$ -channel single top-quark production will be a challenge to observe at the LHC. The  $s$ -channel single top-quark production was observed at the Tevatron collider by the  $D\bar{O}$  experiment and CDF experiments in 2014 using  $9.7 \text{ fb}^{-1}$  of  $p\bar{p}$  collision data at  $\sqrt{s} = 1.96 \text{ TeV}$  [58].

Since the  $Wt$ -channel single top-quark production has a gluon and a  $b$  quark in the initial state, the production cross-section is the same for top quark and top antiquark. The total production cross-section is calculated with a scale of  $\mu = m_t$  and the MSTW2008 NNLO PDF set for  $m_t = 172.5 \text{ GeV}$  at  $\sqrt{s} = 7 \text{ TeV}$  to be [59]:

$$\sigma^{\text{NLO+NNLL}}(Wt) = 15.7 \pm 0.4(\text{scale})_{-1.2}^{+1.0}(\text{PDF}) \text{ pb}.$$

Here, the uncertainties are again evaluated as described for the cross-section calculation of  $t$ -channel single top-quark production. The  $Wt$ -channel was observed for the first time at the LHC by the CMS collaboration in 2012 using  $12.2 \text{ fb}^{-1}$  of  $pp$  collisions at  $\sqrt{s} = 8 \text{ TeV}$  [60].

### 1.3 $t$ -channel single top-quark production

Single top-quark production was discovered at the Tevatron in 2009 combining  $t$ -channel and  $s$ -channel single top-quark production at the same time to achieve the highest possible event rate. At the Tevatron the predicted cross section for both production modes are of a similar size. Due to the overall small production rate, the precision of the measured  $t$ -channel single top-quark production cross-section is limited by the available data statistics. The latest and most precise value is  $\sigma(tq + \bar{t}q) = 3.07_{-0.49}^{+0.54} \text{ pb}$  [61], reaching a precision of about 17%. The measurement was performed by the  $D\bar{O}$  experiment using  $9.7 \text{ fb}^{-1}$  of  $p\bar{p}$  collision data at  $\sqrt{s} = 1.96 \text{ TeV}$ . At the LHC, the  $t$ -channel single top-quark production has a higher cross

section compared to the Tevatron which increases the number of events after event selection from about 400 events [61] at the Tevatron to about 5500 events at the LHC using  $4.59 \text{ fb}^{-1}$  at  $\sqrt{s} = 7 \text{ TeV}$ . The large number of candidate events opens the possibility to not just proof the existence of the process but also measure its characteristics precisely.

In this section the sensitivity of the *t*-channel single top-quark process to the SM input  $|V_{tb}|$ , to PDFs, and to models beyond the SM is shown for the cross-section value as well as some kinematic top-quark distributions e.g. the polarization of the top quark.

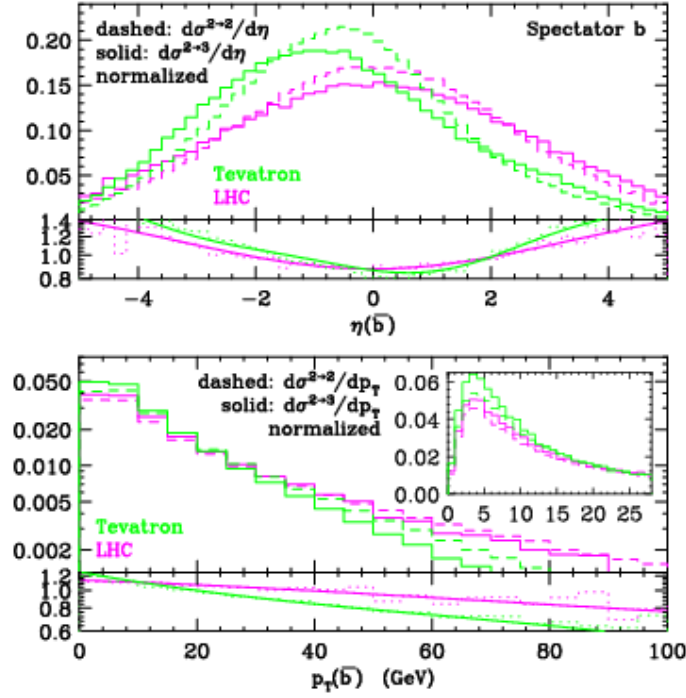
### 1.3.1 Characteristics of the production process

As mentioned above, the perturbative QCD calculation of the *t*-channel single top-quark cross section can be performed following the 5FS or the 4FS. The representative LO Feynman diagrams are shown in Fig. 1.11(a) for the 5FS and in Fig. 1.11(b) for the 4FS. If the calculation were performed at all orders using both approaches separately, the results would be the same. So far, the NLO+NNLL calculation only exists using the 5FS. Comparisons between the 4FS and the 5FS were performed at NLO accuracy e.g. in Ref. [62, 63]. Here, an agreement of about 5% for the cross-section calculation was found. There are further differences between the calculations when looking at the final-state particles.

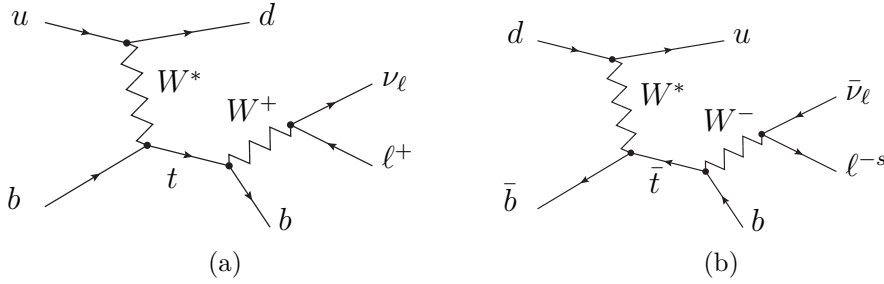
While the 5FS scheme greatly simplifies the calculation and gives stable results for the inclusive cross section, effects related to the “spectator *b*”-quark enter the calculation at NLO precision only [62]. In the 5FS, the mass of the initial-state *b* quark has to be neglected in the hard process calculation due to factorization. In case of the 4FS,  $m_b \neq 0$  appears explicitly in the hard process calculation providing a more realistic description of the kinematic properties of the spectator *b*-quark. Therefore, the 4FS calculation is preferred for fully exclusive studies [64]. The choice of the renormalization and factorization scales in the 4FS calculation is driven by the heavy quark line. In Ref. [62] the smallest dependence on the scale choice is found for a scale of  $\mu = m_t/4$  for the heavy quark line and  $\mu = m_t/2$  for the light quark line.

Fig. 1.13 shows a comparison of the 5FS and the 4FS calculation in the transverse momentum ( $p_T$ ) and in the pseudo rapidity ( $\eta$ ) distribution of the spectator *b*-quark for the Tevatron at  $\sqrt{s} = 1.96 \text{ TeV}$  and the LHC with  $\sqrt{s} = 14 \text{ TeV}$ . It can be seen, that the result of the 4FS calculation predicts a softer and more forward spectator *b*-quark compared to the 5FS calculation. The measurement of the inclusive cross section is sensitive to the *b*-quark PDF, as this is an ingredient in the 5FS calculation providing the best result for the inclusive cross section. By measuring the spectator *b*-quark, the *t*-channel process is also sensitive to the *b*-quark PDF, if compared to the 5FS prediction for the spectator *b*-quark. This measurement might be possible in the future. Currently, it is challenging due to the large background from  $t\bar{t}$  production in the event signature.

At the LHC, the production cross section in the *t*-channel production mode is different for top quarks and top antiquarks. Figure 1.14 shows the LO Feynman



**Figure 1.13:** Shape comparison in the transverse momentum (lower plot) ( $p_T$ ) and the pseudorapidity (upper plot) ( $\eta$ ) of the 4FS and 5FS calculation of the spectator  $b$ -quark at NLO precision [62]. The 5FS calculation is plotted with dashed lines and the 4FS calculation is plotted in solid lines. The green lines represent the prediction for the Tevatron with  $\sqrt{s} = 1.96$  TeV and the purple line the LHC with  $\sqrt{s} = 14$  TeV.



**Figure 1.14:** Representative LO Feynman diagrams of (a) single top-quark production and (b) single top-antiquark production via the  $t$ -channel exchange of a virtual  $W^*$  boson including the decay chain of the top quark. In this illustration  $u$  depicts all up-type quarks and  $d$  all down-type quarks.

diagrams for  $tq$  and  $\bar{t}q$  production. The charge of the initial light quark is directly connected to the charge of the top quark. The momentum fraction  $x$  of the initial light quark is shown in Figure 1.15 for the  $u$  quark and the  $d$  quark for  $t$ -channel single top-quark and top-antiquark production. The typical momentum fraction is in the range of  $0.01 \lesssim x \lesssim 0.6$ , with a median of 0.19 for  $u$ -quarks and a median of 0.15 for  $d$ -quarks. In Fig. 1.8(b) it is shown, that the PDFs of the  $u$ - and  $d$ -quarks peak at momentum fractions of the order of 0.2 due to the contributions from valence

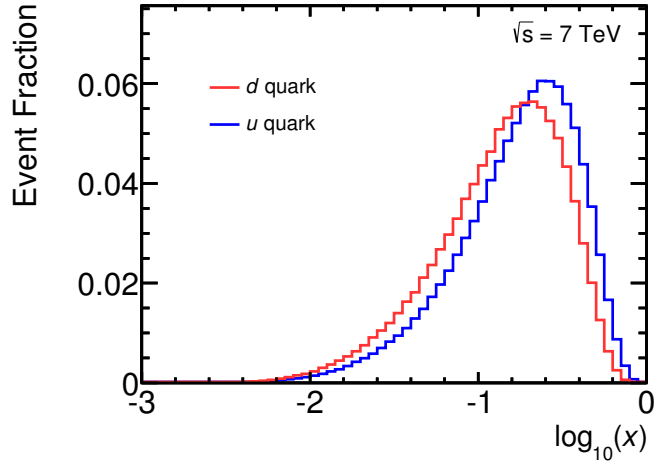


**Figure 1.15:** Momentum fraction  $x$  for the  $u$  quarks and  $d$  quarks in  $t$ -channel single top-quark events. The  $u$  quark belongs to the initial-state parton in the top-quark process, the  $d$  quark to the top-antiquark process.

quarks in the proton. This indicates, that the light quark in the initial state of the  $t$ -channel single top-quark production is mainly a valence quark.

Due to the valence-quark composition of the proton with two  $u$  quarks and one  $d$  quark, the probability to produce a single top quark is about twice as high than for a single top antiquark. While the predictions for the cross sections  $\sigma(tq)$  and  $\sigma(\bar{t}q)$  depend not only on the light quark PDFs but also on the gluon or  $b$  quark in the initial state, the cross-section ratio  $R_t \equiv \sigma(tq)/\sigma(\bar{t}q)$  is sensitive to the ratio of the  $u$ - and  $d$ -quark PDF of the chosen PDF set. For example, the MSTW2008 NNLO PDF set used in Ref. [54] predicts a value of  $R_t = 1.85$ . Thus, by measuring  $R_t$  separately, information on the  $u$ - and  $d$ -quark PDFs can be extracted. In addition, the cross sections  $\sigma(tq)$  and  $\sigma(\bar{t}q)$  provide complementary inputs in constraining PDFs in the PDF fits.

To evaluate the potential of a measurement, the cross-sections  $\sigma(tq)$  and  $\sigma(\bar{t}q)$  are calculated at NLO accuracy in the 5FS using MCFM [65] and HATHOR v2.0 [66] for various PDF sets. In these calculations the following values are used for the electroweak parameters:  $m(W) = 80.403$  GeV,  $m(Z) = 91.1876$  GeV,  $m_t = 172.5$  GeV, and the Fermi constant  $G_F = 1.16637 \cdot 10^{-5}$  GeV $^{-2}$ . The  $b$  quarks are regarded to be massless, and the renormalization and factorization scales are chosen to be  $\mu_r = \mu_f = m_t$ . The considered NLO PDF sets are included in the calculation using LHAPDF v5.8.9 [67].

Uncertainties on the choice of the factorization and renormalization scale, on the parameterization of the given PDF set, and on the dependence of the PDF on  $\alpha_S$  are evaluated. The scale uncertainty is estimated by scanning the complete  $\mu_r - \mu_f$ -plane between  $\frac{1}{2}\mu$  and  $2\mu$ . The difference between the maximal value in this plane and the nominal value is quoted as upward uncertainty, and the difference between the minimal value and the nominal value is quoted as downward uncertainty. The PDF uncertainty is estimated following the prescription of each PDF group for a

68% CL uncertainty. The dependence on  $\alpha_S$  is evaluated by varying  $\alpha_S$  by  $\pm 0.02$  around the nominal value corresponding to a 90% CL uncertainty. Then, the results are divided by a factor of 1.645 to estimate the 68% CL uncertainty.

The results including all systematic uncertainties are summarized in Table 1.3 for  $\sigma(tq)$ , in Table 1.4 for  $\sigma(\bar{t}q)$ , and in Table 1.5 for  $R_t$ . Fig. 1.16 gives an overview on the results for  $\sigma(tq)$ ,  $\sigma(\bar{t}q)$ , and  $R_t$ , as well as the combined cross section  $\sigma(tq + \bar{t}q)$ . It can be observed, that the predictions for the cross-section ratio  $R_t$  fluctuate about 10% between the different PDF sets. Thus, the measurement of  $\sigma(tq)$  and  $\sigma(\bar{t}q)$  and their ratio are interesting to improve the PDF predictions.

**Table 1.3:** Calculated  $\sigma(tq)$  values for different NLO PDF sets in the 5FS, listed with the uncertainties on the renormalization and factorization scales, the internal PDF uncertainties, and the uncertainties on  $\alpha_S$ . The statistical uncertainty is 0.2% for all PDF sets.

PDF set	$\sigma(tq)$	scale unc.	PDF unc.	$\alpha_S$ unc.
ABM11 (5 flav.)	45.25	-2.6% / 2.6%	-0.9% / 1.4%	-1.1% / 1.1%
CT10	41.02	-3.1% / 3.1%	-1.3% / 1.3%	-1.1% / 1.1%
CT10 (+ D0 W asym.)	40.48	-3.0% / 3.0%	-1.2% / 1.1%	-1.1% / 1.1%
GJR08 (VF)	42.21	-3.1% / 3.1%	-2.4% / 1.9%	—
HERAPDF 1.5	41.90	-3.2% / 3.2%	-2.3% / 4.0%	-1.9% / 1.7%
MSTW2008 (68% C.L.)	42.28	-2.9% / 2.9%	-1.7% / 1.6%	
NNPDF 2.3	42.08	-3.2% / 3.2%	-0.6% / 0.6%	-1.2% / 1.0%

**Table 1.4:** Calculated  $\sigma(\bar{t}q)$  values for different NLO PDF sets in the 5FS, listed with the uncertainties on the renormalization and factorization scales, the internal PDF uncertainties, and the uncertainties on  $\alpha_S$ . The statistical uncertainty is 0.2% for all PDF sets.

PDF set	$\sigma(\bar{t}q)$	scale unc.	PDF unc.	$\alpha_S$ unc.
ABM11 (5 flav.)	22.01	-2.6% / 2.6%	-1.4% / 1.8%	-1.6% / 1.7%
CT10	21.31	-3.1% / 3.1%	-1.8% / 2.0%	-1.3% / 1.3%
CT10 (+ D0 W asym.)	21.78	-3.0% / 3.0%	-1.5% / 1.5%	-1.3% / 1.4%
GJR08 (VF)	22.50	-3.2% / 3.2%	-3.3% / 2.4%	—
HERAPDF 1.5	21.18	-3.3% / 3.3%	-5.2% / 4.3%	-2.1% / 1.5%
MSTW2008 (68% C.L.)	22.43	-3.0% / 3.0%	-1.9% / 1.9%	
NNPDF 2.3	22.37	-3.3% / 3.3%	-1.0% / 1.0%	-1.4% / 1.5%

### 1.3.2 The CKM element $|V_{tb}|$

In the SM, single top-quarks are almost exclusively produced via the  $Wtb$  vertex. Therefore, the measurement of single top-quark production cross-section can be used to extract the CKM mixing matrix element  $|V_{tb}|$ , one of the SM input parameters.

**Table 1.5:** Calculated  $R_t$  values for different NLO PDF sets in the 5FS, listed with the uncertainties on the renormalization and factorization scales, the internal PDF uncertainties, and the uncertainties on  $\alpha_S$ . The statistical uncertainty on  $R_t$  is 0.2% for all PDF sets.

PDF set	$R_t$	scale unc.	PDF unc.	$\alpha_S$ unc.
ABM11 (5 flav.)	2.06	-0.2% / 0.1%	-1.2% / 0.9%	-0.5% / 0.5%
CT10	1.93	-0.2% / 0.1%	-2.5% / 2.1%	-0.2% / 0.2%
CT10 (+ D0 W asym.)	1.86	-0.2% / 0.1%	-1.6% / 1.4%	-0.3% / 0.2%
GJR08 (VF)	1.88	-0.1% / 0.1%	-2.5% / 2.7%	—
HERAPDF 1.5	1.98	-0.1% / 0.1%	-3.5% / 2.0%	-0.2% / 0.2%
MSTW2008 (68% C.L.)	1.89	-0.2% / 0.0%	-1.4% / 1.7%	
NNPDF 2.3	1.87	-0.2% / 0.1%	-1.1% / 1.1%	-0.8% / 0.1%

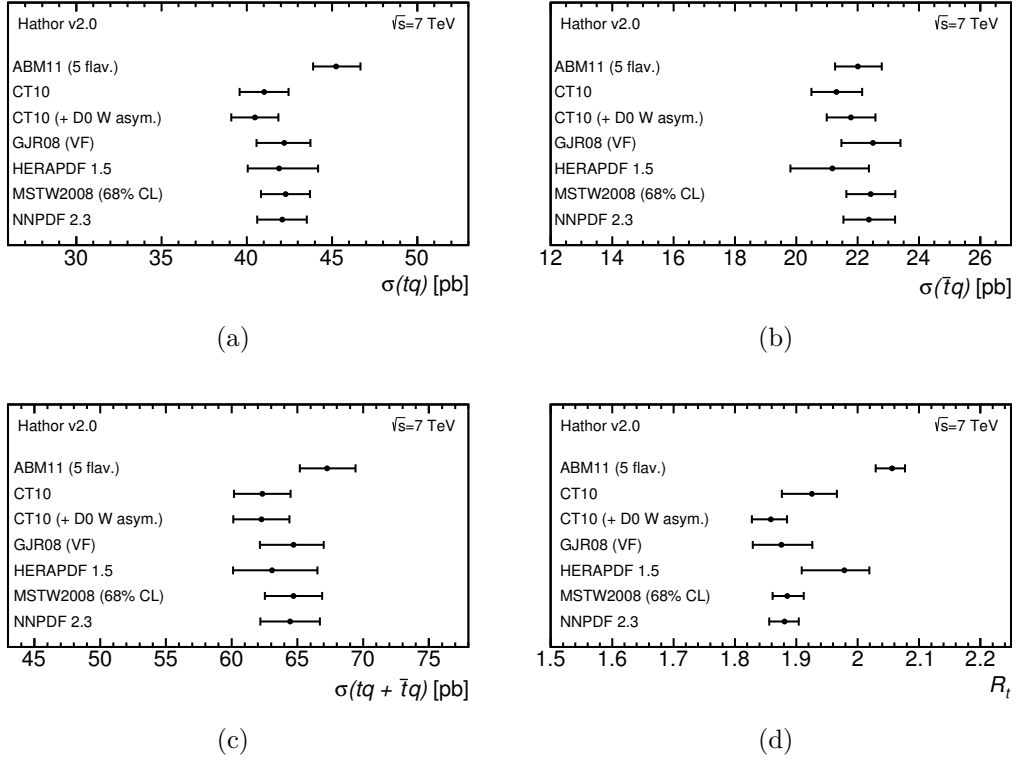


**Figure 1.16:** Calculated values for  $\sigma(tq)$ ,  $\sigma(\bar{t}q)$ ,  $\sigma(tq + \bar{t}q)$ , and  $R_t$  for different NLO PDF sets in the 5FS. The errors contain the uncertainties on the renormalization and factorization scales, the statistical uncertainties of the calculations, the dependencies on  $\alpha_S$ , and the uncertainties on the PDFs themselves.

From indirect measurements,  $|V_{tb}|$  is the best known CKM matrix element with a precision of  $\pm 0.01\%$  assuming three generations of SM fermions and unitarity of the  $3 \times 3$  CKM matrix. If the assumption of three generations is relaxed,  $|V_{tb}|$  is almost not constrained [68]. One way to study  $|V_{tb}|$  directly is to measure the branching

ratio of the top-quark decay  $t \rightarrow Wb$ . In practice, the branching fraction

$$\mathcal{R}_b \equiv \frac{\mathcal{B}(t \rightarrow Wb)}{\mathcal{B}(t \rightarrow Wq)} = \frac{|V_{tb}|^2}{|V_{td}|^2 + |V_{ts}|^2 + |V_{tb}|^2} \quad (1.8)$$

is measured, where  $q$  denotes any down-type quark ( $d, s, b$ ). In the SM  $\mathcal{R}_b$  equals  $|V_{tb}|^2$  due to the unitarity of the CKM matrix. If unitarity is not assumed,  $\mathcal{R}_b$  provides a relation between  $|V_{tb}|^2$  and  $|V_{td}|^2 + |V_{ts}|^2$ . A measurement of  $\mathcal{R}_b$  was performed by the DØ and the CDF experiment at the Tevatron [69, 70] as well as the CMS experiment at the LHC [71]. The most precise result is given by the measurement from CMS where the distribution of the number of  $b$ -jets in  $W$ +jets events is fitted to  $19.7 \text{ fb}^{-1}$  of  $pp$  collision data at  $\sqrt{s} = 8 \text{ TeV}$ . The result is  $\mathcal{R}_b = 1.014 \pm 0.032$ , where the uncertainty includes statistical and systematic uncertainties. The lower limit on  $\mathcal{R}_b$  is determined to be  $\mathcal{R}_b > 0.955$  at 95% CL. In terms of the CKM matrix elements the result can be written as [72]:

$$|V_{td}|^2 + |V_{ts}|^2 < 0.047 \cdot |V_{tb}|^2. \quad (1.9)$$

The  $t$ -channel production cross-section  $\sigma(tq + \bar{t}q)$  can be used to determine the value of  $|V_{tb}|$ , if one assumes  $|V_{tb}| \gg |V_{td}|$ ,  $|V_{tb}| \gg |V_{ts}|$ , and a SM-like left-handed coupling at the  $Wtb$  vertex. Here no assumption on the unitarity of the CKM matrix is made, providing a sensitivity to e.g. a fourth generation of quarks. The requirement of  $|V_{td}|$  and  $|V_{ts}|$  being small enters on the production side, due to possible productions via the  $Wtd$  and the  $Wts$  vertex, and in the branching ratio of the top-quark decay. Equation 1.9 from the  $\mathcal{R}_b$  measurement indicates, that this assumption is justified.

It is further possible to extract  $|V_{tb}|$  from measurements of  $t$ -channel single top-quark production without the assumption  $|V_{tb}| \gg |V_{td}|, |V_{ts}|$ . A strategy for this extraction is given in Ref. [73] where  $|V_{tb}|$ ,  $|V_{td}|$ , and  $|V_{ts}|$  are determined at the same time. This strategy is not applied in the presented analysis due to the strong bounds on  $\mathcal{R}_b$ .

To determine  $|V_{tb}|$ , the measured cross section  $\sigma(tq + \bar{t}q)$  is divided by the predicted SM cross-section value.

### 1.3.3 Kinematic properties and polarization of the top quark

Kinematic properties of the top quark, especially the transverse momentum  $p_T$  and the rapidity  $y$ , contribute to a basic understanding of  $t$ -channel single top-quark production. The  $p_T$  distribution of the top quark is particularly interesting since contributions from physics beyond the SM may appear at large values of  $p_T$  [74]. Predictions for  $p_T(t)$  and  $y(t)$  exist at NLO precision using the 4FS and 5FS calculations [62, 75–77]. Both distributions agree within 10% between both predictions. In case of  $y(t)$ , the 4FS prediction is more central than the 5FS prediction [62]. The transverse momentum  $p_T(t)$  is larger for the 4FS prediction compared with the 5FS prediction [62]. The top-quark  $p_T$  was recently calculated at NLO+NNLL precision [74].

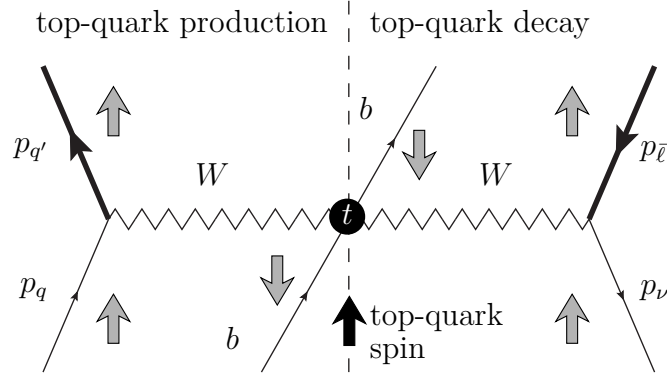


**Figure 1.17:** Spin correlation between top-quark production and top-quark decay for  $t$ -channel single top-quark production. The black circle denotes the top-quark rest frame, while the black arrow shows the direction of the top-quark spin. The grey arrows show the spin direction of the initial particles and the decay products. It can be seen, that the spin of down-type quark in the top production and the spin of the lepton in the top decay are maximally correlated with the top-quark spin. This sketch is taken from Ref. [75].

Another important characteristic of the top quark is its spin. In case of the  $t$ -channel single top-quark production, top-quarks are 100% polarized in their rest frame along the direction of the  $d$  quark in the final state because of the  $V - A$  structure of the charged-current weak interaction [78]. Due to the small lifetime of top-quarks, the spin information is not diluted by hadronization, but transferred to the decay products. Fig. 1.17 illustrates the spin correlation between the top-quark production and the top-quark decay for  $t$ -channel single top-quark production in the rest frame of the top quark. It shows, that the lepton from the top-quark decay as well as the light quark in the production are maximally correlated with the top-quark spin. The initial light quark mostly corresponds to the spectator light quark in the final state. Therefore, a good variable to investigate the polarization is the angle  $\theta$  between the lepton  $\ell$  and the light quark jet  $j$  in the rest frame (r.f.) of the top quark [75]:

$$\cos \theta(\ell, j)_{t.r.f.} = \frac{\vec{p}_j^* \cdot \vec{p}_\ell^*}{|\vec{p}_j^*| |\vec{p}_\ell^*|}. \quad (1.10)$$

The dependence of the  $t$ -channel production in the SM on the polarization variable  $\cos \theta(\ell, j)_{t.r.f.}$  can be expressed by the angular distribution [79]

$$\frac{1}{\sigma} \frac{d\sigma}{d(\cos \theta(\ell, j)_{t.r.f.})} = \frac{1}{2} \left( 1 + \frac{N_- - N_+}{N_- + N_+} \cos \theta(\ell, j)_{t.r.f.} \right) \quad (1.11)$$

where  $N_-$  ( $N_+$ ) is the number of left-handed (right-handed) polarized top quarks. The fraction  $\frac{N_- - N_+}{N_- + N_+}$  is close to one when looking at the inclusive phase space [75].

### 1.3.4 Sensitivity to physics beyond the SM

The  $t$ -channel single-top quark production cross-sections as well as  $|V_{tb}|$  and the kinematic observables described above are characteristic for the  $Wtb$  interactions in

the SM. If these observables are measured with high precision, it will be possible to test the predictive power of the SM. But  $t$ -channel single top-quark production is also interesting for searches of phenomena beyond the SM, and in some cases it is preferred to top-decay studies.

Undiscovered processes are characterized by the energy scale  $Q$  and appear at higher probability with rising partonic center-of-mass energy  $\sqrt{\hat{s}}$ . In single top-quark production undiscovered physics contributions scale with  $(\sqrt{\hat{s}}/Q)^n$  where  $n$  is a positive integer or zero, while it scales with  $(m_t/Q)^n$  in top-decay processes [80]. There are several possibilities for undiscovered physics contributions to influence single top-quark production: by inducing non-standard weak interactions, via loop effects, or by providing additional sources of single top-quark events [81]. The  $t$ -channel production mode is insensitive to additional heavy charged bosons due to the space-like momentum of the exchanged particle which is always virtual. Thus, the amplitude for a heavy particle is suppressed by its mass  $1/m^2$  [81]. Therefore, the focus in this section is on the introduction of additional interactions in an extension of the SM.

A natural extension of the SM would be the existence of a fourth SM-like generation of fermions. If a fourth pair of up-type and down-type quarks exists, the value for  $|V_{tb}|$  could be significantly smaller than one due to the new unitarity bounds of the  $4 \times 4$  CKM matrix [82]. Thus, the cross-section of the  $t$ -channel single top-quark production would deviate from the SM prediction. But recent experimental results disfavor the existence of a SM-like fourth generation of fermions as is discussed in Ref. [83, 84]. Therefore, the existence of heavy extra quarks is only possible in theories beyond the SM e.g. in Ref. [85].

Another ansatz for additional interactions beyond the SM is a modification of the charged-current weak interaction in the  $Wtb$  vertex. A common approach is the formulation of the most general  $\mathcal{CP}$ -conserving  $Wtb$  vertex with the effective Lagrangian density [86]:

$$\begin{aligned} \mathcal{L}_{Wtb} = & -\frac{g_w}{2\sqrt{2}}\bar{b}\gamma^\mu(V_L(1-\gamma^5)+V_R(1+\gamma^5))tW_\mu^- \\ & -\frac{g_w}{2\sqrt{2}}\bar{b}\frac{i\sigma^{\mu\nu}q_\nu}{M_W}(g_L(1-\gamma^5)+g_R(1+\gamma^5))tW_\mu^- + \text{h.c.}, \quad (1.12) \end{aligned}$$

with  $q \equiv p_t - p_b$  equals the momentum of the  $W$  boson,  $g_w$  the weak coupling constant, and  $\sigma^{\mu\nu} = [\gamma^\mu, \gamma^\nu]/2$ . The interaction term at tree level via  $V_L$  is included in the SM with  $V_L \equiv V_{tb} \approx 1$ . The couplings  $V_R$ ,  $g_L$ , and  $g_R$  are called ‘‘anomalous’’ and are all zero in the SM at tree level. If these couplings are different from zero due to undiscovered physics contributions, there is an effect on the  $t$ -channel production cross sections as well as on  $R_t$ , as discussed in detail in Ref. [86].

One special case for an additional interaction using the effective Lagrangian density is the possibility of flavor changing neutral currents (FCNC) in a scenario beyond the SM. To produce the  $tq$  or the  $tg$  final state, three different types of interactions are introduced: the strong FCNC interaction via a  $\bar{t}ug$  vertex, the electroweak FCNC interaction, where a top quark interacts with a  $u$  quark and one of the electroweak gauge bosons, and the four-fermion interaction, where the top quark interacts with three other quarks. The corresponding Feynman diagrams are

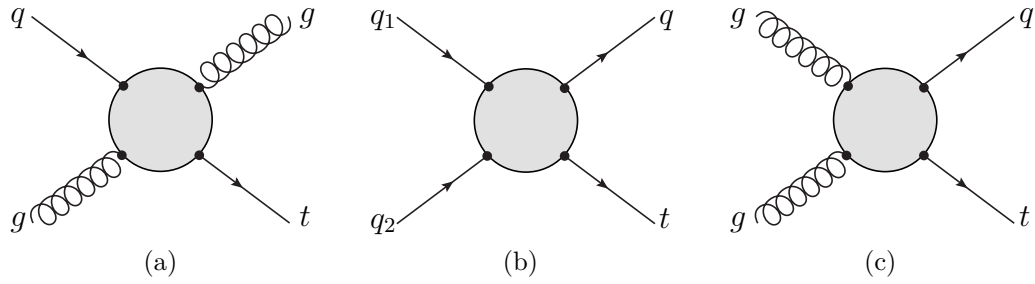


**Figure 1.18:** Representative LO Feynman diagrams of the  $tq$  and  $t\bar{q}$  production in the FCNC channels: (a)  $q\bar{q} \rightarrow t\bar{q}$  via the strong FCNC interaction, (b)  $q\bar{q} \rightarrow t\bar{q}$  via the strong and electroweak FCNC interaction as well as the four-fermion interaction, and (c)  $g\bar{g} \rightarrow t\bar{q}$  via the strong FCNC interaction [87]. In the Feynman diagrams  $q$ ,  $q_1$ , and  $q_2$  represent  $q = u, d, c, s, b$  and the respective antiquarks.

shown in Fig. 1.18. All quarks  $q$ ,  $q_1$ , or  $q_2$  represent all quark flavors except for the top quark. Additional contributions from the interactions shown in Fig. 1.18 not only change the cross sections of the single top-quark production, but also the kinematic properties of the produced top-quark [87].



# Chapter 2

## The ATLAS detector at the LHC

This chapter describes the experimental setup for the production and the detection of singly produced top quarks in  $pp$  collision. The  $pp$  collisions are provided by the Large Hadron Collider (LHC) [88] located at CERN, currently the world's most powerful collider with the highest center-of-mass energy. The measurement of the collision products is done by the ATLAS experiment [89]. In this chapter, the LHC and the accelerator chain at CERN, as well as the ATLAS detector are presented. Finally, the dataset recorded in 2011 is described, that is analyzed in this thesis.

### 2.1 The LHC

The LHC at CERN, near Geneva, is currently the largest particle accelerator in the world with a design center-of-mass energy of  $\sqrt{s} = 14$  TeV. It is a two-ring superconducting synchrotron with a circumference of 26.7 km located in a tunnel, that is on average 100 m below the surface. Protons or lead ions are brought to collisions in four experimental areas. In these areas four large detectors are set up: two general purpose detectors, ATLAS and CMS (Compact Muon Solenoid) [90], a  $b$ -physics experiment LHCb (Large Hadron Collider beauty) [91], and the heavy ion experiment ALICE (A Large Ion Collider Experiment) [92]. In addition, there are three smaller experiments. TOTEM (Total elastic and diffractive cross-section measurement) [93] and LHCf (Large Hadron Collider forward) [94] measure scattering processes close to the beam direction, while the MoEDAL (Monopol and Exotics Detector at the LHC) [95] experiment searches for magnetic monopoles.

A schematic view of the CERN accelerator complex is given in Fig. 2.1. At first, protons are extracted from hydrogen using an electric field. In a second step the resulting proton beam is accelerated to an energy of 50 MeV by the LINAC2 accelerator. The protons then enter the Proton Synchrotron Booster where they are accelerated to 1.4 GeV [96]. To completely fill the Proton Synchrotron (PS), the Booster injects protons six times to the PS, thus resulting into six proton bunches. The PS then divides the six proton bunches into 72 bunches with a length of 4 ns and a bunch spacing of 25 ns [97]. During this process, the proton bunches are accelerated to 25 GeV [97]. The last acceleration step before injecting into the LHC is done by the SPS (Super Proton Synchrotron) up to an energy of 450 GeV [98]. The SPS is

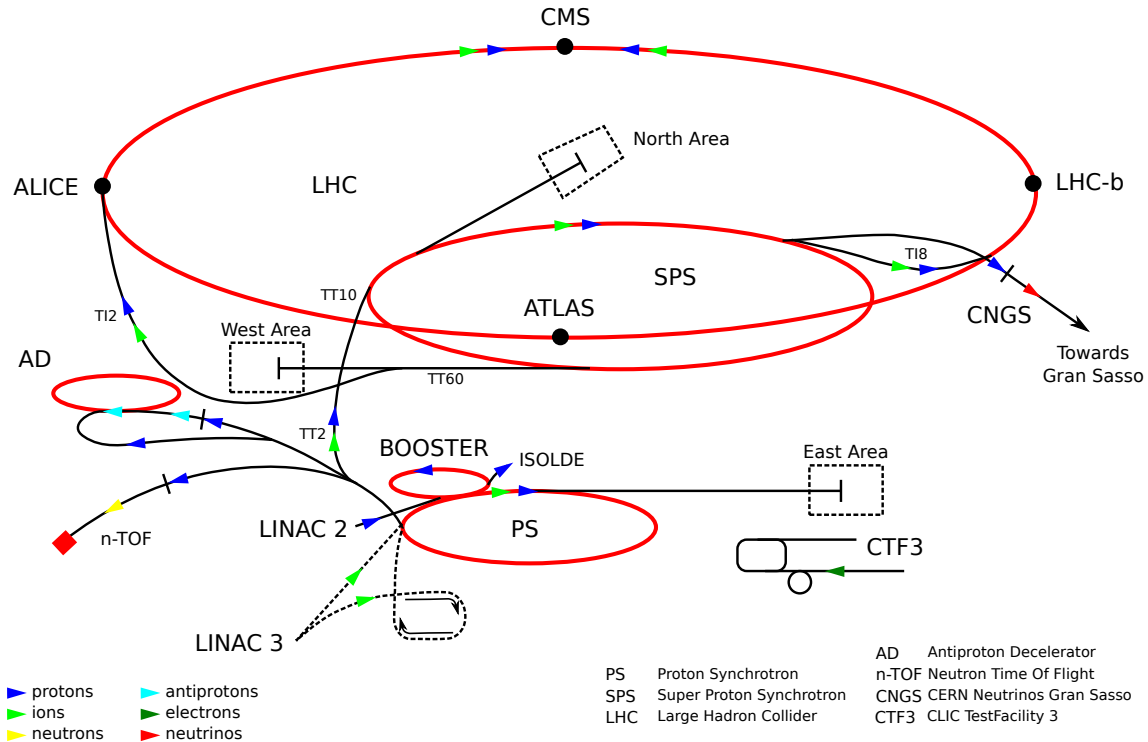


**Figure 2.1:** Schematic [99, 100] showing the accelerator complex at CERN. The path of the protons is represented by the blue arrows and the path of the ions by the green arrow. The Proton Synchrotron Booster is marked with BOOSTER in the figure.

filled with three proton fillings of the PS, resulting into 216 proton bunches. Via two injectors, one for each beam direction, the protons are then injected into the two rings of the LHC. Thus, the LHC is filled with its design configuration of 2808 proton bunches per beam. Each proton bunch consists of 115 billion protons and is accelerated to an energy of 7 TeV (design values).

In the design of the LHC [88] two important goals for the research of particle physics are taken into account: a high center-of-mass energy and a large instantaneous luminosity. Looking at Equation 1.5 it can be seen, that the number of events from rare physics processes increases with rising energy via the cross section of the each process and with a large integrated luminosity. The integrated luminosity is the integral of the instantaneous luminosity and thus increases faster if the instantaneous luminosity reaches higher values. Constrictive factors to achieve high values for the energy are the accelerating field to accelerate the proton beam and the magnetic field to keep the proton beam on the circular path. To reach an energy of 7 TeV per beam, acceleration cavities with an accelerating field strength of 5.5 MV/m and a magnetic dipole field of 8.33 T are necessary. The magnetic field is generated by superconducting electromagnets made from Niobium-Titanium, that are cooled by superfluid Helium to a temperature of 1.9 K.

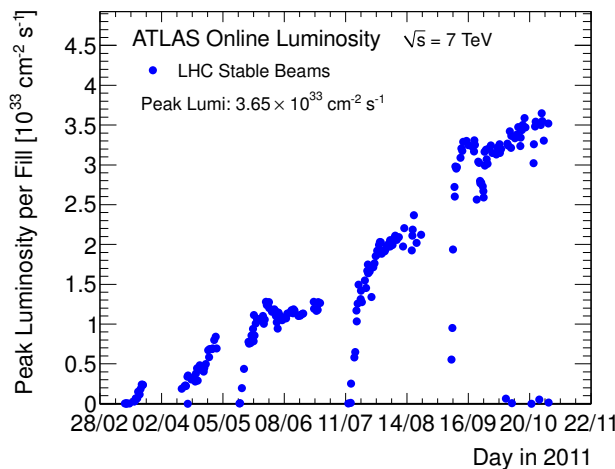
**Table 2.1:** Comparison of LHC parameters between the design values and the values during operation in 2011.

LHC parameter	2011	design
Beam energy	3.5 TeV	7 TeV
$N_b$	$\sim 135$ billions	$\sim 115$ billions
bunch spacing	50 – 75 ns	25 ns
$n_b$	up to 1380	2808
focus ( $\beta^*$ )	1.0 – 1.5 m	0.55 m
L	up to $3.65 \cdot 10^{33} \text{ cm}^{-2}\text{s}^{-1}$	$10^{34} \text{ cm}^{-2}\text{s}^{-1}$

The instantaneous luminosity depends on the following accelerator characteristics:

$$\mathcal{L} = \frac{\gamma}{4\pi} \frac{N_b^2 n_b f_{\text{rev}}}{\epsilon_n \beta^*} F, \quad (2.1)$$

where  $N_b$  is the number of protons per bunch,  $n_b$  is the number of bunches per beam, and  $f_{\text{rev}}$  is the revolution frequency of the protons circulating in the accelerator.  $\epsilon_n$  is the normalized transverse beam emittance,  $\beta^*$  is the value of the beta function at the collision point. The beta function defines the transverse envelope of the beam for every location in the accelerator.  $F$  is the geometric luminosity reduction factor, that depends on the crossing angle, the bunch length, and the transverse beam size at the interaction point (IP). All of these values are optimized for the circumference of the accelerator to reach a design instantaneous luminosity of  $\mathcal{L} = 10^{34} \text{ cm}^{-2}\text{s}^{-1}$ . A full account on the design of the LHC is given in Ref. [88] and an overview on the design parameters is given in Table 2.1.

**Figure 2.2:** The peak instantaneous luminosity per fill of the LHC during the 2011 data-taking period is shown [101]. The luminosity measurement was performed by the ATLAS experiment.

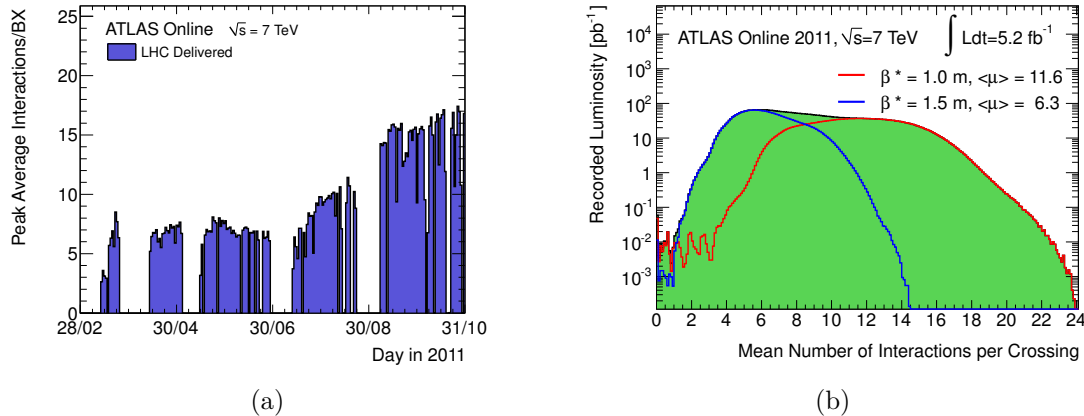


**Figure 2.3:** Panel (a) shows the average number of interactions per bunch crossing at the peak of the fill for each day in 2011 for data used in physics analyses [102]. The number of events per beam crossing is averaged over a short time period. In Panel (b), the mean number of interactions per bunch crossing for the recorded data in 2011 [103]. The mean number of interactions per crossing corresponds the mean of the poisson distribution on the number of interactions per crossing. The red line shows the distribution after the reduction of  $\beta^*$  to 1.0 m.

The first proton-proton collisions in the LHC took place in November 2009 with an energy of  $\sqrt{s} = 900$  GeV. In 2011, the LHC was operated at a beam energy of 3.5 TeV, resulting in  $\sqrt{s} = 7$  TeV. The operation parameters of the LHC in 2011 are compared to the design values in Table 2.1. During the year 2011, the performance of the LHC in instantaneous luminosity increased steadily, see Fig. 2.2. By improving the values for  $\beta^*$  from 1.5 m to 1.0 m, reducing the bunch spacing from 75 ns to 50 ns, and increasing the intensity of the beam, an instantaneous luminosity of  $\mathcal{L} = 3.7 \cdot 10^{33} \text{ cm}^{-2}\text{s}^{-1}$  was reached. Due to the steady rise in the beam intensity until September 2011 and the reduction of  $\beta^*$  in September 2011 the number of  $pp$  collisions in one bunch crossing, called pile-up events, increased. Therefore, the conditions between the different data-taking periods vary in the complete 2011  $pp$ -collision dataset, as can be seen in Fig. 2.3(a). Figure 2.3(b) shows the distribution of pile-up events for the complete 2011 dataset. The mean number of interactions per crossing increased by 5 events, when the  $\beta^*$  value was reduced to 1.0 m. The achieved values for the beam intensity  $N_b$  (compare Table 2.1) even exceeded the design values resulting in more pile-up events in the detectors than anticipated in their design.

## 2.2 The ATLAS experiment

An overview of the ATLAS detector [89] is shown in Fig. 2.4. It is located in a cavern about 80 m underground at the LHC ring. The detector is 46 m long, has a diameter of 25 m, and weighs over 7000 t. Due to its function as general purpose detector, the ATLAS detector needs to cover as much space around the

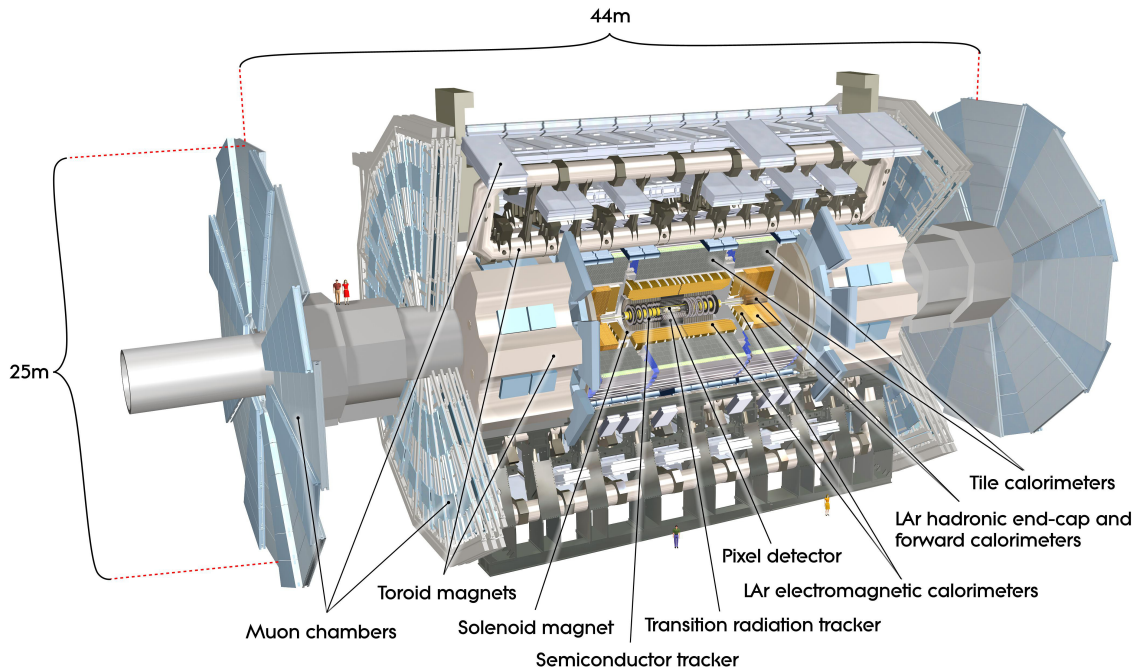


**Figure 2.4:** Computer-generated cut-away image of the ATLAS detector [89]. All sub detectors are pointed out with black lines.

IP as possible. It has a cylindrical form where the subsystems are layered around the interaction point. Therefore, all subsystems consist of a barrel detector part, where detecting layers are arranged at different radii from the beam axis, and a disk or end-cap part where detecting layers are placed perpendicular to the beam axis. Closest to the IP, a tracking system called Inner Detector is located consisting of the Pixel Detector, the Semiconductor Tracker (SCT), and the Transition Radiation Tracker (TRT). The Inner Detector is embedded in the field of the Solenoid Magnet. Outside of the tracking system the calorimeters are built, first the Liquid Argon (LAr) electromagnetic calorimeters and then the hadronic calorimeters (in Fig. 2.4 Tile calorimeters and LAr hadronic end-cap and forward calorimeters). The most outward subsystem is the Muon Spectrometer consisting of muon chambers. Toroid magnets provide a toroidal magnet field in the Muon spectrometer.

Table 2.2 lists the performance goals of the ATLAS detector for each subsystem. Small values for the resolution are necessary to identify the physics objects originating from the collisions and to measure their tracks, momentum, energy, and electric charge as precisely as possible. In the following, the functionality of each subsystem is briefly explained and the coordinate system of the ATLAS detector is introduced.

### 2.2.1 The ATLAS coordinate system

The ATLAS coordinate system is a right-handed Cartesian system with its origin in the nominal interaction point. The beam direction defines the  $z$  axis and the

**Table 2.2:** General performance goals of the ATLAS detector [89]. The units for  $E$  and  $p_T$  are in GeV.

Detector component	Required resolution	$\eta$ coverage
Inner Detector	$\sigma_{p_T}/p_T = 0.05\%/p_T \oplus 1\%$	$\pm 2.5$
EM calorimeter	$\sigma_E/E = 10\%/\sqrt{E} \oplus 0.7\%$	$\pm 3.2$
Hadronic calorimeter		
barrel and end-cap	$\sigma_E/E = 50\%/\sqrt{E} \oplus 3\%$	$\pm 3.2$
forward	$\sigma_E/E = 100\%/\sqrt{E} \oplus 10\%$	$3.1 <  \eta  < 4.9$
Muon spectrometer	$\sigma_{p_T}/p_T = 10\%$ at $p_T = 1$ TeV	$\pm 2.7$

$x$ - $y$  plane is transverse to the beam. The positive  $x$  axis points from the IP to the center of the LHC ring, while the  $y$ -axis points upward. To describe the position of particles in the detector the azimuthal angle  $\phi$  is used in the  $x$ - $y$  plane. The angle  $\phi$  is defined as the angle between the positive  $x$ -axis and the transverse momentum vector  $\vec{p}_T = (p_x, p_y)$  of the particle. The absolute value of the transverse momentum is mostly quoted as

$$p_T \equiv \sqrt{p_x^2 + p_y^2}. \quad (2.2)$$

The polar angle  $\theta$  is the angle between the particle vector and the positive  $z$  axis. The transverse energy

$$E_T \equiv E \sin \theta \quad (2.3)$$

is used for energies measured in the calorimeter. The consideration of a particle in the transverse plane is often used because the initial state has a transverse momentum of zero. Thus, in the transverse plane momentum conservation can be applied. Also, the resolution of the detector is best there. Instead of  $\theta$ , it is often preferred to use the rapidity  $y$  of a particle defined as:

$$y = \frac{1}{2} \ln \left( \frac{E + p_z}{E - p_z} \right). \quad (2.4)$$

If the mass of the particle is small compared to its energy,  $m \ll E$ , the rapidity  $y$  can be approximated with the pseudorapidity

$$\eta = \frac{1}{2} \ln \left( \frac{|\vec{p}| + p_z}{|\vec{p}| - p_z} \right) = -\ln \left( \tan \frac{\theta}{2} \right). \quad (2.5)$$

Thus, the angular distance between two particles in the detector originating from the IP is expressed as

$$\Delta R = \sqrt{(\Delta\eta)^2 + (\Delta\phi)^2}. \quad (2.6)$$

Using the definition of the pseudorapidity, the transverse energy  $E_T$  is also given by

$$E_T = E \cosh \eta. \quad (2.7)$$

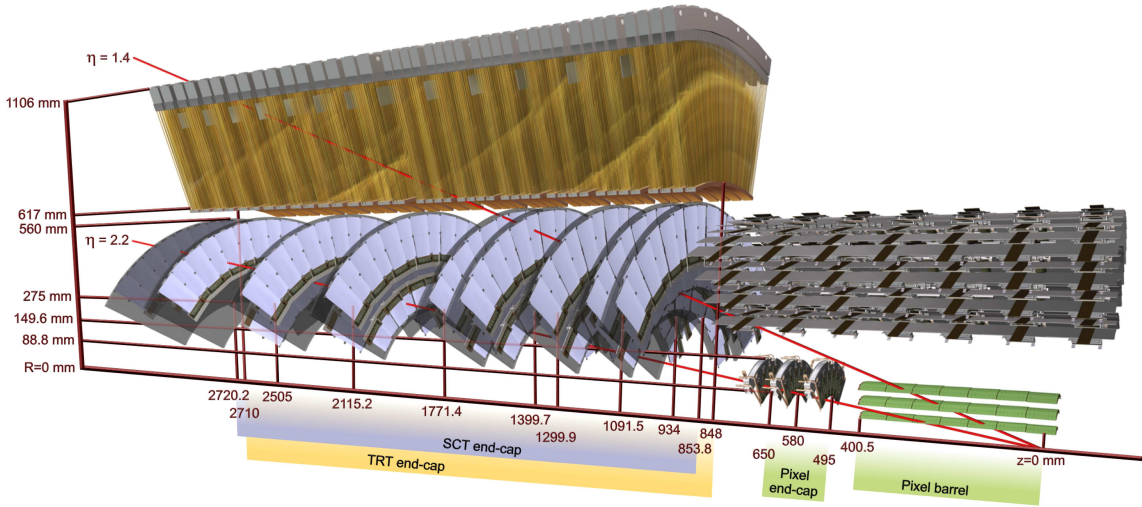


**Figure 2.5:** Computer-generated cut-away image of the Inner Detector [89]. All sub detectors are marked.

## 2.2.2 The Inner Detector

The tasks of the ATLAS Inner Detector [89] (ID) are the tracking of a large number of charged particles (up to 1000 particles per collision), the measurement of the track momenta, the identification of electrons, and the determination of the position of primary interaction vertices. In addition, the ID is used to identify jets originating from  $b$  quarks. All of these tasks of the ID are used in full in the presented analysis. In order to perform these tasks with a high precision, it is important to have a good spatial resolution in the ID.

The ID consists of two high-resolution semiconductor detectors, the Pixel detector and the SCT, as well as a straw tube tracking detector, the TRT. The layout of the ID is illustrated in Fig. 2.5. Here, one quarter of the ID is shown: the barrel and disks of the Pixel detector are closest to the IP, followed by the SCT. Both semiconductor detectors are surrounded by the TRT system. The ID has a diameter of 2.1 m and is 6.2 m long. It covers the  $R - \phi$  plane around the IP completely. On the  $z$  axis, measurements are provided up to a pseudorapidity of  $|\eta| < 2.5$ . The ID is embedded in a solenoid magnetic field with a magnetic strength of 2 T. This bends the path of a charged particle in the  $R - \phi$  plane, and thus enables the momentum measurement of tracks. In the following the design of subdetectors of the ID are described and their performance is reported.

### The Pixel detector

The Pixel detector [104] is the detector closest to the IP and consists of three pixel layers up to  $|\eta| < 2.5$ . Therefore, a charged particle crosses typically three pixel layers leaving three space points to construct a track. The main task of the pixel detector is the track reconstruction in an environment with a large track density due to the proximity of the detector to the IP. Therefore, it needs to have the best spatial resolution in the ID.

In the barrel region the pixel sensors are arranged on staves in concentric cylinders around the beam axis, the first one at a distance of 5.5 cm and the third at a distance of 12.25 cm from the beam axis. In the end-cap region, the sensors are arranged on disks as shown in Fig. 2.5. The pixel detector has the highest granularity of all subdetectors in ATLAS consisting of 1744 pixel sensors and in total about 80.4 million readout channels. The minimal pixel size on the pixel sensors is  $50 \times 400 \mu\text{m}^2$  in  $R-\phi \times z$ . The pixel size defines the intrinsic resolution of  $14 \mu\text{m}$  in the  $R-\phi$  plane and  $115 \mu\text{m}$  in  $z$  for the barrel and in  $R$  for the disks.

The experimental resolution depends additionally on the incident angle of the particle track and the momentum of the track. Finally, good alignment of the detector is necessary. In 2011, the alignment from Fall 2010 described in Ref. [105] was used. It is very close to the simulated perfect detector alignment. A resolution of up to  $15 \mu\text{m}$  in  $R-\phi$  plane is measured for tracks with  $p_{\text{T}} > 5 \text{ GeV}$  from 2010  $pp$  collisions at  $\sqrt{s} = 7 \text{ TeV}$  [106]. In 2011, the pixel detector was operated with a 99.8% efficiency [107].

### The Semiconductor Tracker

The SCT [89] structure is similar to that of the Pixel detector. It consists of a cylindrical barrel layers and disks. The SCT covers the radial region from 30 to 52 cm within  $|\eta| < 2.5$  and has 6.3 million readout channels. As sensors, silicon strips of a size  $80 \mu\text{m} \times 6.4 \text{ cm}$  in  $R-\phi \times z$  are used instead of pixel sensors. In the SCT, a charged particle crosses at least eight strip sensors corresponding to four space points because the layers are double-layered. The strip layers of one double layer are rotated by 40 mrad with respect to each other, so that the resolution along the strip, i.e. in  $z$  for the barrel layers, is improved. Also it facilitates pattern recognition, as ambiguities are avoided using the available 3D information of each hit. With this structure the SCT has an intrinsic resolution of  $17 \mu\text{m}$  in the  $R-\phi$  plane and  $680 \mu\text{m}$  in  $z$  for the barrel and in  $R$  for the disks.

As for the Pixel detector, the alignment of the SCT is very important, and a high precision alignment was achieved for 2011 measurements [105]. The data-taking efficiency of the SCT was 99.6% [107].

### The Transition Radiation Tracker

The TRT [89] covers the radial region from 55 to 108 cm within  $|\eta| < 2.0$ . In the TRT a charged track leaves typically 36 hits in polyamide tubes (straw tubes) with a diameter of 4 mm. The straw tubes are filled with a Xenon-based gas mixture, that is ionized by a charged particle passing through. The resulting electrons drift to an anode wire inside the tube due to the applied electric field. Thus, a signal can be measured. The TRT provides only  $R-\phi$  information, with an intrinsic accuracy of  $130 \mu\text{m}$ . In the barrel region the straw tubes are arranged in parallel to the beam axis. They are 144 cm long. In the end-cap part, the straw tubes are 37 cm long and are arranged radially in wheels. In total, the TRT has 351,000 readout channels.

Apart from just measuring the position of the tracks, the TRT also measures the transition radiation, that is emitted by the charged particles when entering the

gas. The amount of transition radiation is a good discriminator to differentiate an electron from a charged pion. Thus, the TRT provides an important information for the electron identification.

For the data-taking in 2011, the Fall 2010 alignment was used [105]. The resolution was measured using 2011  $pp$  collision data at  $\sqrt{s} = 7$  TeV. For tracks with a  $p_T > 15$  GeV the resolution was measured to be approximately  $118 \mu\text{m}$  in the barrel region and approximately  $132 \mu\text{m}$  in the end-cap region [105]. In 2011, the TRT had a data-taking efficiency of 99.2% [107].

### 2.2.3 Calorimeters

The ATLAS calorimeter system [89] is used to identify and measure the energy and direction of electrons, photons, jets, and missing transverse momentum. All of these objects, except for the photons, are essential for this thesis. Fig. 2.6 shows a view of the calorimeters used in ATLAS. The system covers a region up to a pseudorapidity of  $|\eta| < 4.9$  with several different techniques and designs due to the varying requirements for each region. All calorimeters are sampling calorimeters separating particle absorption in an absorber layer and readout in an active layer. In general, the calorimeters are divided by the kind of particle shower they measure. When a primary particle hits the absorber, it loses energy by bremsstrahlung or pair production in case of electromagnetic particles or by inelastic hadronic interaction in case of hadronic particles. These processes result in a particle shower in the absorbers. Due to their different interaction behavior different materials are used for the absorbers of electromagnetic particles and of hadronic particles. As electromagnetic particles are absorbed faster in material than hadrons, the electromagnetic (EM) calorimeter is located close to the interaction point behind the Inner Detector. Then a system of hadronic calorimeters follows as can be seen in Figure 2.6. Special forward calorimeters ensure a calorimeter coverage up to  $|\eta| < 4.9$ .

#### The electromagnetic calorimeters

The EM calorimeters are separated in a barrel part with  $|\eta| < 1.5$ , two endcaps with  $1.5 < |\eta| < 3.2$ , and two forward calorimeters with  $3.1 < |\eta| < 4.9$ . The active material is liquid Argon (LAr) for all electromagnetic calorimeters. Therefore, all calorimeters are placed in cryostats and are operated at a temperature of approximately 88.5 K. The absorber material in the barrel and endcaps is lead. Copper is used in the forward calorimeters. In the barrel region, the lead/LAr structure is built in an accordion shape to ensure a full symmetry in  $\phi$  without any azimuthal cracks. In the region devoted for precision physics up to  $|\eta| < 2.5$ , a calorimeter module is segmented in three parts: The layer closest to the IP has a very fine granularity in  $(\Delta\phi \times \Delta\eta)$  of at best  $0.1 \times 0.003$ , to measure the direction in  $\eta$ . The second layer is large (about 70% of the module in depths) to measure precisely the energy of the shower with a granularity of at best  $0.025 \times 0.025$ . The tails of the showers are measured in the third layer, that is coarser in  $\eta$ . This layer is also used to trigger events. In total, the barrel has a thickness of 47 cm covering more than

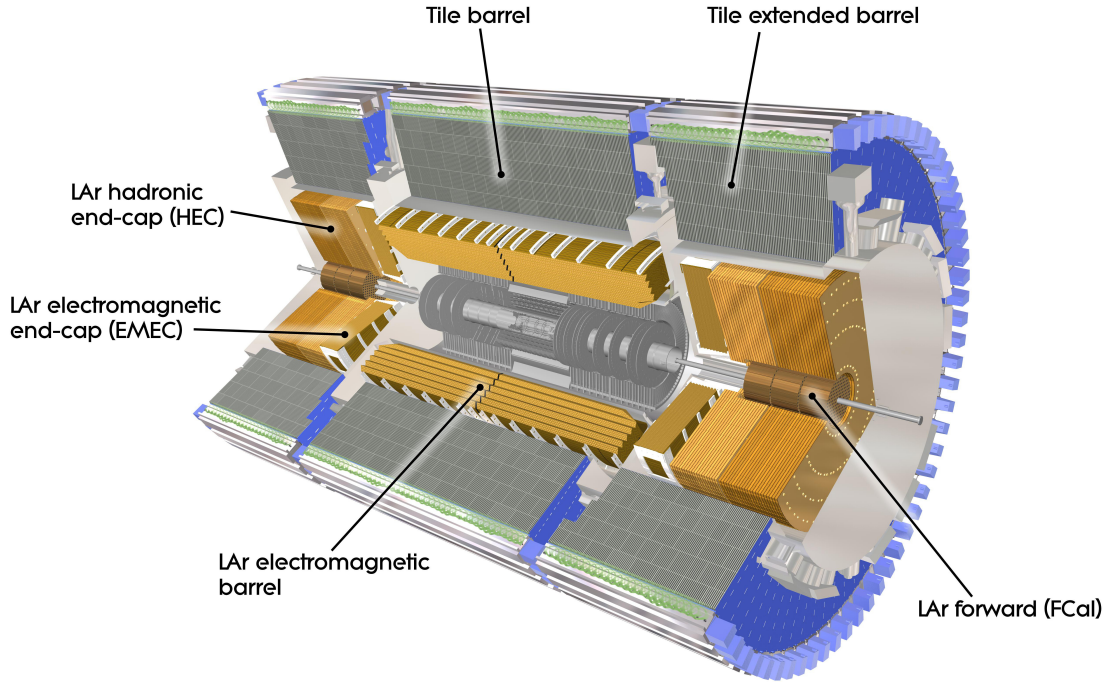


**Figure 2.6:** Computer-generated cut-away image of the calorimeter system [89].

22 radiation lengths,  $X_0^1$ , of an electron. The endcaps have a thickness of  $> 24X_0$ . In the region  $|\eta| < 1.8$ , a pre-sampler filled with LAr is installed in front of the first absorber layer. Its task is the correction of the particle energies due to energy loss in the solenoid.

During operation in 2011, a hardware problem occurred in the LAr calorimeter resulting in a readout problem at  $0 < \eta < 1.475$  and  $-0.791 < \phi < -0.595$  in about 20% of the 2011 dataset. The defect was partly recovered afterwards. Also, noise bursts occurred in parts of the detector, resulting in a data-taking efficiency of 96.9% for the LAr calorimeters [107].

### The hadronic calorimeters

The hadronic calorimeters consist of a barrel with  $|\eta| < 1.0$ , two extended barrels with  $0.8 < |\eta| < 1.7$ , two endcaps with  $1.5 < |\eta| < 3.2$ , and two forward calorimeters with  $3.1 < |\eta| < 4.9$ . The overlap of the subsystems ensures the overall coverage in  $\eta$ . To get a precise result of the energy of jets, it is important to measure the complete shower. Therefore, the hadronic calorimeter is about 2 m thick, with an inner radius of 2.28 m and an outer radius of 4.25 m, and about 11 m long to reach about 10 interaction lengths<sup>2</sup> ( $\lambda$ ) in every direction of  $\eta$ .

<sup>1</sup>The mean distance over which a high-energy electron has lost all but 1/e of its energy by bremsstrahlung.

<sup>2</sup>The interaction length is the mean path length to reduce the energy of hadrons by 1/e.

The barrel and the extended barrel [108] use steel plates as absorber and scintillating tiles as active material. Both calorimeters are segmented in three layers with a thickness of  $1.5 \lambda$ ,  $4.1 \lambda$ , and  $1.8 \lambda$  for the barrel and  $1.5 \lambda$ ,  $2.6 \lambda$ , and  $3.3 \lambda$  for the extended barrel. The module size provides a detector granularity of  $0.1 \times 0.1$  in  $(\Delta\phi \times \Delta\eta)$ , resulting in a good resolution for high energy jets and missing transverse momentum. Due to the harsher radiation environment closer to the beam pipe, the LAr technology is again used as active material for the endcaps and the forward calorimeters. They are placed in the same cryostats as the EM endcap calorimeters. As absorbers, copper is used for the endcaps, and tungsten is used for the forward calorimeters.

The operation of the hadronic calorimeters in 2011 was smooth, and the systems reached a data-taking efficiency of 99.2% [107].

## 2.2.4 The Muon System

Muons are able to cross the complete detector because they don't emit much bremsstrahlung when crossing matter. Therefore, the Muon System [89] is the outermost part of the ATLAS detector with a distance of at least five meters from the IP. The Muon System (MS) has two major tasks. One is to measure the momentum of the muons as precisely as possible up to a pseudorapidity of  $|\eta| < 2.7$  and the other is to trigger interesting physics events with high-energy muons, up to a pseudorapidity of  $|\eta| < 2.4$ .

The MS consists of three cylindrical layers in the barrel at a radius of approximately 5, 7.5 and 10 meters around the beam axis and of four large wheels perpendicular to the beam axis at a distance of about 7.4, 10.8, 14 and 21.5 m. The muon chambers are placed around and within the superconducting coils of the toroid magnets, compare Fig. 2.4. The toroid generates a magnetic field perpendicular to the momentum direction of the muons from the IP with a magnetic field strength of 0.5 T in the barrel and 1 T in the endcaps. Thus, the muon trajectory is bent by the magnetic field and provides information on the momentum of the muon.

The tracks of muons are measured with drift tubes, that are made up of an anode and a cathode and are filled with gas. When a muon crosses a drift tube, it ionizes some of the gas atoms. Due to the electric field in the gas between the anode and cathode wall, the electrons drift towards the anode, the ions drift much slower towards the cathode. The barrel and most of the muon wheels are equipped with Monitored Drift Tubes (MDTs), that provide the best precision with a spatial resolution per tube of  $80 \mu\text{m}$  and per chamber of  $35 \mu\text{m}$  in the  $z$  direction.

Only in the innermost muon endcap layer with  $|\eta| > 2.0$  where many tracks are expected, so-called Cathode-Strip Chambers (CSCs) are used due to their higher rate capability and time resolution. The spatial resolution of the CSC chambers is  $40 \mu\text{m}$  in the bending plane ( $\eta$ ) and 5 mm in the transverse plane ( $\phi$ ). To achieve its design resolution (compare Table 2.2), the position of the MDT wires and CSC strips along the trajectory of a muon must be known better than  $30 \mu\text{m}$ . Therefore, the alignment of the MS is a challenge regarding the size of the system. To assist the alignment done with measurement data, 12,000 optical alignment sensors are

precisely installed to monitor the positions and deformations of the MDT chambers. Trigger chambers are installed in the pseudorapidity range of  $0 < |\eta| < 2.4$ , that can be read out faster than the MDTs and CSCs. In the barrel region Resistive Plate Chambers are used, and in the endcap regions Thin Gap Chambers.

The operation of the MS in 2011 was very successful. All parts of the MS had a data-taking efficiency between 98.8% and 99.4% [107]. The spatial resolution per MDT was measured to agree with its design value of  $80 \mu\text{m}$  for a sufficient drift radius [109].

## 2.2.5 Luminosity detectors

In the forward region of the ATLAS detector three small detector systems are installed to measure the luminosity delivered to ATLAS. Two systems, LUCID and BCM, extract the bunch-by-bunch luminosity by measuring the inelastic  $pp$  collision cross section. It is related to the instantaneous luminosity using the following equation [110]:

$$\mathcal{L} = \frac{\mu_{\text{vis}} n_b f_{\text{rev}}}{\sigma_{\text{vis}}}, \quad (2.8)$$

where  $n_b$  is the number of bunches,  $f_{\text{rev}}$  is the revolution frequency of the protons,  $\mu_{\text{vis}}$  is the visible average number of inelastic interactions, and  $\sigma_{\text{vis}}$  is the total inelastic cross section multiplied with the efficiency of a particular detector. As  $\mu_{\text{vis}}$  is an observable quantity, only  $\sigma_{\text{vis}}$  needs to be determined.

LUCID [89] (Luminosity measurement Using Cerenkov Integrating Detector) is located at  $z = \pm 17 \text{ m}$  on both sides of the IP. LUCID measures the inelastic  $pp$  collisions in the forward direction at  $|\eta| \approx 5.8$ . It covers the azimuthal direction completely by surrounding the beam line at a distance of 10 cm. The Beam Conditions Monitor [111] (BCM) consists of two stations on both sides of the IP at a position of  $z = \pm 184 \text{ cm}$  and surrounds the beam pipe at a radius of  $r = 55 \text{ mm}$ . It measures collision remnants at a pseudorapidity of  $|\eta| \approx 4.2$ . Each detector station consists of four modules with two diamond sensors each. Both, the LUCID and the BCM detector also provide online information on the conditions of the LHC beams.

To calibrate the luminosity measurement of the LUCID and the BCM detector, data of van-der-Meer scans [112] is used, where the beams are moved horizontally and vertically against each other. Here, the luminosity value can be extracted from machine parameters. Thus, the visible cross-section for each detector can be determined [110].

The third detector system is the ALFA [89] (Absolute Luminosity for ATLAS) detector consisting of scintillating fibre trackers located inside four roman pots. With the roman-pot technology it is possible for ALFA to approach the beam as close as 1 mm at a distance of  $z = \pm 240 \text{ m}$  of the IP. Thus, the total luminosity can be extracted by measuring elastic  $pp$  scattering at a small angle and then applying the optical theorem [113]. In 2011, the ALFA detector was not yet commissioned and therefore not used in the luminosity measurement.

### 2.2.6 Trigger system

At design operation, the LHC provides collisions to the ATLAS detector every 25 ns. This corresponds to an event rate of 40 MHz. With an event size of approximately 1.3 Mbyte it is impossible to read out and store all events delivered by the LHC. On the other hand, most processes with new or interesting physics have a very low production rate. The task of the trigger system is the selection of interesting events, while significantly reducing the event rate to about 400 Hz (a factor 1:100000) [114].

The trigger system [89, 115] is divided in three levels: Level-1 (L1), Level-2 (L2), and the event filter (EF). At each level, the decision of the previous level is refined and additional selection criteria are added. The L1 trigger is based on custom hardware, that is implemented in the detector. It searches for high- $p_T$  muons, electrons, photons, jets, taus, and large missing transverse momentum using the trigger chambers in the muon system and reduced granularity from the calorimeter system. The results from the muon and calorimeter systems are processed, and a decision is made in about  $2.4 \mu\text{s}$ . Thus, the rate is reduced to 60 kHz [114]. In 2011, also cuts on pseudorapidity were introduced for electrons at L1 level.

The L2 trigger is a software-based trigger, that uses fine-granularity data of the complete detector, processed only in parts of the detector, so-called Regions-of-Interest (RoI's). The RoI's are defined by the L1 trigger. Then, the triggered object is completely reconstructed. A decision is made in about 40 ms, and the event rate is reduced to approximately 5 kHz [114]. The complete event record is available at the EF level. The EF applies selection criteria using offline analysis procedures and includes more complex criteria for event patterns. This way, a decision is made within 4 s, and the selected events sorted in the corresponding ATLAS physics stream by the EF. In the EF the output rate is reduced to approximately 200 Hz [114].

The trigger menu of the ATLAS detector is configured on a physics-run basis to keep the trigger level rates within their assigned limits, when the conditions of the collisions change. For example, most trigger rates increase linearly with the instantaneous luminosity. It is possible to prescale the trigger items and chains during a run. As the triggers used in this analysis need to be unprescaled, several different triggers were used, depending on the period in the 2011 dataset.

## 2.3 The 2011 dataset

Between March and November 2011, the LHC delivered a total integrated luminosity of  $5.46 \text{ fb}^{-1}$   $pp$  collisions at  $\sqrt{s} = 7 \text{ TeV}$  to the ATLAS detector. The delivered luminosity accounts for the luminosity delivered from the start of stable beams until the LHC requests ATLAS to put the detector in a safe standby mode. The integrated luminosity versus time is shown in Fig. 2.7. Flat parts of the distributions correspond to technical stops throughout the year. It can be observed, that the gradient of the luminosity increases after each technical stop. The reasons are the optimizations done by the LHC operation team during each technical stop to increase the instantaneous luminosity. This effort is discussed in Section 2.1, and the result is shown in Fig. 2.2.

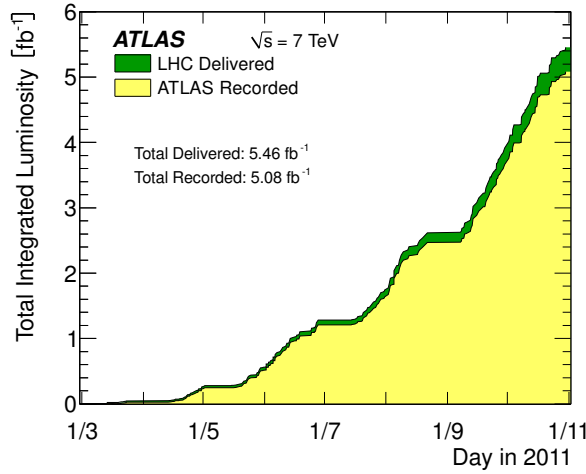


**Figure 2.7:** Total integrated luminosity of  $\sqrt{s} = 7$  TeV  $pp$  collision delivered to the ATLAS detector by the LHC between March (1/3) and November (1/11) 2011 [116]. The delivered luminosity is shown in green. In yellow, the luminosity recorded by the ATLAS detector is illustrated. The luminosity measurements were performed by the ATLAS detector.

In Fig. 2.7 the luminosity delivered by the LHC of  $5.46 \text{ fb}^{-1}$  as well as the luminosity recorded by ATLAS of  $5.08 \text{ fb}^{-1}$  are shown. The reduction of about 7% in luminosity reflects the inefficiencies of the data acquisition as well as the data loss due to the ramping of the tracking detectors at the start of stable beams. The recorded data is evaluated by Data Quality (DQ) requirements within ATLAS using flags, that are set per luminosity block, a data interval recorded during two minutes. DQ flags exist for each sub detector and for each reconstructed physics object. Because this analysis uses all physics objects apart from photons, all reconstructed physics objects need to be of good data quality. Thus, the luminosity used was measured to be  $\mathcal{L}_{\text{int}} = 4.59 \pm 0.08 \text{ fb}^{-1}$  [110]. The DQ decision is provided in so called good-run-lists (GRLs) where valid physics runs and luminosity blocks are listed.

Changing conditions of the  $pp$  collisions, the ATLAS trigger menu, and the functionality of the ATLAS detector lead to a segmentation of the analysis dataset. At each significant change in data taking, a new data period is started. Table 2.3 lists the data periods useful for this analysis and the properties of each period including the luminosity, the average number of interactions  $\langle \mu \rangle$ , as well as changes of the trigger menu or the detecting hardware. This segmentation is used for the calibration of the triggers and the modeling of the pile-up events.

**Table 2.3:** Segmentation of the all-good 2011  $pp$ -collision dataset. For each subset the luminosity, the average number of interactions per collision  $\langle \mu \rangle$ , and the changes in detector conditions and trigger are given.

Data periods	Luminosity [pb <sup>-1</sup> ]	$\langle \mu \rangle$	Changes
1	$174 \pm 3$	5.4	–
2	$920 \pm 20$	5.5	Defect in LAr EM calorimeter.
3	$329 \pm 6$	5.9	Defect in LAr EM recovered.
4	$220 \pm 4$	6.0	Change of trigger menu.
5	$580 \pm 10$	7.2	New trigger menu for $L = 3 * 10^{33} \text{ cm}^{-2}\text{s}^{-1}$ .
6	$2370 \pm 40$	11.2	Pseudorapidity cuts for electron trigger at L1.



# Chapter 3

## Event generation and reconstruction

It is a challenging task to understand and interpret the outcome of  $pp$  collisions at the LHC. The possible final states of physics processes are not only hard to predict (compare Section 1.1.5), but also the experimental setup is complicated with many subdetectors of different geometric coverage and responses (see Section 2.2). To evaluate the collected physics events in a certain final state, Monte Carlo (MC) simulation methods are used. The main goal of an MC event generator is the imitation of Nature's behavior in the real experiment on an event-by-event basis. This is done in several steps: First, the considered physics process of the MC events is generated according to the predictions of the SM, yielding final state particles and their kinematics. Next, the interaction with the detector and its response are simulated for the whole MC event. Finally, simulated events as well as measured collision data undergo the same reconstruction algorithms. Thus, simulated and measured events can be compared.

### 3.1 Event generation

Goal of the event generation with MC methods is to provide a complete picture of final states, that consist of a large number of particles. To generate the collision outcome, the concept of factorization is again used. Thus, the complexity of the proton structure and of the final state hadron formation is separated from the hard interaction among partons. Fig. 3.1 illustrates the steps, that are calculated during the generation of the final state: the hard process, the parton shower, the hadronization, the decays of unstable particles, and the modeling of the underlying event.

The generation of the hard process follows Equation 1.6. To solve the equation, the input PDFs, the parton-level matrix elements (MEs), and the integration over the complete phase space need to be provided. The MEs are evaluated using Feynman diagrams at LO or at NLO precision depending on the available generator for a given process and on the process itself. The integration over the phase space is performed using MC methods where also other free parameters, e.g. polarizations and colors,

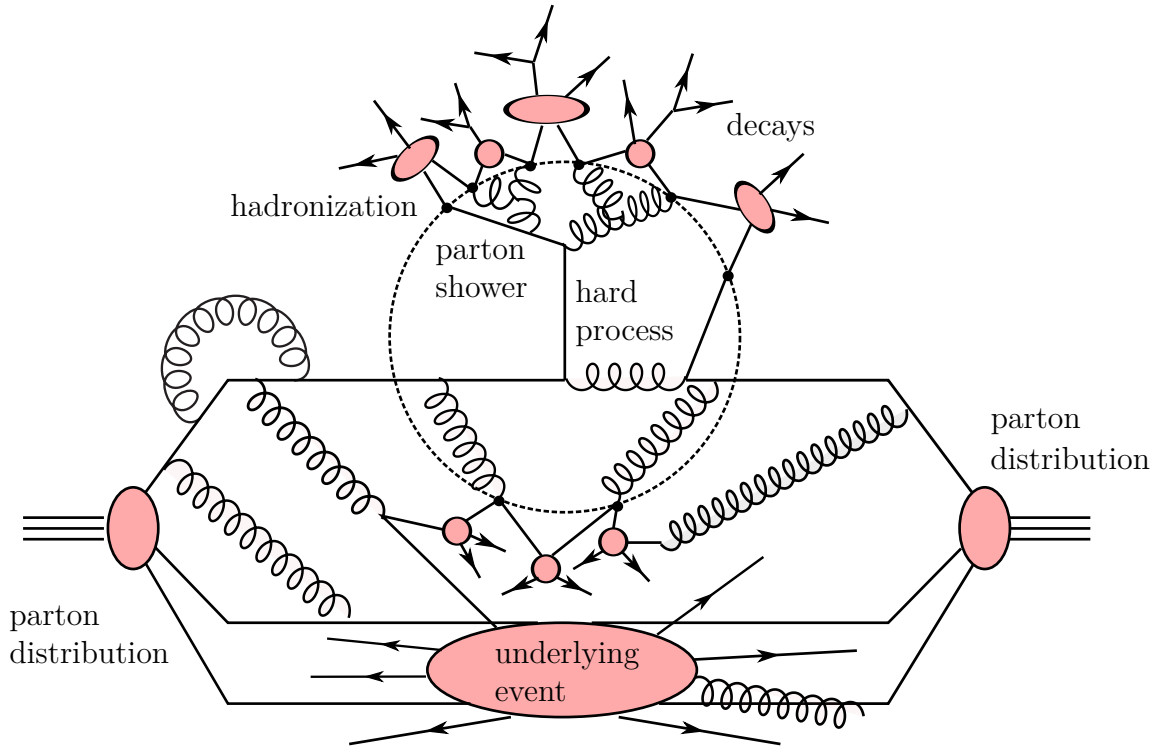


**Figure 3.1:** General structure of a hard  $pp$  collision [117].

are included. The hard process describes the momenta and spins of leptons, quarks, and gluons. Jets are not described.

Parton showers are used for the description of jet structures. Starting with the final-state or initial-state partons from the hard process, partons are evolved into partons with smaller momenta. The partons radiate gluons, that again cause further gluon radiation and parton multiplication, following a  $1 \rightarrow 2$  splitting. Here, the splitting functions (given in Equation 1.7) are used as probability for the splitting of the partons and gluons. The evolution of the parton shower continues until a cut-off scale of about 1 GeV where the non-perturbative effects of confinement become relevant [118].

Once the evolution of the parton shower reaches the cut-off scale, the formation of color-neutral hadrons takes place. The hadronization of partons is a non-perturbative hadronic phenomenon and could be calculated via lattice QCD methods. Because such a calculation has never been performed due to the complexity of the problem, specific models are used in event generators to describe the formation of hadrons. These models are tuned to data. The confinement process of the partons is modeled either via strings or via color-singlet parton-clusters in the most common models [119, 120]. After hadronization, a number of unstable hadrons are produced, that have to decay into long-lived particles at the end of the generation of the event.

Additionally, the remnants of the colliding protons undergo shower and hadronization processes, thus constructing the underlying event. This is also depicted in Fig. 3.1. The underlying event is connected to the initial hard process, to regain color-neutrality via color exchanges. Finally, additional pile-up events with low mo-

momentum exchange are added to the event to simulate the additional interactions taking place in the same bunch crossing. The events are generated such, that the distribution of the number of collisions per bunch crossing is the same as in collision data. Both, the hard-scattering and the pile-up events are generated distributed along the  $z$  axis in the complete luminous region of the collision. After event generation, all samples are passed through a detailed simulation of the ATLAS detector to emulate the detector response.

### 3.1.1 Monte-Carlo generators

The current generators are divided into ME generators and multi-purpose generators. ME generators are used to generate the final state of specific hard processes and to calculate the corresponding cross section at a fixed order (depending on the generator). The output of these generators is then fed to multi-purpose generators, that provide the showering and the hadronization mechanisms.

The combination of a fixed-order ME calculation with the parton shower generation is not trivial, as both approaches can lead to the same  $n$ -parton final state. This results in an overlap in phase space of partons from the ME calculation and partons from the parton shower. One example, where double counting occurs, is the exclusive generation of a hard process with  $n$  additional partons. Here, all  $n$  partons could originate from the ME calculation, or  $n - m$  partons originate from the ME calculation and  $m$  partons are radiated during the parton shower. To avoid double counting these events, the partons after the parton shower have to be matched to the final-state partons of the hard process. Common generators use mainly two methods to perform the matching: the CKKW method [121] or the MLM matching [122]. The matching criteria are chosen with regard of the advantages of each method. In general, hard and well separated jets are better described by the ME generation, while soft emissions are better modeled with jets from parton showers.

In the following the generators used in this thesis are briefly introduced.

#### **PowHeg-Box**

POWHEG-BOX [123–125] is a ME generator, that uses a ME calculation of the specific hard process at NLO accuracy. In addition, it provides a method to match the NLO calculation with a parton-shower generator, that uses preferably a  $p_T$ -ordered shower algorithm (e.g. PYTHIA). Here, the hardest emission of the parton shower is replaced by the NLO accurate emission. Therefore, all matrix-element events are taken along. A matching with angular-ordered shower algorithms (e.g. used in HERWIG) is also possible, but more complicated.

#### **aMC@NLO**

The matrix-element generator aMC@NLO [126] is a fully automated approach to the complete event generation and parton shower at NLO accuracy in QCD. The matching of the generated hard process at NLO accuracy to the parton showers

is performed with the MC@NLO method [127]. The overlap is subtracted dealing with infrared and collinear singularities.

### **AcerMC**

The ACERMC [128] generator (version 3.7) is a flexible generator designed to generate processes with a “not-straightforward generation”. A library of massive matrix elements at LO accuracy is provided, that were derived with the MADGRAPH [129] package. In ACERMC, the hard process can be completed with parton shower, initial- and final-state radiation and hadronization provided by all known multi-purpose event generators. In this thesis, ACERMC is used for the generation of  $t$ -channel single-top quark events. It is possible to combine events generated with the LO 5FS and with the LO 4FS calculation to one consistent sample based on an implementation [130] of the ACOT [131] matching prescription to avoid kinematic overlaps.

### **ALPGEN**

The ALPGEN [132] event generator (version 2.13) is a generator dedicated to hard processes with  $n$  additional jets in hadron colliders. The calculation of MEs is performed at LO precision for final states. Each jet multiplicity is simulated with the corresponding matrix element and then dressed with the parton shower by an external shower algorithm. The overlap of events with jets from ME calculation only and events with jets from both ME calculation and parton shower emissions is removed via the MLM matching method.

### **Pythia**

PYTHIA [133] (version 6.4.27) is a multi-purpose generator. It is used to generate complete events up to the final-state particles. Thus, it is able to perform all steps shown in Fig. 3.1. PYTHIA includes ME calculations at LO and initial- and final-state parton showers. The parton shower is generated in a  $p_T$ -ordered way. The Lund model [119], a string model, is employed for the hadronization. Also, a model is provided for the simulation of the underlying event. PYTHIA can also be interfaced to ME generators, providing then only parton shower, hadronization, decay, and underlying event simulation. In this analysis PYTHIA is used as both a complete event generator and an interfaced generator where it provides the event simulation starting from the generated hard process. The parameters of the PYTHIA generator controlling the modeling of the parton shower and the underlying event are always set to the values of the Perugia 2011 tune [134].

### **Herwig**

Another multi-purpose generator is the HERWIG [135] package (version 6.5.20) providing LO ME calculations, parton-shower generation, and models for hadronization and decays. The parton-shower simulation is ordered with the azimuthal angular

distribution to include color-coherence effects and azimuthal correlations both within and between jets. The hadronization is performed utilizing the cluster model [120]. HERWIG does not provide the simulation of the underlying event and is therefore interfaced to the JIMMY [136] generator (version 4.31). In this analysis, HERWIG and JIMMY are always interfaced to a different ME generator. The parameters for the parton shower in HERWIG and the underlying event in JIMMY are set to values of the ATLAS Underlying Event Tune 2 [137].

### 3.1.2 Detector simulation

After the generation of the MC events, the simulation of interactions with the detector material as well as the detector response is performed based on the GEANT4 particle-simulation toolkit [138]. Here, the electromagnetic and hadronic interaction of the particles with matter within a magnetic field is simulated. A detailed simulation of the ATLAS detector geometry [139] was implemented to study the detector response and digitize it in voltages and currents. The data format of the simulated events is identical to the real data, so that the same trigger and reconstruction mechanisms can be applied. It is further possible to adapt the ATLAS detector geometry emulating the data-taking conditions of the collision data. For example, the defects in the LAr calorimeter during data period 2 of the 2011 run was successfully included in the simulation.

## 3.2 Event reconstruction

To interpret the detector signals of the various sub-detector systems, reconstruction algorithms are applied. First, tracks of charged particles are reconstructed using detector hits from the Inner Detector and the Muon System. With this information vertices of the event are found. In this section the reconstruction of the physics objects used in the presented analysis are described: electrons, muons, jets, b-quark jets, and missing transverse momentum. For these reconstructions the signals of all sub-detector systems are used. Finally, the reconstruction of top-quark candidates utilizing the physics objects is described.

### 3.2.1 Tracks of charged particles

The tracking of charged particles is performed with measured hits in the Inner Detector (ID). For the measurement of muon tracks signals from the Muon System are used in addition. The reconstruction of muons will be discussed later.

Charged particles are deflected in the ID volume by the solenoid magnetic field resulting in a curvature of the track in the  $x - y$  plane of the detector. Thus, the path of charged particles inside the detector is described by a helix curve and can be reconstructed by fitting detector hits with such a curve.

To find the detector hits, that belong to one track, patterns are searched for within the measurements of the detectors. In ATLAS, the primary ID pattern recognition follows an inside-out strategy [140]. At first, the measurements of the

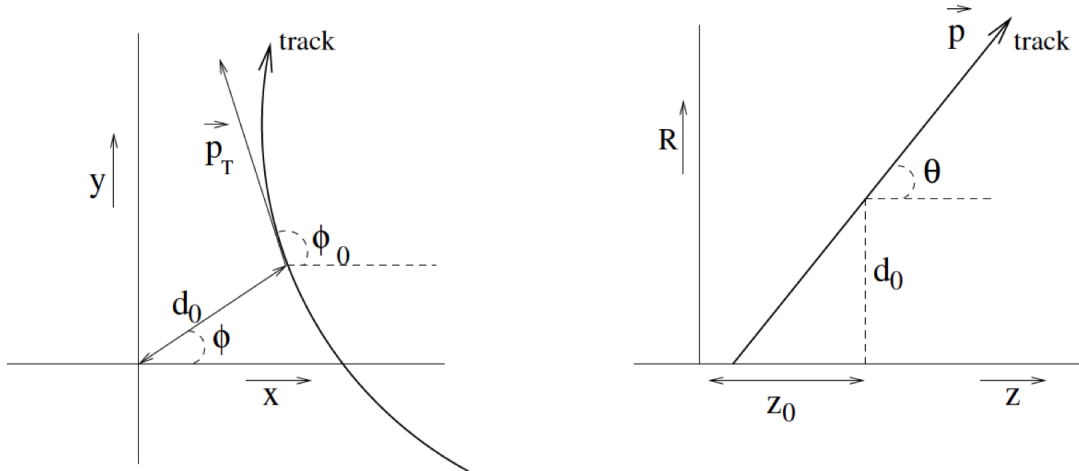


**Figure 3.2:** Illustration of the track parameterization shown in the  $x - y$  plane (left) and in the  $R - z$  plane (right) [143]. The deflection of the particle is only present in the  $x - y$  plane due to the magnetic field.

silicon detectors (SCT and Pixel) are processed and space points are formed from the measured hits. Three-point seeds for track candidates are formed, if three space points are compatible with a minimum transverse momentum cut of 500 MeV. Then, silicon hits are added to the seed moving away from the interaction point using a combinatorial Kalman filter [141, 142]. The thus reconstructed track segment is fitted with a  $\chi^2$  fit after each hit is added. To reduce the number of track candidates, the tracks are refitted with all found silicon hits, and quality criteria are applied before the inclusion of TRT data. Then, the remaining tracks are extended to the TRT.

Track candidates are parametrized with respect to the point of closest approach to the center of the luminous region [143]. Impact parameters are defined for each track in the transverse  $x - y$  plane,  $d_0$ , and in the longitudinal  $R - z$  plane,  $z_0$ , with respect to the center of the luminous region. This is illustrated in Fig. 3.2. Tracks are efficiently reconstructed in the ATLAS detector with a minimal transverse momentum of 500 MeV [140]. The default track quality requirements for inside-out tracks in 2011 demand at least seven silicon hits and allow at most two holes in the pixel detector [102]. A hole is a missing expected measurement hit on the track trajectory.

### 3.2.2 Primary vertex

A typical  $pp$  collision features several interaction points. To locate the interaction point of the hard scattering in the collision, so-called primary vertex candidates are reconstructed. Here, an iterative vertex-finding algorithm is used, that applies a finding-through-fitting approach [144]. First, tracks are selected, that are compatible with the bunch-crossing region. The global maximum in the distributions of the  $z$  coordinates of these tracks is used as vertex seed. The vertex seed and the tracks are then given as input to the adaptive fitting algorithm [145] which is used to determine the vertex position. Here, the vertex candidate is reconstructed using

a  $\chi^2$  fitting algorithm. Then, those tracks which are considered to be outliers (incompatible with the vertex by more than  $7\sigma$ ) are used to create a new vertex seed. In the next step a simultaneous fit of the two vertices is performed. This procedure is repeated until all tracks in the event are associated to a vertex.

Pile-up events are often events with small transverse momentum. Therefore, the vertex is chosen as primary vertex out of all candidates, that has at least five associated tracks and the largest sum of the squared transverse momenta  $\sum p_T^2$  of the tracks associated to the vertex. The vertex resolution achieved with the ATLAS detector for events with more than 70 tracks was measured to be about  $30 \mu\text{m}$  in the transverse plane and about  $50 \mu\text{m}$  in the longitudinal plane [146].

### 3.2.3 Electrons

Isolated electrons are an important component of a single top-quark event signature. Therefore, their efficient identification as well as good background rejection are important. The electron track is reconstructed with signals from the ID and the energy deposition of the electron is measured in the EM calorimeter. Hadronic activity is vetoed using signals from the hadronic calorimeter to differentiate electron candidates from jet candidates. In this analysis only central electrons with  $|\eta| < 2.5$  are taken into account.

The electron reconstruction is performed in three steps [147]. First, clusters of energy deposition are reconstructed in the EM calorimeter. A cluster is seeded, if an energy deposit of a transverse energy  $E_T > 2.5 \text{ GeV}$  is found in a window of  $3 \times 5$  in units of  $0.025 \times 0.025$  in the  $(\eta, \phi)$  space. In the next step, tracks are associated to the EM cluster. Only tracks with  $p_T > 500 \text{ MeV}$  are considered. The associated tracks are refitted to correct for the large amount of Bremsstrahlung emitted by an electron. Then, the tracks are extrapolated from their last measurement point to the seed position of the cluster in the middle layer of the EM calorimeter. A match of track and cluster is achieved, if the absolute difference in pseudorapidity  $|\Delta\eta|$  is smaller than 0.05 between the extrapolated track and the cluster seed. If more than one tracks are matched to the cluster, the tracks with the largest number of silicon hits are preferred and then the track with the smallest  $\Delta R$  distance to the cluster is chosen. After the track-cluster match, a veto against converted photons is applied. The third step is the full reconstruction of the electron candidate.

The energy of the electron candidate is measured in an enlarged cluster size of  $3 \times 7$  ( $5 \times 5$ ) units of  $0.025 \times 0.025$  in  $(\eta, \phi)$  space in the barrel (endcaps). Then, the measured energy is corrected for the estimated energy deposit in the material located in front of the EM calorimeters, the estimated external energy deposit outside the cluster, and the estimated energy deposit beyond the EM calorimeter using simulation. The absolute energy scale is determined using electrons from  $Z \rightarrow ee$  decays in data, that are selected by applying tight quality constraints. Then, correction scale factors are extracted by comparing the measurement results with the simulation. The resulting calibration is validated with electron candidates from  $J/\psi \rightarrow ee$  decays [148]. The spatial coordinates  $(\eta, \phi)$  of the electron candidate are taken from the parameters of the matched track at the primary vertex.

To determine with a high probability, that the candidate is an electron, sequential cuts are applied on calorimeter, tracking, and combined track-cluster variables. The shape of the shower in the EM calorimeter is taken into account, as well as the hadronic leakage information. Stringent constraints on the track quality are applied, e.g. number of hits in the ID and transverse impact-parameter cuts. Also, the angular position of the cluster in the first layer of the calorimeter and the extrapolated track must agree well. Charged hadron background is identified using the TRT measurements, and then rejected. The strictest electron identification in ATLAS is the *tight* criteria, that is specified in Ref. [114]. All signal electron candidates in this thesis fulfill the *tight* identification criteria.

In addition to the *tight* identification criteria, the following quality cuts are applied to the electron candidate:

- The electron candidate must have minimal transverse energy  $E_T > 25$  GeV and  $|\eta_{cl}| < 2.47$ , where  $\eta_{cl}$  denotes the pseudorapidity of the calorimeter cluster.
- Electron candidates in the transition region between the calorimeter barrel and endcap, corresponding to  $1.37 < |\eta_{cl}| < 1.52$ , are ignored.
- The  $z$  position of the matched track has to be compatible with the primary vertex. This is ensured by requiring the longitudinal impact-parameter to be  $|z_0| < 2$  mm.
- Electron candidates detected in calorimeter clusters with defect readout electronic are ignored.

High- $p_T$  electrons from  $W$ -boson decays are typically isolated from jet activity. Thus, further isolation criteria are applied on the electron candidates to identify and reject electrons from  $b$ -hadron or  $c$ -hadron decays, hadronic jets mimicking the signature of an electron, and photon conversions. Here, minimal calorimeter activity (calorimeter isolation) and only a few tracks (track isolation) are allowed in an  $\eta - \phi$  cone around the electron. The calorimeter isolation is realized by placing a cut on the scalar sum of the transverse calorimeter energy deposits  $\sum E_T^{\text{calo}}$  within a cone of the size  $\Delta R = 0.2$ , excluding the energy deposit associated to the candidate. The  $\sum E_T^{\text{calo}}$  variable is corrected for pile-up effects depending on the number of reconstructed primary vertices. The track isolation requires a cut on the scalar sum of the transverse momenta of tracks  $\sum p_T^{\text{track}}$  in a cone of  $\Delta R = 0.3$  around the candidate excluding the matched track. The thresholds applied to  $\sum E_T^{\text{calo}}$  and  $\sum p_T^{\text{track}}$  depend on the electron  $p_T$ , the electron  $\eta$ , and the number of reconstructed primary vertices. They are chosen such, that the efficiency of electrons from  $W$ -boson or  $Z$ -boson decays to pass this isolation requirement is 90%.

After all quality criteria are applied, a resolution of 1.35 GeV is reached for the transverse momentum and a resolution of 0.0007 for the pseudorapidity of the electron in simulated  $t$ -channel single top-quark signal events. The residual distributions are shown in Fig. 3.3(a) for the  $p_T$  and in Fig. 3.3(b) for the  $\eta$  distribution. The tail towards negative values as well as the slightly negative mean of the residual distribution of  $p_T(e)$  is due to bremsstrahlung, that is not fully recovered in the reconstruction.

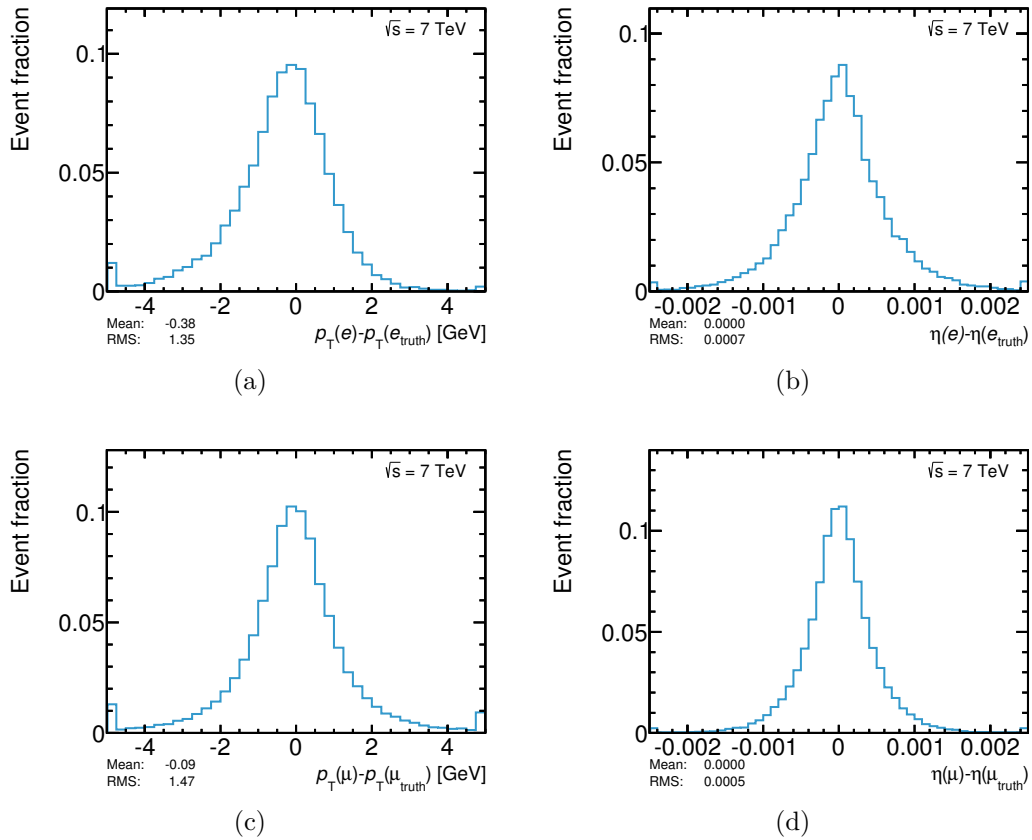


**Figure 3.3:** Residual distributions of kinematic properties of the reconstructed leptons evaluated with simulated  $t$ -channel single top-quark signal events. The distributions are normalized to unit area. The mean of the distribution gives information on an eventual offset of the measured value compared to the true value. The root-mean square (RMS) gives the resolution with which the variable is measured. Panel (a) shows the transverse momentum of the electron, (b) the pseudorapidity of the electron, (c) the transverse momentum of the muon, and (d) the pseudorapidity of the muon.

### 3.2.4 Muons

Muons are reconstructed using the measurements of the MS and the reconstructed tracks, that are described in Section 3.2.1, using ID data. While the MS has an acceptance for muons up to  $|\eta| < 2.7$ , only muons measured with both, the MS and the ID, within the acceptance of  $|\eta| < 2.5$  are used in the presented analysis. To reject muons from hadronic jets, calorimeter information is used.

Muon candidates are reconstructed by combining track segments from the Muon System [149]. Straight-line track segments are searched for in the bending planes of the toroidal field. The segment candidates are required to point loosely to the center of ATLAS. If a drift tube is crossed by a potential track, a hit is required in the tube. If more than two muon segments are found in different muon chambers in a constrained  $\eta - \phi$  region, than they are combined to a muon-track candidate using three-dimensional tracking in the magnetic field. For each muon-track candidate a

reconstructed ID track candidate is searched for by extrapolating the muon track to the vertex. If such a track is found, a global  $\chi^2$  refit of the ID track and the MS track is performed.

To determine the momentum resolution and momentum scale, di-muon decays of  $Z$ ,  $J/\psi$ , and  $\Upsilon$  resonances are used [149]. A Gaussian fit is performed to the di-muon resonances, and the results are used to calibrate the MC simulation samples. The momentum of the candidate muon measured in the ID is required to agree with the momentum measured in the MS after correcting for the predicted muon energy loss in the calorimeter. The reconstruction, identification, and trigger efficiencies of muons are measured using tag-and-probe methods on samples enriched with  $Z \rightarrow \mu\mu$  or  $J/\psi \rightarrow \mu\mu$  events [149].

In this analysis only muon candidates are used with  $p_T > 25$  GeV and  $|\eta| < 2.5$ . The muon tracks also need to fulfill the following track criteria:

- At least two hits in the Pixel Detector.
- At least six hits in the SCT.
- Less than three missing hits in the Pixel and SCT detectors.
- Reject tracks with an excessive number of outlier hits in the TRT.

As for the electrons, isolation criteria are applied to the muon candidates to reject background muons. Isolated muon candidates are selected by requiring  $\sum E_T^{\text{calo}} < 4$  GeV within a cone of radius  $\Delta R = 0.2$ , and  $\sum p_T^{\text{track}} < 2.5$  GeV within a cone of radius  $\Delta R = 0.3$ . The efficiency for this combined isolation requirement varies between 95% and 97%, depending on the data period. The resolution of the reconstructed muon candidates is 1.47 GeV in  $p_T$  and 0.0005 in  $\eta$ . These values are extracted from the corresponding residual distributions in Fig. 3.3(c) and 3.3(d) using simulated  $t$ -channel single top-quark signal events.

### 3.2.5 Jets

Partons in the final state of a physics process cannot be observed in the detector as isolated particles, but they form particle jets. Therefore, the reconstruction of jets is crucial to the presented analysis. Jets are observed as groups of energy deposits (clusters) in the calorimeters of the ATLAS detector. The reconstruction of jets is performed in the following steps: Identification of energy clusters in the calorimeter, reconstruction of the jets with a jet-finding algorithm, and calibration of the energy of the jet depending on its properties.

First, energy clusters are found in adjacent calorimeter cells using cluster algorithms. In ATLAS, the topological cluster algorithm is used [150]. Here, a calorimeter cell with a large amount of energy is used as a seed cell. Iteratively, neighboring cells are added as long as their signal-to-noise ratio is significant. The noise of a cell is the quadratic sum of the electronic noise and the noise from pile-up events. The default pile-up correction applied to the energy clusters corresponds to an average of eight additional  $pp$  collisions per bunch crossing [151]. Then, the energy of

the resulting clusters is reconstructed at the well-known EM scale [152], that correctly measures the energy deposited by particles in an electromagnetic shower in the calorimeter. It is established using electron test-beam results for all calorimeter parts. The direction of the energy cluster is reconstructed from the weighted averages of the pseudorapidities and azimuthal angles of the constituent calorimeter cells. Then, the reconstructed clusters are used as input to the jet-finding algorithm.

The jet-finding algorithm used in ATLAS is the anti- $k_t$  algorithm [153]. A special feature of the anti- $k_t$  algorithm is, that only hard particles (clusters with a significant amount of energy) can modify the area of the jet. Soft particles do not influence the jet area, as the clusters are accumulated by the closest hard particle. Thus, the anti- $k_t$  algorithm is a simple, infrared- and collinear-safe jet algorithm because the jet algorithm is stable with respect to a quasi-collinear splitting of the hardest particle (collinear-safe) as well as the introduction of new stable jet cones originating from soft particles (infrared-safe). The algorithm starts from the distances  $d_{ij}$ , between the clusters  $i$  and  $j$ , and  $d_{iB}$  between the cluster  $i$  and the LHC beam  $B$ . The distances are defined as:

$$d_{ij} = \min(p_{Ti}^{-2}, p_{Tj}^{-2}) \frac{(\Delta R_{ij})^2}{R^2} \quad \text{and} \quad (3.1)$$

$$d_{iB} = p_{Ti}^{-2}, \quad (3.2)$$

where  $p_{Ti}$  ( $p_{Tj}$ ) is the transverse momentum of the cluster  $i$  ( $j$ ) and  $\Delta R_{ij}$  is the angular distance between clusters  $i$  and  $j$ . The radius parameter  $R$  gives the cone-radius of one jet. In case of this analysis,  $R$  equals 0.4. For each cluster  $i$  the smallest distance is identified. If  $d_{ij}$  is the smallest distance, clusters  $i$  and  $j$  are combined. If  $d_{iB}$  is the smallest,  $i$  is defined as a jet and removed from the list of clusters. All distances are recalculated, and the procedure is repeated until all clusters are used, and only a list of jets is left. The four-momentum of each jet is defined as the four-momentum sum of its constituent clusters.

The jets are still reconstructed at the EM scale, that does not take into account the lower detector response to hadronic particle showers compared to electromagnetic ones. Furthermore, the energy reconstruction is influenced by other factors e.g. detector inefficiencies, the composition of the particles showers, and the presence of pile-up events. Thus, the four-momenta of the jets need to be calibrated. This calibration is done in several steps. First, the jet energy scale (JES) is corrected for the effect of multiple  $pp$  interactions in the event itself. Here, not only the pile-up collisions in the recorded event are taken into account, but also effects due to past and future collisions, called out-of-time pile-up, are included. Then, a correction is applied to the calorimeter-jet direction, so that the four-momentum of the jet points to the primary vertex of the event.

A simple calibration of the energy and the pseudorapidity of the jets is based on truth jets, that are formed from stable MC truth particles in simulated inclusive jet events. These truth jets do not include final-state muons and neutrinos because they do not leave a significant observable signal in the detector. The calibration is derived by using isolated reconstructed jets, that are matched to truth jets by

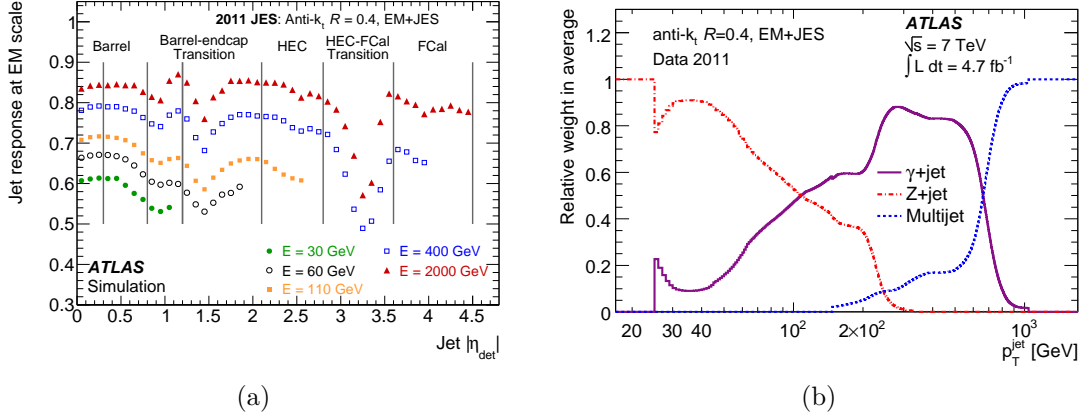


**Figure 3.4:** Panel (a) shows the average energy response of reconstructed jets at EM scale as a function of the pseudorapidity measured in the detector frame of reference [154]. The different calorimeter regions are indicated. Panel (b) shows the weight carried by each in-situ measurement in the combination to derive the in-situ JES calibration as a function of  $p_T^{\text{jet}}$  [154].

requiring  $\Delta R < 0.3$ . The EM-scale energy response  $\mathcal{R}_{\text{EM}}^{\text{jet}}$  is defined as:

$$\mathcal{R}_{\text{EM}}^{\text{jet}} = E_{\text{EM}}^{\text{jet}} / E_{\text{EM}}^{\text{truth}} \quad (3.3)$$

which is the inverse of the jet-energy calibration-function. It is given in bins of the truth jet energy  $E_{\text{EM}}^{\text{truth}}$  and the jet pseudorapidity  $\eta_{\text{det}}$  measured in the detector frame of reference, shown in Fig. 3.4(a). Large correction factors are applied in the transition regions between the detector systems and in the forward calorimeters. A similar correction is applied for the pseudorapidity of the reconstructed jet to remove a bias from poorly instrumented regions of the calorimeter [152].

To further improve the calibration of the JES, differences between data events and simulated events are evaluated using in-situ techniques and are corrected for in an additional step [154]. This calibration exploits the  $p_T$  balance between the jet and a well-measured reference object. Thus, correction factors are derived by comparing the  $p_T$  balance in data and MC:

$$\langle p_T^{\text{jet}} / p_T^{\text{ref}} \rangle_{\text{data}} / \langle p_T^{\text{jet}} / p_T^{\text{ref}} \rangle_{\text{MC}}. \quad (3.4)$$

Explicitly, Z+jet and  $\gamma$ +jet data events are used to set the JES in the central detector region up to  $p_T^{\text{jet}} = 800$  GeV. The results from the Z-jet  $p_T$ -balance measurement dominate the calibration up to  $p_T^{\text{jet}} = 100$  GeV, as is shown in Fig. 3.4(b). In the region  $100 \text{ GeV} < p_T^{\text{jet}} < 800$  GeV the  $\gamma$ -jet  $p_T$ -balance measurement is mainly used. Jets with a  $p_T$  above 800 GeV are not important for this analysis. Therefore, their calibration is not described here.

To calibrate the jets in the forward regions relative to jets in the central region, an  $\eta$  intercalibration between those jets is employed, that is based on the  $p_T$  balancing in dijet events. The central reference region is located within  $|\eta_{\text{det}}| < 0.8$ . In dijet events the asymmetry  $\mathcal{A}$  between transverse momenta of the “left” and the “right”

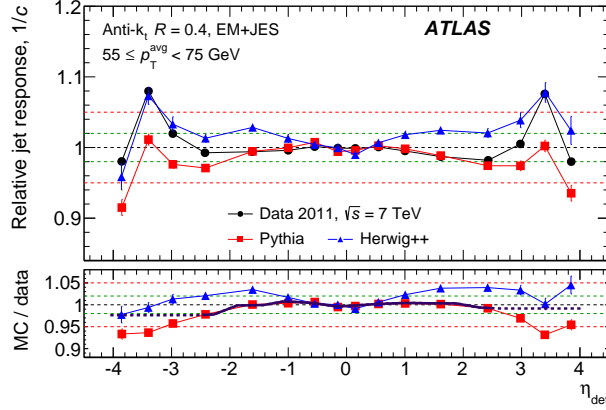


**Figure 3.5:** Relative jet response  $1/c$  as a function of the pseudorapidity  $\eta_{\text{det}}$  for dijet events with  $55 \text{ GeV} < p_{\text{T}}^{\text{avg}} < 75 \text{ GeV}$  [154]. In the lower panel the ratio between the data and MC relative response is given for both MC predictions. In addition, the default applied correction is shown as a thick black line. The line is solid over the range, where the measurement is used to constrain the calibration, and dashed where an extrapolation is applied.

jets, defined by  $\eta_{\text{det}}^{\text{left}} < \eta_{\text{det}}^{\text{right}}$ , is measured and the ratio of the jet responses  $\mathcal{R}$  is extracted. The asymmetry and the ratio are given by [154]:

$$\mathcal{A} = \frac{p_{\text{T}}^{\text{left}} - p_{\text{T}}^{\text{right}}}{p_{\text{T}}^{\text{avg}}} \quad \text{and} \quad \mathcal{R} = \frac{p_{\text{T}}^{\text{left}}}{p_{\text{T}}^{\text{right}}} = \frac{c^{\text{left}}}{c^{\text{right}}} = \frac{2 + \mathcal{A}}{2 - \mathcal{A}},$$

where  $c^{\text{left}}$  and  $c^{\text{right}}$  are the  $\eta$ -intercalibration correction factors for the left and right jet, respectively, and  $p_{\text{T}}^{\text{avg}}$  is the average of  $p_{\text{T}}^{\text{left}}$  and  $p_{\text{T}}^{\text{right}}$ . The  $\eta$ -intercalibration correction factor  $c_i$  with respect to the central reference region is determined via a matrix method, described in Ref. [154], for bin  $i$  of the  $\eta_{\text{det}}$  distribution. The calibration factors are then derived from the ratio  $C_i = c_i^{\text{data}}/c_i^{\text{MC}}$  of the  $\eta$ -intercalibration factors. The default calibration is extracted from an inclusive dijet simulated sample generated with PYTHIA. Figure 3.5 shows the relative jet response  $1/c$  for events with  $55 \text{ GeV} < p_{\text{T}}^{\text{avg}} < 75 \text{ GeV}$  for measured events and simulated events from the generators PYTHIA and HERWIG++ [155]. It can be observed, that the MC modeling differs for  $1/c$  in forward bins of  $\eta_{\text{det}}$  within up to 5% [154]. This difference in modeling is the largest uncertainty to the  $\eta$ -intercalibration correction factors.

After calibration, selection cuts are applied to the jet candidates. Jet candidates overlapping with selected electron candidates within  $\Delta R < 0.2$  are removed, as in these cases the jet and the electron very likely correspond to the same physics object. Additionally, it is evaluated how well the origin of each selected jet candidate agrees with the primary vertex to reject candidates from pile-up events. Therefore, a quantity called jet-vertex fraction  $\epsilon_{\text{jvf}}$  is defined as the ratio of  $\sum p_{\text{T}}$  for all tracks within the jet that originate from the primary vertex to the  $\sum p_{\text{T}}$  of all tracks matched to the jet. It is required, that  $\epsilon_{\text{jvf}} > 0.75$  for those jet candidates which have associated tracks. The  $\epsilon_{\text{jvf}}$  criterion is omitted for jet candidates without matched tracks. An overlap removal between jet and muon candidates is applied, removing any muon within a  $\Delta R < 0.4$  cone of a jet with  $p_{\text{T}} > 25 \text{ GeV}$  and  $\epsilon_{\text{jvf}} > 0.75$ . In

the same way an overlap removal is applied between jet and electron candidates, removing any electron within  $0.2 < \Delta R < 0.4$  of a jet.

In the presented analysis, jet candidates are required to have  $p_T > 30$  GeV and  $|\eta| < 4.5$ . Jet candidates in the transition region of the endcap and forward calorimeters, corresponding to a pseudorapidity of  $2.75 < |\eta| < 3.5$ , must have  $p_T > 35$  GeV. To investigate the performance of the jet reconstruction and calibration, truth jets are defined using stable MC truth particles with a mean lifetime greater than 30 ps. Particle-level jets are reconstructed using the anti- $k_t$  algorithm with a width of  $R = 0.4$ , implemented in the FASTJET [156] package. All stable particles, except for the leptons from  $W$ -boson decays, are used for the clustering. The same selection cuts are applied to the truth jets, that are applied to the reconstructed jet candidates. The comparison between the truth jets and the reconstructed jets is shown in Fig. 3.6. Selected jets have a resolution of about 10 GeV (see Fig. 3.6(a) and Fig. 3.6(c)) in  $p_T$  and 0.02 in  $\eta$  (see Fig. 3.6(b) and Fig. 3.6(d)) for simulated  $t$ -channel single top-quark signal events.

### Identification of $b$ -quark jets

The identification of jets containing  $b$  hadrons is not only important to identify top-quark candidate events, but is also used in this analysis to reject the large backgrounds with light-quark jets and  $c$ -quark jets in the final state. The algorithms used for the identification are called  $b$ -tagging algorithms and an overview of them is given in Ref. [157, 158]. The tagging is performed on a subset of tracks in the event, that are associated to the jet under consideration. The tracks are associated using a spatial matching in  $\Delta R(\text{track}, \text{jet})$ , that depends on the transverse momentum of the jet in order to have a smaller cone for high- $p_T$  jets. Due to the usage of tracks,  $b$ -tagging algorithms can only be applied within the geometrical coverage of the ID ( $|\eta| < 2.5$ ). All tagging algorithms exploit the properties of a  $b$ -hadron decay: its long lifetime of  $\tau \approx 1.5$  ps and its decay length of  $c\tau \approx 450 \mu\text{m}$  [12].

Figure 3.7 depicts a typical  $b$ -hadron decay. A  $b$ -hadron candidate can be found by exploiting the impact parameters  $d_0$  and  $z_0$  of tracks and by reconstructing a secondary vertex. Instead of the transverse and longitudinal impact parameters ( $d_0$  and  $z_0$ ), the impact-parameter significances,  $d_0/\sigma_{d_0}$  and  $z_0/\sigma_{z_0}$ , are used where  $\sigma$  represents the uncertainty of the impact-parameter measurement. Thus, the significances give more weight to well-measured tracks. The IP3D tagger [158] combines the impact-parameter significances  $d_0/\sigma_{d_0}$  and  $z_0/\sigma_{z_0}$  of all tracks in a jet using a likelihood-ratio technique to differentiate between  $b$ -quark jets and light quark jets. In another approach, the secondary vertex is reconstructed using tracks associated to the jet with large impact parameter by allowing  $|d_0|$  up to values of 3.5 mm and by applying no cut on  $z_0$ . The following vertex properties allow a good discrimination between  $b$ -quark jets and light-quark jets: the invariant mass of all tracks associated with the vertex, the jet-vertex fraction with respect to the reconstructed secondary vertex, the number of two-track vertices, and the angular distance between the jet axis and the line between the primary vertex and the secondary vertex. All four

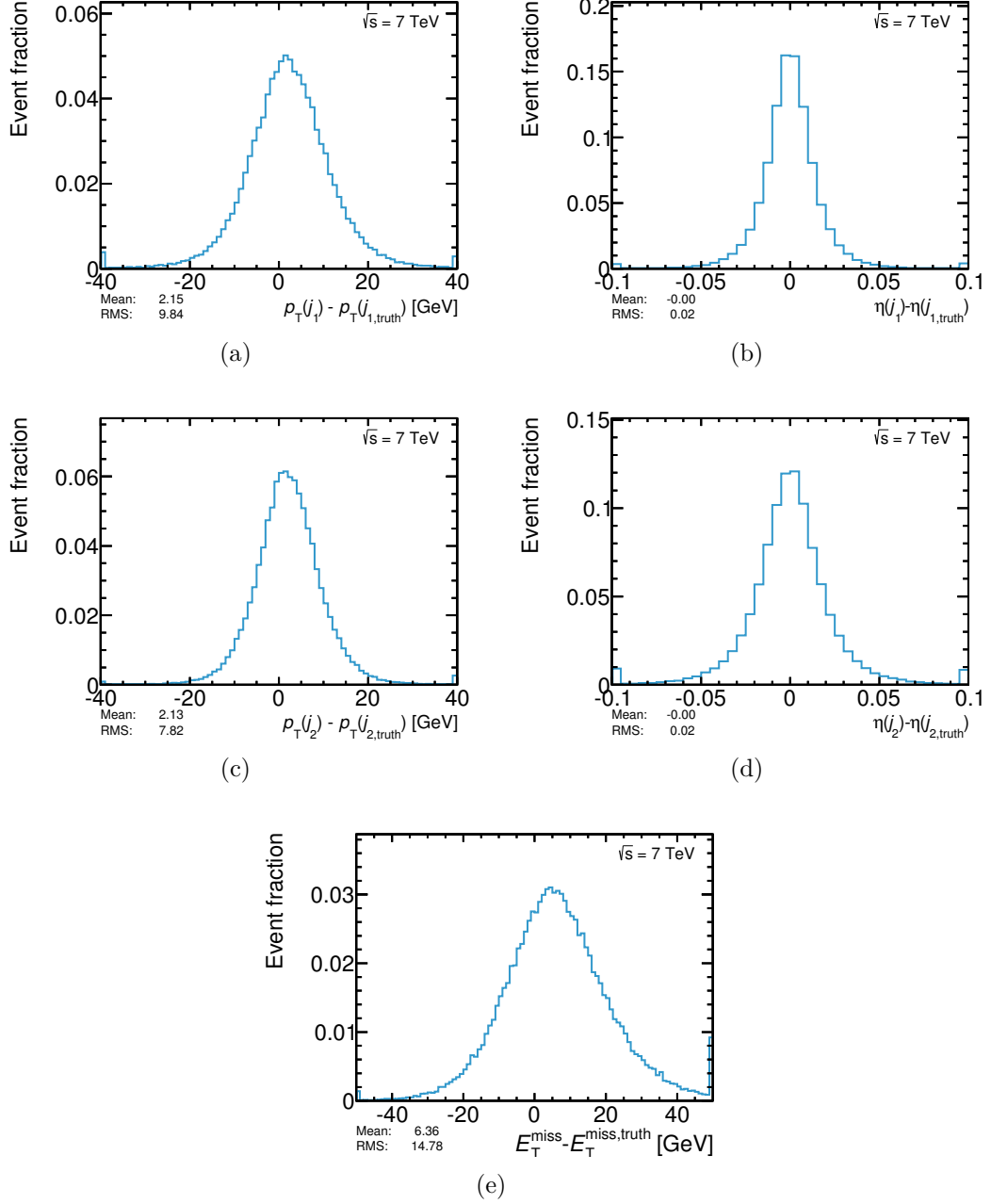


**Figure 3.6:** Residual distributions of reconstructed jets and  $E_T^{\text{miss}}$  using simulated  $t$ -channel single top-quark signal events. The distributions are normalized to unit area. The mean of the distribution gives information on a possible offset of the measured value compared to the true value. The RMS gives the resolution with which the variable is measured. Panel (a) shows the transverse momentum of the leading jet, (b) the pseudorapidity of the leading jet, (c) the transverse momentum of the sub-leading jet, (d) the pseudorapidity of the sub-leading jet, and (e) the missing transverse momentum.

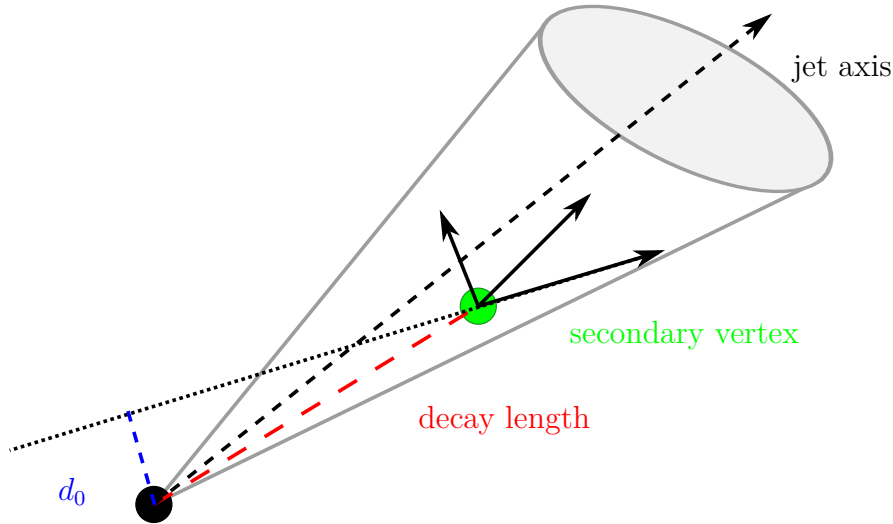


**Figure 3.7:** Schematic view of the decay of a  $b$ -hadron resulting into a secondary vertex with a significant decay length. The secondary vertex is reconstructed by selecting tracks with a large transverse impact parameter  $d_0$ . The tracks in the schematic are represented by black arrows.

variables are combined with a likelihood-ratio technique to one discriminant in the SV1 tagging algorithm [158].

To also separate  $b$ -quark jets from  $c$ -quark jets, the decay chain of the  $b$ -hadron candidate inside the jet is investigated. The JetFitter algorithm [159] uses a Kalman filter to check whether vertices of  $b$ - and  $c$ -hadron decays lay on a common line with the primary vertex. Again, a likelihood technique is used to combine properties of the found vertices to a discriminant which differentiates between  $b$ -quark,  $c$ -quark, and light quark jets.

To build a high-performance tagger, the discriminating variables of the IP3D tagger and the JetFitter tagger are then combined with additional variables describing the topology of the  $b$ -hadron decay chain using a neural network technique [158]. Three different neural network discriminants  $p_b$ ,  $p_c$ , and  $p_l$  are trained providing an optimal separation for  $b$ -quark jets,  $c$ -quark jets, and light-quark jets. In this analysis, the JetFitterCombNNc tagger is used as default tagger which is calculated as  $p_b/p_c$  [160]. It was shown in Ref. [161], that the JetFitterCombNNc tagger performs best for this analysis. In addition to the JetFitterCombNNc tagging algorithm, the MV1 tagging algorithm [160] is used to define the control regions for the presented analysis. This algorithm is a combination of the IP3D, the JetFitterCombNN, and the SV1 algorithm.

The performance of the introduced  $b$ -tagging algorithms is evaluated by comparing the  $b$ -tagging efficiency of each tagger with its light-quark jet rejection and  $c$ -quark jet rejection. Here, the rejection rate is given by the inverse of the misidentification efficiency. In Fig. 3.8 the performance of the JetFitterCombNNc tagger with other taggers is shown with respect to the light-quark jet rejection and the  $c$ -quark jet rejection. It can be observed in Fig. 3.8(b), that the JetFitterCombNNc tagger has the best  $c$ -quark jet rejection which is the property for which this tagger

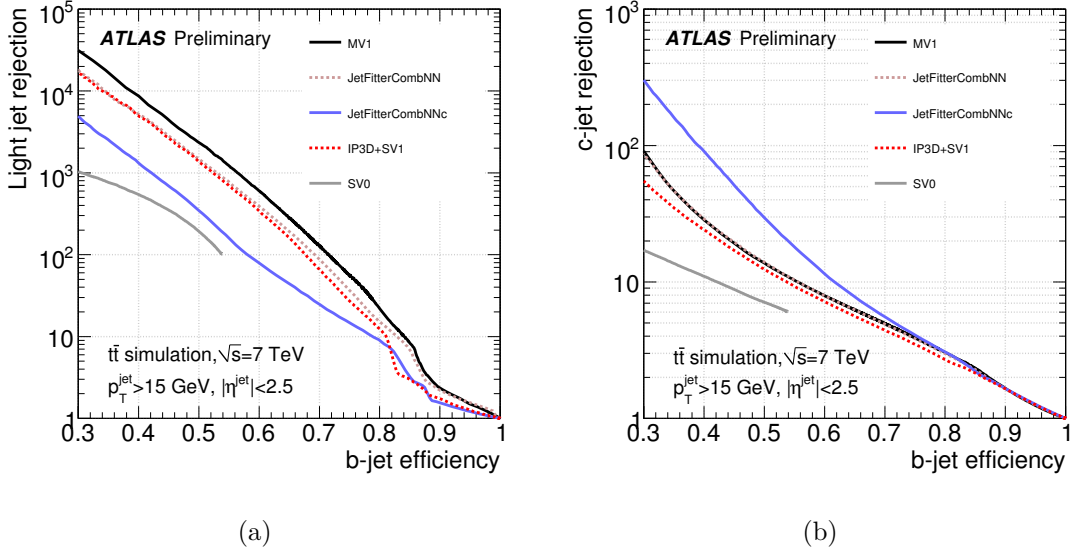


**Figure 3.8:** (a) Light quark jet rejection and (b)  $c$ -quark jet rejection as a function of the  $b$ -tag efficiency for several  $b$ -tagging algorithms including the *JetFitterCombNNc* tagger, investigated using simulated  $t\bar{t}$  events [160].

is chosen as default tagger. The light-quark jet rejection is worse for the *JetFitterCombNNc* tagger compared to the *MV1* tagger, shown in Fig. 3.8(a). But at a low  $b$ -tagging efficiency good values are achieved for the light-quark jet rejection. In order to compromise between good background rejection and efficient  $b$ -tagging, the *JetFitterCombNNc* tagger is used at a  $b$ -quark jet-identification efficiency of 54%, corresponding to a cut on the discriminant at 0.98. At this working point the light-quark jet rejection is 207 and the  $c$ -quark jet rejection is 20.7 for jets in simulated  $t\bar{t}$  events. The *MV1* tagging algorithm is used at a  $b$ -quark jet-identification efficiency of 85% corresponding to a cut on the tagging weight of 0.0714255. This point is chosen due to the low background rejection.

The  $b$ -tagging efficiency can be different for measured and simulated events. To calibrate it, the  $b$ -quark jet fraction before and after tagging needs to be determined. In case of the calibration of the *JetFitterCombNNc* tagger, this is done using the so-called  $p_T^{\text{rel}}$  method [160] where events with two or more jet candidates are selected. Here, one of the jets is required to have a reconstructed muon inside. The  $b$ -quark jet fraction is determined by exploiting the fact, that the momentum direction of the muons in  $b$ -hadron decays is further apart from the direction of the jet axis, than that of muons in  $c$ -quark or light-quark jets. This is contained in the variable  $p_T^{\text{rel}}$  defined as the momentum of the muon transverse to the combined muon-plus-jet axis. Templates for all jet flavors are fitted in the  $p_T^{\text{rel}}$  distribution in the pre-tagged sample and in the tagged sample. Thus, the  $b$ -tagging efficiency is derived in several bins of the jet  $p_T$  for measured and simulated events. In Fig. 3.9 the measured and simulated  $b$ -tagging efficiencies are compared and the derived scale factors are shown. The measurement of the  $b$ -tagging efficiency of the *JetFitterCombNNc* tagger with the  $p_T^{\text{rel}}$  method has an uncertainty of 5-27%.

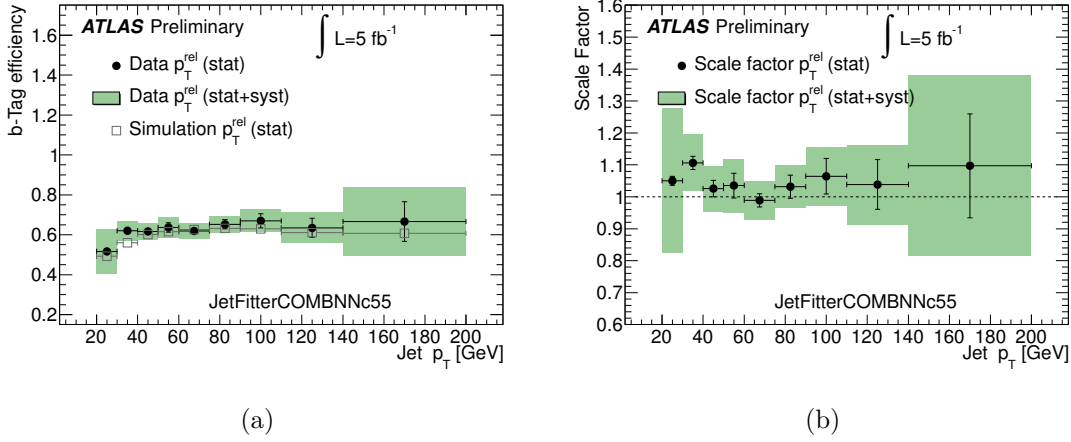


**Figure 3.9:** (a)  $b$ -tagging efficiency in data and simulation and (b) correction scale factors for the JetFitterCombNNc55 tagger at 55% efficiency obtained from the  $p_T^{\text{rel}}$  method [160].

### 3.2.6 Missing transverse momentum

While the momentum of the colliding partons is not known due to the composite nature of the proton, the transverse momentum at the initial state is known:  $p_T = 0$  GeV. Therefore, momentum conservation can only be expected in the transverse plane of the ATLAS detector. If a momentum imbalance is measured, it may have been caused due to the presence of unseen particles such as neutrinos. Because the final state of semileptonically decaying top quarks also includes a neutrino, a good measurement of the missing transverse momentum  $E_T^{\text{miss}}$  is important. The missing transverse momentum is calculated as follows:

$$E_T^{\text{miss}} = \sqrt{(E_x^{\text{miss}})^2 + (E_y^{\text{miss}})^2}. \quad (3.5)$$

The  $E_T^{\text{miss}}$  reconstruction [162] is mainly based on the energy deposits in the calorimeter and the muons reconstructed in the MS. The  $E_T^{\text{miss}}$  is calculated using the calibrated reconstructed physics objects. In addition, calorimeter cells not associated to a physics object are taken into account. Thus, the  $E_T^{\text{miss}}$  components can be expressed as:

$$E_{x(y)}^{\text{miss}} = E_{x(y)}^{\text{miss},e} + E_{x(y)}^{\text{miss},\gamma} + E_{x(y)}^{\text{miss},\tau} + E_{x(y)}^{\text{miss},\text{jets}} + E_{x(y)}^{\text{miss},\text{softjets}} + E_{x(y)}^{\text{miss},\text{CellOut}} + E_{x(y)}^{\text{miss},\mu}. \quad (3.6)$$

The  $E_{x(y)}^{\text{miss}}$  terms for  $e$ ,  $\gamma$ ,  $\tau$ , jets, and soft jets are calculated as the negative sum of the calibrated calorimeter cell energies of the corresponding objects up to a pseudorapidity of  $|\eta| < 4.5$ . “Soft jets” denote reconstructed jets with a transverse momentum of  $7 \text{ GeV} < p_T \leq 20 \text{ GeV}$  calibrated at the EM scale, and “jets” denote reconstructed jets with  $p_T > 20 \text{ GeV}$ . The  $E_{x(y)}^{\text{miss},\text{CellOut}}$  term is calculated from topological clusters outside the reconstructed objects with the EM-scale calibration and from reconstructed tracks with a  $p_T > 400 \text{ MeV}$ .  $E_{x(y)}^{\text{miss},\mu}$  is the negative sum of the momenta of the reconstructed muon tracks. A combined measurement of the muon in the ID and in the MS is used for isolated muons. If the muon is not isolated

( $\Delta R(\mu, \text{jet}) < 0.3$ ), then the MS measurement is used in addition to the energy loss of the muons measured in the calorimeter.

To define a truth  $E_{\text{T}}^{\text{miss}}$ , the momentum vectors of all neutrinos in the event are summed up. Neutrinos from hadron decays are not included. Using this truth definition, the resolution of the reconstructed  $E_{\text{T}}^{\text{miss}}$  is investigated. Figure 3.6(e) shows an achieved  $E_{\text{T}}^{\text{miss}}$  resolution of 15 GeV for simulated  $t$ -channel single top-quark signal events and an offset of 6 GeV for the reconstructed value of  $E_{\text{T}}^{\text{miss}}$ . More information on the  $E_{\text{T}}^{\text{miss}}$  reconstruction and the performance of the measurement can be found in Ref. [162].

### 3.2.7 Top quarks

As introduced in Section 1.2 a top quark decays into a  $b$  quark and a  $W$  boson. In the presented analysis only  $W$  bosons, that decay leptonically, are considered. Therefore, the  $W$  boson decays into a lepton and a neutrino. The reconstruction of the charged lepton (electron or muon) is already discussed in Sections 3.2.3 and 3.2.4, respectively. To fully reconstruct the four-momentum of the  $W$  boson  $\vec{p}(W) = \vec{p}(\ell) + \vec{p}(\nu)$ , the four-momentum of the neutrino  $\vec{p}(\nu)$  has to be determined.

It is only possible to extract the transverse vector components of the neutrino from the measurement of the event because the  $E_{\text{T}}^{\text{miss}}$  is the only available information. To determine the  $z$ -component of the neutrino  $p_z(\nu)$ , the  $W$ -boson system is constrained with the pole mass of the  $W$  boson:

$$m_W = \sqrt{(E(\ell) + E(\nu))^2 - |(\vec{p}(\ell) + \vec{p}(\nu))|^2} = 80.4 \text{ GeV}. \quad (3.7)$$

The  $z$ -component of the neutrino  $p_z(\nu)$  can then be determined by solving the following quadratic equation:

$$p_z^2(\nu) - 2 \frac{\mu \cdot p_z^2(\ell)}{E^2(\ell) - p_z^2(\ell)} \cdot p_z(\nu) + \frac{E^2(\ell) \cdot p_{\text{T}}^2(\nu) - \mu^2}{E^2(\ell) - p_z^2(\ell)} = 0 \quad (3.8)$$

with

$$\mu = \frac{m_W}{2} + p_{\text{T}}(\ell)p_{\text{T}}(\nu) \cos(\Delta\phi(\ell, E_{\text{T}}^{\text{miss}})). \quad (3.9)$$

Here,  $\Delta\phi(\ell, E_{\text{T}}^{\text{miss}})$  is the azimuthal angle difference between the charged lepton and the missing transverse momentum. In general, a quadratic equation has two solutions. These solutions are real, if the reconstructed transverse mass of the  $W$  boson  $m_{\text{T}}(W) = \sqrt{(p_{\text{T}}(\ell) + p_{\text{T}}(\nu))^2 - (p_x(\ell) + p_x(\nu))^2 - (p_y(\ell) + p_y(\nu))^2}$  is smaller or equal  $m_W$ . It was shown on simulated data in Ref. [163], that the smaller real solution reproduces the generated neutrino better in most of the cases. Therefore, the smallest real solution is chosen.

If  $m_{\text{T}}(W) > m_W$  due to an inaccurate  $E_{\text{T}}^{\text{miss}}$  measurement, the solutions for  $p_z(\nu)$  are complex. In these cases,  $m_{\text{T}}(W)$  is set to  $m_W$ , resulting into one real solution for  $p_z(\nu)$ . Then, the value for  $p_{\text{T}}(\nu)$  is modified such, that Equation 3.8 is still valid. Thus, two possible solutions are obtained for the components  $p_x(\nu)$  and  $p_y(\nu)$  of the neutrino momentum. By minimizing the distance  $\delta_{1/2}$  between the modified

$p_T(\nu)$  and the measured  $E_T^{\text{miss}}$ , the  $x$  and  $y$  components of the modified neutrino are chosen:

$$\delta_{1/2} = \sqrt{(p_{x,1/2}(\nu) - E_x^{\text{miss}})^2 + (p_{y,1/2}(\nu) - E_y^{\text{miss}})^2}. \quad (3.10)$$

The modified  $x$  and  $y$  components of the neutrino are then used to recalculate  $p_z(\nu)$ . Then, the  $W$  boson is reconstructed by adding the four-momenta of the reconstructed lepton and the reconstructed neutrino.

Finally, the four-momentum of a top quark is then determined by adding up the four-momenta of the  $b$ -tagged jet and the reconstructed  $W$  boson. The  $b$ -tagged jet is chosen as  $b$ -quark jet from the top-quark decay because it corresponds to the  $b$  quark from the top decay in 90% of all simulated  $t$ -channel single top-quark signal events with one  $b$ -tagged jet. This was shown in Ref. [164].

# Chapter 4

## Signal extraction

The final state of  $t$ -channel single top-quark events consists of one charged lepton, one neutrino, and one  $b$ -quark jet which form the decay products of the top-quark, one spectator light-quark jet, and one jet stemming from the second spectator  $b$ -quark. Consequently, in reconstructed  $pp$ -collision events the signal is searched for in a dataset consisting of a reconstructed electron or muon, a significant amount of missing transverse momentum, and two or three reconstructed jets where one of the jets is  $b$ -tagged. This dataset is also called lepton+jets dataset. Not only signal events are selected but also background events. The background processes can be separated in background processes, that have a lepton, a neutrino, and jets in the final state, and background processes, that are selected due to mis-measurement or limited geometric coverage of the detector. Both, the signal and background processes are modeled using MC methods.

In this thesis two consecutive strategies are applied to separate the background events from the signal candidate events. In a first step, a series of selection cuts is applied. Then, a neural network is constructed to fully exploit the kinematic properties of the signal process. This chapter is structured as follows. First, the modeling of the signal process and the background processes is discussed. Then, the event selection is introduced and finally, the neural networks are discussed, that are used in the analysis.

### 4.1 Modeling of signal and background processes

In the following, the signal and background processes are introduced, and their modeling is described. Furthermore, the corresponding theoretical cross section as well as its uncertainty is given for each process.

#### 4.1.1 Signal modeling

As discussed in Section 1.3.1 the 4FS calculation provides the best kinematic description of the final-state particles of the signal process. Thus, event generators based on 4FS NLO calculations are used to simulate signal events. One of these generators is the NLO ME generator POWHEG-BOX, that is interfaced to PYTHIA

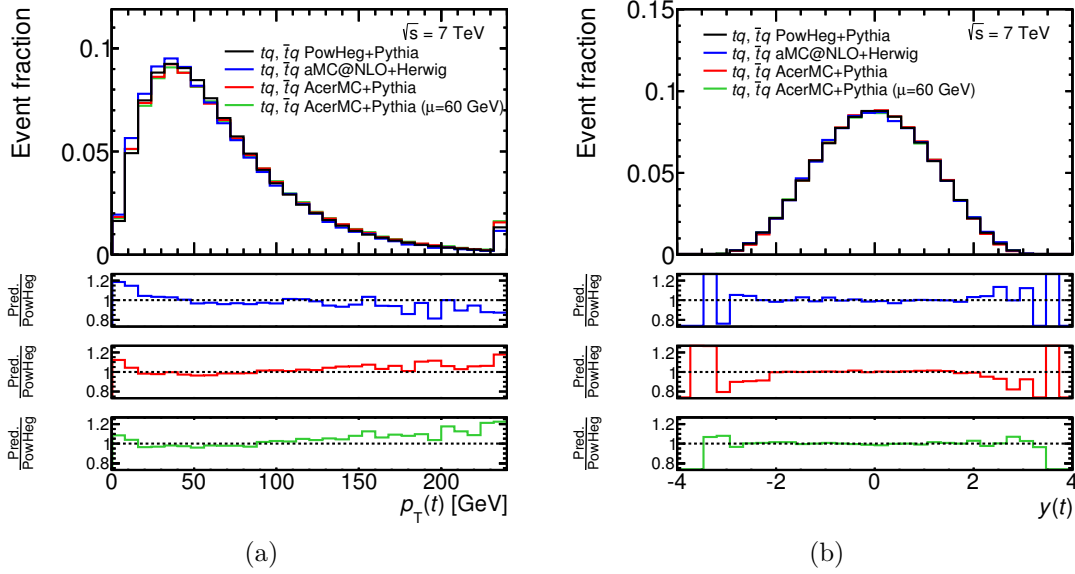


**Figure 4.1:** Comparison of the different signal generators: POWHEG-BOX+PYTHIA, aMC@NLO+HERWIG, and ACERMC+PYTHIA in the following parton-level top-quark properties: (a) the transverse momentum of the top quark and (b) the rapidity of the top quark. The distributions are normalized to unit area. In the lower panels, the ratio of the prediction of each generator compared to the POWHEG-BOX+PYTHIA prediction is shown.

for showering and hadronization. In POWHEG-BOX the top-quark mass is set to  $m_t = 172.5$  GeV, and the renormalization and factorization scales are calculated event-by-event with  $\mu = 4 \cdot \sqrt{m_b^2 + p_{T,b}^2}$  [77] where  $m_b = 4.75$  GeV and  $p_{T,b}$  are the mass and the transverse momentum of the  $b$  quark from the initial gluon splitting. This scale choice is motivated in the same way as the scale choice for the calculation given in Ref. [62]. All events are generated using the fixed four-flavor PDF set CT104f [35].

Another generator to simulate signal events at NLO accuracy using the 4FS calculation is aMC@NLO. Here, parton shower and hadronization are done with HERWIG and JIMMY. The scales, the top-quark mass, and the PDF set used are the same as for the generation with POWHEG-BOX described above.

In previous ATLAS analyses (e.g. Ref. [56]) the LO ACERMC generator interfaced to PYTHIA was used to simulate signal events. ACERMC includes both processes:  $qb \rightarrow tq$  and  $qg \rightarrow tqb$ . Events generated according to the 5FS and the 4FS are combined to one consistent sample based on the ACOT matching prescription to avoid kinematic overlap. For the event generation the MRST LO\*\* [165] PDF set is used. The default scale is set to  $\mu = m_t$ .

In the following, the predictions from all three generators are compared for several kinematic properties of the final state particles. Two ACERMC samples are included, that differ in the scale choice. One sample is generated with  $\mu = m_t$  and one with  $\mu = 60$  GeV.

In Fig. 4.1, the transverse momentum and the rapidity of the top quark are shown. In the lower panels, the ratio of the prediction from each generator to the prediction from the default POWHEG-BOX+PYTHIA generator is shown. The top quark is evaluated at parton level without any selection cuts applied. It can be observed, that the  $p_T$  distribution of the top-quark peaks at approximately 40 GeV, while its rapidity distribution peaks at zero.

The predictions of all generators agree well with each other in both distributions. In particular, good agreement is observed between the ACERMC+PYTHIA samples generated with different scales. Consequently, top-quark observables do not depend heavily on the scale choice. Small differences are observed for the  $p_T(t)$  distribution. The prediction by the aMC@NLO+HERWIG generator gives lower  $p_T$  values than the POWHEG-BOX+PYTHIA generator, while the ACERMC+PYTHIA generator predicts more events with large values of  $p_T(t)$ .

To compare the properties of the light quark and the spectator  $b$ -quark, truth jets are defined as introduced in Section 3.2.5. Also, the truth  $E_T^{\text{miss}}$  defined in Section 3.2.6 is used. Requirements on  $p_T$  and  $\eta$  are applied to the truth jets, the truth leptons, and the truth  $E_T^{\text{miss}}$ , that correspond to the object definitions in Section 3.2. Also, the overlap removals are applied. Events with exactly one lepton and at least one  $b$ -quark jet are selected. A truth jet is tagged as a  $b$ -quark jet, if at least one  $B$  hadron is found within the jet.

To investigate the properties of the light-quark jet, events are selected with two jets where one of them is  $b$ -tagged. In Fig. 4.2(a) the transverse momentum of the light quark jet is shown and in Fig. 4.2(b) the pseudorapidity of the light quark jet. The transverse momentum of the light quark jet peaks at small values, such that the cut on the jet  $p_T$  at 30 GeV already cuts hard in the distribution. The light quark jet is produced forward, so that its pseudorapidity peaks at  $|\eta(j)| \approx 2.5$ .

Predictions by the generators POWHEG-BOX+PYTHIA and aMC@NLO+HERWIG agree well with each other. In case of  $\eta(j)$  the predictions by ACERMC+PYTHIA using  $\mu = 60$  GeV agree better with the NLO generators, while ACERMC+PYTHIA using  $\mu = m_t$  predicts the light quark jets to be less forward. But in case of  $p_T(j)$ , ACERMC+PYTHIA using  $\mu = 60$  GeV predicts light quark jets with higher values of  $p_T$  compared to all other generators.

The truth jet originating from the spectator  $b$ -quark is evaluated in events with three jets where two jets are tagged as  $b$ -quark jet. The  $b$ -quark jet with the lowest value in  $p_T$  is chosen as the jet  $b_2$  originating from the spectator  $b$ -quark. In Fig. 4.2(c) and Fig. 4.2(d) the transverse momentum and the pseudorapidity of the spectator  $b$ -quark jet are displayed. The spectator  $b$ -quark jet is produced centrally with a low transverse momentum. Fig. 4.2(c) shows, that the distribution of the transverse momentum decreases rapidly. The  $p_T$  of the spectator  $b$ -quark jet is mostly below 80 GeV.

Again, the distributions of the spectator  $b$ -quark jet are compared for all generators. Here, the generators POWHEG-BOX+PYTHIA, aMC@NLO+HERWIG, and ACERMC+PYTHIA using  $\mu = m_t$  agree well with each other. The ACERMC+PYTHIA generator using  $\mu = 60$  GeV predicts larger values for  $p_T(b_2)$ .

In Fig. 4.3(a), the distribution of the number of truth jets,  $n_{\text{jet}}$ , is shown for all four signal models. Here, events are selected, if one or more jets are present in the event with at least one  $b$ -tagged jet. It can be observed, that the distribution peaks

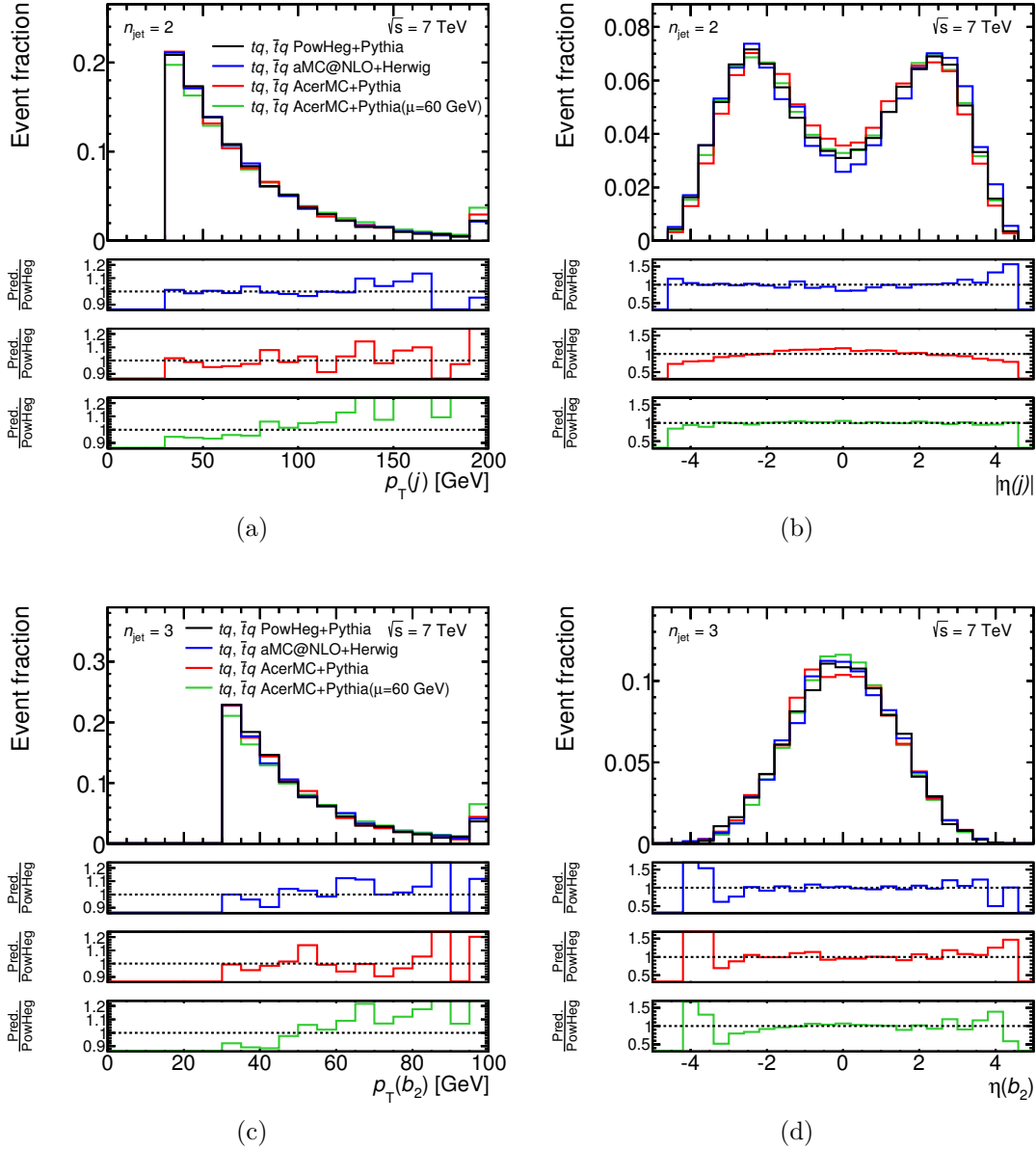


**Figure 4.2:** Comparison of the different signal generators: POWHEG-BOX+PYTHIA, aMC@NLO+HERWIG, and ACERMC+PYTHIA in the following particle-level variables: (a) the transverse momentum of the light-quark jet, (b) the pseudorapidity of the light-quark jet, (c) the transverse momentum of the spectator  $b$ -quark jet, and (d) the pseudorapidity of the sepectator  $b$ -quark jet. The distributions are normalized to unit area. In the lower panels, the ratio of the prediction of each generator compared to the POWHEG-BOX+PYTHIA prediction is shown.

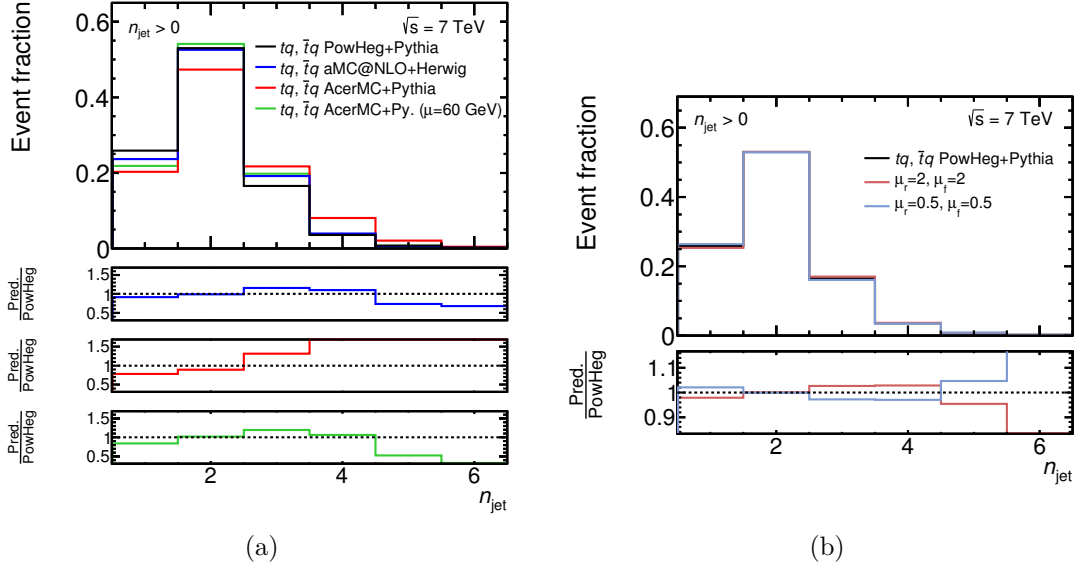


**Figure 4.3:** Comparison of the  $n_{\text{jet}}$  distribution at particle level in events with one or more jets for (a) the different signal generators POWHEG-BOX+PYTHIA, aMC@NLO+HERWIG, and ACERMC+PYTHIA and for (b) different scale choices for the generation with POWHEG-BOX+PYTHIA. The distribution is normalized to unit area. In the lower panels, the ratio between the prediction of each generator compared to the POWHEG-BOX+PYTHIA prediction is shown.

at  $n_{\text{jet}} = 2$ . Also a significant fraction of signal events have three selected truth jets. Thus, the chosen final state for the analysis is motivated.

While the agreement between the predictions by the POWHEG-BOX+PYTHIA and the aMC@NLO+HERWIG generator is good for events with two jets and differs only slightly for events with three jets, the prediction of the ACERMC+PYTHIA generator with the scale  $\mu = m_t$  differs substantially in all bins of the distribution. If the scale is set to  $\mu = 60$  GeV, the agreement of the predictions by the ACERMC+PYTHIA generator with the NLO generators is much improved. In this distribution a large dependence on the choice of the scale is observed for the ACERMC+PYTHIA generator.

To investigate the scale dependence of the default POWHEG-BOX+PYTHIA generator, two samples are evaluated where the renormalization scale and factorization scale are varied by a factor of 0.5 and 2.0. The scale of the parton shower is varied consistently with the scales. In Fig. 4.3(b), the  $n_{\text{jet}}$  distribution is shown for the POWHEG-BOX+PYTHIA prediction and the two scale variations. Only small differences in the shape of the distribution are observed.

In summary, the predictions by ACERMC+PYTHIA feature a large dependence on the scale choice in case of the light quark jet and the second  $b$ -quark jet. This is especially visible in the  $n_{\text{jet}}$  distributions. The effect of the scale variations is not as distinctive on the variables of the ME objects. Therefore, the scale variations mainly effect the modeling of the shower. Due to this scale dependence of the predictions,

ACERMC was replaced with the POWHEG-BOX+PYTHIA generator as the default event model, since the scale dependence of the generation with POWHEG-BOX is much smaller.

In the presented analysis the signal process is separated in top-quark and top-antiquark production, noted with  $tq$  and  $\bar{t}q$  respectively, that differ in the charge of the lepton in the final state. This is done to independently measure the  $t$ -channel single top-quark and top-antiquark production cross-sections,  $\sigma(tq)$  and  $\sigma(\bar{t}q)$ .

### 4.1.2 Background modeling

The largest background contributions originate from background processes with one leptonic  $W$ -boson decay. These processes are  $W$ +jets production, top-quark pair production ( $t\bar{t}$ ), and the single top-quark production in the  $s$ - and  $Wt$ -channel. Other background contributions arise from misidentified physics objects. These background processes are QCD-multijet production,  $Z$ +jets production, and diboson production. All background processes except for QCD-multijet production are modeled with simulated events using the methods described in Section 3.1. In the following each background process and its simulation are introduced, and the strategies for the modeling of each background process are described.

#### Top-quark background

The dominant contribution of top-quark backgrounds is  $t\bar{t}$  production either in the semi-leptonic decay channel, depicted in Fig. 4.4(a), or in the di-leptonic decay channel. The  $t\bar{t}$  event signature mimics the signal final state, if some of the decay products are not observed in the detector due to its limited geometric coverage and due to the reconstruction and selection efficiencies of the defined objects. Other top-quark background processes are the  $Wt$ -channel and  $s$ -channel single top-quark production modes. The semi-leptonic decay modes are depicted in Fig. 4.4(b) for the  $Wt$ -channel production and in Fig. 4.4(c) for the  $s$ -channel production. Due to their small production cross-sections of the single top-quark processes their contribution to the top-quark background is small.

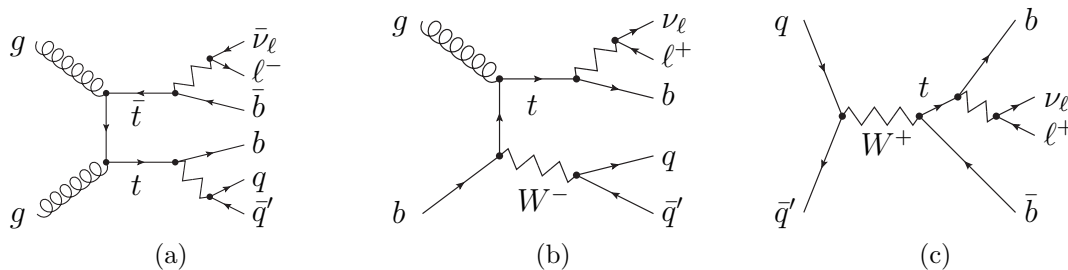


**Figure 4.4:** Example Feynman diagrams of background events from top-quark production. The dominant source of top-quark background is the  $t\bar{t}$  production in the (a) semi-leptonic decay mode and the di-leptonic decay mode. Smaller rates are expected from the (b) associated  $Wt$  production and the (c)  $s$ -channel single top-quark production.

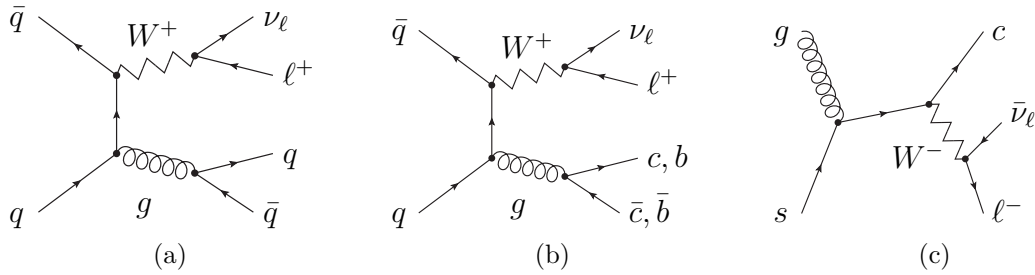


**Figure 4.5:** Example Feynman diagrams of background events from  $W$ +jets production. Several different MC samples are used: Samples with only light quarks ( $u, d, s$ ) in the ME (a) and those with heavy-flavor quarks in the ME ((b) and (c)).

MC samples of  $t\bar{t}$ ,  $Wt$ -channel single top-quark, and  $s$ -channel single top-quark events are generated with the NLO ME generator POWHEG-BOX interfaced to PYTHIA using the CT10 PDF set. The top-quark mass is set to  $m_t = 172.5$  GeV for all three processes. The theory cross-sections and their uncertainties correspond to the values introduced in Section 1.2.

In the presented analysis all top-quark background processes are grouped together to a single process. The asymmetry between single top-quark production and top-antiquark production in the  $s$ -channel is taken from the NLO+NNLL prediction.

### $W$ +jets

Large background contributions are expected from the production of a  $W$  boson in the leptonic decay mode accompanied by jet production. The jet production mostly occurs via a radiated gluon, that splits either into a light-quark pair, depicted in Fig. 4.5(a), or into a heavy-flavor quark-pair ( $c\bar{c}$ ,  $b\bar{b}$ ), depicted in Fig. 4.5(b). Another significant background contribution arises from the production of a  $W$  boson together with a single  $c$ -quark jet, depicted in Fig. 4.5(c).

$W$ -boson production in association with jets is simulated with the ALPGEN generator using the CTEQ6L1 set of PDFs [166]. The partonic events are showered with HERWIG, and the underlying event is simulated with the JIMMY model. Here,  $W$ +light jets events are generated via the ME calculation taking into account the production of up to five additional partons where a parton is defined as a massless light quark ( $u, d, s$ , or  $c$ ) or a gluon. In these samples  $b$ -quark jets are only produced in the parton shower. The MLM matching scheme is used to remove overlap between partonic configurations generated by the ME calculation and by the parton-shower evolution. In addition, samples with massive heavy-flavor quarks ( $c$  and  $b$ ) are simulated with ALPGEN for the processes  $W + c\bar{c} + n$  partons and  $W + b\bar{b} + n$  partons and for the  $W + c + n$ -parton production where  $n$  corresponds to the number of additional partons.

There is no procedure implemented in the ALPGEN generator which removes the overlap between the inclusive  $W + n$ -parton samples and the dedicated  $W$ +heavy flavor-jet samples. Therefore, the overlap is removed with an external matching scheme. The utilized matching procedure exploits the different advantages of the

ME calculation and the parton-shower evolution. The matrix element describes those jets best, that originate from well-separated partons with large transverse momentum, while collinear gluon splitting is better described by the parton shower. These properties are exploited using a matching based on the distance  $\Delta R$  between two heavy-flavor quarks. If  $\Delta R < R_0$ , the events from the parton shower are used, and the ME events are removed. If  $\Delta R > R_0$ , the associated heavy-flavor production with the ME calculation is chosen, and the parton-shower events are removed. The parameter  $R_0 = 0.4$  is set to the same value as the cone size of the reconstructed jets. This matching procedure is called heavy-flavor overlap-removal [56].

The cross sections for inclusive  $W$ -boson production are predicted with NNLO accuracy using the FEWZ program [167], resulting in a LO-to-NNLO scale factor of 1.2 and an uncertainty of 4%. The uncertainty includes the uncertainties on the PDF and scale choices. The scale factor is applied to the prediction based on the LO ALPGEN calculation for the  $W+b\bar{b}$ ,  $W+c\bar{c}$ , and  $W$ +light jets samples. An uncertainty for associated jet production is estimated using variations of the factorization and renormalization scale and the ALPGEN matching parameter. These variations yield an uncertainty of 5% for the production of two additional light-quark jets and 15% for two additional heavy-quark jets. An additional relative uncertainty of 50% is assigned to the  $W+b\bar{b}$  and  $W+c\bar{c}$  production to take the uncertainty on heavy-flavor production into account. This uncertainty is estimated using a tag-counting method in control regions [56]. The ALPGEN prediction for the  $W+c$  process is scaled by a factor of 1.52 that is obtained from a study based on NLO calculations using MCFM. Normalization uncertainties on the factorization and renormalization scale and PDF uncertainties are 24%.

At the LHC, the production of  $W^++b\bar{b}$ ,  $W^++c\bar{c}$ , and  $W^+$ +light jets has a larger cross section than the production of  $W^-+b\bar{b}$ ,  $W^-+c\bar{c}$ , and  $W^-$ +light jets. Here, the ratio  $W^+/W^-$  is the same for all three production processes. Therefore, these processes are combined in the analysis. In case of  $W+c$  production, the cross sections for  $W^++c$  production and  $W^-+c$  production are of the same size [168, 169]. Thus,  $W+c$  production is treated separately from the other  $W$ +jets processes.

### **$Z$ +jets and diboson**

A small background contribution arises from  $Z$ +jets production, shown in Fig. 4.6(a). Here, one of the leptons from the  $Z$  decay is either lost due to the limited geometric coverage of the detector or mis-identified as a jet.  $Z$ -boson production in association with jets is simulated using the multileg LO generator ALPGEN with the CTEQ6L1 PDF set. The partonic events are showered with HERWIG, and the underlying event is simulated with JIMMY. Inclusive  $Z$ +jets samples are generated with up to five additional partons in the ME calculation. Then, the MLM matching scheme is again used to remove the overlap between the ME calculation and the parton-shower evolution. In case of  $Z$ +jets production, heavy-flavor quarks are produced exclusively in the parton shower. A scale factor of 1.25 is derived with the FEWZ program to correct the LO ALPGEN prediction to NNLO accuracy. A cross-section uncertainty of 60% is assigned for  $Z$ +jets production.

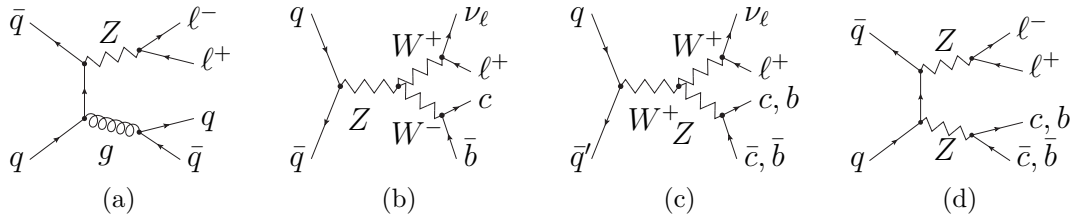


**Figure 4.6:** Example Feynman diagrams of background events from (a)  $Z$ +jets production and (b)  $WW$ , (c)  $WZ$ , and (d)  $ZZ$  production.

Another small background is the diboson production consisting of  $WW$ ,  $WZ$ , and  $ZZ$  production, shown in Fig. 4.6(b)-(d). In case of  $WW$  and  $WZ$  production, there is a  $W$  boson in the final state, that decays leptonically. Similar to  $Z$ +jets events, one of the leptons of the leptonic  $Z$  decay is lost in case of the  $ZZ$  production. All three diboson processes are simulated with HERWIG and JIMMY using the MRST LO\*\* PDF set. The events are normalized to the NLO cross-section prediction calculated with MCFM. The cross-section uncertainty for these processes is 5%.

Due to the small contribution of diboson and  $Z$ +jets production, all processes are grouped together to one process, denoted with “ $Z$ +jets, diboson”.

### Summary of MC simulated samples

A summary of the MC simulated samples used in this thesis is given in Table 4.1. For each process the generator, the cross-section, and the sample size are listed. Table 4.2 presents a list of samples which are used to evaluate systematic uncertainties in the choice of the generator, of the parton-shower model, and of the modeling of the radiation of additional jets in the initial or final state (ISR/FSR), e.g. by varying the renormalization scale  $\mu_r$  and the factorization scale  $\mu_f$ . These uncertainties are investigated for all top-quark production processes. Further samples exist for top-quark processes where the top-quark mass is set to different values. These samples are used to determine the dependence of the measurement of the inclusive cross sections on the top-quark mass.

### QCD multijet

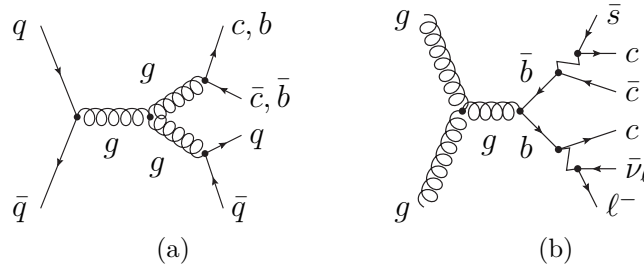
Another background process is multijet production via the strong interaction. These events contribute to the background, if a jet is misidentified as a lepton, usually an electron as shown in Fig 4.7(a), combined with a simultaneous mis-measurement of  $E_T^{\text{miss}}$ . In a different scenario, a real high- $p_T$  lepton is produced within a jet due to a semileptonic decay of a heavy-flavor ( $b$  or  $c$ ) hadron and satisfies the lepton-isolation criteria, shown in Fig. 4.7(b). The mis-identification of a jet as a lepton has a small probability of  $10^{-4}$  [170]. Due to the large cross section for multijet production in  $pp$  collisions at the order of 1 mb [171], the amount of multijet events in the lepton+jets dataset is significant. Since it is not possible to simulate these events with sufficient statistics and to calculate their production rate, different techniques are employed

**Table 4.1:** Overview of the MC simulated samples used in this analysis. The cross-section values include, if necessary, the branching ratios.

Process	Generator	$\sigma$ [pb]	Events
$tq + \bar{t}q$ ( $W \rightarrow l\nu$ )	POWHEG+PYTHIA	20.9	2,000,000
$t\bar{t}$ no fully hadronic	POWHEG+PYTHIA	96.1	10,000,000
$Wt$	POWHEG+PYTHIA	15.7	5,000,000
$t\bar{b} + \bar{t}b$ ( $W \rightarrow l\nu$ )	POWHEG+PYTHIA	1.50	1,500,000
$W \rightarrow l\nu + 0$ partons	ALPGEN+HERWIG	24,954	17,300,000
$W \rightarrow l\nu + 1$ parton	ALPGEN+HERWIG	4,699	12,500,000
$W \rightarrow l\nu + 2$ partons	ALPGEN+HERWIG	1,361	11,300,000
$W \rightarrow l\nu + 3$ partons	ALPGEN+HERWIG	367	3,030,000
$W \rightarrow l\nu + 4$ partons	ALPGEN+HERWIG	92.5	1,750,000
$W \rightarrow l\nu + 5$ partons	ALPGEN+HERWIG	25.2	903,000
$W \rightarrow l\nu + b\bar{b} + 0$ partons	ALPGEN+HERWIG	56.8	475,000
$W \rightarrow l\nu + b\bar{b} + 1$ parton	ALPGEN+HERWIG	42.9	205,000
$W \rightarrow l\nu + b\bar{b} + 2$ partons	ALPGEN+HERWIG	20.8	175,000
$W \rightarrow l\nu + b\bar{b} + 3$ partons	ALPGEN+HERWIG	9.13	70,000
$W \rightarrow l\nu + c\bar{c} + 0$ partons	ALPGEN+HERWIG	153	1,270,000
$W \rightarrow l\nu + c\bar{c} + 1$ parton	ALPGEN+HERWIG	126	1,050,000
$W \rightarrow l\nu + c\bar{c} + 2$ partons	ALPGEN+HERWIG	62.5	525,000
$W \rightarrow l\nu + c\bar{c} + 3$ partons	ALPGEN+HERWIG	20.4	170,000
$W \rightarrow l\nu + c + 0$ partons	ALPGEN+HERWIG	980	6,500,000
$W \rightarrow l\nu + c + 1$ parton	ALPGEN+HERWIG	312	2,070,000
$W \rightarrow l\nu + c + 2$ partons	ALPGEN+HERWIG	77.2	520,000
$W \rightarrow l\nu + c + 3$ partons	ALPGEN+HERWIG	17.3	115,000
$W \rightarrow l\nu + c + 4$ partons	ALPGEN+HERWIG	4.3	30,000
$Z \rightarrow ll + 0$ partons	ALPGEN+HERWIG	2,506	19,900,000
$Z \rightarrow ll + 1$ parton	ALPGEN+HERWIG	504	4,000,000
$Z \rightarrow ll + 2$ partons	ALPGEN+HERWIG	151	5,010,000
$Z \rightarrow ll + 3$ partons	ALPGEN+HERWIG	42.0	1,610,000
$Z \rightarrow ll + 4$ partons	ALPGEN+HERWIG	10.5	445,000
$Z \rightarrow ll + 5$ partons	ALPGEN+HERWIG	3.0	145,000
$WW$	HERWIG	16.9	2,490,000
$ZZ$	HERWIG	1.10	250,000
$WZ$	HERWIG	5.54	1,000,000

**Table 4.2:** Overview of the MC simulated samples with different event generators or different settings in the generators.

Process	Variation	Generator	Events
$tq + \bar{t}q (W \rightarrow \ell\nu)$	Diff. generator	aMC@NLO+HERWIG	1,000,000
	$2 \cdot \mu_r, 2 \cdot \mu_f$	POWHEG+PYTHIA	2,000,000
	$0.5 \cdot \mu_r, 0.5 \cdot \mu_f$	POWHEG+PYTHIA	2,000,000
	$m_t = 170.0 \text{ GeV}$	ACERMC+PYTHIA	1,500,000
	$m_t = 175.0 \text{ GeV}$	ACERMC+PYTHIA	1,500,000
$t\bar{t}$ no fully hadronic	Diff. generator	ALPGEN+HERWIG	4,420,000
	ISR/FSR	ACERMC+PYTHIA	10,000,000
	$m_t = 170.0 \text{ GeV}$	POWHEG+PYTHIA	4,990,000
	$m_t = 175.0 \text{ GeV}$	POWHEG+PYTHIA	5,000,000
$Wt$	$m_t = 170.0 \text{ GeV}$	POWHEG+PYTHIA	1,000,000
	$m_t = 175.0 \text{ GeV}$	POWHEG+PYTHIA	1,000,000
$t\bar{b} + \bar{t}b (W \rightarrow \ell\nu)$	$m_t = 170.0 \text{ GeV}$	POWHEG+PYTHIA	150,000
	$m_t = 175.0 \text{ GeV}$	POWHEG+PYTHIA	150,000

**Figure 4.7:** Example Feynman diagrams of background events from multijet production. In (a) an example for a hadronic multijet event is shown. It contributes to the background, when one of the jets is mis-identified as an electron. An example for a semi-leptonic heavy flavor decay is shown in (b). These events have a small probability to satisfy the lepton identification criteria.

to model multijet events and to estimate their rate in the electron and in the muon channel.

In the electron channel, the jet-lepton model [170] is used to model mis-identified jets. The model is based on the selection of electron-like jets in simulated QCD-dijet events. The dijet sample is generated with PYTHIA and filtered for jets with a transverse momentum of  $p_T^{\text{jet}} > 17 \text{ GeV}$ . The sample is selected using the signal selection except for the selection of the electron. The electron is replaced by a jet, that fulfills the following criteria to model the kinematic properties of a jet mis-identified as an electron. A candidate jet must have an energy deposit in the EM calorimeter between 80% and 95% of the jet energy. This jet is then called the jet-

**Table 4.3:** Identification criteria for the selection of a jet-lepton.

Variable	Cut
EM fraction	$0.8 < f_{\text{EM}} < 0.95$
Transverse momentum	$p_{\text{T}}^{\text{EM scale}} > 25 \text{ GeV}$
Pseudorapidity	$ \eta  < 2.47$ and $1.37 <  \eta  < 1.52$

lepton candidate and meets the same kinematic properties in  $p_{\text{T}}$  and  $\eta$  as a signal electron. Hereby, the transverse momentum of the jet-lepton candidate is defined at the EM scale. This choice is consistently propagated to the  $E_{\text{T}}^{\text{miss}}$  calculation of the event. If one or more jet-lepton candidates are found, the event is accepted and the jet with the largest energy fraction in the EM calorimeter is chosen as jet-lepton. In Table 4.3 the selection requirements for the jet-lepton are summarized.

In Ref. [170] it is shown, that the jet-lepton template reproduces the shape of multijet background events in the electron channel well using jet-triggered data as input to the model. Due to the rise of the  $p_{\text{T}}$  threshold of the jet triggers the data-derived model suffered from poor statistics. Thus, a simulated dijet sample is used in this analysis, since it reproduces the shape of the template derived from measured data events. To estimate the rate of multijet events, a binned maximum-likelihood fit is performed in the  $E_{\text{T}}^{\text{miss}}$  distribution where the difference between multijet events and events with true  $E_{\text{T}}^{\text{miss}}$  is most pronounced.

In the muon channel, the matrix method [172, 173] is used to obtain the normalization and shape of the multijet background. Multijet events in the muon channel are mainly caused by semi-leptonic heavy-flavor decays within a jet. This characteristic is exploited in the matrix method by choosing two single-muon datasets, one with tight muon-isolation criteria and the other with loose muon-isolation criteria. The tight isolation selection corresponds to the muon definition described in Section 3.2.4. In the loose dataset the isolation cuts on  $\sum E_{\text{T}}^{\text{calo}}$  and  $\sum p_{\text{T}}^{\text{track}}$  are removed. Thus, the tightly selected dataset is a subset of the loosely selected dataset.

The number of selected events  $N^{\text{tight}}$  in the tight dataset and  $N^{\text{loose}}$  in the loose dataset can be expressed by:

$$N^{\text{loose}} = N_{\text{real}}^{\text{loose}} + N_{\text{fake}}^{\text{loose}} \quad (4.1)$$

$$N^{\text{tight}} = N_{\text{real}}^{\text{tight}} + N_{\text{fake}}^{\text{tight}} = \epsilon_{\text{real}} N_{\text{real}}^{\text{loose}} + \epsilon_{\text{fake}} N_{\text{fake}}^{\text{loose}} \quad (4.2)$$

where  $\epsilon_{\text{real}}$  and  $\epsilon_{\text{fake}}$  are the efficiencies for real and fake loose muons being selected as tightly isolated muons. Then, the number of multijet events  $N_{\text{fake}}^{\text{tight}}$  satisfying the tight isolation criteria can be written as

$$N_{\text{fake}}^{\text{tight}} = \frac{\epsilon_{\text{fake}}}{\epsilon_{\text{real}} - \epsilon_{\text{fake}}} (N^{\text{loose}} \epsilon_{\text{real}} - N^{\text{tight}}). \quad (4.3)$$

The fake efficiencies are extrapolated from the ratio between the loose and tight muons derived from collision data in a dataset of selected muon candidates with a

high impact-parameter significance. The signal efficiency is measured from collision data where the “tag-and-probe” method is applied to find  $Z \rightarrow \mu\mu$  candidate events.

By calculating  $N_{\text{fake}}^{\text{tight}}$ , the normalization of QCD multijet events is determined. In practice, to retrieve a template to model the kinematic shape of multijet events, Equation 4.3 is turned into two weighting factors by inserting one for  $N^{\text{loose}}$  and zero or one for  $N^{\text{tight}}$ . One negative weighting factor  $w^{\text{tight}}$  is applied to events in the loose dataset, that also pass the tight selection, and the other weighting factor  $w^{\text{loose}}$  is applied to all other events. The weighting factors are defined by:

$$w^{\text{tight}} = \frac{\epsilon_{\text{fake}}(\epsilon_{\text{real}} - 1)}{\epsilon_{\text{real}} - \epsilon_{\text{fake}}} \quad (4.4)$$

$$w^{\text{loose}} = \frac{\epsilon_{\text{fake}}\epsilon_{\text{real}}}{\epsilon_{\text{real}} - \epsilon_{\text{fake}}}. \quad (4.5)$$

The matrix method and the measurement of the efficiencies are explained in more detail in Ref. [173].

## 4.2 Event selection

A series of selection cuts is applied to measured and simulated events to suppress background events as much as possible, while maintaining a good signal-selection efficiency. The choice of the selection cuts is motivated by the signal final-state and its kinematic properties. In addition, cuts are applied to account for limited acceptance of measured events due to the choice of the trigger and due to the operative state of the sub-detectors during data taking.

After the definition of the signal region, the multijet background is determined using the data-driven techniques described in Section 4.1.2. With this estimation an event yield is constructed, that is the basis for the following signal-extraction methods and measurements.

### 4.2.1 Selection cuts

As discussed in Section 4.1.1, the final state of a  $t$ -channel single top-quark candidate events consists of a high- $p_{\text{T}}$  charged lepton  $\ell$  (electron or muon), a neutrino, and two or three jets. Due to its low transverse momentum the spectator  $b$ -quark jet is often not observed. Thus, based on the object definitions defined in Section 3.2, selected events are required to have one tight electron or muon, two or three jets, and  $E_{\text{T}}^{\text{miss}} > 30$  GeV.

Among a large number of collisions the recorded events are selected by high- $p_{\text{T}}$  single electron or single muon triggers. In order to keep the trigger-output rates at an acceptable level, the trigger had to be readjusted several times during the data taking in 2011 (compare Section 2.3). Therefore, several triggers were used in this analysis. The trigger choice is also accounted for in simulated events because the behavior of the triggers is included in the detector simulation.

An electron candidate is required to have an electromagnetic energy deposit in the calorimeter of  $E_{\text{T}} > 14$  GeV up to data period four and of  $E_{\text{T}} > 16$  GeV after

data period four at trigger level L1. At the EF level the electromagnetic cluster is matched to a track and quality criteria are applied. The energy threshold is increased from  $E_T = 20$  GeV up to period four to  $E_T = 22$  GeV in period five. In period six the quality requirements are further tightened and  $\eta$ -dependent  $E_T$  thresholds are introduced at L1 [114]. The nominal  $E_T$  threshold remains at 22 GeV.

The single muon triggers are defined using reconstructed muon candidates measured by the muon spectrometer. At L1, a  $p_T$  threshold of  $p_T = 10$  GeV is applied. The  $p_T$  threshold is tightened at EF level to  $p_T = 18$  GeV. From data period three on, additional muon-quality criteria are required to reduce the output rate of the trigger.

In addition to passing the trigger requirement, the selected tight lepton in the event needs to match the trigger-level lepton. Therefore, the radial distance between the tight lepton and the trigger-level lepton is required to be  $\Delta R < 0.15$ .

Furthermore, each event is required to contain at least one good primary vertex, that is defined as described in Section 3.2.2. To ensure a good quality of the interpretation of the data, events which contain noise bursts in the electromagnetic calorimeter are removed. Furthermore, events containing jets with  $p_T > 20$  GeV, that fail quality criteria against mis-reconstruction [152], are rejected.

One goal of the event selection is the suppression of multijet-background events in the signal region due to the low precision of the multijet-background estimation and the difficult modeling of kinematic distributions. Their contribution is reduced by placing a requirement on the transverse mass of the lepton- $E_T^{\text{miss}}$  system,  $m_T(\ell E_T^{\text{miss}}) > 30$  GeV. The transverse mass is defined as:

$$m_T(\ell E_T^{\text{miss}}) = \sqrt{2p_T(\ell) \cdot E_T^{\text{miss}} [1 - \cos(\Delta\phi(\ell, E_T^{\text{miss}}))]} \quad (4.6)$$

Figure 4.8(a) illustrates, that multijet background events tend to have small values of  $m_T(\ell E_T^{\text{miss}})$ , while events containing a real  $W$  boson in the final state peak at a value of  $m_T(\ell E_T^{\text{miss}}) \approx 75$  GeV. The small peak of the multijet distribution at about 55 GeV is a result from the cut on the missing transverse momentum  $E_T^{\text{miss}} > 30$  GeV, that already removes a large portion of multijet events. Thus, the multijet distribution is altered.

To further reduce the multijet background, a cut is placed on leptons with low values for  $p_T$ , that are back-to-back with the leading jet in  $p_T$  in the event:

$$p_T(\ell) > 40 \text{ GeV} \cdot \left(1 - \frac{\pi - |\Delta\phi(j_1, \ell)|}{\pi - 1}\right). \quad (4.7)$$

The effect of this cut is visualized in Fig. 4.8(b) where  $p_T(\ell)$  is shown as a function of  $\Delta\phi(j_1, \ell)$  in the 2-jet- $\ell$  final-state. The figure shows collision data after the subtraction of all known backgrounds. Therefore, the content in the plot corresponds approximately to the multijet background. The applied cut is illustrated with the black lines, cutting away large contributions from the multijet background.

For the remainder of this thesis, signal events are divided into different analysis channels depending on the charge of the lepton and the number of jets in the event. For the measurements of  $\sigma(tq)$ ,  $\sigma(\bar{t}q)$ , and  $R_t$  the signal and control regions are

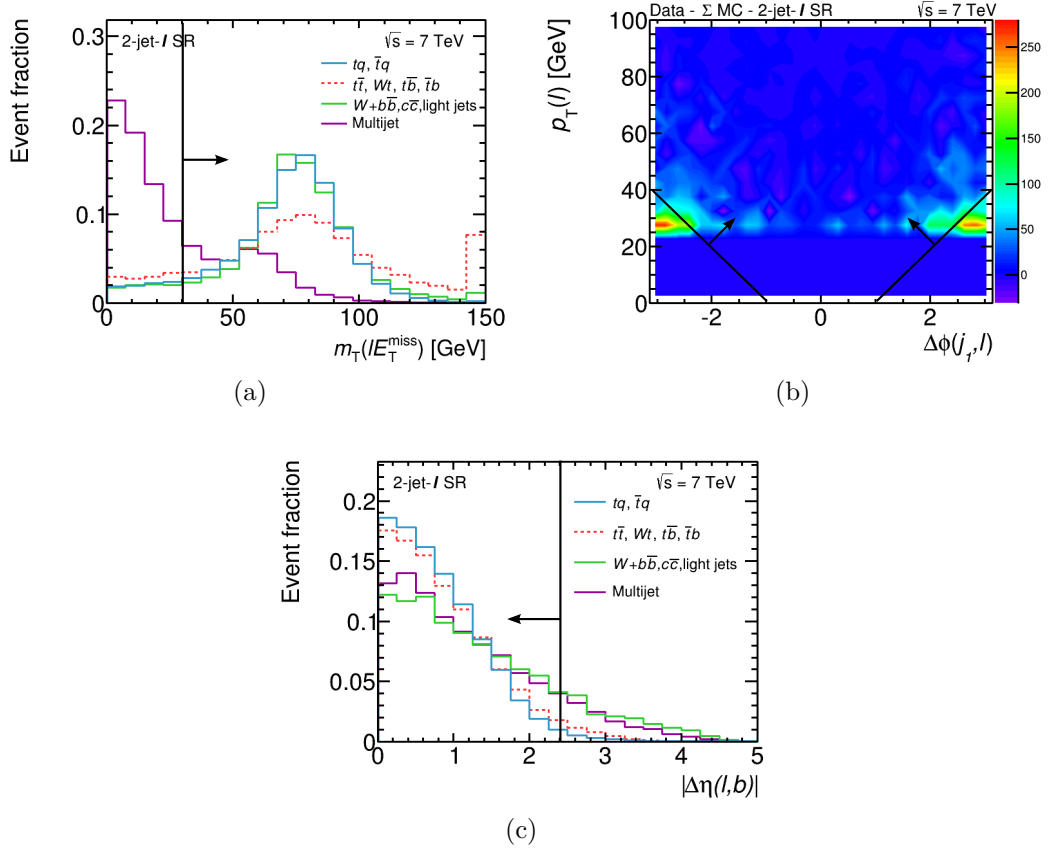


**Figure 4.8:** Illustration of the selection cuts. All distributions are done in the 2-jet- $\ell$  channel with all cuts applied except for all three cuts discussed in this figure. In Panel (a) the  $m_T(\ell E_T^{\text{miss}})$  distribution of the signal and background processes are compared. The cut value is indicated by the black line at 30 GeV. The distribution of each process is normalized to unit area. In Panel (b)  $p_T(\ell)$  is shown as a function of  $\Delta\phi(j_1, \ell)$  where all processes estimated by MC predictions are subtracted from the data. The content in the plot corresponds approximately to the multijet background. The cut formulated in Equation 4.7 is indicated by the black lines. The  $|\Delta\eta(\ell, b)|$  distribution is shown for the signal and main background processes in Panel (c). The cut is indicated by the black line and the distribution of each process is normalized to unit area.

separated for each lepton charge to be sensitive to the different cross sections. In case of the measurement of the combined inclusive cross section  $\sigma(tq + \bar{t}q)$  no separation is done to gain statistics. In the 2-jet channels, exactly one jet is required to be  $b$ -tagged. To remove measured events, that are difficult to model in these channels, the absolute value of the difference in pseudorapidity of the lepton and the  $b$ -tagged jet  $|\Delta\eta(\ell, b)|$  is required to be smaller than 2.4. The signal and background shape distributions in  $|\Delta\eta(\ell, b)|$  are shown in Fig. 4.8(c). The resulting 2-jet analysis channels are the 2-jet- $\ell^+$ , the 2-jet- $\ell^-$ , and the 2-jet- $\ell$  channels with signal-selection efficiencies of 2.7%, 1.4%, and 4.1%, respectively. In the 3-jet channels, events with exactly one or exactly two  $b$ -tagged jets are considered. In the 3-jet-2-tag channel, no distinction is made regarding the lepton charge, because this channel is dominated

by  $t\bar{t}$  background and is used to further constrain the  $b$ -tagging efficiency correction-factor. The resulting 3-jet channels are referred to as: 3-jet- $\ell^+$ , 3-jet- $\ell^-$ , 3-jet- $\ell$ , and 3-jet-2-tag and have a signal efficiency of 0.9%, 0.4%, 1.3%, and 0.5%, respectively.

In addition to the various signal regions (SR), control regions (CR) are used to validate the modeling of the backgrounds by simulated events. The control regions are defined to be orthogonal to the signal regions in the same kinematic phase space. Therefore, events in the control region have exactly one  $b$ -tagged jet, that is tagged with the less stringent MV1 tagging-algorithm at an efficiency of 85%. The signal region is excluded from the control region by applying a veto.

## 4.2.2 Normalization of the multijet background

In the  $e$ +jets final state, the multijet background is estimated via a binned maximum-likelihood fit to the observed data in the  $E_T^{\text{miss}}$  distributions after applying all selection criteria except for the  $E_T^{\text{miss}}$  requirement. Using the selection acceptance of the jet-lepton template, the multijet fraction is determined in the signal region with  $E_T^{\text{miss}} > 30$  GeV.

The electron channel is separated in one channel with electrons detected in the central region ( $\eta < 1.5$ ) and another channel with electrons detected in the endcap region of the EM calorimeter. To fit the jet-lepton template, all  $W$ +jets processes and all top-quark processes are grouped to one template each. These templates are constrained in the fit with their theoretical acceptance uncertainty. The  $Z$ +jets and diboson background processes are grouped together and the rate of the joint “ $Z$ +jets, diboson” background is fixed in the fit due to their small rate in the signal and control regions.

Table 4.4 provides multijet estimates for all analysis channels in the control and signal region in the electron channel.  $E_T^{\text{miss}}$  distributions normalized to the fit result in the central  $e^+$  and  $e^-$  signal regions are shown in Fig. 4.9.

**Table 4.4:** Estimates  $n$  of the multijet background in the  $e$ +jets final state for all analysis channels in the control and signal region. In addition, the fraction  $f$  of multijet events in each region is given.

Channel	Control region				Signal region			
	Central		Forward		Central		Forward	
	$n$	$f$	$n$	$f$	$n$	$f$	$n$	$f$
2-jet- $\ell$	1569	4.6%	1443	11.4%	649	6.2%	315	11.0%
2-jet- $\ell^+$	809	4.3%	765	10.3%	320	5.7%	170	10.4%
2-jet- $\ell^-$	753	4.9%	667	12.9%	324	6.9%	145	11.9%
3-jet- $\ell$	870	6.1%	1110	20.8%	356	4.2%	158	7.0%
3-jet- $\ell^+$	435	6.8%	591	19.2%	142	3.2%	65	5.4%
3-jet- $\ell^-$	439	8.5%	534	23.6%	209	5.3%	102	10.2%
3-jet-2-tag	—	—	—	—	0	0.0%	13	2.6%

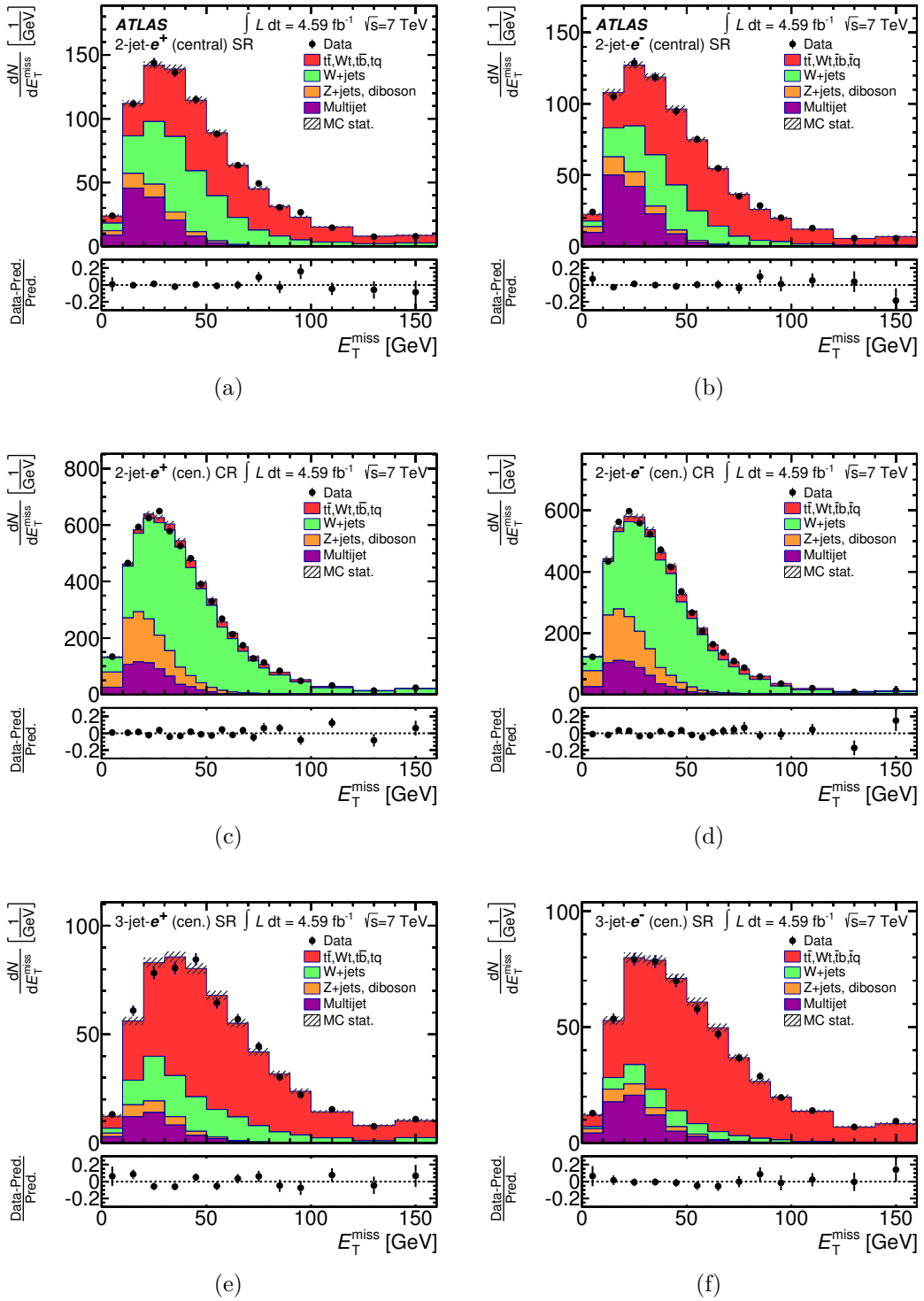


**Figure 4.9:**  $E_T^{\text{miss}}$  distributions for the central  $2\text{-jet-}e^+$  and  $2\text{-jet-}e^-$  channels in the SR and CR, as well as for the central  $3\text{-jet-}e^+$  and  $3\text{-jet-}e^-$  channels in the SR. The distributions are normalized to the result of a binned maximum-likelihood fit. The relative difference between the observed and expected number of events in each bin is shown in the lower panels. The figures with the label ATLAS are published in Ref. [174].

In the  $\mu$ +jets final state the matrix method, formulated in Equation 4.3, is evaluated in each analysis channel using the observed data events.  $N^{\text{loose}}$  and  $N^{\text{tight}}$  are determined from data, and the selected loose dataset is then weighted according to Equations 4.4 and 4.5. In Table 4.5 the multijet estimates in the  $\mu$ +jets final state are listed for all analysis channels in the control and signal regions.

**Table 4.5:** Estimates  $n$  of the multijet background in the  $\mu$ +jets final state for all analysis channels in the control and signal region. In addition, the fraction  $f$  of multijet events in each region is given.

Channel	Control region		Signal region	
	$n$	$f$	$n$	$f$
2-jet- $\ell$	817	1.5%	536	3.4%
2-jet- $\ell^+$	468	1.5%	264	3.0%
2-jet- $\ell^-$	407	1.8%	272	4.0%
3-jet- $\ell$	330	1.7%	237	1.9%
3-jet- $\ell^+$	166	1.5%	112	1.7%
3-jet- $\ell^-$	164	2.0%	124	2.1%
3-jet-2-tag	—	—	8	0.2%

A normalization uncertainty of 50% is assigned to the data-driven normalization of the multijet background. This value is a result of studies in each lepton-flavor channel separately. In the muon channel, the estimation of the matrix method was compared to the estimation with the jet-lepton method. In the electron channel, the matrix method does not give a sufficient description of multijet-sensitive variables. Therefore, studies were performed to assign a normalization uncertainty on the estimation with the jet-lepton model. The fit in the  $E_{\text{T}}^{\text{miss}}$  distribution was repeated with no constraints on the  $W$ +jets and top-quark background. Also, the multijet normalization was determined using a less sensitive variable, the transverse mass of the  $W$  boson  $m(\ell E_{\text{T}}^{\text{miss}})$ . Since the multijet production depends on the number of pile-up events, the jet-lepton model was split into two models with  $n_{\text{vtx}} > 8$  and  $n_{\text{vtx}} \leq 8$ . Each model with different pile-up conditions was fitted to the full  $E_{\text{T}}^{\text{miss}}$  distribution. All of these studies show a spread the normalization of the multijet background. The quoted uncertainty on the normalization was defined such, that it covers the observed spread of results.

### 4.2.3 Event yield

Table 4.6 and Table 4.7 provide the event yields after event selection for the signal region and the control region, respectively. All processes except for the multijet background are normalized to their theory prediction introduced in Section 4.1.2. The yields are presented for the tagged channels (SR and CR), separated according to the lepton charge and for the 3-jet-2-tag channel. The uncertainties assigned correspond to the uncertainties of the theoretical cross sections. In case of the multijet

background the normalization uncertainty of 50% is applied. Small contributions from the  $tq$  process in the  $\ell^-$  regions and the  $\bar{t}q$  process in the  $\ell^+$  regions originate from lepton-charge misidentification. In the 2-jet- $\ell$  channel the fraction of signal events corresponds to 13.2%, which splits into 15.8% for the 2-jet- $\ell^+$  channel and 11.0% for the 2-jet- $\ell^-$  channel due to the different background compositions in each lepton-charge channel. In the 3-jet- $\ell$  channel the signal fraction is 5.4% with 6.8% for the 3-jet- $\ell^+$  channel and 3.9% for the 3-jet- $\ell^-$  channel, respectively.

**Table 4.6:** Predicted and observed event yields for the 2-jet and 3-jet channels in the SR. The multijet background is estimated as described in Sect. 4.2.2. All the other expectations are derived using theoretical cross sections and their uncertainties (see Section 4.1.2).

	2-jet channels		3-jet channels		2-tag
	$\ell^+$	$\ell^-$	$\ell^+$	$\ell^-$	
$tq$	$2550 \pm 220$	$3.6 \pm 0.3$	$845 \pm 74$	$1.2 \pm 0.1$	$309 \pm 26$
$\bar{t}q$	$1.5 \pm 0.1$	$1390 \pm 120$	$0.52 \pm 0.05$	$435 \pm 38$	$162 \pm 14$
$t\bar{t}, Wt, t\bar{b}, \bar{t}b$	$5250 \pm 530$	$5130 \pm 510$	$8200 \pm 820$	$8180 \pm 820$	$5850 \pm 580$
$W+c$	$1460 \pm 350$	$1620 \pm 390$	$388 \pm 93$	$430 \pm 100$	$6.5 \pm 1.6$
$W^+$ +light, $c\bar{c}, b\bar{b}$	$5700 \pm 2500$	$16.3 \pm 8.2$	$2400 \pm 1200$	$11.5 \pm 5.7$	$200 \pm 100$
$W^-$ +light, $c\bar{c}, b\bar{b}$	$9.2 \pm 4.6$	$3400 \pm 1700$	$4.1 \pm 2.0$	$1470 \pm 740$	$137 \pm 68$
$Z$ +jets, diboson	$370 \pm 220$	$310 \pm 180$	$190 \pm 120$	$180 \pm 110$	$22 \pm 13$
Multijet	$750 \pm 340$	$740 \pm 370$	$320 \pm 160$	$440 \pm 220$	$21 \pm 11$
Total expectation	$16100 \pm 2600$	$12600 \pm 2000$	$12400 \pm 1500$	$11100 \pm 1100$	$6710 \pm 610$
Data	16198	12837	12460	10819	6403

**Table 4.7:** Predicted and observed event yields for the 2-jet and 3-jet channels in the CR. The multijet background is estimated as described in Sect. 4.2.2. All the other expectations are derived using theoretical cross sections and their uncertainties (see Section 4.1.2).

	2-jet channels		3-jet channels	
	$\ell^+$	$\ell^-$	$\ell^+$	$\ell^-$
$tq$	$1200 \pm 100$	$1.4 \pm 0.1$	$227 \pm 24$	$0.20 \pm 0.02$
$\bar{t}q$	$1.1 \pm 0.1$	$642 \pm 56$	$0.30 \pm 0.03$	$137 \pm 12$
$t\bar{t}, Wt, t\bar{b}, \bar{t}b$	$2310 \pm 230$	$2350 \pm 230$	$2610 \pm 260$	$2600 \pm 260$
$W+c$	$12500 \pm 3000$	$13800 \pm 3300$	$3160 \pm 760$	$3440 \pm 830$
$W^+$ +light, $c\bar{c}, b\bar{b}$	$38000 \pm 17000$	$89 \pm 39$	$13300 \pm 6700$	$35 \pm 18$
$W^-$ +light, $c\bar{c}, b\bar{b}$	$49 \pm 24$	$23000 \pm 12000$	$22 \pm 11$	$7800 \pm 3900$
$Z$ +jets, diboson	$3200 \pm 1900$	$3000 \pm 1800$	$1370 \pm 820$	$1300 \pm 780$
Multijet	$1980 \pm 990$	$1840 \pm 920$	$1200 \pm 600$	$1130 \pm 570$
Total expectation	$59000 \pm 17000$	$45000 \pm 12000$	$21900 \pm 6800$	$16500 \pm 4100$
Data	57548	43622	20583	15532

### 4.3 Event classification

After the definition of the signal region, that is described in the previous section, the signal content in the observed data has to be determined. The strategy employed to separate signal events from background events is to combine several kinematic variables to one discriminant. To profit from the discrimination power of many variables, a multivariate event-classification approach is used, that also takes the correlations among the input variables into account. In this analysis artificial neural networks are deployed as event classifiers.

In the following the concept of neural networks and their training is briefly introduced. Then, suitable discriminating input variables for the  $t$ -channel signal process are discussed. Finally, the networks used in the analysis are derived.

#### 4.3.1 Neural networks

The artificial neural networks (NNs) deployed in this analysis are provided by the NeuroBayes<sup>®</sup> package [175, 176]. In an NN a vector of input variables is mapped to an output  $o_{\text{NN}}$ . As a first step, the raw input variables are transformed into suitable input variables for the NN, taking into account the correlation between the inputs. This step is called preprocessing. In a second step, the NN is trained on a special dataset, called training dataset.

#### Preprocessing of input variables

While it is possible to train an NN using the raw input variables, sophisticated preprocessing procedures find a more optimal starting point for the NN training. This optimization increases the training speed and the robustness of the classification.

In NeuroBayes<sup>®</sup> each input variable is first transformed to a flat distribution with the same number of events in each bin. Thus, the signal purity in each bin of the flattened distribution is obtained. A spline curve is fitted to the purity distribution to remove statistical outliers. Then, the fitted purity curve is converted into a Gaussian distribution with a mean of zero and a width of one to improve the numerical stability in the learning process of the training.

After the preprocessing of each variable the correlation of all transformed input variables to the target is computed. Via the correlation matrix of the input variables, the total correlation to the target of the set of input variables is computed. Then, the ranking of variables is determined via the loss in total correlation to target caused by removing variables from the computation one after the other. Each time, the variable causing the smallest loss of information is discarded. This procedure is repeated until the most important variable is left. Then, variables are removed before the training, that do not add significant additional information to the set of input variables.

As a last step of the preprocessing, the chosen set of input variables is decorrelated by diagonalizing the covariance matrix of the input variables using iterative Jacobian rotations. The rotated input vectors are normalized with the square root of the corresponding eigenvalues.

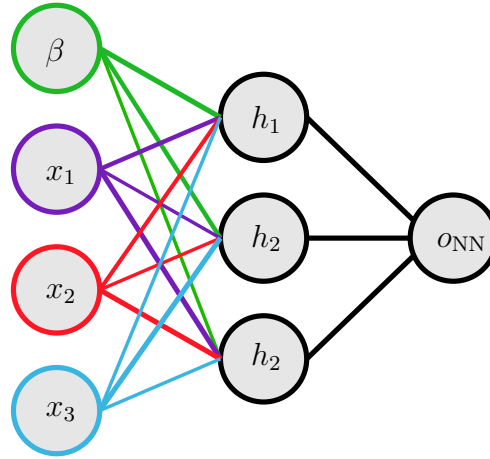


**Figure 4.10:** Topology of a three-layer feed-forward neural network, that is composed of input layer, hidden layer, and output node. The thickness of the connecting line represents the different weighting between all nodes.

### Neural networks in NeuroBayes<sup>®</sup>

The NN implemented in NeuroBayes<sup>®</sup> is a three-layer feed-forward NN. Fig. 4.10 shows an exemplary architecture of an NN with four input nodes, three hidden nodes ( $h_1, h_2, h_3$ ), and one output node  $o_{\text{NN}}$ . The output node gives a continuous output distribution between minus one and plus one.

The  $n + 1$  input nodes consist of one input node,  $x_i$ , for each of the  $n$  input variables,  $i$ , plus one bias node  $\beta$ . The input variables correspond to the decorrelated and preprocessed variables. The number of hidden nodes can be chosen freely in a reasonable range and is set to 15 in the presented analysis. Each hidden node  $h_j$  is connected to each input variable  $i$  via the weights  $w_{ij}$ . The input of each hidden node can thus be expressed by:

$$h_j(x_1 \dots x_n; \beta_j) = \sum_{i=1}^n w_{ij} x_i + \beta_j.$$

In each hidden node, the input  $h_j$  is transferred with a symmetric Sigmoid function  $S$  from the interval  $]-\infty, \infty[$  to the interval  $[-1, +1]$ . The Sigmoid function is given by:

$$S(h_j) = \frac{2}{1 + e^{-h_j}} - 1$$

and is sensitive in a small range around zero. Each hidden node is also connected to the output node  $o_{\text{NN}}$  with the weight  $w_j$ . Thus, the output of an NN with  $n$  input variables and  $m$  hidden nodes is given by:

$$o_{\text{NN}} = S \left( \sum_{j=1}^m w_j \cdot S \left( \sum_{i=1}^n w_{ij} x_i + \beta_j \right) \right).$$

## Training

To use an NN as an event classifier, the weights  $w_{ij}$  and  $w_j$ , introduced in the previous section, have to be determined. To achieve the so-called training of the NN, a training dataset is needed where the true category of an input event is known. In this analysis MC simulated samples for signal and background processes are used to compose a training dataset. Thus, the target for the NN is known for each event in the training sample being either  $t = 1$  for signal events or  $t = -1$  for background events.

The weights  $w_{ij}$  and  $w_j$  are then fitted as free parameters to describe the known target values as good as possible. To achieve the best possible description, an entropy loss function is minimized for the sum of all events  $k$  of the training dataset. The loss function is given by:

$$E = \sum_k \log \left( \frac{1}{2} (1 + t_k \cdot o_k + \epsilon) \right),$$

where  $\epsilon$  is a regularization constant to avoid numerical problems with untrained networks. It is reduced to zero after a few iterations. Here,  $t_k$  is the true target value of the event and  $o_k$  is the target value for the set of weights tested. A wrong classification leads to an indefinitely large value of  $E$ , e.g. for  $o_k = 1$  and  $t_k = -1$ . Thus, this distinction is quickly learned by the NN. Multiple iterations are performed on the training dataset to optimize the output of the NN.

If the signal or background event-fraction in the training dataset is limited or there are many input nodes, a few specific patterns might be able to trigger an extreme output value. This phenomenon is called over-training and typically leads to a non-general discrimination power of the resulting network. The NeuroBayes<sup>®</sup> package uses Bayesian regularization techniques where the weights are systematically reduced during the training process. Thus, the network forgets again part of the information and is stripped altogether off insignificant network connections or even nodes. More details of the training and its regularization can be found in reference [176].

To validate the trained network against over-training, 20% of the training dataset are not included in the training, but used to check the network training. If the values of the entropy loss function in the test sample differ from the values in the training sample, over-training is indicated. This has never been observed in the context of the presented analysis.

### 4.3.2 Input variables

Several potential input variables are investigated concerning their discrimination power between  $t$ -channel single top-quark signal events and background events. Not only kinematic variables of the identified physics objects in the  $\ell + E_T^{\text{miss}} + \text{jets}$  final-state are looked at, but also variables obtained from the reconstructed  $W$  boson and the reconstructed top quark. Candidates for discriminating variables are simple kinematic distributions of the above mentioned objects, e.g.  $p_T$ ,  $\eta$ , or  $m$ , as well

as relations between two or more objects. These can be angular variables between the objects, e.g.  $\Delta R$  or  $\Delta y$ , the invariant mass of several objects, the difference in transverse momentum  $\Delta p_T$ , and the scalar sum  $H_T$  of the transverse momenta of all jets, the charged lepton and the  $E_T^{\text{miss}}$ .

In total, over 80 kinematic variables were studied for the presented analysis. 13 input variables were chosen for the 2-jet- $\ell$  channel and 11 variables for the 3-jet- $\ell$  channel. The network trained in the 2-jet- $\ell$  channel is also applied in the 2-jet- $\ell^+$  and 2-jet- $\ell^-$  channels. Analogously, the network trained in the 3-jet- $\ell$  channel is used in the 3-jet- $\ell^+$ , and 3-jet- $\ell^-$  channels. The selection of the input variables is based on their separation power between signal and background events. In addition, the description of each variable by the modeling is taken into account. The modeling of the input variables is checked in the CR, that includes only a small signal fraction and is enriched in  $W$ +jets events. For the chosen variables good modeling is observed.

In the following, the chosen variables are introduced. In the 2-jet- $\ell$  channels and in the 3-jet- $\ell$  channels, exactly one jet is required to be  $b$ -tagged. In the 2-jet- $\ell$  channels, the jet without a  $b$ -tag is denoted untagged jet. The signal distribution of each variable is shown in comparison to the distributions of the two largest background contributions, the top-quark background and the combined  $W+b\bar{b}$ ,  $W+c\bar{c}$ , and  $W$ +light jets background.

- $m(\ell\nu b)$ : The invariant mass of the reconstructed top quark is defined as the invariant mass of the four-momentum sum of the three physics objects in the top quark: the charged lepton, the  $b$ -tagged jet, and the reconstructed neutrino. The distributions of the signal process and the two most important background processes are shown normalized to unit area in Fig. 4.11(a) for the 2-jet- $\ell$  channel and in Fig. 4.14(a) for the 3-jet- $\ell$  channel. It can be seen, that  $t$ -channel signal events peak sharply at 140 – 180 GeV. The distribution of top-quark background events is broader because the  $b$ -quark jet chosen in the top reconstruction in  $t\bar{t}$  events is not always the jet, that belongs to the leptonically decaying top-quark. Due to the kinematic selection cuts applied to the physics objects the distribution of the  $W$ +jets background peaks at 120 GeV.
- $m_T(\ell E_T^{\text{miss}})$ : The transverse mass of the lepton- $E_T^{\text{miss}}$  system, as defined in Equation 4.6, that corresponds to the transverse mass of the  $W$  boson. Figure 4.11(b) shows the signal distribution compared to the  $W$ +jets and the top-quark background distributions in the 2-jet channel and Figure 4.14(b) in the 3-jet channel. The variable has good separation power against the top-quark background process, that has a broader distribution, compared to the signal and  $W$ +jets process. The distribution is different for the top background because both, the  $t\bar{t}$  process and the  $Wt$  process, have two  $W$  bosons in the final state instead of one.
- $\eta(\ell\nu)$ : The pseudorapidity of the reconstructed  $W$  boson. The signal and background distributions are presented in Fig. 4.11(c) for the 2-jet channel and in Fig. 4.14(c) for the 3-jet channel. In both cases, the  $W$  boson from

a top-quark decay is produced centrally, while the  $W$  bosons from  $W$ +jets production are distributed more forward in pseudorapidity.

- $m(lb)$ : The invariant mass of the charged lepton and the  $b$ -tagged jet. The signal and background distributions are displayed in Fig. 4.11(d) for the 2-jet channel and in Fig. 4.14(d) for the 3-jet channel. Here, the signal distribution peaks sharply around 100 GeV. Almost no  $t$ -channel single top-quark events are located above 200 GeV, since both objects are part of the reconstructed top quark. The background distributions are broader and especially the  $W$ +jets distribution has a long tail up to large values of  $m(lb)$ .
- $H_T$ : The scalar sum of the transverse momenta of the jets, the charged lepton, and the  $E_T^{\text{miss}}$ . The signal and background distributions are compared in Fig. 4.11(e) for the 2-jet channel and in Fig. 4.14(e) for the 3-jet channel. In general,  $W$ +jets events have the lowest values for  $H_T$ , followed by  $t$ -channel single top-quark signal events. Top-quark background events have the largest values in  $H_T$  resulting in a peak at about 250 GeV for 2-jet events and at about 320 GeV for 3-jet events. On average  $t\bar{t}$  events have the largest amount of transverse momentum in each event because two top quarks are produced.

The following variables are used in the 2-jet neural network only:

- $|\eta(j)|$ : The absolute value of the pseudorapidity of the untagged jet. One of the main characteristics of the  $t$ -channel single top-quark signal process is the production of the spectator light-quark jet in forward direction. This characteristic is directly visible in this variable, shown in Fig. 4.11(f). Therefore, a very good distinction between signal and background events is possible. Thus, this variable is thus the most important input variable in the 2-jet NN.
- $m(jb)$ : The invariant mass of the untagged jet and the  $b$ -tagged jet. The separation power of this variable is again driven by the characteristic forward untagged jet in signal events. Since the  $b$ -tagged jet from the top-quark decay is usually centrally produced, a large invariant mass is typical for signal events, as can be seen in Fig. 4.12(a).
- $\Delta R(\ell, j)$ : The distance  $\Delta R$  between the charged lepton and the untagged jet. Signal events tend to have larger values for the angular difference between the charged lepton from the top decay and the untagged jet. The reason for this is the same as for  $m(jb)$ . A direct comparison to the main background distributions is shown in Fig. 4.12(b).
- $\Delta R(\ell vb, j)$ : The distance  $\Delta R$  between the reconstructed top quark and the untagged jet. In this distribution, shown in Fig. 4.12(c),  $\Delta R$  is larger for the  $t$ -channel signal process than for the background processes.
- $\eta(b)$ : The pseudorapidity of the  $b$ -tagged jet. This variable mainly provides good separation against the  $W$ +jets background. As can be seen in Fig. 4.12(d), the  $b$ -tagged jets from top-quark decays are produced centrally in the detector

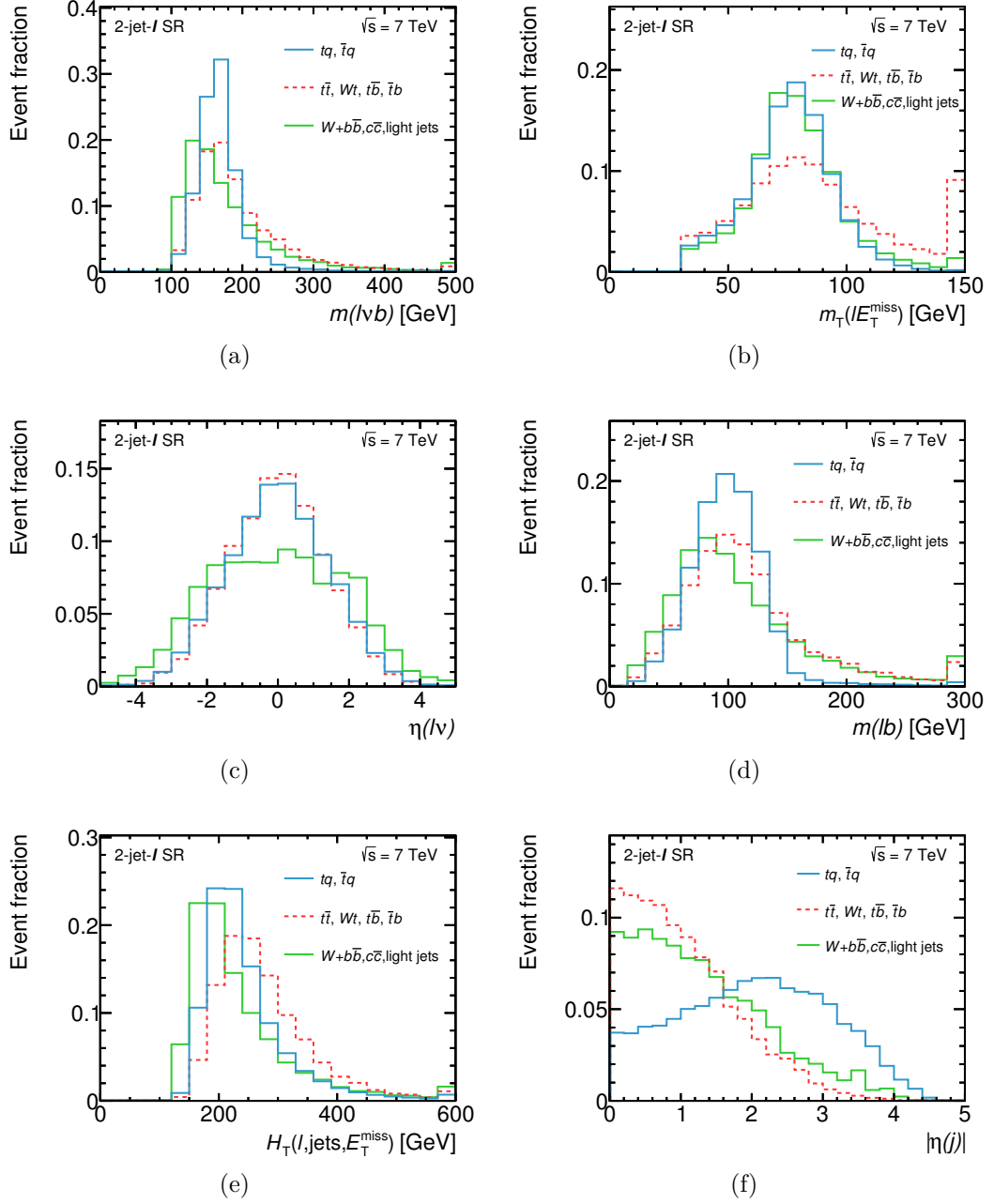


**Figure 4.11:** Comparison of the kinematic distributions for the signal, the combined  $W+b\bar{b}$ ,  $W+c\bar{c}$ , and  $W$ +light jets background, and the combined top-quark background normalized to unit area in the 2-jet- $l$  channel. Panel (a) shows the reconstructed top-quark mass, Panel (b) the transverse mass of the  $l$ - $E_T^{\text{miss}}$  system, Panel (c) the pseudorapidity of the reconstructed  $W$  boson, Panel (d) the invariant mass of the charged lepton and the  $b$ -tagged jet, Panel (e) the scalar sum  $H_T$  of all transverse momenta in the event, and Panel (f) the absolute value of the pseudorapidity of the untagged jet.

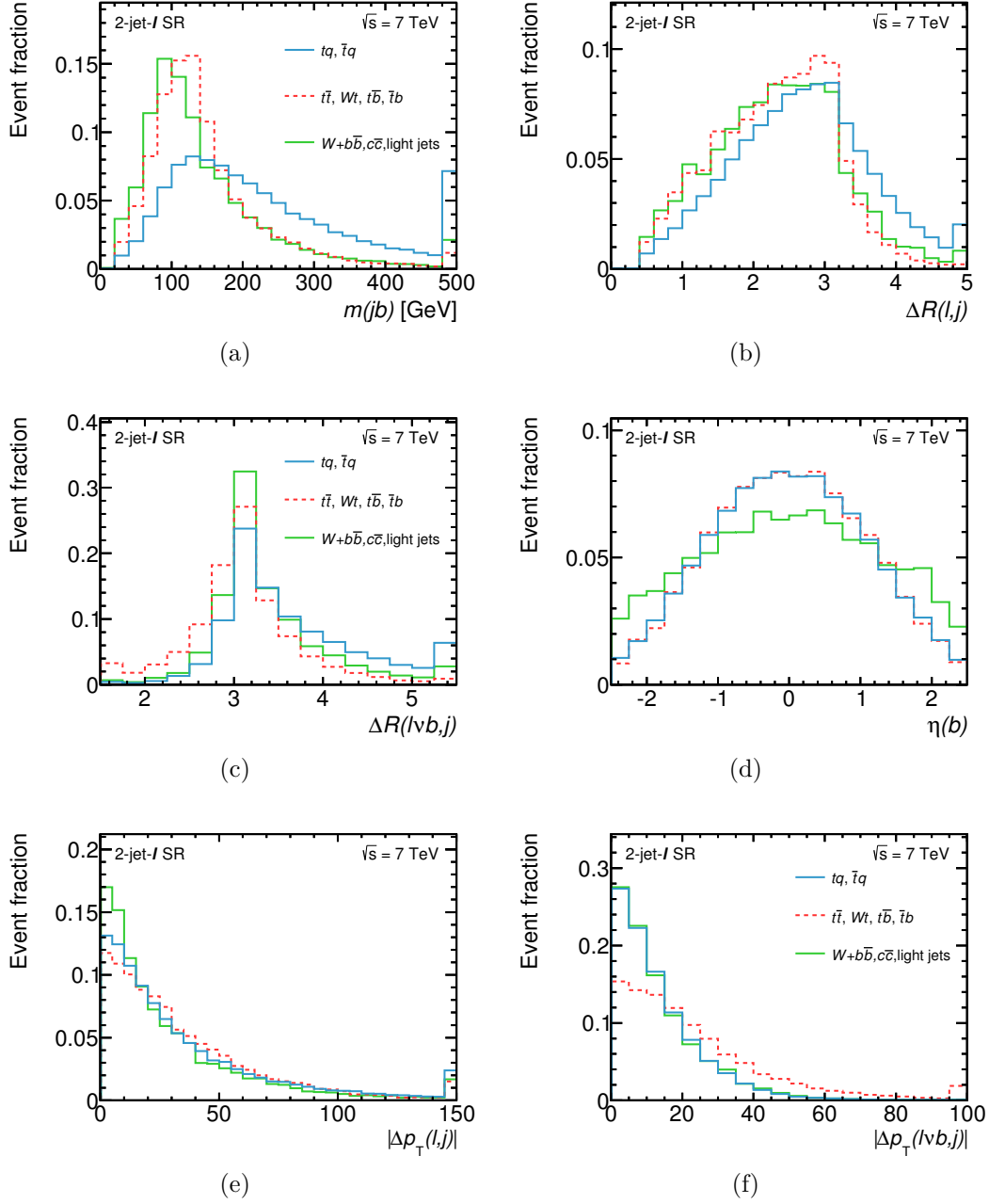


**Figure 4.12:** Comparison of the kinematic distributions for the signal, the combined  $W + b\bar{b}$ ,  $W + c\bar{c}$ , and  $W + \text{light jets}$  background, and the combined top-quark background normalized to unit area in the 2-jet- $\ell$  channel. Panel (a) shows the invariant mass of the untagged jet and the  $b$ -tagged jet, Panel (b)  $\Delta R$  between the charged lepton and the untagged jet, Panel (c)  $\Delta R$  between the reconstructed top quark and the untagged jet, Panel (d) the pseudorapidity of the  $b$ -tagged jet, Panel (e) the absolute value of the difference in transverse momentum of the charged lepton and the untagged jet, and Panel (f) the absolute value of the difference in transverse momentum of the reconstructed top quark and the untagged jet.

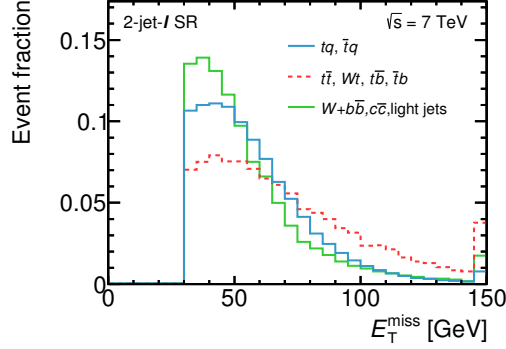


**Figure 4.13:** Comparison of the  $E_T^{\text{miss}}$  distribution for the signal, the combined  $W+b\bar{b}$ ,  $W+c\bar{c}$ , and  $W+\text{light jets}$  background, and the combined top-quark background normalized to unit area in the 2-jet- $\ell$  channel.

since they have a larger  $p_T$  from the top-quark decay and are not boosted in the direction of the beam, while  $b$ -tagged jets from  $W+\text{jets}$  production are more equally distributed. For the  $W+\text{jets}$  processes,  $b$ -tagged jets are produced via the radiation of a gluon which is independent of the direction of the  $W$ -boson.

- $|\Delta p_T(\ell, j)|$ : The absolute value of the difference in transverse momentum of the charged lepton and the untagged jet. The signal and background distributions peak at zero, as shown in Fig. 4.12(e). The peak of the  $W+\text{jets}$  background is the sharpest, while the tail of distribution of the  $t$ -channel signal process is the largest.
- $|\Delta p_T(\ell\nu b, j)|$ : The absolute value of the difference of transverse momenta of the reconstructed top quark and the untagged jet. The largest difference of transverse momentum is observed for top-quark background events, as can be seen in Fig. 4.12(f). Good separation of the top-quark background events from signal events and  $W+\text{jets}$  events is observed.
- $E_T^{\text{miss}}$ : The distribution of the reconstructed missing transverse momentum shown for background and signal processes in Fig. 4.13 clearly separates top-quark background events with large values of  $E_T^{\text{miss}}$  in the event from signal events.

The following variables are only used in the 3-jet neural network. Here, the definitions of the variables use the term leading jet and 2<sup>nd</sup> leading jet, defined as the jet with the highest or 2<sup>nd</sup> highest value in  $p_T$ , respectively.

- $|\Delta y(j_1, j_2)|$ : The absolute value of the difference in rapidity of the leading and 2<sup>nd</sup> leading jets. The rapidity difference is largest for the signal process as can be observed in Fig. 4.14(f). In signal events with three jets, it is probable, that  $j_1$  corresponds to the central jet from the top-quark decay and  $j_2$  to the forward light-quark jet, resulting in a large difference in rapidity.

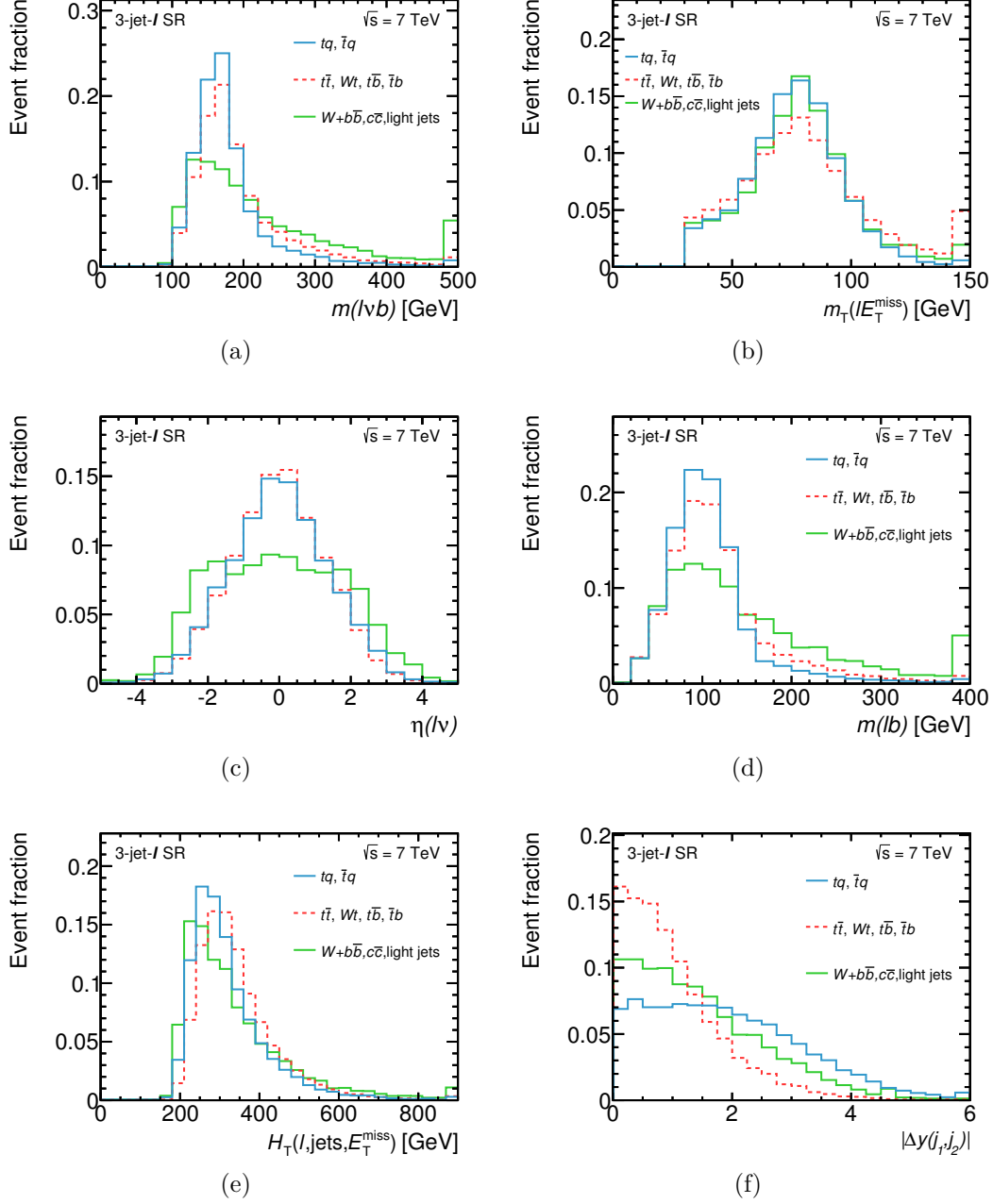


**Figure 4.14:** Comparison of the kinematic distributions for the signal, the combined  $W+b\bar{b}$ ,  $W+c\bar{c}$ , and  $W+\text{light jets}$  background, and the combined top-quark background normalized to unit area in the 3-jet- $\ell$  channel. Panel (a) shows the reconstructed top-quark mass, Panel (b) the transverse mass of the  $\ell$ - $E_T^{\text{miss}}$  system, Panel (c) the pseudorapidity of the reconstructed  $W$  boson, Panel (d) the invariant mass of the charged lepton and the  $b$ -tagged jet, Panel (e) the scalar sum of the transverse momenta of all objects in the event, and Panel (f) the absolute value of the rapidity difference of the leading and second leading jets.

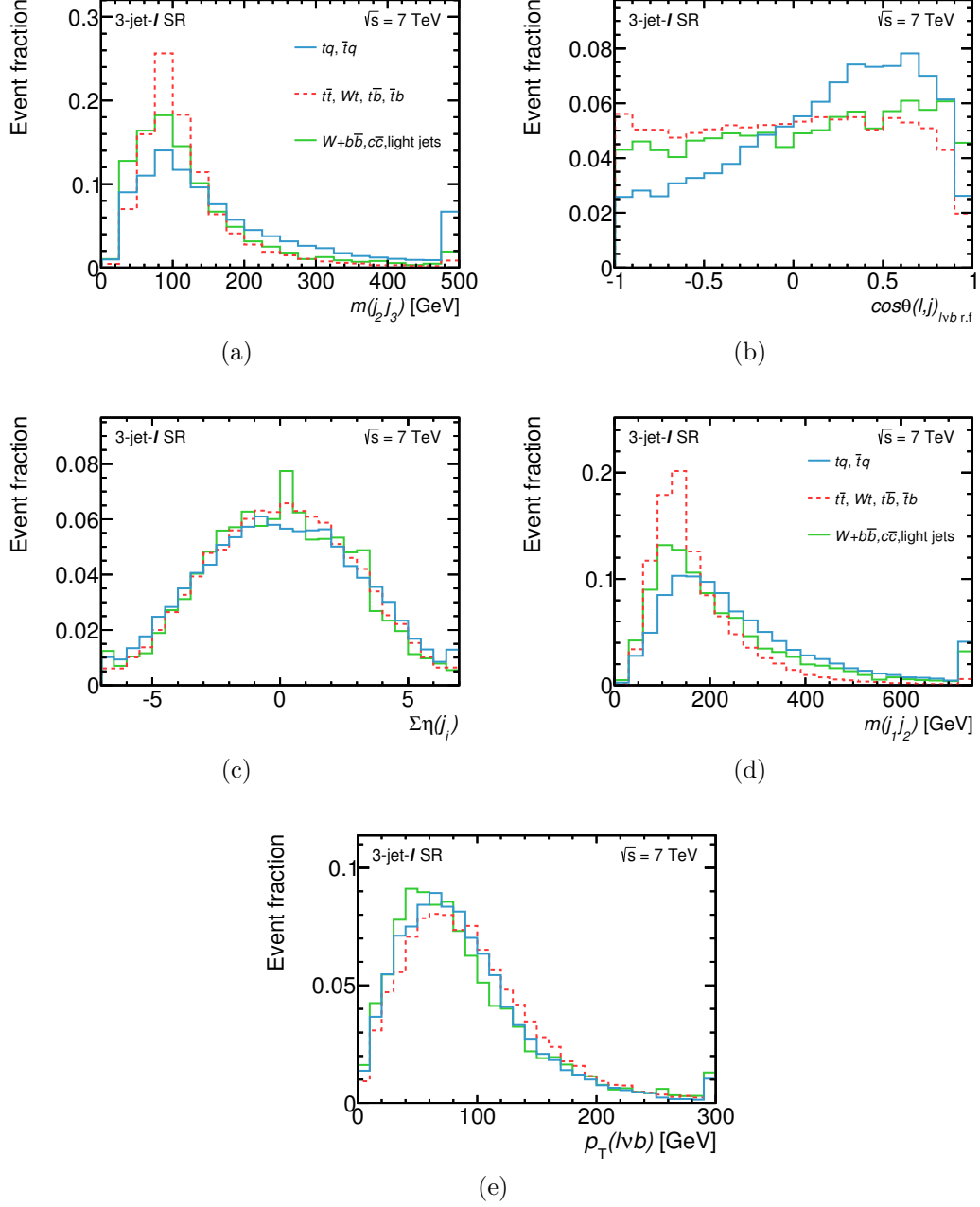


**Figure 4.15:** Comparison of the kinematic distributions for the signal, the combined  $W+b\bar{b}$ ,  $W+c\bar{c}$ , and  $W$  +light jets background, and the combined top-quark background normalized to unit area in the 3-jet- $\ell$  channel. Panel (a) shows the invariant mass of the second leading jet and the third leading jet, Panel (b) the cosine of the angle  $\theta$  between the charged lepton and the leading untagged jet in the rest frame of the reconstructed top quark, Panel (c) sum of the pseudorapidities of all jets in the event, Panel (d) the invariant mass of the the two leading jets, and Panel (e) the transverse momentum of the reconstructed top quark.

- $m(j_2 j_3)$ : The invariant mass of the 2<sup>nd</sup> leading jet and the 3<sup>rd</sup> leading jet, shown in Fig. 4.15(a). Due to the characteristically forward jet of signal events, the invariant mass between two jets in the event is larger for signal events compared to background events.
- $\cos\theta(\ell, j)_{\ell\nu b, \text{r.f.}}$ : The cosine of the angle  $\theta$  between the charged lepton and the leading untagged jet in the rest frame of the reconstructed top quark. As described in Section 1.3.3, single top-quarks are produced polarized. Therefore, a linear behavior is observed for signal events with the lowest number of events close to  $\cos\theta = -1$  and the largest number of events close to  $\cos\theta = 1$ , compare Fig. 4.15(b). The background events are approximately evenly distributed in this distribution.
- $\Sigma\eta(j_i)$ : The sum of the pseudorapidities of all jets in the event is larger for signal events compared to the background events, as can be observed in Fig. 4.15(c).
- $m(j_1 j_2)$ : The invariant mass of the two leading jets, shown in Fig. 4.15(d). Again, signal events exhibit a larger invariant mass of two jets, especially compared to the  $t\bar{t}$  background, which is dominant in the 3-jet channel,.
- $p_T(\ell\nu b)$ : The transverse momentum of the reconstructed top quark. As can be observed in Fig. 4.15(e), the transverse momentum distribution of top quarks reconstructed from  $t\bar{t}$  background events has larger values compared to those of signal events.

The modeling of the chosen input variables is checked in the CR for the  $\ell^+$  and  $\ell^-$  channels separately. This is necessary due to the different background composition, as is pointed out in Section 4.2.3. In Fig. 4.16-4.20 the input variables for the 2-jet neural network are shown in the CR for the 2-jet- $\ell^+$  channel and the 2-jet- $\ell^-$  channel. The variables are sorted by their ranking in the preprocessing. Analogously, the input variables for the 3-jet neural network are shown in Fig. 4.21-4.24 in the CR for the 3-jet- $\ell^+$  channel and the 3-jet- $\ell^-$  channel.

In all distributions the multijet and the  $W$ +jets event yields are determined by a fit to the  $E_T^{\text{miss}}$  distribution as described in Section 4.2.2. All other processes are normalized to their theory prediction. To check the agreement between the prediction and the data, one of the largest systematic uncertainties, the knowledge of the jet energy scale, is denoted as an uncertainty band on top of the prediction. All distributions show good agreement between data and the prediction.

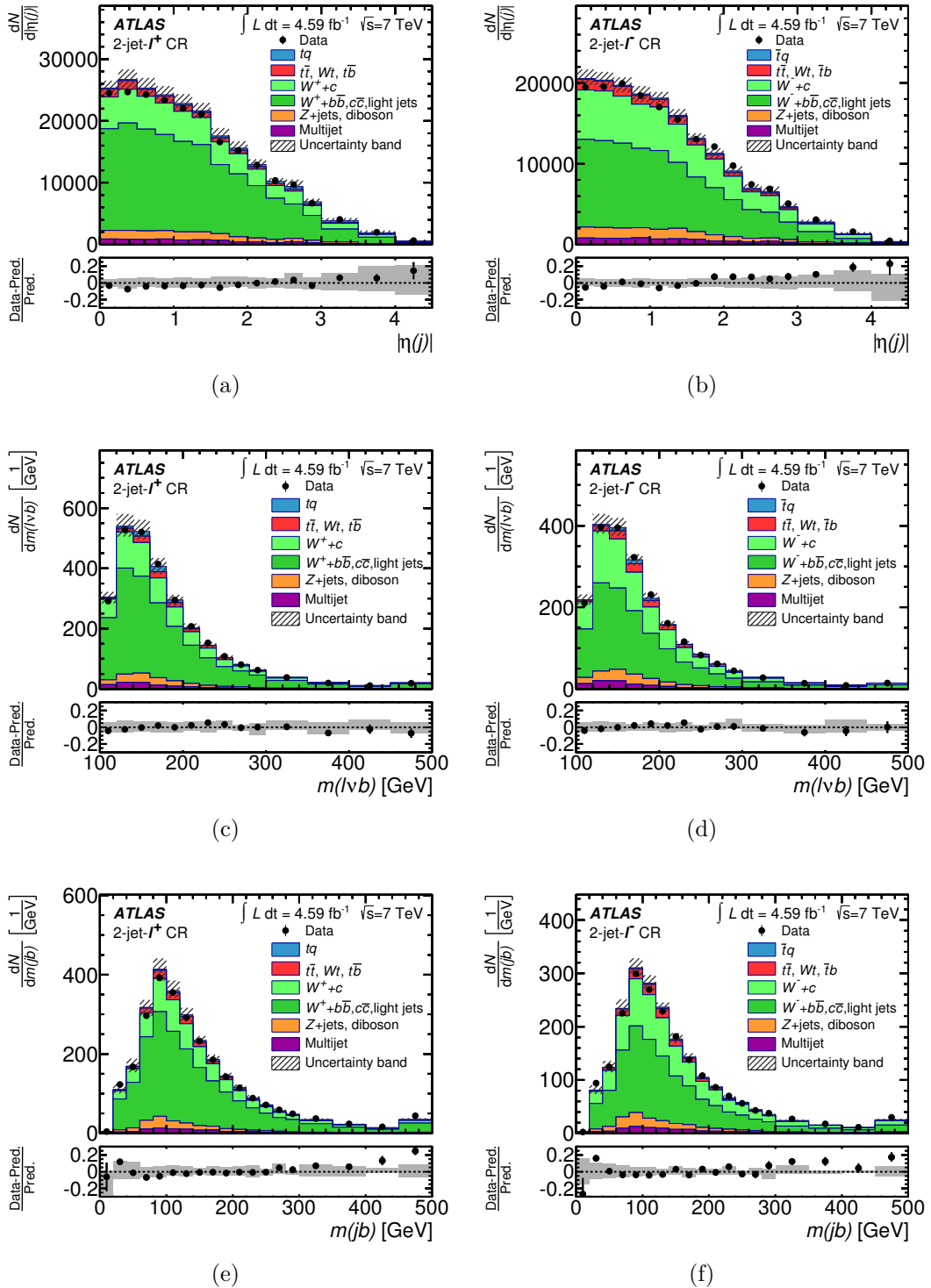


**Figure 4.16:** Distributions of the three most important discriminating variables in the 2-jet- $\ell^+$  and 2-jet- $\ell^-$  channels in the CR [174]. Panels (a) and (b) show the absolute value of the pseudorapidity of the untagged jet  $|\eta(j)|$ , (c) and (d) the invariant mass of the reconstructed top quark  $m(\ell\nu b)$ , and (e) and (f) the invariant mass of the untagged and the  $b$ -tagged jet  $m(jb)$ . The last histogram bin includes overflows. The uncertainty band represents the normalization uncertainty due to the uncertainty on the jet energy scale and the Monte Carlo statistical uncertainty. The relative difference between the observed and expected number of events in each bin is shown in the lower panels.

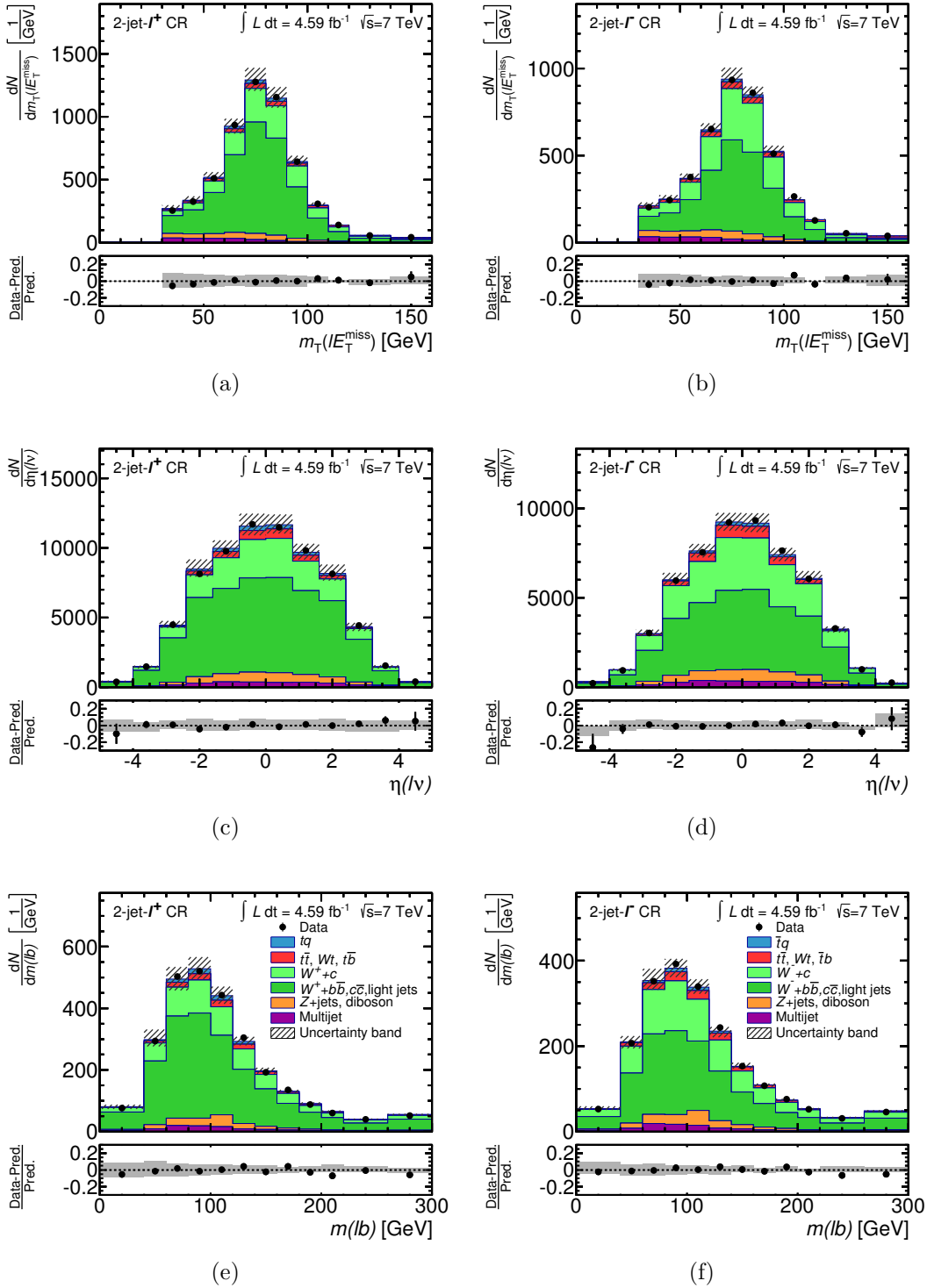


**Figure 4.17:** Distributions of three discriminating variables in the 2-jet- $l^+$  and 2-jet- $l^-$  channels in the CR. Panels (a) and (b) show the transverse mass of the  $l$ - $E_T^{\text{miss}}$  system  $m_T(lE_T^{\text{miss}})$ , (c) and (d) the pseudorapidity of the reconstructed  $W$  boson  $\eta(l\nu)$ , and (e) and (f) the invariant mass of the lepton and the  $b$ -tagged jet  $m(lb)$ . The last histogram bin includes overflows. The uncertainty band represents the normalization uncertainty due to the uncertainty on the jet energy scale and the Monte Carlo statistical uncertainty. The relative difference between the observed and expected number of events in each bin is shown in the lower panels.

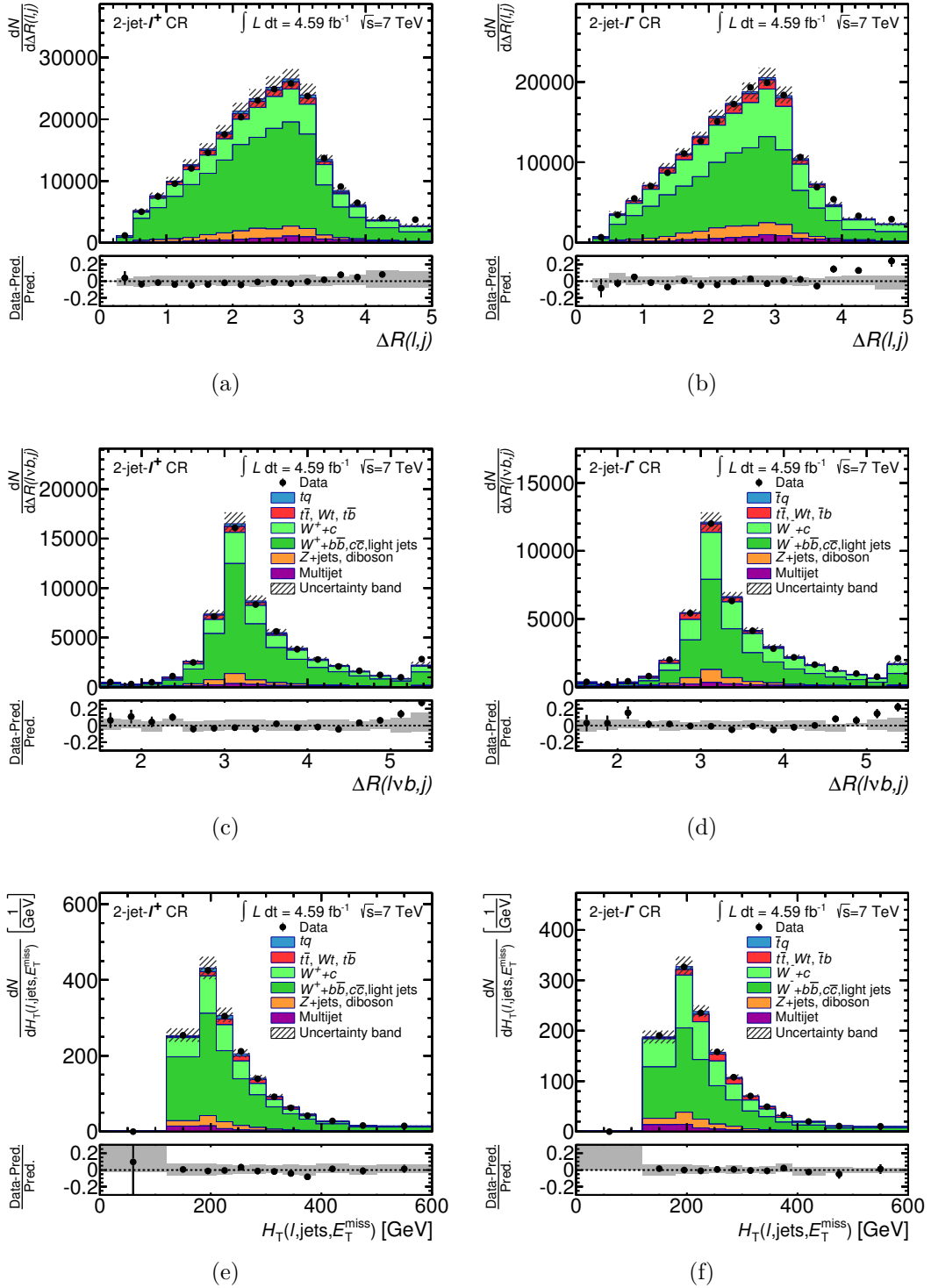


**Figure 4.18:** Distributions of three discriminating variables in the 2-jet- $\ell^+$  and 2-jet- $\ell^-$  channels in the CR. Panels (a) and (b) show the  $\Delta R$  of the lepton and the untagged jet  $\Delta R(\ell, j)$ , (c) and (d) the  $\Delta R$  of the reconstructed top quark and the untagged jet  $\Delta R(t, j)$ , and (e) and (f)  $H_T$ . The last histogram bin includes overflows. The uncertainty band represents the normalization uncertainty due to the uncertainty on the jet energy scale and the Monte Carlo statistical uncertainty. The relative difference between the observed and expected number of events in each bin is shown in the lower panels.

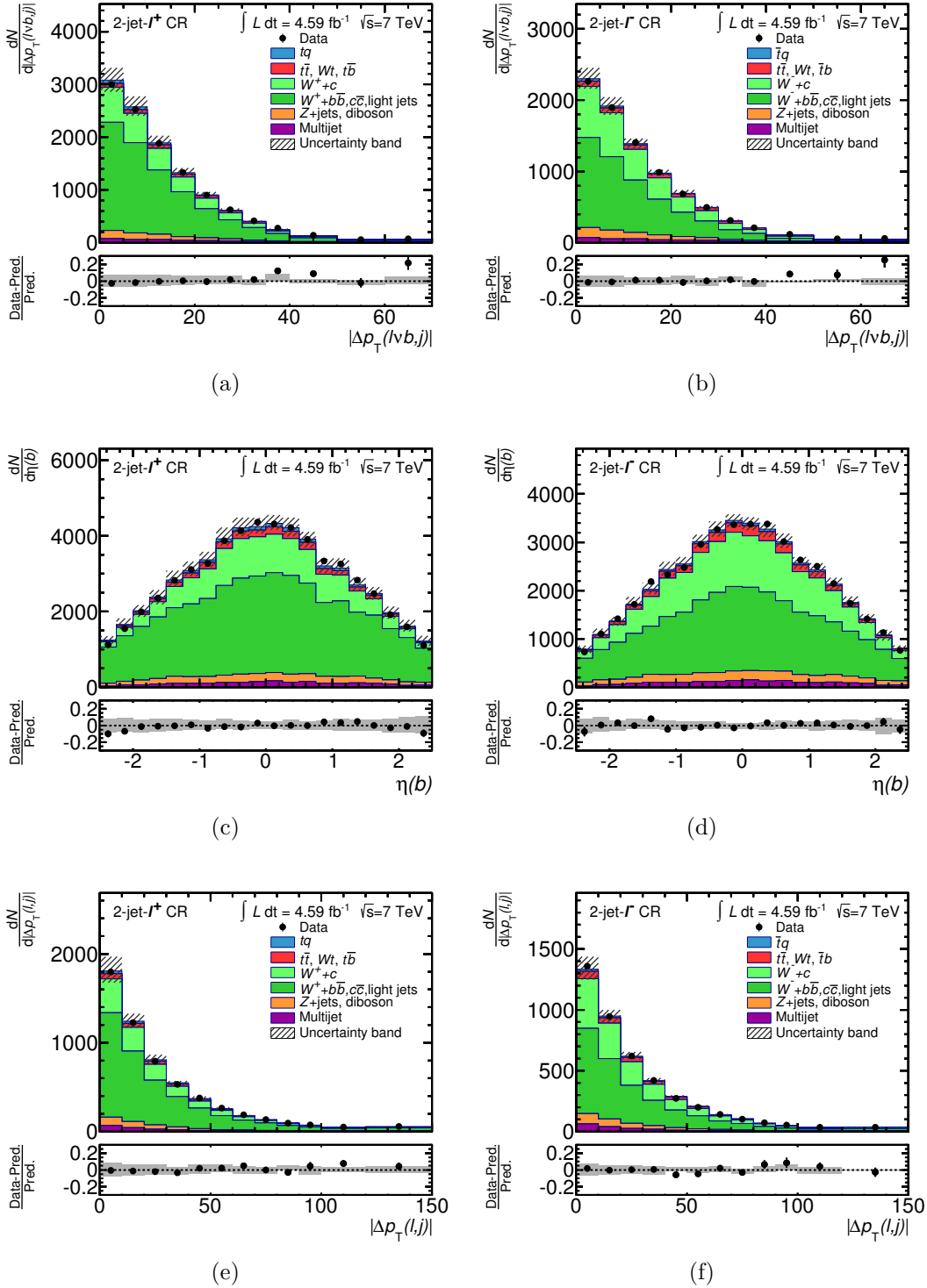


**Figure 4.19:** Distributions of three discriminating variables in the 2-jet- $\ell^+$  and 2-jet- $\ell^-$  channels in the CR. Panels (a) and (b) show the difference in  $p_{\Gamma}$  of the reconstructed top quark and the untagged jet  $\Delta p_{\Gamma}(\nu b, j)$ , (c) and (d) the pseudorapidity of the  $b$ -tagged jet  $\eta(b)$ , (e) and (f) the absolute value of the difference in  $p_{\Gamma}$  of the lepton and the untagged jet  $|\Delta p_{\Gamma}(\ell, j)|$ . The last histogram bin includes overflows. The uncertainty band represents the normalization uncertainty due to the uncertainty on the jet energy scale and the Monte Carlo statistical uncertainty. The relative difference between the observed and expected number of events in each bin is shown in the lower panels.

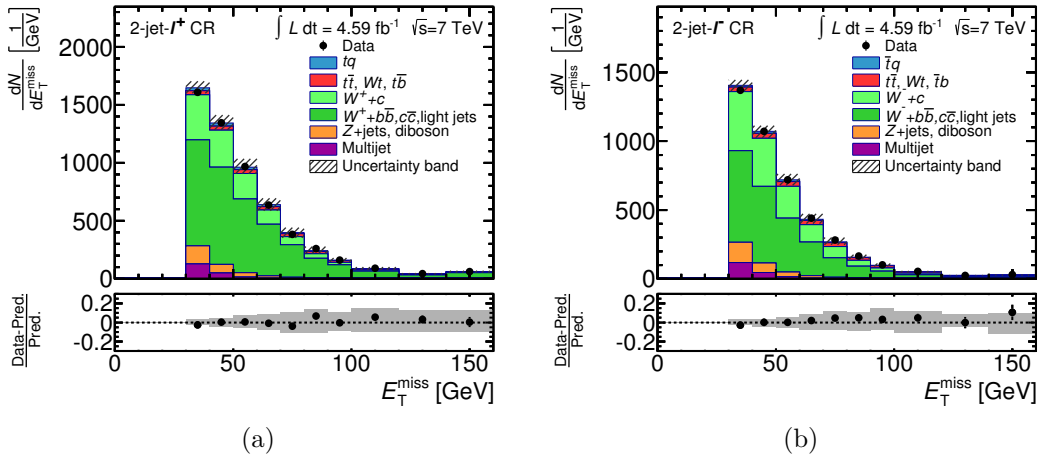


**Figure 4.20:** Distributions of the missing transverse momentum  $E_T^{\text{miss}}$  in the 2-jet- $\ell^+$  and 2-jet- $\ell^-$  channels in the CR. The last histogram bin includes overflows. The uncertainty band represents the normalization uncertainty due to the uncertainty on the jet energy scale and the Monte Carlo statistical uncertainty. The relative difference between the observed and expected number of events in each bin is shown in the lower panels.

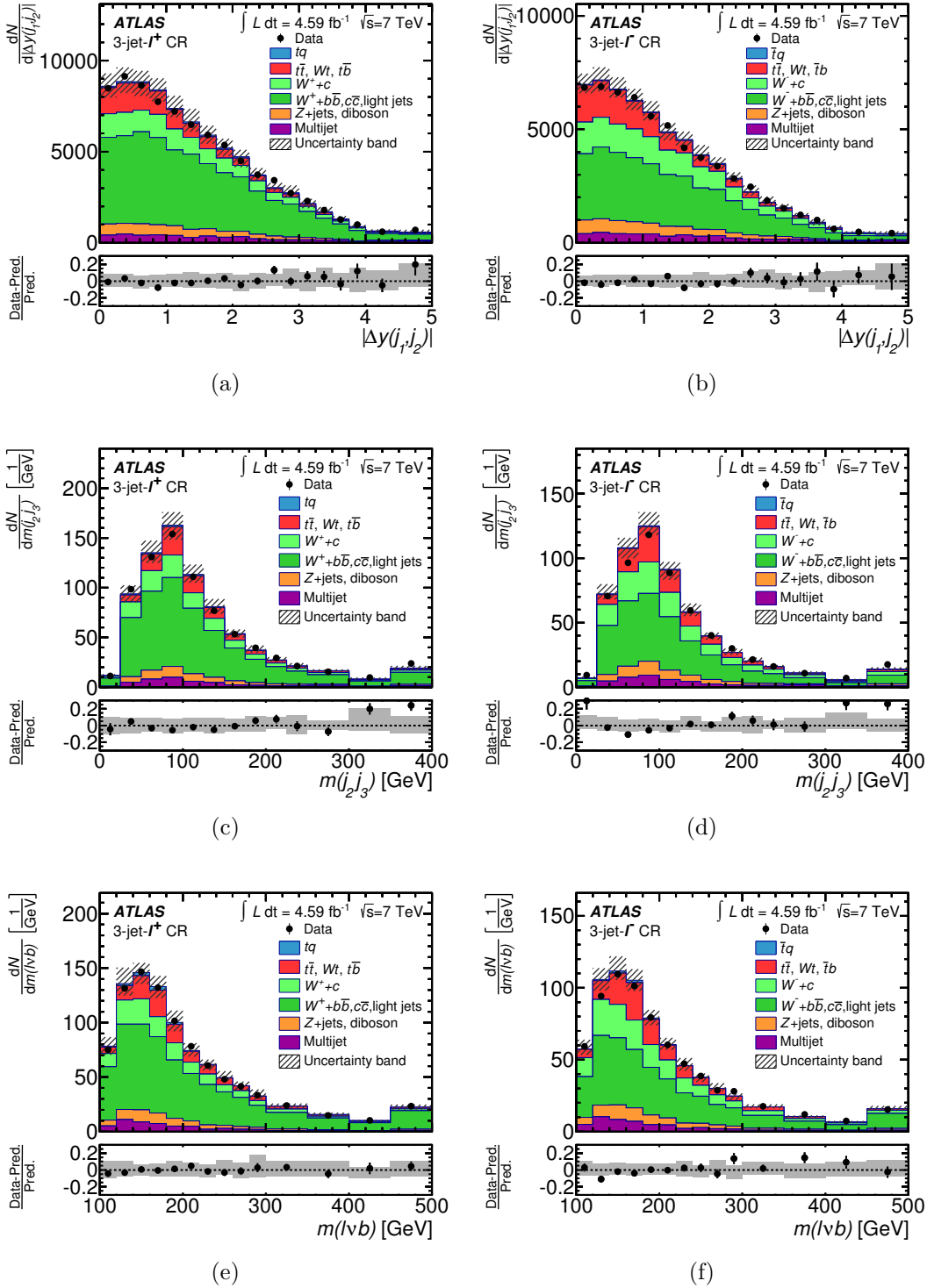


**Figure 4.21:** Distributions of the three most important discriminating variables in the 3-jet- $\ell^+$  and 3-jet- $\ell^-$  channels in the CR [174]. Panels (a) and (b) show the absolute value of the rapidity difference of the leading and second leading jet  $|\Delta y(j_1, j_2)|$ , (c) and (d) the invariant mass of the second leading jet and the third jet  $m(j_2, j_3)$ , and (e) and (f) the invariant mass of the reconstructed top quark  $m(\ell\nu b)$ . The last histogram bin includes overflows. The uncertainty band represents the normalization uncertainty due to the uncertainty on the jet energy scale and the Monte Carlo statistical uncertainty. The relative difference between the observed and expected number of events in each bin is shown in the lower panels.

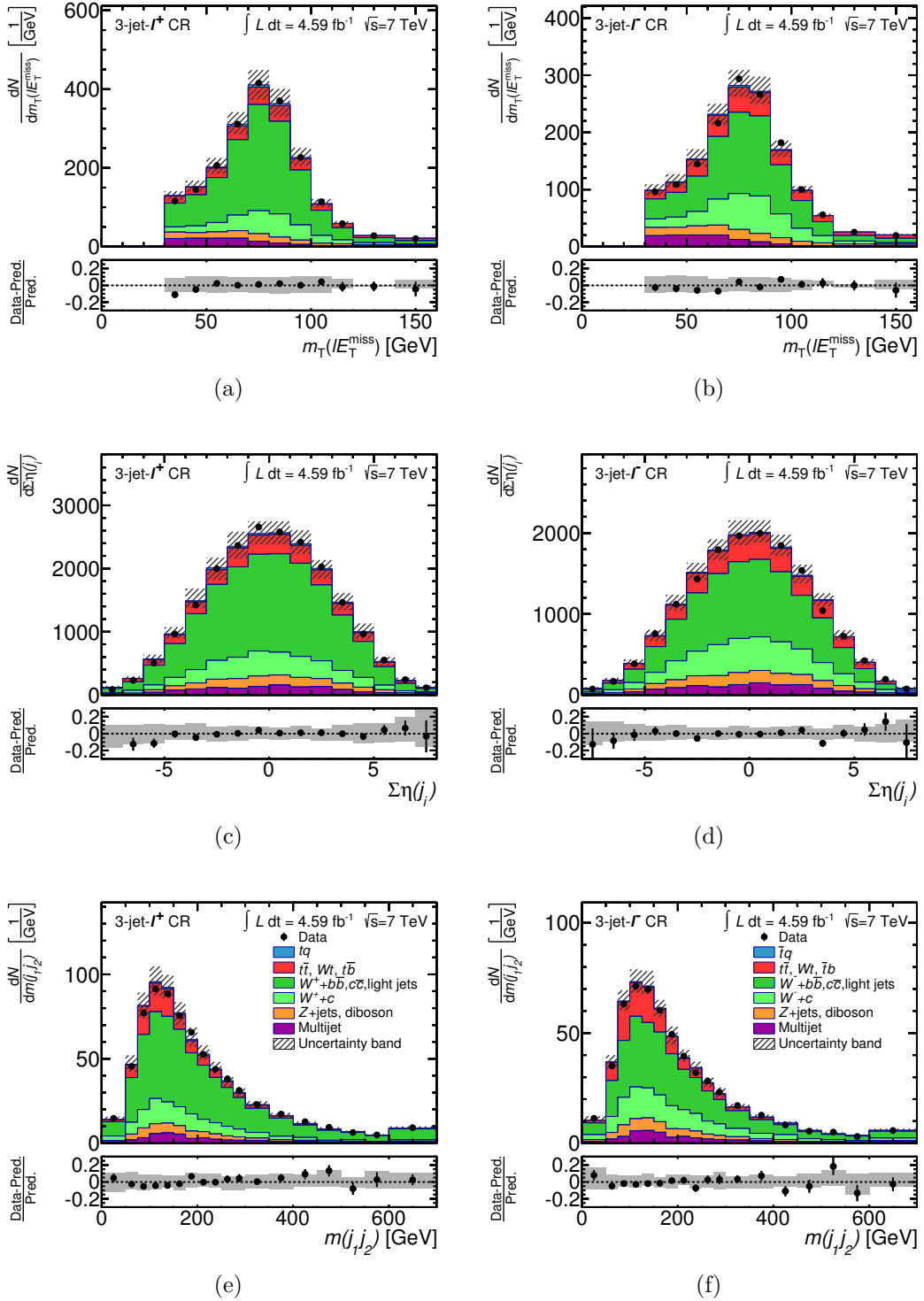


**Figure 4.22:** Distributions of three discriminating variables in the 3-jet- $\ell^+$  and 3-jet- $\ell^-$  channels in the CR. Panels (a) and (b) display the transverse mass of the  $\ell$ - $E_T^{\text{miss}}$  system  $m_T(\ell E_T^{\text{miss}})$ , (c) and (d) the sum of pseudorapidity of the all jets in the event  $\Sigma\eta(j_i)$ , and (e) and (f) the invariant mass of the two leading jets  $m(j_1, j_2)$ . The last histogram bin includes overflows. The uncertainty band represents the normalization uncertainty due to the uncertainty on the jet energy scale and the Monte Carlo statistical uncertainty. The relative difference between the observed and expected number of events in each bin is shown in the lower panels.

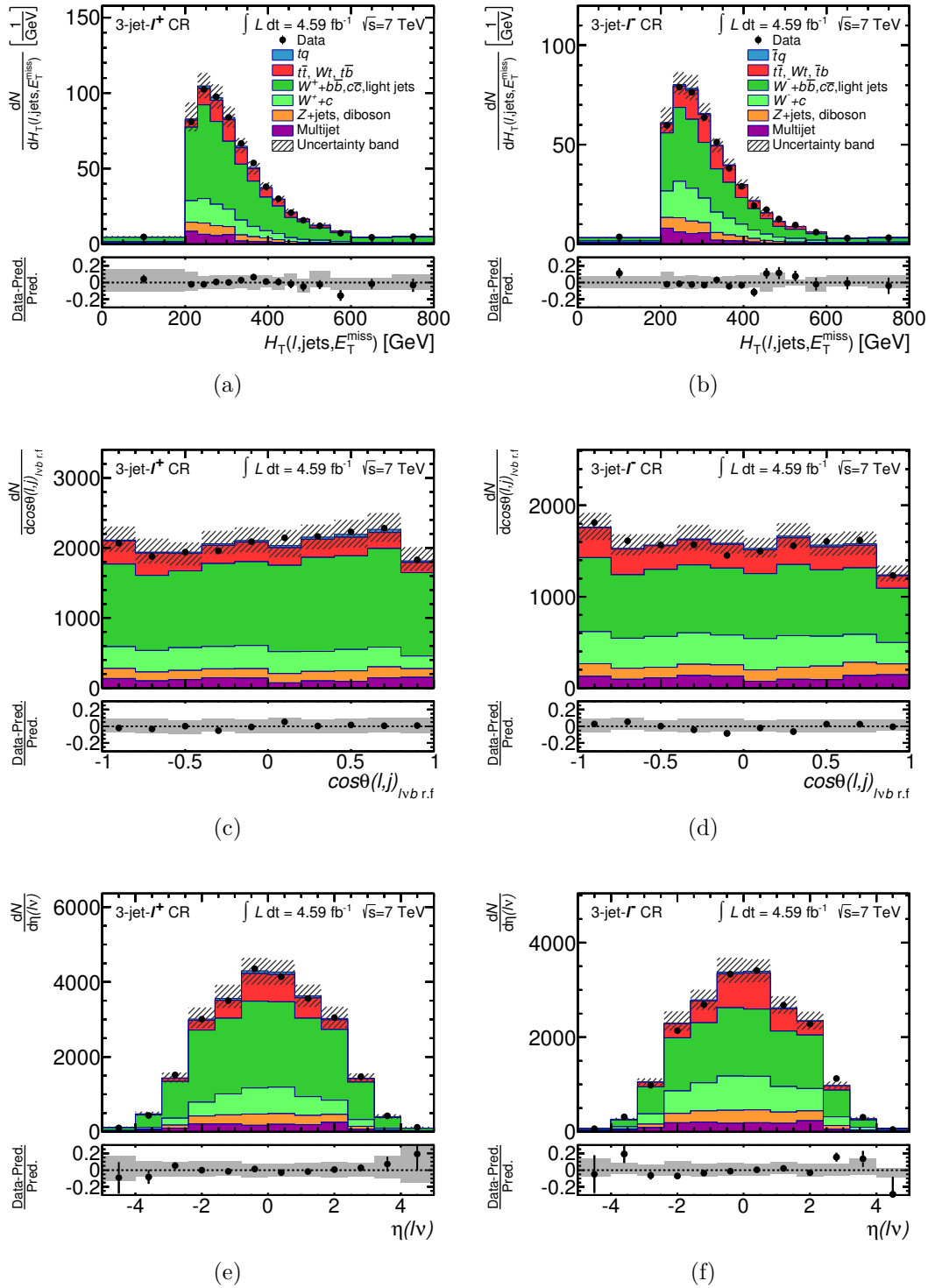


**Figure 4.23:** Distributions of three discriminating variables in the 3-jet- $\ell^+$  and 3-jet- $\ell^-$  channels in the CR. Panels (a) and (b) display  $H_T$ , (c) and (d) the cosine of the angle  $\theta$  between the charged lepton and the leading untagged jet in the rest frame of the reconstructed top quark  $\cos\theta(l, j)_{lvb, r.f.}$ , and (e) and (f) the pseudorapidity of the reconstructed  $W$  boson  $\eta(l\nu)$ . The last histogram bin includes overflows. The uncertainty band represents the normalization uncertainty due to the uncertainty on the jet energy scale and the Monte Carlo statistical uncertainty. The relative difference between the observed and expected number of events in each bin is shown in the lower panels.

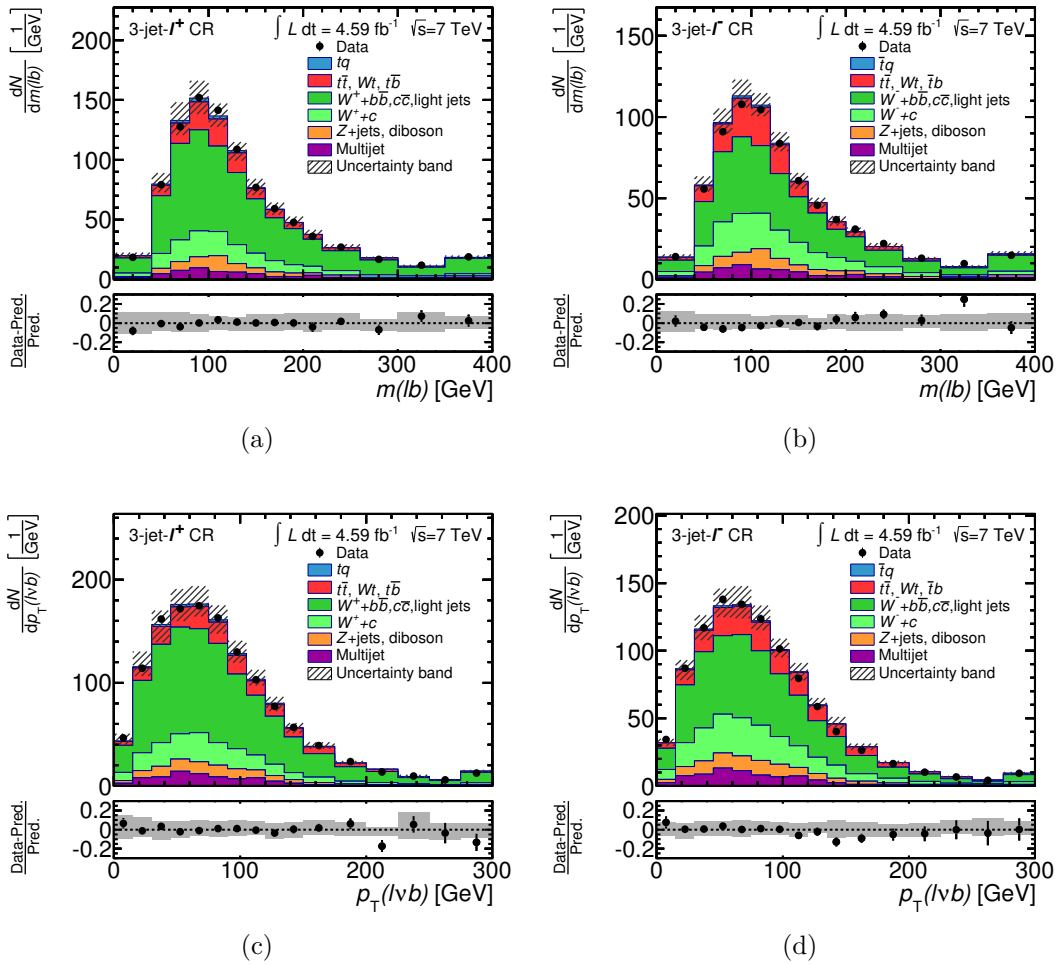


**Figure 4.24:** Distributions of two discriminating variables in the 3-jet- $\ell^+$  and 3-jet- $\ell^-$  channels in the CR. Panels (a) and (b) show the invariant mass of the lepton and the  $b$ -tagged jet  $m(\ell b)$ , (c) and (d) the  $p_T$  of the reconstructed top quark  $p_T(\ell\nu b)$ . The last histogram bin includes overflows. The uncertainty band represents the normalization uncertainty due to the uncertainty on the jet energy scale and the Monte Carlo statistical uncertainty. The relative difference between the observed and expected number of events in each bin is shown in the lower panels.

### 4.3.3 Trained neural networks

In both, the 2-jet- $\ell$  and 3-jet- $\ell$  channels, one neural network is trained utilizing a training sample for each channel. The training sample is used to perform the preprocessing of the input variables and the training of the neural network. In this analysis, the simulated sample of the  $t$ -channel single top-quark process is used as training sample for the signal, while the simulated samples of the  $W$ +jets, top-quark,  $Z$ +jets, and diboson background processes are used as background training samples. The multijet background is not considered in the training.

To construct the training sample, the signal and background contributions are weighted, so that the signal fraction of the sample as well as the background fraction are 50%. In Table 4.8 the fraction of each process in each training sample is listed for the 2-jet and the 3-jet sample, as well as the number of simulated events in each sample. The background fractions are the relative fractions determined by the background estimation in Section 4.2.3. In the 2-jet channels the top-quark background and the  $W$ +jets background are of the same size and are thus trained almost equally. In the 3-jet channels, the top-quark background dominates the background training sample. For both training samples, sufficient statistic of the simulated samples is available.

After the preprocessing, the 13 input variables for the 2-jet NN and the 11 input variables for the 3-jet NN are ranked according to their contribution to the total correlation to the target, if each variable is added to the set of input variables. Thus, the rankings of the variables, displayed in Table 4.9, are determined. The most important variable is the pseudorapidity of the forward untagged jet in the 2-jet NN, and the difference in rapidity between the two leading jets in the 3-jet NN.

The neural networks are then trained with 15 hidden nodes in 14 (10) iterations for the 2-jet (3-jet) NN. To test the NNs for over-training, the NNs are trained using 80% of the training sample, while the other 20% are used to test the training.

**Table 4.8:** Composition of the training samples for the 2-jet and 3-jet NN. The fraction  $f$  of each process is given in %. Additionally, the number of simulated events,  $n$ , in each sample is listed.

Process	$f(2\text{-jet})$ [%]	$f(3\text{-jet})$ [%]
$tq + \bar{t}q$	50	50
$t\bar{t}, Wt, t\bar{b}, \bar{t}b$	22.3	38.1
$W+c$	6.6	1.9
$W^+ + \text{light}, c\bar{c}, b\bar{b}$	19.6	9.2
$Z + \text{jets}, \text{diboson}$	1.4	0.9
	$n(2\text{-jet})$	$n(3\text{-jet})$
	165656	84113

**Table 4.9:** Ranking of the NN input variables in the 2-jet and 3-jet channels. The ranking is determined by the additional correlation to the target  $\kappa$ , if the variable is added to the set of input variables.

2-jet NN		3-jet NN	
variable	$\kappa$ [%]	variable	$\kappa$ [%]
$ \eta(j) $	40.0	$ \Delta y(j_1, j_2) $	34.5
$m(\ell\nu b)$	26.1	$m(j_2 j_3)$	20.7
$m(jb)$	22.0	$m(\ell\nu b)$	17.8
$m_T(\ell E_T^{\text{miss}})$	15.3	$m_T(\ell E_T^{\text{miss}})$	14.1
$\eta(\ell\nu)$	10.1	$\Sigma\eta(j_i)$	8.5
$m(lb)$	9.8	$m(j_1 j_2)$	7.3
$\Delta R(\ell, j)$	4.5	$H_T$	7.7
$\Delta R(\ell\nu b, j)$	7.6	$\cos\theta(\ell, j)_{\ell\nu b, \text{r.f.}}$	6.2
$H_T$	6.6	$\eta(\ell\nu)$	6.2
$ \Delta p_T(\ell\nu b, j) $	5.2	$m(lb)$	3.8
$\eta(b)$	4.8	$p_T(\ell\nu b)$	2.8
$ \Delta p_T(l, j) $	4.5		
$E_T^{\text{miss}}$	2.3		

Since the entropy loss function agrees between the test sample and the training sample (see Fig. 4.25), both networks pass the overtraining check. The normalized output distributions of the obtained networks are shown in Fig. 4.26 for the 2-jet- $\ell^+$ , the 2-jet- $\ell^-$ , the 3-jet- $\ell^+$ , and the 3-jet- $\ell^-$  channel. Here, the signal process is shown together with the top-quark background and the  $W+b\bar{b}$ ,  $c\bar{c}$ , and light jets background. The output distributions  $o_{\text{NN}}$  have good separation power between the main backgrounds and the signal. In Fig. 4.27 the kinematic modeling of the output distributions  $o_{\text{NN}}$  is validated in the corresponding channels of the CR. It can be observed, that the output distributions are well modeled and thus, can be used in the analysis.

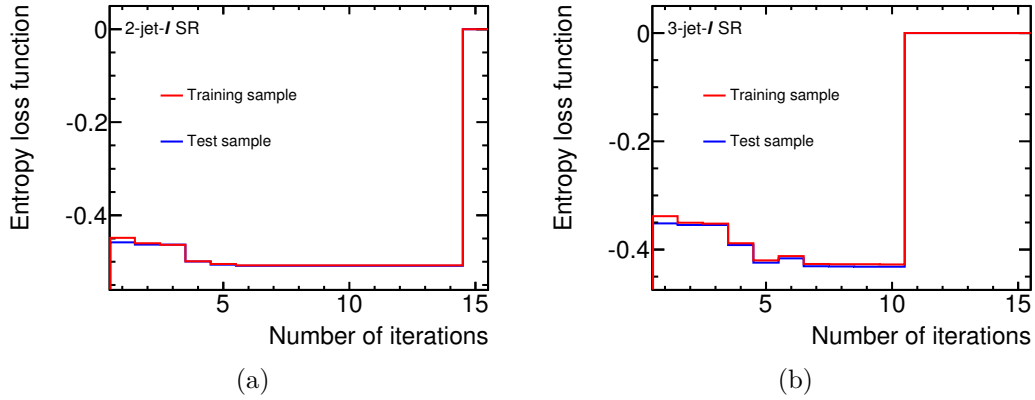


**Figure 4.25:** Entropy loss function as a function of the number of iterations for the training sample (red line) and the test sample (blue line) during the training of the NN discriminants in the 2-jet- $\ell$  SR and 3-jet- $\ell$  SR. The end of the training is indicated by the rise of the entropy loss function to zero.

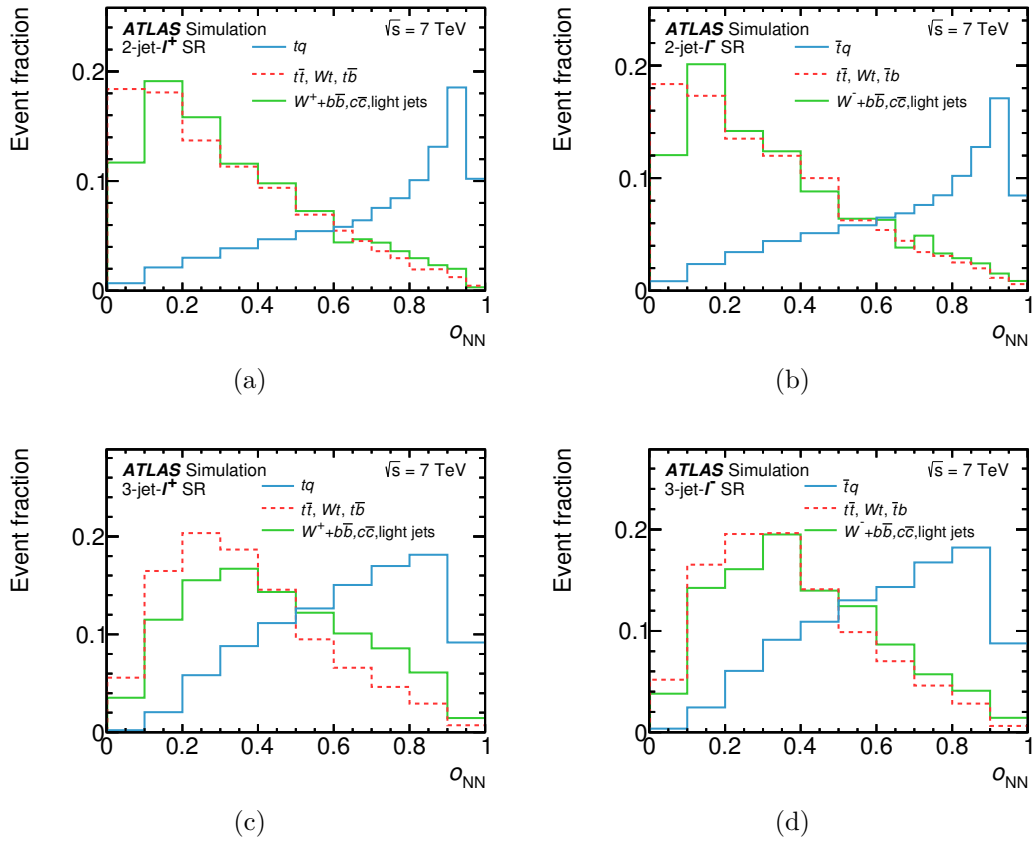


**Figure 4.26:** Template-shape distributions of the NN discriminants in the 2-jet channels and 3-jet channels in the SR [174]: (a) 2-jet- $\ell^+$  channel, (b) 2-jet- $\ell^-$  channel, (c) 3-jet- $\ell^+$  channel, and (d) 3-jet- $\ell^-$  channel. The distributions are normalized to unit area.

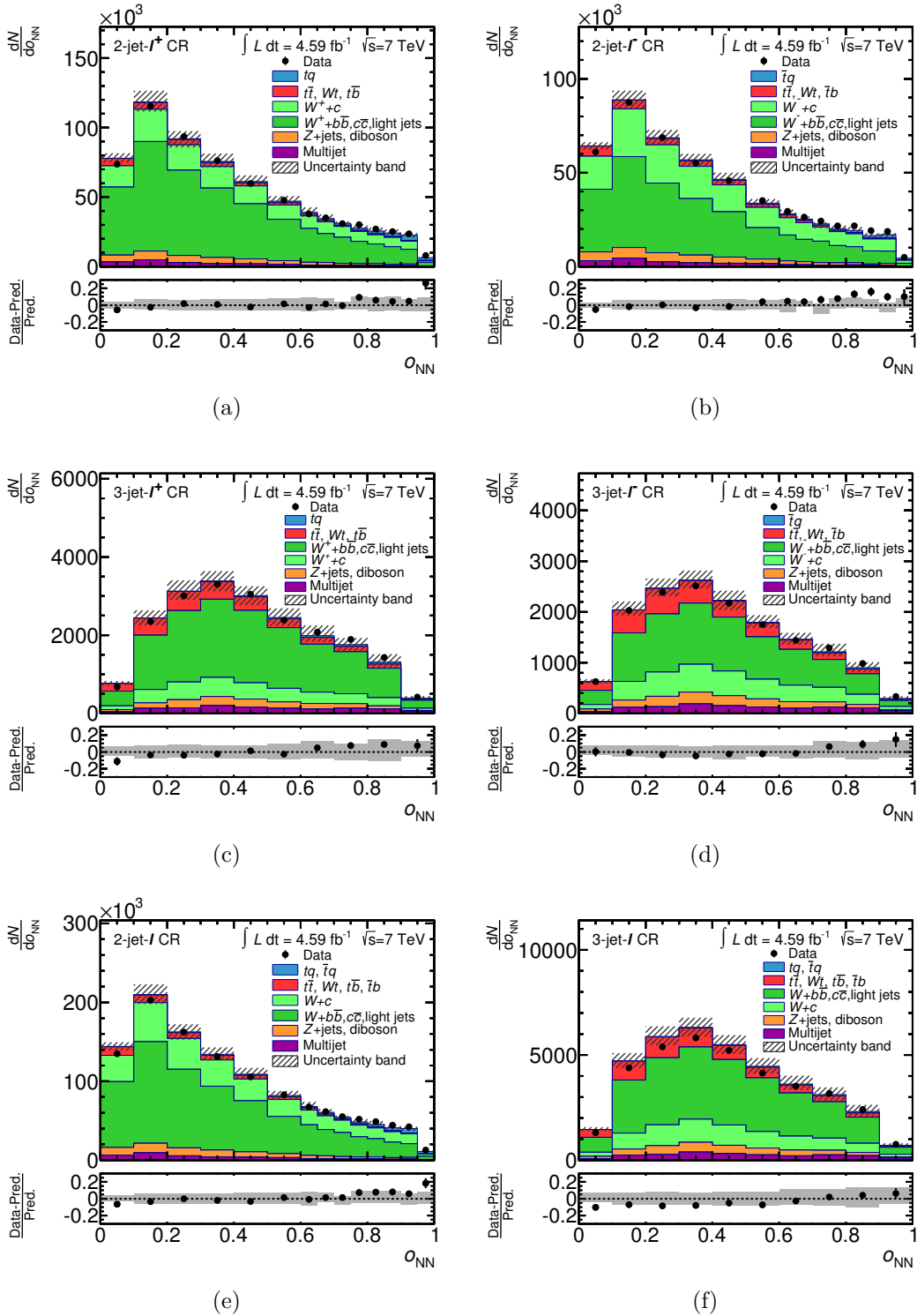


**Figure 4.27:** Distributions of neural networks in the CR in the (a) 2-jet- $\ell^+$ , the (b) 2-jet- $\ell^-$ , the (e) 2-jet- $\ell$ , the (c) 3-jet- $\ell^+$ , the (d) 3-jet- $\ell^-$  and the (f) 3-jet- $\ell$  channels. The uncertainty band represents the normalization uncertainty due to the uncertainty on the jet energy scale and the Monte Carlo statistical uncertainty. The relative difference between the observed and expected number of events in each bin is shown in the lower panels.



# Chapter 5

## Inclusive cross-section and $R_t$ measurements

One part of the presented work is the measurement of the inclusive cross sections,  $\sigma(tq)$ ,  $\sigma(\bar{t}q)$ , and  $\sigma(tq + \bar{t}q)$ , as well as the measurement of the cross-section ratio  $R_t$ . The following strategy is used for all these measurements: A binned maximum-likelihood (ML) fit-method is applied to the NN discriminants to determine the signal cross-sections and the background normalization. Then, the statistical and systematic uncertainties are evaluated using a frequentist approach. Uncertainties affect the number of predicted events for each process as well as the shapes of the template distributions of each process.

This chapter is structured as follows. First, the statistical methods, that are used to extract the cross sections and to evaluate the effect of uncertainties on the measurements, are introduced. Then, the application of the binned ML fit-method is described. Sources of systematic uncertainties are introduced and their effect on the results is evaluated. At the end of the chapter, the final results of the inclusive cross sections and the ratio  $R_t$  are presented.

### 5.1 Statistical methods

The binned ML fit-method and the frequentist estimation of the uncertainties are introduced. Both methods are only briefly explained. The level of information is restricted to the concrete application in this thesis. More general descriptions for the ML fit-method and the generation of pseudo experiments can be found elsewhere, e.g. in Ref. [177].

#### 5.1.1 Binned maximum-likelihood fit-method

To estimate the signal fraction of the data sample, a simultaneous fit is applied to the NN discriminants in several analysis channels. In the fit, a binned likelihood function  $L$  is maximized. This binned likelihood function is given by the product of the Poisson functions  $P$ , describing the content of each bin in the NN discriminant, and the product of Gaussian distributions, that constrain the background processes

and systematic uncertainties included in the fit:

$$L(\beta_{tq}^s, \beta_{\bar{t}q}^s; \beta_j^b; \delta^{b\text{-tag}}) = \prod_{k=1}^K P(n_k; \mu_k(\beta_{tq}^s, \beta_{\bar{t}q}^s, \beta_j^b)) \cdot \prod_{j=1}^B G(\beta_j^b; 1, \Delta_j) \cdot G(\delta^{b\text{-tag}}; 0; 1). \quad (5.1)$$

The parameters in the likelihood function are the scale factors  $\beta_{tq}^s$  and  $\beta_{\bar{t}q}^s$  for the two signal processes, in case of the measurement of  $\sigma(tq)$  and  $\sigma(\bar{t}q)$ , the scale factors  $\beta_j^b$  for the considered background processes, and the correction factor  $\delta^{b\text{-tag}}$  for the uncertainty due to the  $b$ -tagging efficiency correction factor. The index  $k$  runs over the number of bins  $K$  of the NN discriminant. Each background process is denoted by the index  $j$ , that runs over the number of background processes  $B$  considered in the fit.

The Poisson function in bin  $k$  is defined as:

$$P(n_k; \mu_k) = \frac{e^{-\mu_k} \cdot \mu_k^{n_k}}{n_k!} \quad (5.2)$$

where  $n_k$  is the number of measured events in bin  $k$ . The parameter  $\mu_k$  is given by the sum of the estimated number of expected background events  $\mu_{jk}^b$  and the estimated number of expected signal events  $\mu_{tq,k}^s$  and  $\mu_{\bar{t}q,k}^s$  in bin  $k$ :

$$\mu_k = \mu_{tq,k}^s + \mu_{\bar{t}q,k}^s + \sum_{j=1}^B \mu_{jk}^b, \quad \mu_{t(\bar{t})q,k}^s = \beta_{t(\bar{t})q}^s \cdot \tilde{\nu}_{t(\bar{t})q} \cdot \alpha_{t(\bar{t})q,k}, \quad \text{and} \quad \mu_{jk}^b = \beta_j^b \cdot \tilde{\nu}_j \cdot \alpha_{jk}.$$

Each estimated number of expected events  $\mu_k$  in bin  $k$  can be expressed for each process as a product of the number of predicted events  $\tilde{\nu}$  in the selected dataset, the scale factor  $\beta$ , and the fraction of events in bin  $k$  given by  $\alpha_k$  for each template. The set of  $\alpha_k$  constitute the normalized histogram for each process with  $\sum_{k=1}^K \alpha_k = 1$ .

Finally, the constraint of each background process  $j$  is given by a Gaussian distribution with mean of one and a RMS corresponding to the relative uncertainty  $\Delta_j$  on the number of predicted events:

$$G(\beta_j^b; 1; \Delta_j) = \frac{1}{\sqrt{2\pi\Delta_j^2}} \cdot \exp\left(-\frac{(\beta_j^b - 1)^2}{2\Delta_j^2}\right). \quad (5.3)$$

The  $b$ -tagging efficiency correction factor is fitted together with the signal and background scale factors. Therefore, another Gaussian term is multiplied to the likelihood function constraining the  $b$ -tagging efficiency by its uncertainty.

Instead of calculating the maximum of the likelihood function, it is equivalent and numerically more stable to minimize the negative logarithm of the likelihood function. The computation of the minimum is then performed with the MINUIT program [178]. Thus, the estimators of the signal scale-factors, called  $\hat{\beta}_{tq}^s$  and  $\hat{\beta}_{\bar{t}q}^s$ , are determined, and the cross sections are calculated by multiplying the estimator with the respective predicted cross section. Analogously, the inclusive combined cross section  $\sigma(tq + \bar{t}q)$  is determined. Here, the likelihood function is changed such, that only one signal scale-factor  $\hat{\beta}_{tq+\bar{t}q}^s$  remains. The cross section is then computed as  $\sigma(tq + \bar{t}q) = \hat{\beta}_{tq+\bar{t}q}^s \cdot \sigma^{\text{NLO+NNLL}}(tq + \bar{t}q)$ .

### 5.1.2 Frequentist estimation of uncertainties

A frequentist approach to estimate the uncertainty is the evaluation of all possible outcomes of the measurement by repeating the same experiment with independent datasets. In the presented analysis, this is realized by running a set of MC pseudo experiments. In each pseudo experiment, pseudo data is created, that is altered according to the expected statistical and systematic uncertainties. Then, the binned ML fit is repeated on the pseudo data and the estimated signal scale-factor  $\hat{\beta}^s$  is obtained.

Systematic uncertainties cause variations in the acceptance and the template shape of each physics process, resulting to different values for the number of predicted events  $\tilde{\nu}$  and for the relative fraction of events in bin  $k$ ,  $\alpha_k$ . For each source of systematic uncertainty  $i$ , a Gaussian-distributed random-number  $\delta_i$  is introduced, that specifies the strength and sign of the variation in the pseudo experiment. The parameter  $\delta_i$  is then used to determine the fluctuated values for  $\tilde{\nu}$  and  $\alpha_k$  of all processes ensuring a full correlation between the acceptance and shape variation caused by the uncertainty  $i$ . An additional uncertainty on the number of predicted events  $\tilde{\nu}_j$  for each background process  $j$  is the normalization uncertainty  $\Delta_j$ . This uncertainty is included in the pseudo experiments by varying  $\tilde{\nu}_j$  according to a log-normal distribution. Also, the limited size of the simulated templates for each physics process is taken into account in the pseudo experiments. Here,  $\alpha_k$  is fluctuated with a Gaussian distribution where the RMS corresponds to the statistical uncertainty in the number of simulated events in bin  $k$ . More details on the generation of the pseudo experiments and the implementation of the variations can be found in Ref. [170] and [179].

In the presented analysis 100,000 pseudo experiments are generated to estimate the uncertainty of the measurement. The estimator of the uncertainty on the measurement is given by the root mean square of the  $\hat{\beta}^s$  distribution of the signal process. As an example the  $\hat{\beta}$  distribution for the  $t$ -channel single top-quark signal process is given in Fig. 5.1. The relative uncertainty obtained from the distribution is 12.4% with a statistical uncertainty of 0.3%.

## 5.2 Binned maximum-likelihood fit to the NN discriminants

The cross sections  $\sigma(tq)$  and  $\sigma(\bar{t}q)$  are measured by performing a simultaneous binned ML fit to the NN discriminant distributions in the 2-jet- $\ell^+$ , 2-jet- $\ell^-$ , 3-jet- $\ell^+$ , and 3-jet- $\ell^-$  channels and to the event yield in the 3-jet-2-tag channel. Thus, the measured scale factors  $\hat{\beta}_{tq}^s$  and  $\hat{\beta}_{\bar{t}q}^s$  are determined. In addition, the fraction of the combined top-quark background, the fraction of the combined  $W+bb$ ,  $W+c\bar{c}$ , and  $W$ +light jets background, the fraction of the combined  $Z$ +jets and diboson background, and the  $b$ -tagging efficiency correction factor are fitted in all channels simultaneously. Here, the  $W+bb$ ,  $W+c\bar{c}$ , and  $W$ +light jets background process is fitted independently for the  $W^+$  fraction and the  $W^-$  fraction. The relative normalization uncertainty,  $\Delta_j$ ,

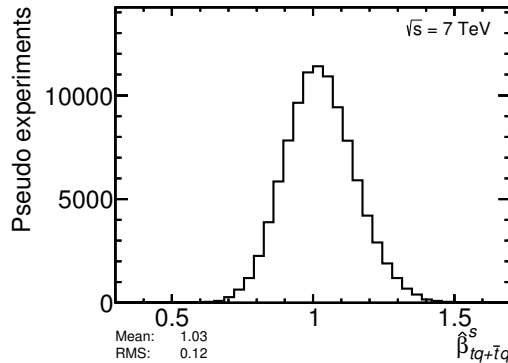


**Figure 5.1:** Distribution of the estimator  $\hat{\beta}_{tq+\bar{t}q}^s$  for the  $t$ -channel single top-quark signal process from 100,000 pseudo experiments. The root-mean square of the distribution is an estimator of the total uncertainty due to all sources of statistical and systematic uncertainties.

**Table 5.1:** Values of the Gaussian constraints  $\Delta_j$  for each background process whose normalization is determined in the fit. The constraint corresponds to the relative uncertainty in the theory prediction of each process.

Process	$\Delta_j$
$t\bar{t}, Wt, t\bar{b}, \bar{t}b$	0.065
$W^+ + b\bar{b}, c\bar{c}, \text{light jets}$	0.36
$W^- + b\bar{b}, c\bar{c}, \text{light jets}$	0.36
$W + b\bar{b}, c\bar{c}, \text{light jets}$	0.36
$Z + \text{jets, diboson}$	0.15

for each fitted background  $j$  is given by the relative uncertainty in the theory prediction. In Table 5.1 the values for  $\Delta_j$  are listed for each of the combined background processes. The number of predicted events  $\tilde{\nu}$  of the multijet background and the  $W+c$  background are fixed to the predictions given in Table 4.6 in Section 4.2.3.

Table 5.2 presents the results of the binned ML fit to the measured NN discriminant distributions in the 2-jet- $\ell^+$ , 2-jet- $\ell^-$ , 3-jet- $\ell^+$ , and 3-jet- $\ell^-$  channels and to the event yield in the 3-jet-2-tag channel. The estimated number of events after the fit are named  $\hat{\nu}$  and are computed by  $\hat{\nu} = \hat{\beta} \cdot \tilde{\nu}$ . The results of the fit are the estimated signal scale-factors of  $\hat{\beta} = 1.10 \pm 0.04$  for the  $tq$  production and of  $\hat{\beta} = 0.99 \pm 0.06$  for the  $\bar{t}q$  production. The quoted uncertainty on  $\hat{\beta}$  is given by the statistical uncertainty of the fit.

The cross section  $\sigma(tq + \bar{t}q)$  is extracted by performing a binned ML fit to the measured NN discriminant distributions in the combined 2-jet- $\ell$  and 3-jet- $\ell$  channels and to the event yield in the 3-jet-2-tag channel. Here, the top-quark-to-antiquark ratio of the signal is assumed to be the one of the NLO+NNLL prediction, see Section 1.2.2. The fit includes the same processes as the fit for the separate lepton-charge channels; just the charge separated processes are now combined to one process. Ta-

**Table 5.2:** Estimators of the parameters of the likelihood function resulting from the fit for  $\beta_{tq}^s$  and  $\beta_{\bar{t}q}^s$ . The quoted uncertainties on  $\hat{\beta}$ ,  $\hat{\delta}^{b\text{-tag}}$ , and  $\hat{\nu}$  include the statistical uncertainty of the fit.

Process	$\hat{\beta}$	$\hat{\nu}$				
		2-jet- $\ell^+$	2-jet- $\ell^-$	3-jet- $\ell^+$	3-jet- $\ell^-$	3-jet-2-tag
$tq$	$1.10 \pm 0.04$	$2799 \pm 94$	–	$929 \pm 31$	–	$340 \pm 11$
$\bar{t}q$	$0.99 \pm 0.06$	–	$1380 \pm 77$	–	$430 \pm 24$	$160 \pm 9$
nuisance parameters						
$t\bar{t}, Wt, t\bar{b}, \bar{t}b$	$0.96 \pm 0.01$	$5061 \pm 78$	$4942 \pm 76$	$7900 \pm 120$	$7890 \pm 120$	$5637 \pm 87$
$W^+ + \text{light}, c\bar{c}, b\bar{b}$	$1.04 \pm 0.03$	$5910 \pm 160$	$17 \pm 0$	$2537 \pm 69$	$12 \pm 0$	$213 \pm 6$
$W^- + \text{light}, c\bar{c}, b\bar{b}$	$1.11 \pm 0.04$	$10.3 \pm 0.4$	$3780 \pm 150$	$4.5 \pm 0.2$	$1658 \pm 64$	$150 \pm 6$
$W+c$	–	1460	1620	388	430	6.5
$Z+\text{jets}, \text{diboson}$	$1.08 \pm 0.15$	$401 \pm 55$	$333 \pm 45$	$209 \pm 28$	$193 \pm 26$	$24 \pm 3$
Multijet	–	750	740	320	440	21
Total	–	$16400 \pm 210$	$12810 \pm 190$	$12290 \pm 150$	$11040 \pm 140$	$6552 \pm 88$
Data	–	16198	12837	12460	10819	6403
$\hat{\delta}^{b\text{-tag}}$	$-0.12 \pm 0.11$	–	–	–	–	–

Table 5.3 lists the estimated parameters of the likelihood function. The estimated scale factor  $\hat{\beta}_{tq+\bar{t}q}^s$  for the  $t$ -channel signal process is  $1.05 \pm 0.03$  where only the statistical uncertainty is taken into account. Altogether it can be observed, that the  $\hat{\beta}$  values for the charge-symmetric background processes, the  $t\bar{t}$ ,  $Wt$ ,  $t\bar{b}$ , and  $\bar{t}b$  process and the  $Z$ +jets, diboson process, are consistent between the two fits performed to extract the inclusive cross sections.

To test the robustness of the fits, several cross checks are performed. The binned ML fit is done in different combinations of analysis channels and without the  $b$ -tagging efficiency correction factor in the likelihood function. In Table 5.4 the results are compared for the fit in the 2-jet- $\ell$ , 3-jet- $\ell$ , and 3-jet-2-tag channels. The removal of the  $b$ -tagging efficiency correction factor from the likelihood function does not change the estimators for the signal and background processes significantly. This is also the case, when the 3-jet-2-tag channel is removed from the fit.

The gain of adding the 3-jet- $\ell$  channel to the analysis is evaluated by performing a fit without this channel (in the 2-jet- $\ell$  and 3-jet-2-tag channels only). It can be observed, that the sensitivity to the normalization of the  $t\bar{t}$ ,  $Wt$ ,  $t\bar{b}$ , and  $\bar{t}b$  process decreases because the differentiation between the  $W$ +jets background and the top background processes is not strong in the NN discriminant in the 2-jet- $\ell$  channels (as can be seen in Fig. 4.26). Studies have also shown, that the effect of the systematic uncertainties decreases when the 3-jet- $\ell$  signal regions are added to the analysis.

The sensitivity to the  $b$ -tagging efficiency correction factor stems from the event yield in the 3-jet-2-tag channel with respect to the event yields in the 3-jet- $\ell$  channel. Therefore, the statistically most precise result for the  $b$ -tagging efficiency correction factor is achieved in the default fit. If the 3-jet-2-tag channel is left out of the fit, the sensitivity to the  $b$ -tagging efficiency correction factor is very low (see Table 5.4, last column). Also, the 2-jet- $\ell$  channel alone with the 3-jet-2-tag channel performs less good than the default fit. Here, a two sigma deviation is observed for the value

**Table 5.3:** Estimators of the parameters of the likelihood function resulting from the fit for  $\beta_{tq+\bar{t}q}^s$ . The quoted uncertainties on  $\hat{\beta}$ ,  $\hat{\delta}^{b\text{-tag}}$ , and  $\hat{\nu}$  include the statistical uncertainty of the fit.

Process	$\hat{\beta}$	$\hat{\nu}$		
		2-jet- $\ell$	3-jet- $\ell$	3-jet-2-tag
$tq+\bar{t}q$	$1.05 \pm 0.03$	$4150 \pm 130$	$1348 \pm 40$	$495 \pm 15$
nuisance parameters				
$t\bar{t}, Wt, t\bar{b}, \bar{t}b$	$0.96 \pm 0.01$	$9990 \pm 150$	$15760 \pm 240$	$5628 \pm 87$
$W+\text{light}, c\bar{c}, b\bar{b}$	$1.08 \pm 0.03$	$9800 \pm 260$	$4230 \pm 110$	$367 \pm 10$
$W+c$	–	3080	818	6.5
$Z+\text{jets}, \text{diboson}$	$1.07 \pm 0.15$	$720 \pm 100$	$394 \pm 55$	$23 \pm 3$
Multijet	–	1490	760	21
Total	–	$29220 \pm 340$	$23320 \pm 280$	$6541 \pm 88$
Data	–	29035	23279	6403
$\hat{\delta}^{b\text{-tag}}$	$-0.11 \pm 0.11$	–	–	–

of  $\hat{\delta}^{b\text{-tag}}$ . This can be related to the less precise determination of the  $t\bar{t}$  background normalization in the 2-jet- $\ell$  channel only.

To further test the quality of the fits and the quality of the background model, the observed distributions of the NN discriminants and the input variables to the NN are compared to the signal and background model normalized to the fit results. In Fig. 5.2 the observed NN discriminant distributions are shown compared to the compound model of signal and background processes. A good agreement is observed for the NN discriminant distributions in all channels. Figures 5.3-5.7 show the input variables normalized to the fit results in the 2-jet- $\ell^+$  and 2-jet- $\ell^-$  channels, and Figures 5.8-5.11 in the 3-jet- $\ell^+$  and 3-jet- $\ell^-$  channels, respectively. Differences between data and prediction are covered by normalization uncertainty of the different processes after the fit.

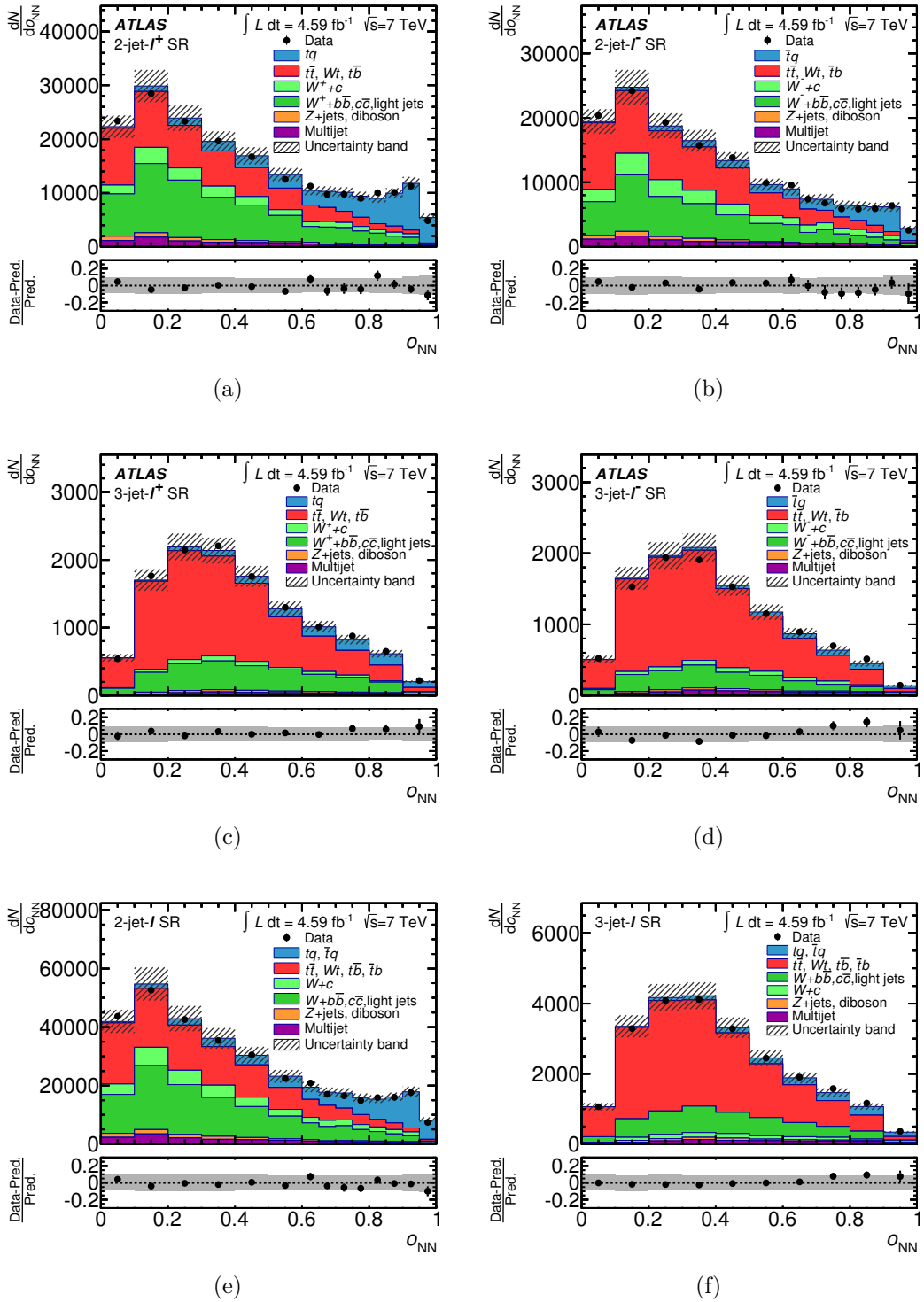


**Figure 5.2:** Neural network discriminant distributions normalized to the result of the binned maximum-likelihood fit in (a) the 2-jet- $\ell^+$  channel, (b) the 2-jet- $\ell^-$  channel, (c) the 3-jet- $\ell^+$  channel, (d) the 3-jet- $\ell^-$  channel, (e) the 2-jet- $\ell$  channel, and (f) the 3-jet- $\ell$  channel. The uncertainty band represents the normalization uncertainty of all processes after the fit and the Monte Carlo statistical uncertainty, added in quadrature. The relative difference between the observed and expected number of events in each bin is shown in the lower panels. The figures with the label ATLAS are published in Ref. [174].

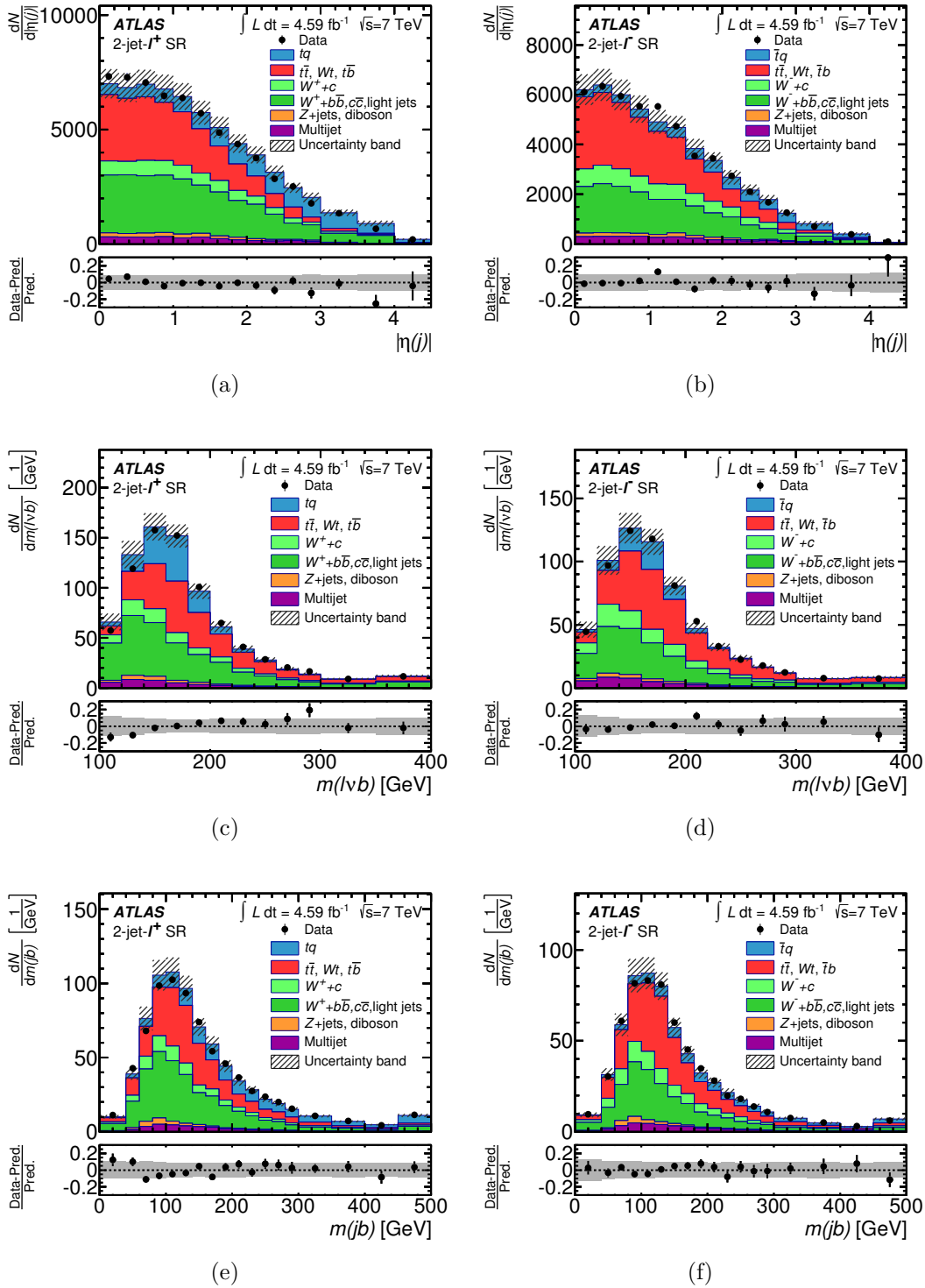


**Figure 5.3:** Distributions of the three most important discriminating variables in the 2-jet- $\ell^+$  and 2-jet- $\ell^-$  channels in the SR normalized to the result of the binned ML fit [174]. Panels (a) and (b) display the absolute value of the pseudorapidity of the untagged jet  $|\eta(j)|$ . Panels (c) and (d) show the invariant mass of the reconstructed top quark  $m(\ell\nu b)$  and (e) and (f) the invariant mass of the  $b$ -tagged and the untagged jet  $m(jb)$ . The last histogram bin includes overflows. The uncertainty band represents the normalization uncertainty of all processes after the fit and the Monte Carlo statistical uncertainty, added in quadrature. The relative difference between the observed and expected number of events in each bin is shown in the lower panels.

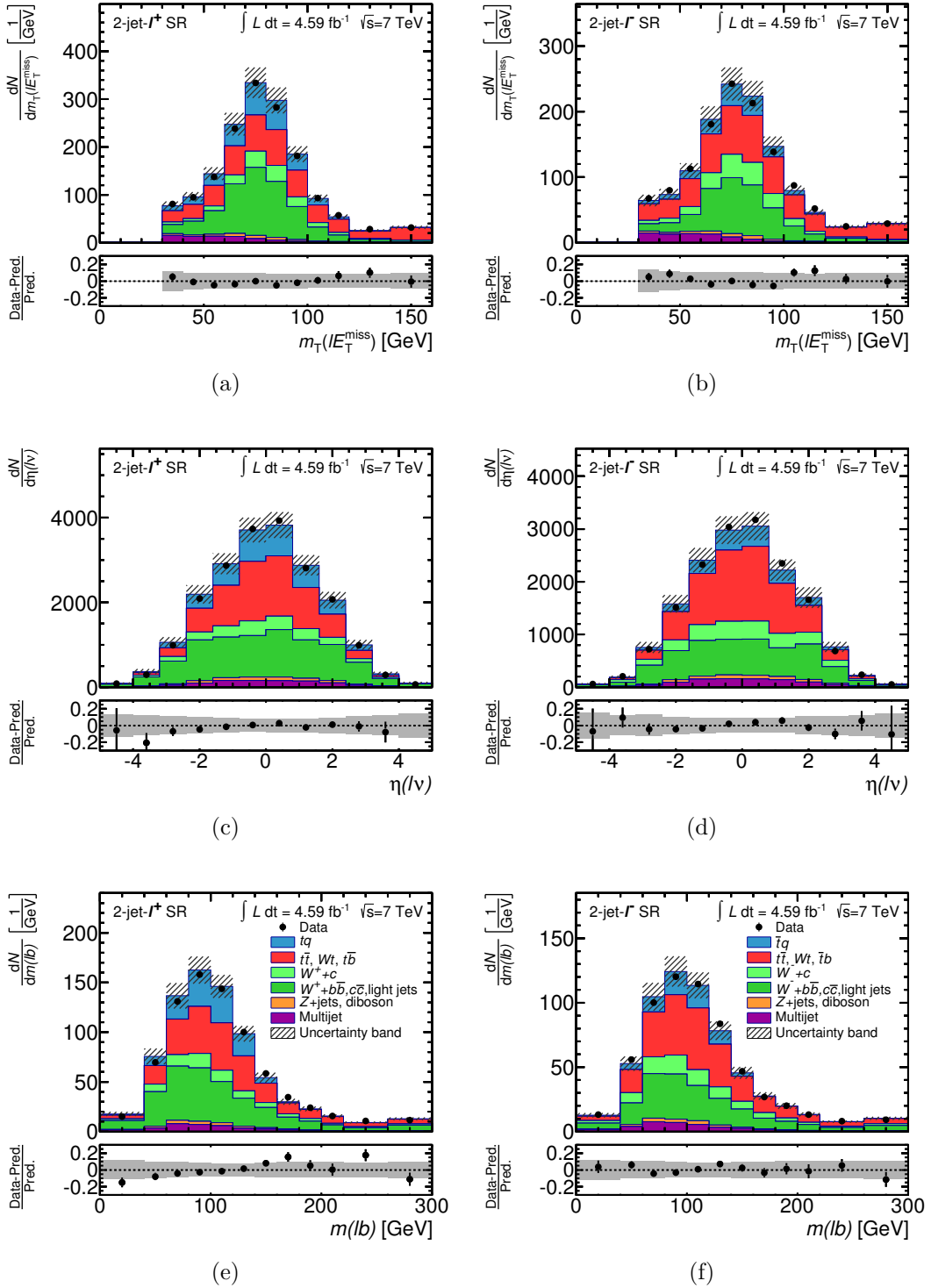


**Figure 5.4:** Distributions of three discriminating variables in the 2-jet- $l^+$  and 2-jet- $l^-$  channels in the SR normalized to the result of the binned ML fit. Panels (a) and (b) display the transverse mass of the  $l$ - $E_T^{\text{miss}}$  system  $m_T(lE_T^{\text{miss}})$ . Panels (c) and (d) show the pseudorapidity of the reconstructed  $W$  boson  $\eta(l\nu)$  and (e) and (f) the invariant mass of the lepton and the  $b$ -tagged jet  $m(lb)$ . The last histogram bin includes overflows. The uncertainty band represents the normalization uncertainty of all processes after the fit and the Monte Carlo statistical uncertainty, added in quadrature. The relative difference between the observed and expected number of events in each bin is shown in the lower panels.

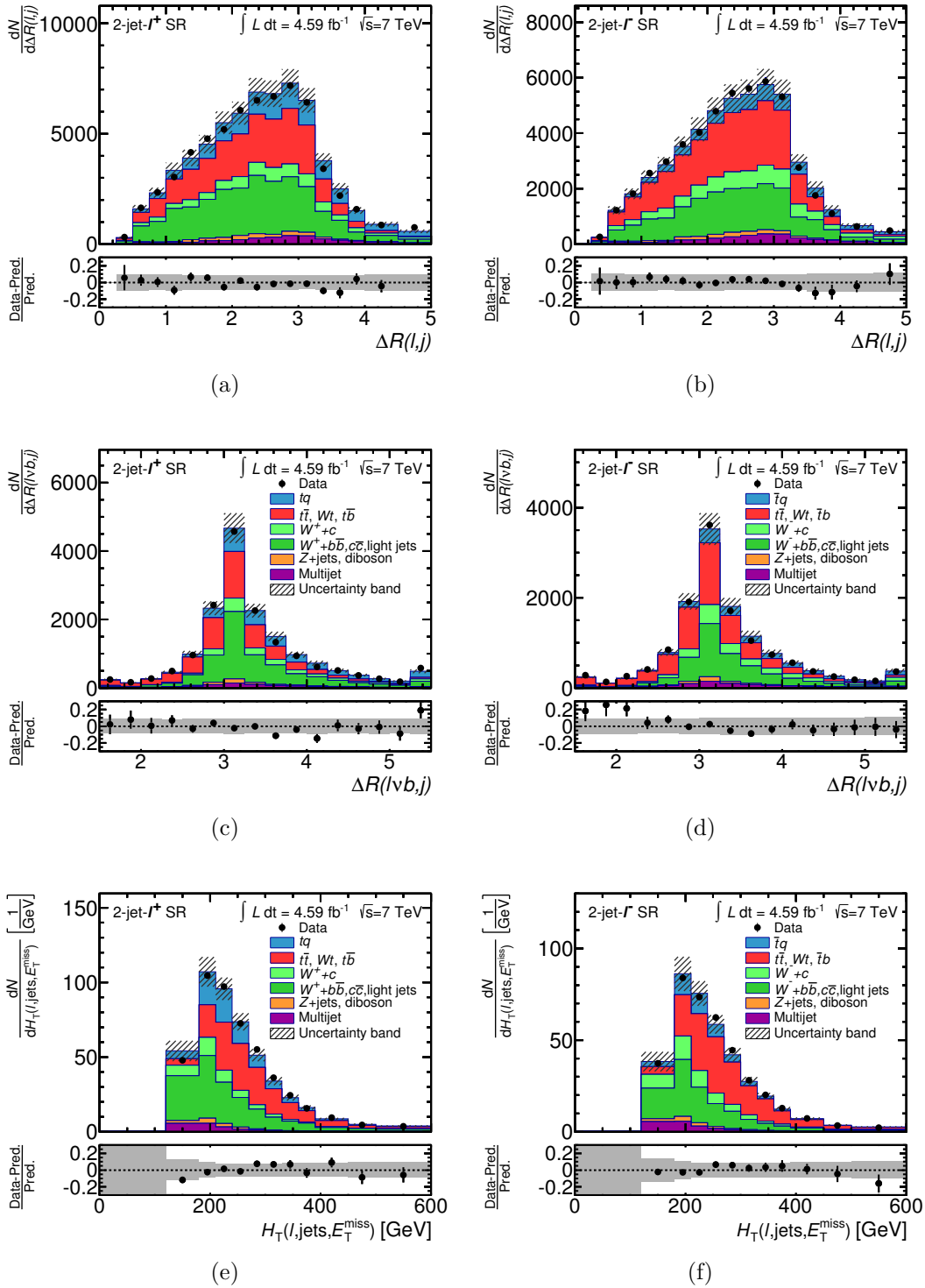


**Figure 5.5:** Distributions of three discriminating variables in the 2-jet- $\ell^+$  and 2-jet- $\ell^-$  channels in the SR normalized to the result of the binned ML fit. Panels (a) and (b) display the  $\Delta R$  of the lepton and the untagged jet  $\Delta R(\ell, j)$ . Panels (c) and (d) show the  $\Delta R$  of the reconstructed top quark and the untagged jet  $\Delta R(\ell vb, j)$  and (e) and (f)  $H_T$ . The last histogram bin includes overflows. The uncertainty band represents the normalization uncertainty of all processes after the fit and the Monte Carlo statistical uncertainty, added in quadrature. The relative difference between the observed and expected number of events in each bin is shown in the lower panels.

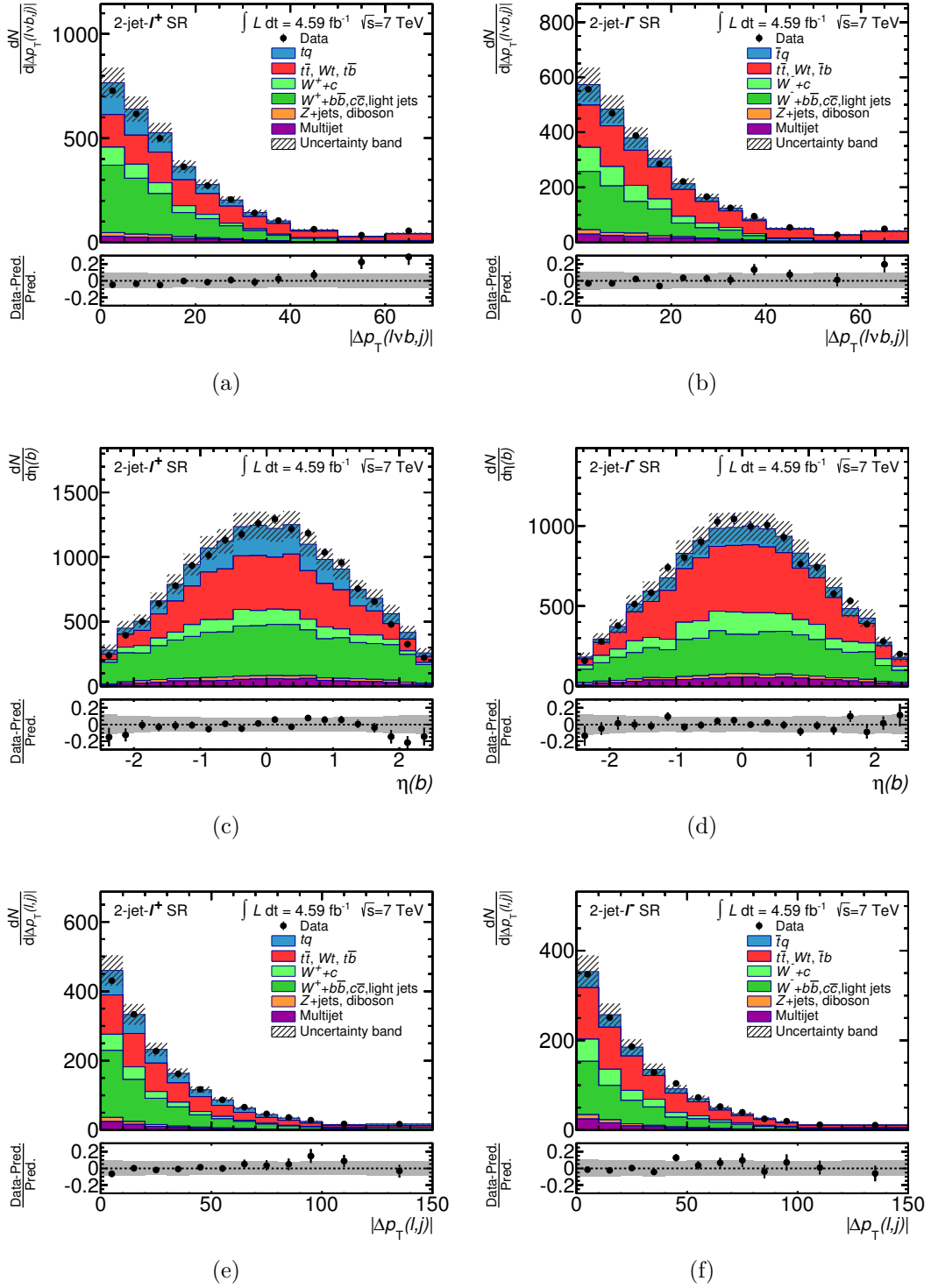


**Figure 5.6:** Distributions of three discriminating variables in the 2-jet- $\ell^+$  and 2-jet- $\ell^-$  channels in the SR normalized to the result of the binned ML fit. Panels (a) and (b) display the difference in  $p_T$  of the reconstructed top quark and the untagged jet  $\Delta p_T(\ell v b, j)$ . Panels (c) and (d) show the pseudorapidity of the  $b$ -tagged jet  $\eta(b)$  and (e) and (f) the absolute value of the difference in  $p_T$  of the lepton and the untagged jet  $|\Delta p_T(\ell, j)|$ . The last histogram bin includes overflows. The uncertainty band represents the normalization uncertainty of all processes after the fit and the Monte Carlo statistical uncertainty, added in quadrature. The relative difference between the observed and expected number of events in each bin is shown in the lower panels.

**Table 5.4:** Estimators of the parameters of the likelihood function for different fit scenarios studied in the fit for  $\beta_{tq+\bar{t}q}^s$ . The quoted uncertainties on  $\hat{\beta}$  and  $\hat{\delta}^{b\text{-tag}}$  include the statistical uncertainty of the fit.

Process	$\hat{\beta}$			
	default	no fit of $\delta^{b\text{-tag}}$	2-jet- $\ell$ +3-jet-2-tag	2-jet- $\ell$ +3-jet- $\ell$
$tq+\bar{t}q$	$1.05 \pm 0.03$	$1.04 \pm 0.03$	$1.06 \pm 0.04$	$1.04 \pm 0.03$
$t\bar{t}, Wt, t\bar{b}, \bar{t}b$	$0.96 \pm 0.01$	$0.95 \pm 0.01$	$1.07 \pm 0.06$	$0.96 \pm 0.02$
$W+\text{light}, c\bar{c}, b\bar{b}$	$1.08 \pm 0.03$	$1.08 \pm 0.03$	$1.01 \pm 0.04$	$1.06 \pm 0.04$
$Z+\text{jets}, \text{diboson}$	$1.07 \pm 0.15$	$1.07 \pm 0.15$	$1.04 \pm 0.15$	$1.06 \pm 0.15$
$\hat{\delta}^{b\text{-tag}}$	$-0.11 \pm 0.11$	–	$-0.60 \pm 0.27$	$0.08 \pm 0.43$

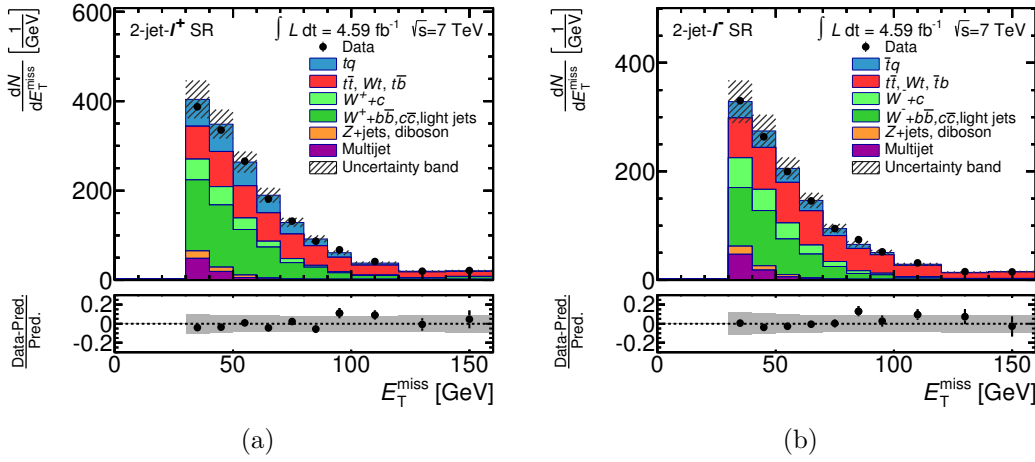


**Figure 5.7:** Distributions of the missing transverse momentum  $E_T^{\text{miss}}$  in the 2-jet- $\ell^+$  and 2-jet- $\ell^-$  channels in the SR normalized to the result of the binned ML fit. The last histogram bin includes overflows. The uncertainty band represents the normalization uncertainty of all processes after the fit and the Monte Carlo statistical uncertainty, added in quadrature. The relative difference between the observed and expected number of events in each bin is shown in the lower panels.

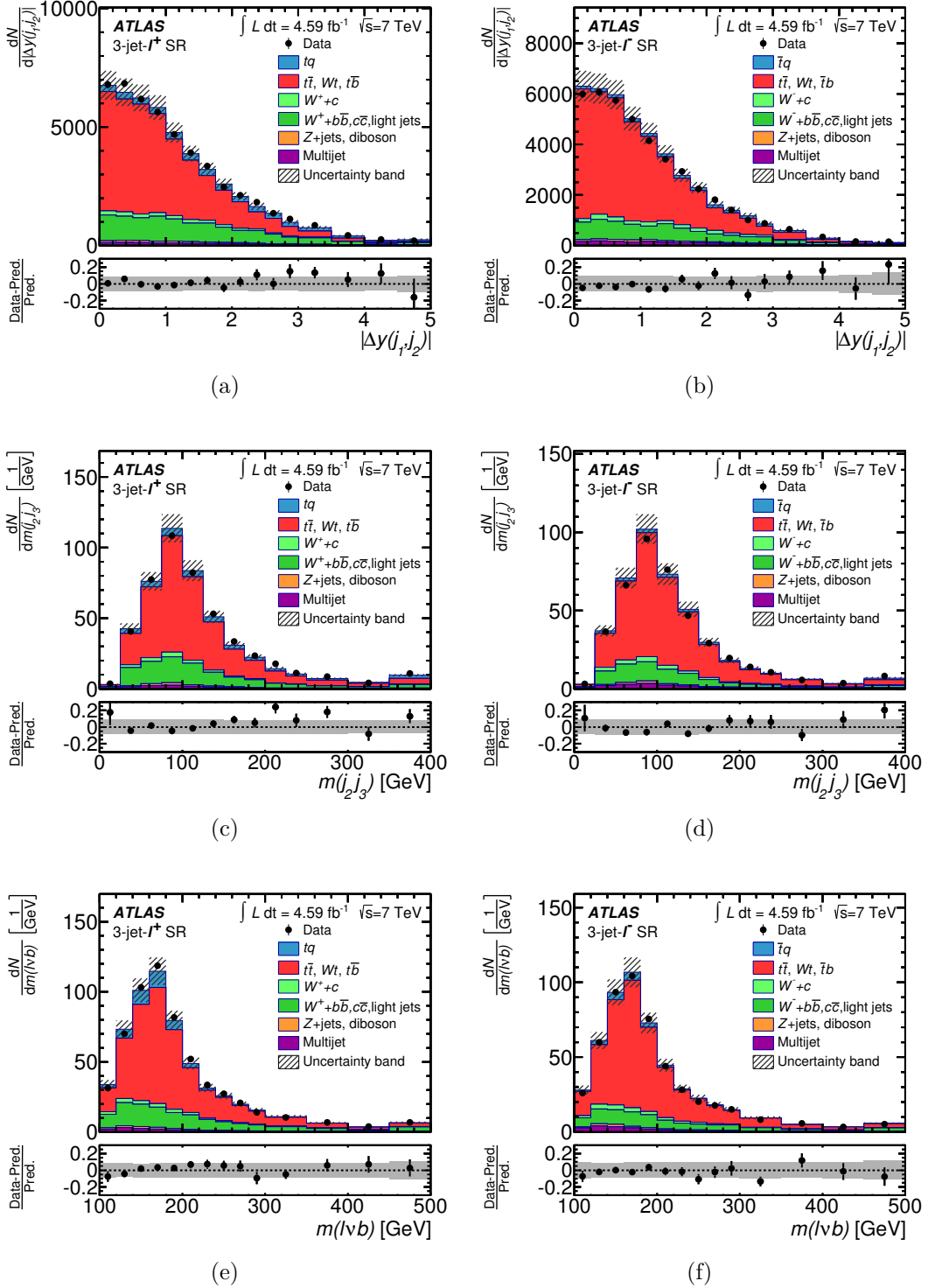


**Figure 5.8:** Distributions of the three most important discriminating variables in the 3-jet- $\ell^+$  and 3-jet- $\ell^-$  channels in the SR normalized to the result of the binned ML fit [174]. Panels (a) and (b) display the absolute value of the rapidity difference of the leading and second leading jet  $|\Delta y(j_1, j_2)|$ . Panels (c) and (d) show the invariant mass of the second leading jet and the third jet  $m(j_2, j_3)$  and (e) and (f) the invariant mass of the reconstructed top quark  $m(\ell vb)$ . The last histogram bin includes overflows. The uncertainty band represents the normalization uncertainty of all processes after the fit and the Monte Carlo statistical uncertainty, added in quadrature. The relative difference between the observed and expected number of events in each bin is shown in the lower panels.

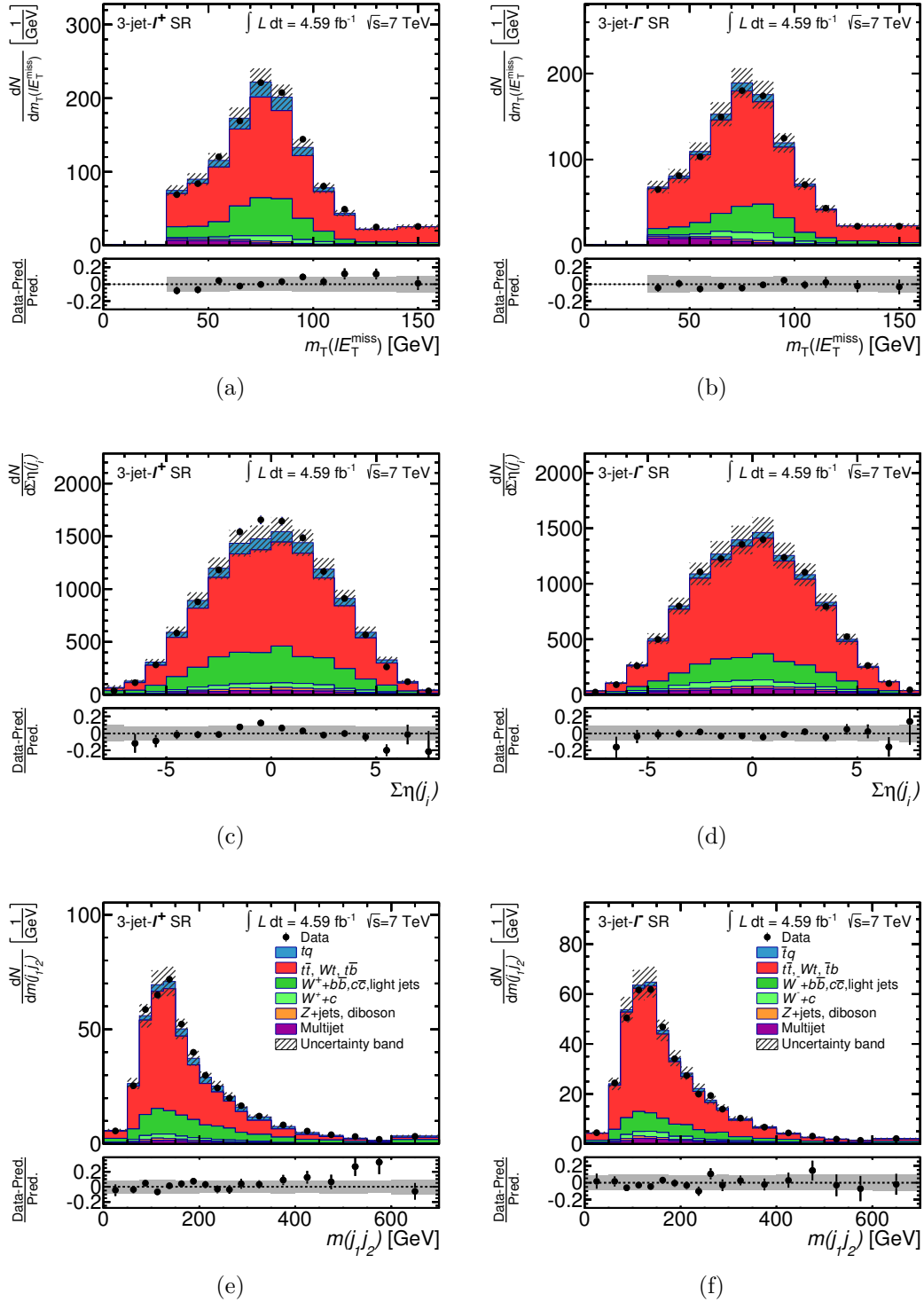


**Figure 5.9:** Distributions of three discriminating variables in the 3-jet- $\ell^+$  and 3-jet- $\ell^-$  channels in the SR normalized to the result of the binned ML fit. Panels (a) and (b) display the transverse mass of the  $\ell$ - $E_T^{\text{miss}}$  system  $m_T(\ell E_T^{\text{miss}})$ . Panels (c) and (d) show the sum of pseudorapidity of the all jets in the event  $\Sigma\eta(j_i)$  and (e) and (f) the invariant mass of the two leading jets  $m(j_1j_2)$ . The last histogram bin includes overflows. The uncertainty band represents the normalization uncertainty of all processes after the fit and the Monte Carlo statistical uncertainty, added in quadrature. The relative difference between the observed and expected number of events in each bin is shown in the lower panels.

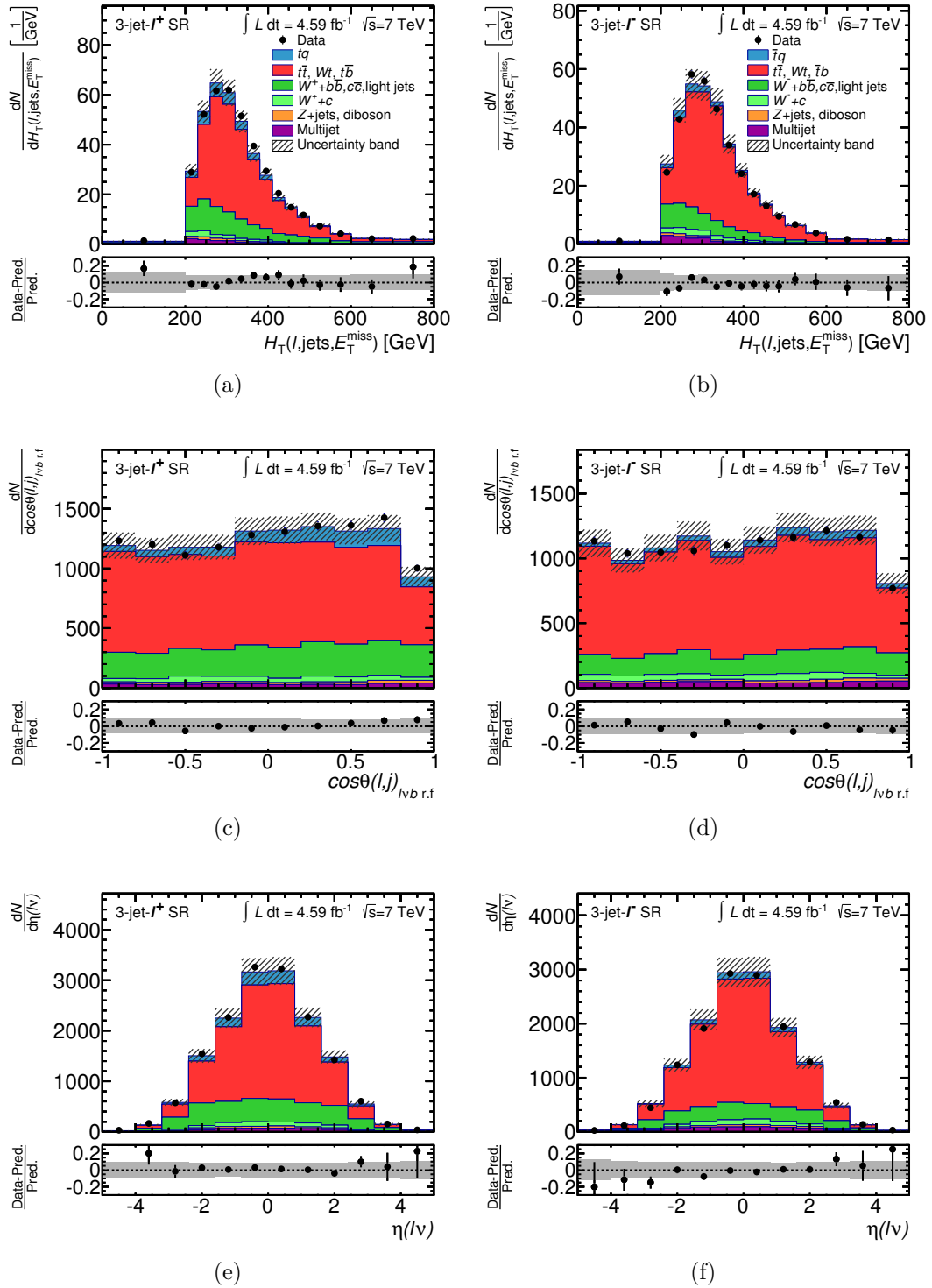


**Figure 5.10:** Distributions of three discriminating variables in the 3-jet- $\ell^+$  and 3-jet- $\ell^-$  channels in the SR normalized to the result of the binned ML fit. Panels (a) and (b) display  $H_T$ . Panels (c) and (d) show the cosine of the angle  $\theta$  between the charged lepton and the leading untagged jet in the rest frame of the reconstructed top quark  $\cos\theta(l, j)_{lvb, r.f.}$  and (e) and (f) the pseudorapidity of the reconstructed  $W$  boson  $\eta(l\nu)$ . The last histogram bin includes overflows. The uncertainty band represents the normalization uncertainty of all processes after the fit and the Monte Carlo statistical uncertainty, added in quadrature. The relative difference between the observed and expected number of events in each bin is shown in the lower panels.

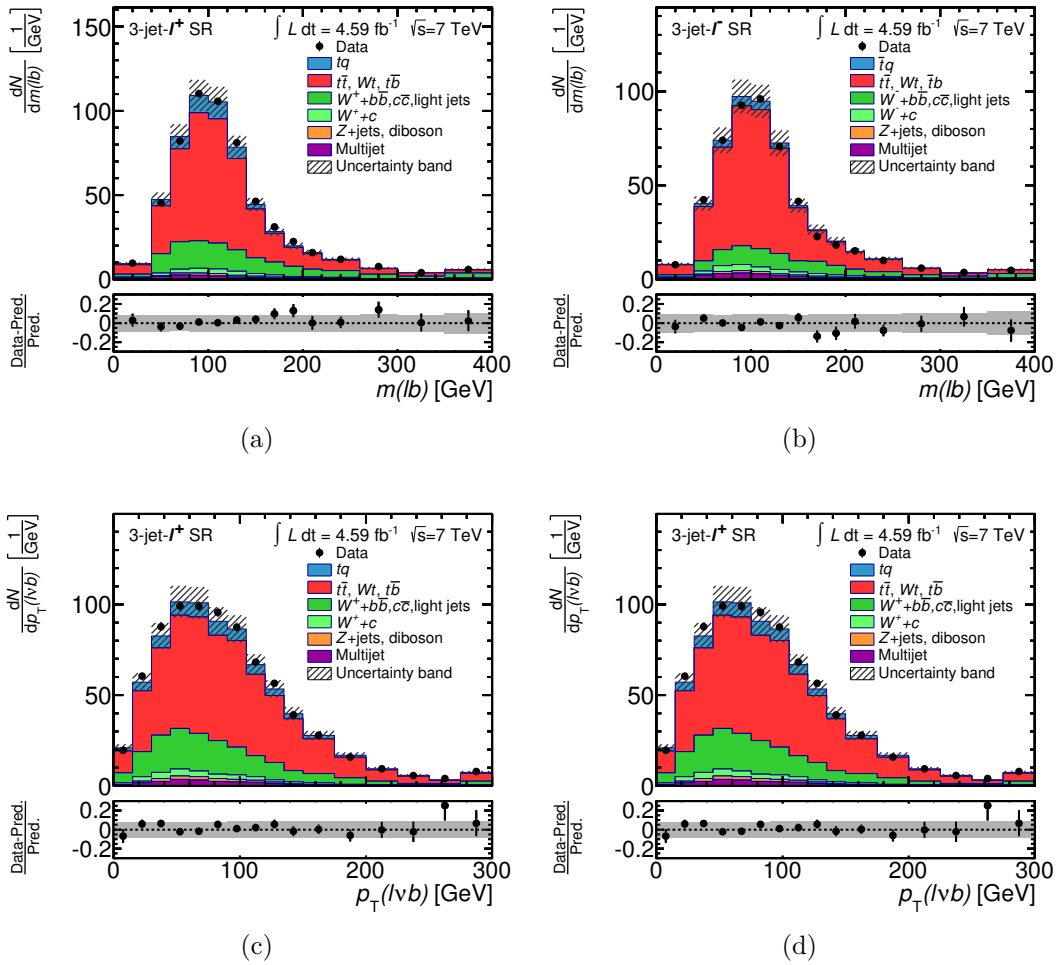


**Figure 5.11:** Distributions of two discriminating variables in the 3-jet- $\ell^+$  and 3-jet- $\ell^-$  channels in the SR normalized to the result of the binned ML fit. Panels (a) and (b) display the invariant mass of the lepton and the b-tagged jet  $m(\ell b)$ , (c) and (d) the  $p_T$  of the reconstructed top quark  $p_T(\ell vb)$ . The last histogram bin includes overflows. The uncertainty band represents the normalization uncertainty of all processes after the fit and the Monte Carlo statistical uncertainty, added in quadrature. The relative difference between the observed and expected number of events in each bin is shown in the lower panels.

## 5.3 Systematic uncertainties

In this section the different sources of systematic uncertainties affecting the measurements of the  $t$ -channel single top-quark production are introduced. These uncertainties have an impact on both normalization and shape of distributions for signal and background processes. Subsequently, the effect of each uncertainty on the measurement results is determined.

### 5.3.1 Sources of systematic uncertainties

Systematic uncertainties are assigned to account for detector calibration and resolution as well as the uncertainties of the theoretical predictions. In the following, the systematic uncertainties are split into the following categories: physics object modeling, MC generators, PDFs, theoretical cross-section normalization, and luminosity.

#### Physics object modeling: jet energy scale

In the presented analysis the main source of uncertainty comes from the jet energy scale (JES). The JES uncertainty was evaluated for the in-situ jet calibration [154], that is extracted by  $p_T$ -balance measurements in data, as described in Section 3.2.5. The uncertainties on the in-situ calibrations using  $Z$ +jet,  $\gamma$ +jet, and dijet data are estimated in several different categories:

- $\eta$ -intercalibration modeling: The uncertainty in the dijet  $p_T$ -balance technique due to the modeling of additional parton radiation is estimated by comparing dijet events simulated with PYTHIA and HERWIG++. It is shown in Ref. [154], that the modeling uncertainty dominates the uncertainty of the  $\eta$  intercalibration and that it increases with the absolute value of  $\eta_{\text{jet}}$ . Therefore, the  $\eta$ -intercalibration modeling-term gives the largest contributions to the JES uncertainty in this analysis because the variable  $|\eta(j)|$  is important for the signal extraction of  $t$ -channel single top-quark production.
- Detector: The different  $p_T$ -balance measurements have uncertainties due to the jet resolution, the electron and photon energy scale and the photon purity.
- Physics modeling: The uncertainties in the in-situ calibration techniques due to the choice of the MC generator, radiation modeling, and the extrapolation of  $\Delta\phi$  between the jet and the  $Z$  boson.
- Statistics: The uncertainty due to the limited size of the datasets of the in-situ measurements.
- Mixed detector and modeling: In this category the uncertainty due to the modeling of the underlying event and soft radiation as well as modeling of the jet fragmentation are considered.

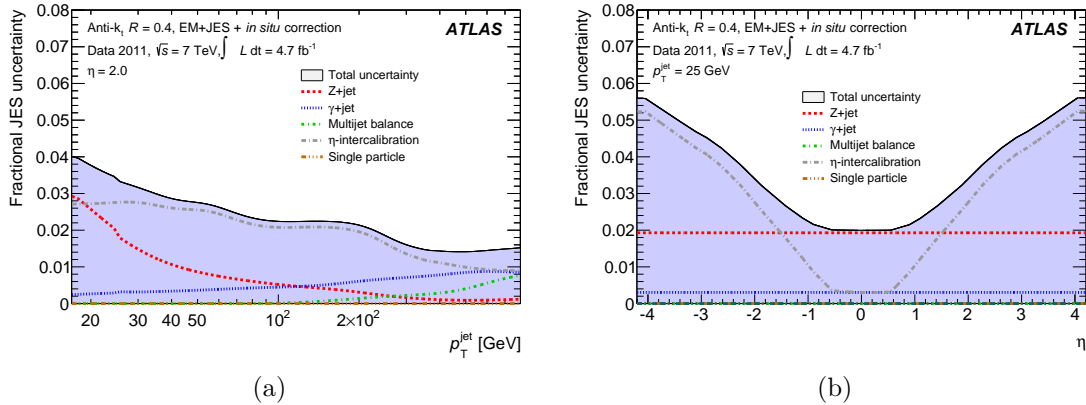


**Figure 5.12:** The fractional in-situ JES systematic uncertainty is shown as a function of jet  $p_T$  for jets with  $\eta = 2.0$  in Panel (a) and as a function of the jet  $\eta$  for jets with  $p_T = 25$  GeV in Panel (b) [154]. The contributions from each in-situ calibration are shown separately. The single particle and the multijet balance contributions are not described in this section because their effect on the presented analysis is negligible.

In Fig. 5.12(a) and 5.12(b) the fractional uncertainty of the different in-situ calibration methods to the total JES is shown separately for each method together with the total relative in-situ uncertainty as a function of the jet  $p_T$  and  $\eta$ . The largest contributions originate from the  $\eta$  intercalibration and the  $Z$ +jet calibration.

Apart from the uncertainties on the in-situ measurements, other sources of systematic uncertainties affect the JES. An uncertainty is assigned to the pile-up correction of the JES derived from simulated events. The jet response is further influenced by the presence of close-by jets, by the flavor composition of the jets, and by the different flavor content of the jets. Therefore, the following categories are added to the systematic uncertainty:

- Pile-up: Uncertainties due to the modeling of the pile-up events in data are included as a function of jet  $p_T$  and  $\eta$ .
- Close-by jets: The jet calibration can be affected by the presence of close-by jets, located at radii  $\Delta R < 1.0$ .
- Flavor composition: This uncertainty covers effects due to the difference in quark-gluon composition between the jets used in the calibration and the jets used in this analysis. Since the response to quark and gluon jets is different, the uncertainty in the quark-gluon fraction in a given data sample leads to an uncertainty in the jet calibration.
- Flavor response: In this category an uncertainty is considered due to imperfect knowledge of the calorimeter response to light-quark jets and gluon jets.
- $b$ -JES: An additional JES uncertainty is evaluated for  $b$ -quark jets by varying the modeling of  $b$ -quark fragmentation.

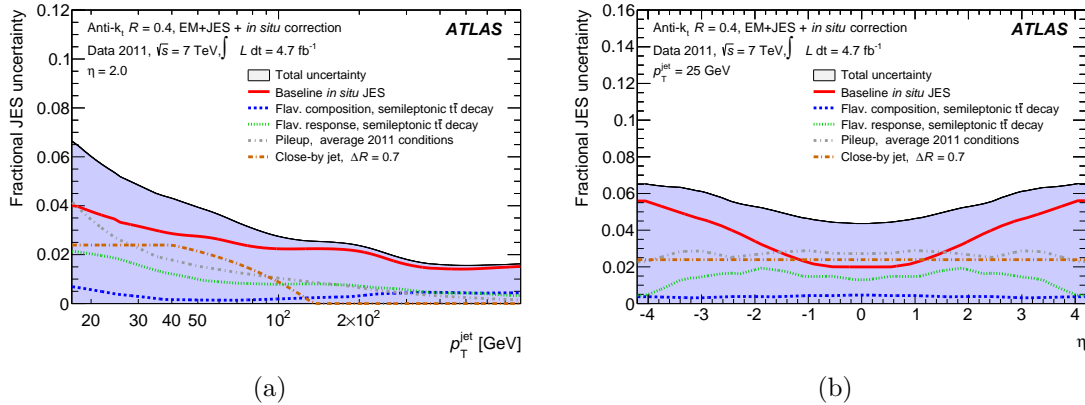


**Figure 5.13:** The fractional JES systematic uncertainty is shown as a function of jet  $p_T$  for jets with  $\eta = 2.0$  in Panel (a) and as a function of the jet  $\eta$  for jets with  $p_T = 25$  GeV in Panel (b) [154]. The uncertainty shown applies to jets originating from semileptonic  $t\bar{t}$ -decays with average 2011 pile-up conditions, and does not include the uncertainty on the JES of  $b$ -jets.

The total JES uncertainty is shown in Fig. 5.13(a) and 5.13(b) as a function of the jet  $p_T$  and  $\eta$  for simulated events of semileptonic  $t\bar{t}$ -decays including contributions from pile-up, flavor composition, flavor response, and close-by jets.

### Further contributions to physics object modeling

Additionally to the JES, systematic uncertainties in the reconstruction of jets, electrons and muons are propagated through the entire analysis. All contributions are described in the following:

The jet-energy resolution is measured via two different methods: the dijet  $p_T$ -balance method and the bisector method [180]. The jet-energy resolution measured in data events is described by simulated events within 10% for jets with  $30 \text{ GeV} < p_T < 500 \text{ GeV}$ . Thus, the uncertainty due to the jet-energy resolution is estimated by varying the  $p_T$  of the jets according to the systematic uncertainties in the resolution measurement depending on the  $p_T$  and  $\eta$  of the jet.

To reject jets, that originate from pile-up events, a cut on the jet-vertex fraction  $\epsilon_{\text{jvf}}$  is applied to all jets with  $|\eta| < 2.5$ . The efficiency of the  $\epsilon_{\text{jvf}}$  cut is measured in  $Z \rightarrow \mu\mu + \text{jets}$  data. Here, the leading jet is mostly back-to-back with the  $Z$  boson. Then, the measurement is used to calibrate the efficiencies in simulated events. The uncertainty in the calibration of  $\epsilon_{\text{jvf}}$  is propagated to the analysis.

Other sources of systematic uncertainties are the tagging efficiencies of  $b$ -quark jets,  $c$ -quark jets, and light-quark jets, that are derived from data [160, 181, 182] and parameterized as a function of  $p_T$  and  $\eta$  of the jet. The largest impact on the measurements arises from the calibration of  $b$ -quark jets, that is introduced in Section 3.2.5. The corresponding efficiencies in simulated events are corrected to be the same as those observed in data, and the uncertainties in the calibration method between 5% and 27% are propagated to the analysis. To reduce the influence of the

uncertainty from the  $b$ -tagging efficiency correction factor, the correction factor is measured from data together with the  $t$ -channel single top-quark production cross-sections. More details of this measurement are given in the next section.

Furthermore, it is investigated, if the  $b$ -tagging efficiency differs between jets initiated by  $b$ -quarks and  $b$ -antiquarks. Differences in acceptance might occur due to the different matter-antimatter composition in the particle shower of the jets, causing a difference in the interaction with the detector. The acceptance was evaluated using simulated signal events and a difference of about 1% was found. This difference is assigned as an acceptance uncertainty.

The impact of the lepton-energy scale uncertainty in the signal region is evaluated by scaling the  $p_T$  of the lepton in the one standard-deviation uncertainty band before any selection criteria are applied [148, 183]. To study the uncertainty due to the lepton-energy resolution, the lepton energy is smeared per event with a random number drawn from a Gaussian with a width of one standard deviation [148, 183]. The uncertainties due to lepton reconstruction, identification and trigger efficiencies are extracted from the calibration with the tag-and-probe method in  $Z \rightarrow \ell\ell$  events. The calibration is modified according to its uncertainty of one standard deviation [114, 183]. This modification is propagated to the analysis. Additionally, the lepton charge mis-identification was evaluated on simulated events to be of the order of 0.1% [114]. All lepton uncertainties are summarized in the following under “lepton uncertainties”.

Further uncertainties arise from the reconstruction of the  $E_T^{\text{miss}}$  and the impact of pile-up collisions on the calculation of  $E_T^{\text{miss}}$ . Both contributions to the uncertainty on the  $E_T^{\text{miss}}$  measurement are summarized under “ $E_T^{\text{miss}}$  modeling” in the following.

### Monte Carlo generators

Uncertainties arise from the choice of the MC generator and of the parton shower model, and from modeling of additional radiated jets for each process, and are evaluated utilizing MC simulated samples. In the presented analysis these uncertainties are taken into account for the modeling of the  $t$ -channel single top-quark signal and the  $t\bar{t}$  background processes.

The uncertainty in the choice of the  $t$ -channel single top-quark signal generator and the parton shower model is estimated comparing events generated with POWHEG-BOX interfaced to PYTHIA and events generated with aMC@NLO and showered with HERWIG and JIMMY. The full difference of the predictions is taken as uncertainty. Details of the differences between both signal models can be found in Section 4.1.1. The uncertainty in the modeling of initial-state and final-state radiation is evaluated by changing the scales,  $\mu_R$  and  $\mu_F$ , in the generation done with POWHEG-BOX. Here, factorization and renormalization scales are varied simultaneously by a factor of 0.5 and 2.0. The scale of the parton shower which determines the level of radiation is varied consistently with the renormalization scale.

The modeling uncertainty for the  $t\bar{t}$ -background process is evaluated by comparing events simulated with POWHEG-BOX interfaced to PYTHIA and ALPGEN interfaced to HERWIG. An additional uncertainty for the  $t\bar{t}$  process comes from

the amount of jet radiation. This is estimated by using dedicated ACERMC samples interfaced to PYTHIA where parameters controlling initial-state and final-state radiation (ISR/FSR) emission are varied. The variations of the parameters are constrained by a measurement of  $t\bar{t}$  production with a veto on additional central jet activity [184].

In case of the  $W$ +jets background, it is evaluated how the matching of jets from the ME calculation and the parton-shower evolution influences the kinematic shape of the NN discriminant. For this purpose, the chosen matching scale and the chosen functional form of the factorization scale are varied in ALPGEN. The matching scale is changed from 15 GeV to 10 GeV, and the factorization scale is determined by  $Q^2 = m_W^2 + p_T^2(W)$  instead of  $Q^2 = m_W^2 + \sum_{\text{jets}} p_T^2$  where  $m_W$  is the mass of the  $W$  boson and  $\sum_{\text{jets}} p_T^2$  is the sum over the  $p_T^2$  of all final-state jets in the event [185]. A template-shape uncertainty is assigned to the  $W$ +jets background by comparing each varied template shape of the NN discriminant with the nominal ALPGEN prediction.

### Parton distribution functions

The systematic uncertainties on the acceptance related to the PDFs are taken into account following the instructions given in Ref. [51]. First, the uncertainty of each PDF set is calculated following the recommendation of the respective PDF group. The final PDF uncertainty is then estimated by the envelope of the estimated uncertainties for the CT10 PDF set, the MSTW2008nlo PDF set and the NNPDF2.3 PDF set. Figure 5.14 shows the acceptances for all eigenvectors of all three PDF sets for the  $tq$  and the  $\bar{t}q$  process. The envelope of all acceptances and their uncertainties corresponds to the acceptance uncertainty applied to the analysis. The PDF acceptance uncertainty is evaluated with ACERMC+PYTHIA samples for the single top-quark processes and with a  $t\bar{t}$  sample generated with MC@NLO [186] interfaced to HERWIG and JIMMY.

### Theoretical cross-section normalization

In Table 5.5 the relative uncertainties of the theoretical cross-sections are quoted for each background process. Since the  $t\bar{t}$ , and  $Wt$  and  $s$ -channel single top-quark processes are grouped together in the statistical analysis, their uncertainties are added in proportion to their relative fractions, leading to a combined uncertainty of 6.7%. The uncertainty on the prediction of the combined  $Z$ +jets and diboson background is 60% including a conservative estimate of the uncertainty of the heavy-flavor fraction of 50%.

The normalization uncertainties of the  $W$ +jets backgrounds are 24% for  $W+c$  and 36% for the combined  $W+b\bar{b}$ ,  $c\bar{c}$  and light jets including the heavy-flavor-fraction uncertainty of 50% on the  $b\bar{b}$  and  $c\bar{c}$  contributions. Additionally, an uncertainty on the relative fraction of 2-jet to 3-jet events of 5% for events with light-flavor jets and 7% for events with heavy-flavor jets is applied for the  $W$ +jets estimation. This uncertainty was estimated by varying the following input parameters of the generation with ALPGEN independently by a factor of two: the hard scattering

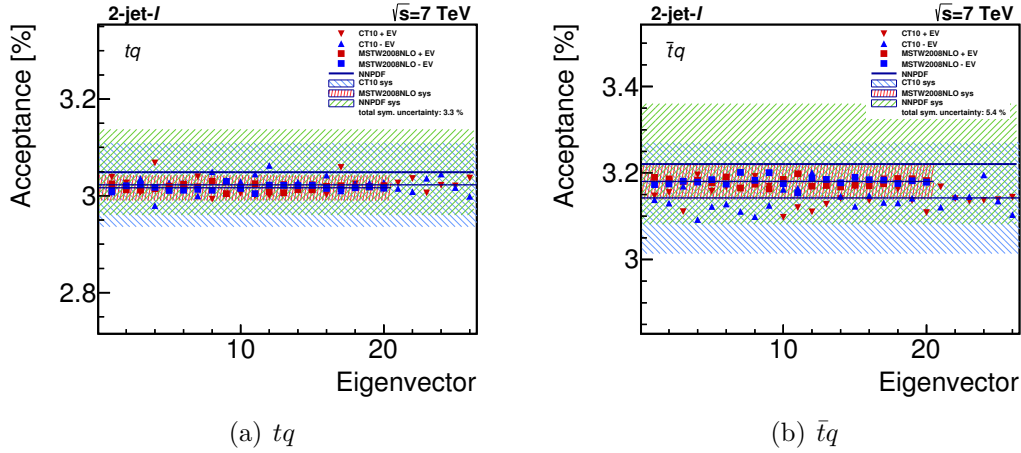


**Figure 5.14:** Acceptances for all systematic variations (eigenvectors) of all three PDF sets together with their envelope, which determines the final PDF uncertainty for (a)  $tq$  production and (b)  $\bar{t}q$  production in the 2-jet- $l$  channels.

**Table 5.5:** Relative uncertainties  $\frac{\Delta\sigma}{\sigma}$  on the theoretical cross-sections for the background processes.

Process	$\frac{\Delta\sigma}{\sigma}$
$t\bar{t}$	6%
$Wt$	7%
$t\bar{b}, \bar{t}b$	4.4%
$W$ +light jets	6.5%
$W+b\bar{b}, c\bar{c}$ jets	50%
$W+c$	24%
$Z$ +jets	60%
Diboson	5%

scale, the coupling of the hard interaction, and the minimum  $p_T$  and  $\Delta R$  of the final-state partons.

### Multijet background

A normalization uncertainty of 50% is assigned to the estimation of the multijet background. The studies leading to this number are introduced in Section 4.2.2. An additional uncorrelated normalization uncertainty is assigned for the multijet estimations for the different lepton charges. It is assumed, that the multijet background is lepton-charge symmetric. Therefore, the estimation should give the same result for the  $\ell^+$  and  $\ell^-$  channels. The difference between the estimation in each lepton-charge channels to the half of the estimation in the respective combined channel is taken as an additional acceptance uncertainty. This corresponds to an uncertainty of 1.5% in the 2-jet channels and of 15% in the 3-jet channels.

To assign an uncertainty on the template shape of the multijet background, the matrix method and the jet-lepton method are compared in the electron and in the muon channel. An additional shape uncertainty is assigned to the electron channel due to the different treatment of forward and central electrons. A template shift is generated by varying the acceptance for forward and central electrons by 50% with respect to each other.

### Luminosity

The luminosity measurement is calibrated using dedicated beam-separation scans, referred to as van der Meer scans, where the absolute luminosity can be inferred from the measurement of the beam parameters [110]. The resulting uncertainty is 1.8%.

### Summary

The sources of systematic uncertainties discussed above cause variations on the signal and background acceptances and on the shape of the NN discriminants. In Table 5.6 the relative acceptance uncertainties are exemplarily given for the 2-jet- $\ell$  channel. The tables of the acceptance uncertainties in all other analysis channels can be found in Appendix A.1.

Figures 5.15 and 5.16 exemplarily show the template-shape variation of the NN discriminant for the signal and background processes due to the JES  $\eta$ -intercalibration variation in the 2-jet- $\ell$  and the 3-jet- $\ell$  channel, respectively. Similar shape variations are produced for all other sources of systematic uncertainties, unless they are explicitly described as an acceptance uncertainty in Section 5.3.1. Each systematic shape variation is compared to the statistical uncertainty of the MC simulated sample in each bin, visualized by the error band in Fig. 5.15 and 5.16. Only those shape variations are included in the pseudo experiments, that are of equal or larger size than the variation due to the limited MC statistics. Studies show, that the total uncertainty does not decrease by dropping very small shape uncertainties, but noise originating from statistical fluctuations in the systematic variations is suppressed. This noise results into an artificial asymmetry of the total uncertainty on the measurement. In addition, the computation time of the pseudo experiments is significantly decreased.

### 5.3.2 Evaluation of the uncertainties

In the following, the evaluation of the impact of the different systematic uncertainties on the results is described. The number of predicted events  $\tilde{\nu}$  and the template fractions  $\alpha$  are fluctuated according to all acceptance and template-shape uncertainties simultaneously in the pseudo experiments. Thus, pseudo data is generated. In each pseudo dataset the fit for  $\beta^s$  is performed and the estimator  $\hat{\beta}^s$  is extracted. This way, 100,000 pseudo experiments are conducted. As illustrated in Fig. 5.1, the RMS of the estimator distribution is used to determine the total uncertainty of the measurement.

**Table 5.6:** List of relative acceptance uncertainties for each process given in percent in the 2-jet- $\ell$  channel.

Source	$tq + \bar{t}q$ [%]	$t\bar{t}, Wt, t\bar{b}$ [%]	$W+c$ [%]	$W+b\bar{b},c\bar{c},$ light jets [%]	$Z$ +jets, diboson [%]
JES statistical	+0.3 -0.1	-1.2 +1.4	+2.5 -1.2	+1.0 -1.4	+0.3 -1.6
JES detector	+0.4 -0.1	-0.9 +1.1	+1.9 -1.1	+1.1 -1.3	-0.1 -1.2
JES mixed det. and mod.	+0.2 +0.2	-0.3 +0.3	+1.2 -0.4	+0.2 -0.5	-0.4 -0.2
JES $\eta$ intercalibration	+1.0 -1.0	-2.2 +2.9	+3.7 -2.3	+2.2 -3.0	+3.2 -3.1
JES physics modeling	+0.1 -0.0	-2.0 +2.1	+3.0 -2.2	+1.7 -2.0	+1.8 -2.3
JES close-by jets	+0.0 +0.2	-1.5 +1.8	+2.0 -1.2	-0.5 -0.6	+0.1 +0.2
JES flavor composition	+0.1 +0.3	-0.7 +0.8	+7.3 -6.5	+3.2 -3.3	+4.5 -6.0
JES flavor response	+0.1 +0.3	-1.6 +1.7	+4.5 -3.5	+1.7 -1.3	+2.2 -3.2
$b$ -JES	+0.5 -0.2	-0.3 +0.6	+1.0 -0.3	+0.6 -0.8	+0.2 +0.4
JES pile-up	+0.2 +0.2	-0.0 +0.2	+0.5 +0.2	+0.0 -0.1	-0.5 -0.1
Jet energy resolution	-0.5 +0.5	-0.0 +0.0	+1.0 -1.0	+0.5 -0.5	+3.9 -3.9
Lepton efficiencies	+2.6 -2.6	+2.6 -2.6	+2.6 -2.6	+2.6 -2.6	+2.7 -2.6
Lepton reconstruction (MS)	+0.3 +0.2	+0.2 +0.4	+0.9 +0.5	+0.3 -0.3	-0.0 -0.7
Lepton reconstruction (ID)	+0.2 +0.2	+0.5 +0.4	-0.1 +0.2	+0.1 -0.0	+0.1 +0.0
Lepton energy scale	+0.3 +0.1	+0.2 +0.3	+0.7 -0.2	+0.7 -0.4	-0.1 -1.8
$b$ -tagging efficiency	+7.0 -7.1	+5.0 -5.7	+0.1 -0.1	+3.8 -3.9	+2.4 -2.5
$c$ -tagging efficiency	-0.0 +0.0	+0.0 -0.0	+12.7 -12.7	+1.9 -1.9	+3.8 -3.8
Mistag rate	+0.0 -0.0	+0.0 -0.0	+2.2 -2.2	+8.5 -8.5	+8.1 -8.1
$t\bar{t}$ generation	-	-0.3 +0.3	-	-	-
$W$ +jets shape variations	-	-	+0.2 +0.4	+0.4 +0.6	-
$E_T^{\text{miss}}$ cell-out softjet	+0.4 +0.0	+0.4 -0.1	+1.0 -0.3	+0.4 -0.3	+0.7 -0.7
$E_T^{\text{miss}}$ pile-up	+0.3 +0.1	+0.3 -0.0	+1.2 -0.2	-0.1 -0.3	-0.6 -0.2
Jet vertex fraction	+0.4 -0.6	+1.2 -1.1	+0.8 -0.8	+1.2 -1.0	+1.1 -1.0
PDF	+3.3 -3.0	+8.3 -7.7	-	-	-
$tq$ generator+parton shower	+2.2 -2.2	-	-	-	-
$t\bar{t}$ ISR/FSR	-	-3.3 +3.3	-	-	-
$tq$ scale variations	+3.0 -3.0	-	-	-	-

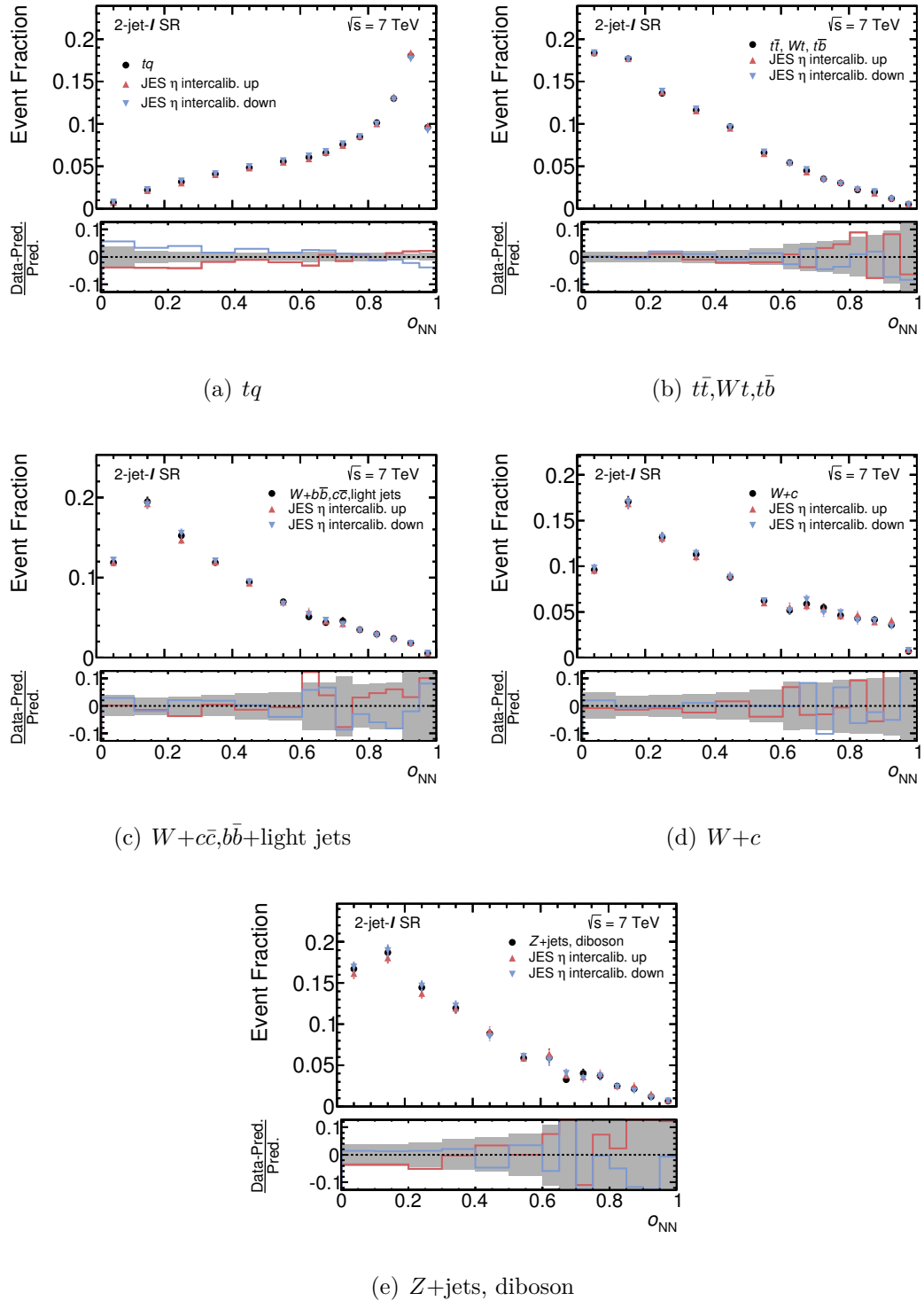


**Figure 5.15:** The normalized template-shape variation of the NN discriminant for the JES variation due to the uncertainty in the  $\eta$ -intercalibration modeling in the 2-jet- $\ell$  channel, shown for all considered processes. The nominal shape is shown by the black points. Red denotes the JES shift-up and blue the NN response for JES shift-down. In the lower panel the relative difference between the event fraction of the systematic variation and the nominal distribution is shown for each bin. The grey uncertainty band in the lower histogram represents the normalization uncertainty due to the Monte Carlo statistical uncertainty.

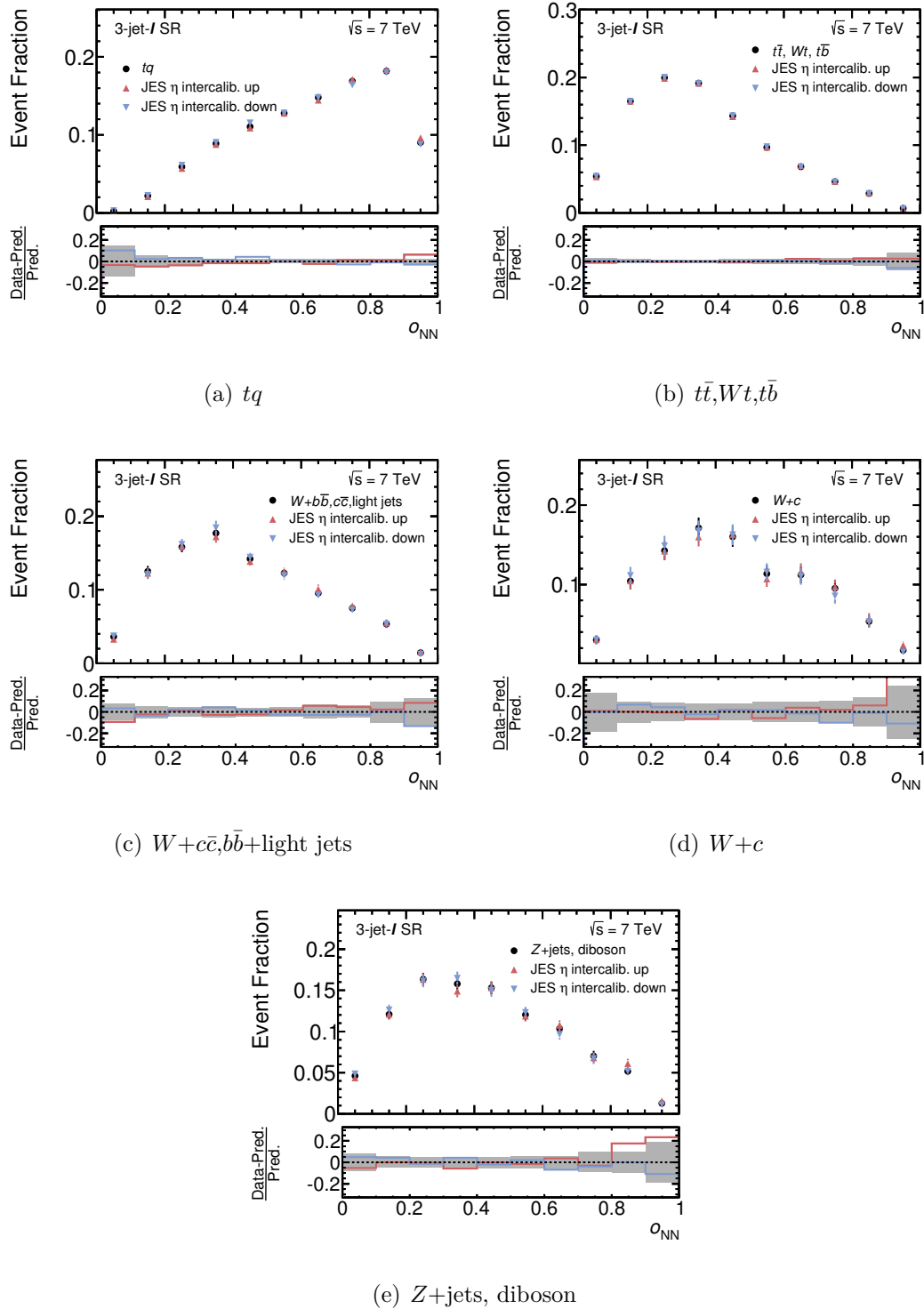


**Figure 5.16:** The normalized template-shape variation of the NN discriminant for the JES variation due to the uncertainty in the  $\eta$ -intercalibration modeling in the 3-jet- $\ell$  channel, shown for all considered processes. The nominal shape is shown by the black points. Red denotes the JES shift-up and blue the NN response for JES shift-down. In the lower panel the relative difference between the event fraction of the systematic variation and the nominal distribution is shown for each bin. The grey uncertainty band in the lower histogram represents the normalization uncertainty due to the Monte Carlo statistical uncertainty.

Table 5.7 summarizes the contributions of the different sources of systematic uncertainties to the total uncertainty on the measurements of  $\sigma(tq)$ ,  $\sigma(\bar{t}q)$ ,  $R_t$ , and  $\sigma(tq + \bar{t}q)$ . Each single contribution is evaluated with a separate set of 100,000 pseudo experiments where only fluctuations originating from the corresponding uncertainty are taken into account. A total precision of 12.4% is achieved for the measurements of  $\sigma(tq)$  and  $\sigma(tq + \bar{t}q)$ . The  $\sigma(\bar{t}q)$  cross section is measured with a precision of 15.9%. The larger uncertainty for  $\sigma(\bar{t}q)$  is mainly caused by the larger statistical uncertainties. Altogether, systematic uncertainties dominate the uncertainty on each measured cross-section. The largest contributions originate from the JES  $\eta$ -intercalibration and the  $b$ -tagging efficiency correction factor. These uncertainties are discussed in more detail in the next sections.

Many systematic uncertainties cancel for the cross-section ratio  $R_t$ . A precision of 8.7% is achieved for  $R_t$  where the contribution from data statistic is equal to the combined contribution of all systematic uncertainties and the limited MC statistics. The largest contributions to the total systematic uncertainty originate from the limited MC statistics and the PDF uncertainty.

### Acceptance and shape uncertainties

It is interesting to study the contributions of the uncertainties originating from acceptance and template-shape variations separately to improve the understanding of the systematic uncertainties. Two sets of pseudo experiments are generated for the measurement of  $\sigma(tq + \bar{t}q)$  where only the number of predicted events or the template shapes are varied.

The results are shown in Table 5.8 for the largest systematic contributions except for the  $b$ -tagging efficiency, that is discussed in the next section: JES  $\eta$  intercalibration, lepton uncertainties,  $E_T^{\text{miss}}$  modeling, PDF uncertainties,  $tq$  scale variations, and  $tq$  generator and parton shower. It can be observed, that the template shape of the NN discriminant is only distorted significantly by the JES  $\eta$  intercalibration and the  $E_T^{\text{miss}}$  modeling. This can be well understood because the absolute value of the pseudorapidity of the light jet is the most important input variable to the 2-jet NN discriminant. The resulting large distortion for the signal template-shape is shown in Fig. 5.15(a) for the JES  $\eta$ -intercalibration uncertainty. PDF uncertainties and lepton uncertainties contribute per definition exclusively to the acceptance uncertainties. In case of the signal modeling the template-shape variation has a small effect on the cross-section measurement. Due to the correlated variation of acceptance and template-shape uncertainty, the combined impact of the signal modeling uncertainties on the measurement is slightly reduced compared to the quadratic sum of the separate acceptance and shape uncertainties.

### Simultaneous measurement of the $b$ -tagging efficiency

The knowledge of the  $b$ -tagging efficiency is one of the most important sources of systematic uncertainty in the measurement of the  $t$ -channel single top-quark process. Its influence on the cross-section measurements is of the order of 10% originating

**Table 5.7:** Detailed list of the contribution of each source of uncertainty to the total uncertainty on the measured values of  $\sigma(tq)$ ,  $\sigma(\bar{t}q)$ ,  $R_t$ , and  $\sigma(tq + \bar{t}q)$ . The evaluation of the systematic uncertainties has a statistical uncertainty of 0.3%. Uncertainties contributing less than 1.0% are marked with " $< 1$ ".

Source	$\frac{\Delta\sigma(tq)}{\sigma(tq)}$ [%]	$\frac{\Delta\sigma(\bar{t}q)}{\sigma(\bar{t}q)}$ [%]	$\frac{\Delta R_t}{R_t}$ [%]	$\frac{\Delta\sigma(tq+\bar{t}q)}{\sigma(tq+\bar{t}q)}$ [%]
Data statistic	$\pm 3.1$	$\pm 5.4$	$\pm 6.2$	$\pm 2.7$
Monte Carlo statistic	$\pm 1.9$	$\pm 3.2$	$\pm 3.6$	$\pm 1.9$
Multijet normalization	$\pm 1.1$	$\pm 2.0$	$\pm 1.6$	$\pm 1.4$
Other background normalization	$\pm 1.1$	$\pm 2.8$	$\pm 1.9$	$\pm 1.6$
JES detector	$\pm 1.6$	$\pm 1.4$	$< 1$	$\pm 1.4$
JES statistical	$< 1$	$< 1$	$< 1$	$< 1$
JES physics modeling	$< 1$	$< 1$	$< 1$	$< 1$
JES $\eta$ intercalibration	$\pm 6.9$	$\pm 8.4$	$\pm 1.8$	$\pm 7.3$
JES mixed detector and modeling	$< 1$	$< 1$	$< 1$	$< 1$
JES close-by jets	$< 1$	$< 1$	$< 1$	$< 1$
JES pile-up	$< 1$	$< 1$	$< 1$	$< 1$
JES flavor composition	$\pm 1.4$	$\pm 1.4$	$\pm 1.2$	$\pm 1.6$
JES flavor response	$< 1$	$< 1$	$\pm 1.0$	$< 1$
$b$ -JES	$< 1$	$< 1$	$< 1$	$< 1$
Jet energy resolution	$\pm 2.1$	$\pm 1.6$	$\pm 1.0$	$\pm 1.9$
Jet vertex fraction	$< 1$	$< 1$	$< 1$	$< 1$
$b$ -tagging efficiency	$\pm 3.8$	$\pm 4.1$	$< 1$	$\pm 3.9$
$c$ -tagging efficiency	$< 1$	$\pm 1.4$	$< 1$	$< 1$
Mistag efficiency	$< 1$	$< 1$	$< 1$	$< 1$
$b/\bar{b}$ acceptance	$\pm 1.0$	$< 1$	$< 1$	--
$E_T^{\text{miss}}$ modeling	$\pm 2.3$	$\pm 3.4$	$\pm 1.6$	$\pm 2.6$
Lepton uncertainties	$\pm 2.8$	$\pm 3.0$	$\pm 1.0$	$\pm 2.8$
PDF	$\pm 3.2$	$\pm 5.8$	$\pm 2.5$	$\pm 3.2$
$W$ +jets shape variation	$< 1$	$< 1$	$< 1$	$< 1$
$tq$ generator + parton shower	$\pm 1.9$	$\pm 1.6$	$< 1$	$\pm 1.9$
$tq$ scale variations	$\pm 2.6$	$\pm 3.0$	$< 1$	$\pm 2.6$
$t\bar{t}$ generator + parton shower	$< 1$	$\pm 2.1$	$\pm 1.6$	$< 1$
$t\bar{t}$ ISR / FSR	$< 1$	$< 1$	$\pm 1.0$	$< 1$
Luminosity	$\pm 1.8$	$\pm 1.8$	$< 1$	$\pm 1.8$
Total systematic	$\pm 12.0$	$\pm 14.9$	$\pm 6.1$	$\pm 12.1$
Total	$\pm 12.4$	$\pm 15.9$	$\pm 8.7$	$\pm 12.4$

from a large acceptance uncertainty on the signal process and the top-quark background processes. This can be seen in the corresponding acceptance uncertainties e.g. 7% on the signal process in the 2-jet- $\ell$  channel (shown in Table 5.6). To improve the knowledge of the  $b$ -tagging efficiency, its correction factor is included in the binned ML fit as a nuisance parameter. The  $b$ -tagging efficiency correction factor is measured to be:

$$\hat{\delta}^{b\text{-tag}} = -0.11 \pm 0.11 \quad (5.4)$$

in the fit for  $\beta_{tq+\bar{t}q}^s$  shown in Table 5.3.

The effect of fitting the  $\delta^{b\text{-tag}}$  parameter simultaneously is illustrated in Fig. 5.17(a). Here, the profile of the signal estimator  $\hat{\beta}_{tq+\bar{t}q}^s$  is shown against the generated  $\delta_{\text{gen.}}^{b\text{-tag}}$  for the pseudo experiments where all uncertainties are fluctuated. It can be observed, that there is a large dependence of the estimator  $\hat{\beta}_{tq+\bar{t}q}^s$  on the parameter  $\delta^{b\text{-tag}}$  when it is not included in the fit, marked in the figure with “No fitting”. This dependence decreases, when  $\delta^{b\text{-tag}}$  is included in the fit.

The consistency of the fit for the parameter  $\delta^{b\text{-tag}}$  is tested by varying the generated parameter  $\delta_{\text{gen.}}^{b\text{-tag}}$  in the pseudo experiments and comparing the estimated correction factor  $\hat{\delta}_{\text{fit}}^{b\text{-tag}}$  in each pseudo experiment with the generated value. This is shown in Fig. 5.17(b). A perfect linear behavior without any bias is found.

The gain for the measurement due to the inclusion of the parameter  $\delta^{b\text{-tag}}$  in the binned ML fit can be quantified with the residuum  $\hat{\delta}_{\text{fit}}^{b\text{-tag}} - \delta_{\text{gen.}}^{b\text{-tag}}$ . The residual distribution of the fit for the different lepton charges is shown in Fig. 5.18(a), and the residual distribution of the fit for the combined lepton charges in Fig. 5.18(b). The root mean square of the residual distribution corresponds to the relative gain on the  $b$ -tagging efficiency uncertainty. Thus, the uncertainty due to the  $b$ -tagging efficiency is reduced to approximately 45% of its original value in the measurements of  $\sigma(tq)$ ,  $\sigma(\bar{t}q)$ , and  $\sigma(tq + \bar{t}q)$ .

**Table 5.8:** Evaluation of acceptance and template shape uncertainties for the sources of uncertainty with the largest contributions to the total uncertainty on the measured value of  $\sigma(tq + \bar{t}q)$ . The evaluation of the systematic uncertainties has a statistical uncertainty of 0.3%.

Source	acceptance only	shape only	$\frac{\Delta\sigma(tq+\bar{t}q)}{\sigma(tq+\bar{t}q)}$ [%]
JES $\eta$ intercalibration	$\pm 1.8$	$\pm 5.6$	$\pm 7.3$
Lepton uncertainties	$\pm 2.8$	$\pm 0.1$	$\pm 2.8$
$E_{\text{T}}^{\text{miss}}$ modeling	$\pm 0.5$	$\pm 2.6$	$\pm 2.6$
PDF	$\pm 3.2$	$\pm 0.2$	$\pm 3.2$
$tq$ scale variations	$\pm 3.1$	$\pm 0.6$	$\pm 2.6$
$tq$ generator + parton shower	$\pm 2.9$	$\pm 0.8$	$\pm 1.9$

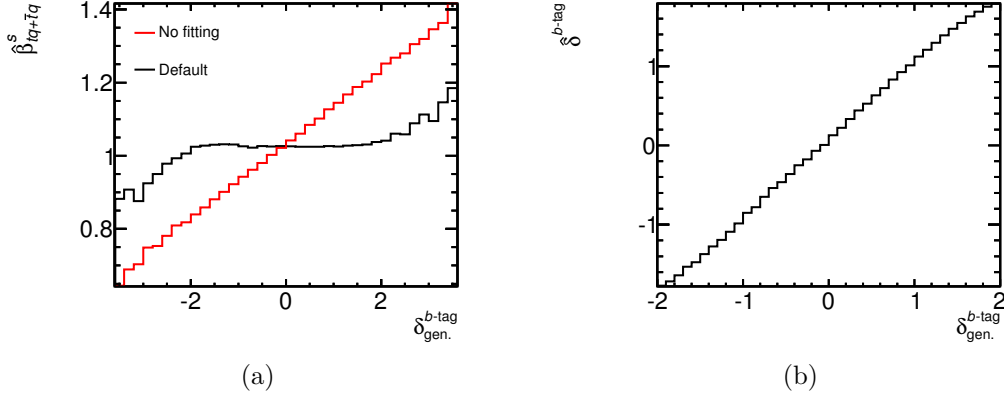


**Figure 5.17:** In Panel (a) the profile of the estimator  $\beta(tq + \bar{t}q)$  against the generated nuisance parameter for the  $b$ -tagging efficiency  $\tilde{\delta}_{\text{gen}}^{b\text{-tag}}$  is shown for the default scenario, where the parameter  $\delta^{b\text{-tag}}$  is included in the binned ML fit (marked with “Default”) and the scenario, where the parameter  $\delta^{b\text{-tag}}$  is not included in the fit (marked with “No profiling”). Panel (b) shows the linearity check for the fit of the parameter  $\delta^{b\text{-tag}}$ .

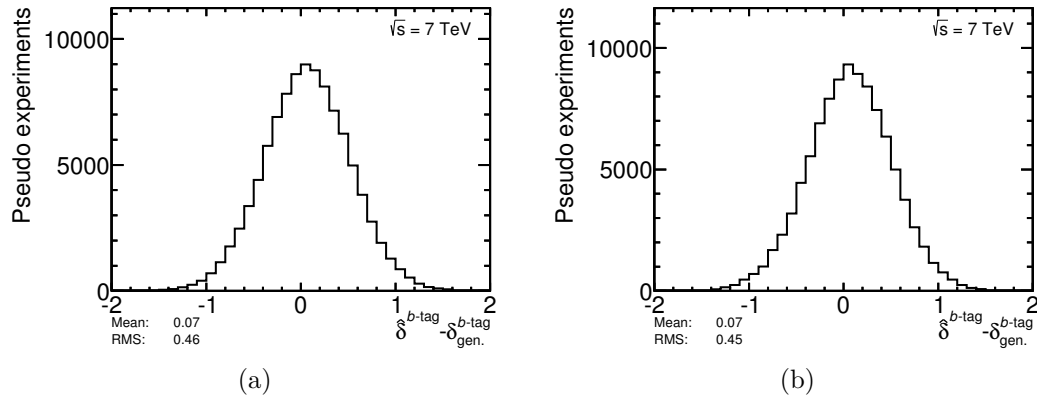


**Figure 5.18:** The residual distribution of the nuisance parameter  $\delta^{b\text{-tag}}$  shown for (a) the fit of the analysis channels 2-jet- $\ell^+$ , 2-jet- $\ell^-$ , 3-jet- $\ell^+$ , 3-jet- $\ell^-$ , and 3-jet-2-tag and for (b) the fit of the analysis channels 2-jet- $\ell$ , 3-jet- $\ell$ , and 3-jet-2-tag.

## 5.4 Results

After performing the binned ML fit and estimating the total uncertainties, the results of the measurements can be extracted and compared to the corresponding theory prediction. Additionally, the CKM matrix element  $|V_{tb}|$  is extracted from the combined inclusive cross section  $\sigma(tq + \bar{t}q)$ .

### 5.4.1 Inclusive cross-section measurements

The results of the binned ML fits in Tables 5.2 and 5.3 and the evaluation of the systematic uncertainties given in Table 5.7 give the following measured values for the inclusive cross sections of  $t$ -channel single top-quark production:

$$\begin{aligned}\sigma(tq) &= 46 \pm 1 \text{ (stat.)} \pm 6 \text{ (syst.) pb} = 46 \pm 6 \text{ pb,} \\ \sigma(\bar{t}q) &= 23 \pm 1 \text{ (stat.)} \pm 3 \text{ (syst.) pb} = 23 \pm 4 \text{ pb} \quad \text{and} \\ \sigma(tq + \bar{t}q) &= 68 \pm 2 \text{ (stat.)} \pm 8 \text{ (syst.) pb} = 68 \pm 8 \text{ pb,}\end{aligned}$$

assuming a top-quark mass of  $m_t = 172.5$  GeV. The measured values of  $\sigma(tq)$ ,  $\sigma(\bar{t}q)$ , and  $\sigma(tq + \bar{t}q)$  are compared to NLO predictions calculated using MCFM and HATHOR with different PDF sets in Fig. 5.19. Details of the calculation of the predictions and on the estimation of the uncertainties are given in Section 1.3.1.

All PDF predictions are in agreement with all measurements. For  $\sigma(\bar{t}q)$  and  $\sigma(tq + \bar{t}q)$ , the predictions of all PDF sets agree well with each other and with the measured value. The prediction for  $\sigma(tq)$  with the ABM11 PDF set shows an offset compared to the other predictions.

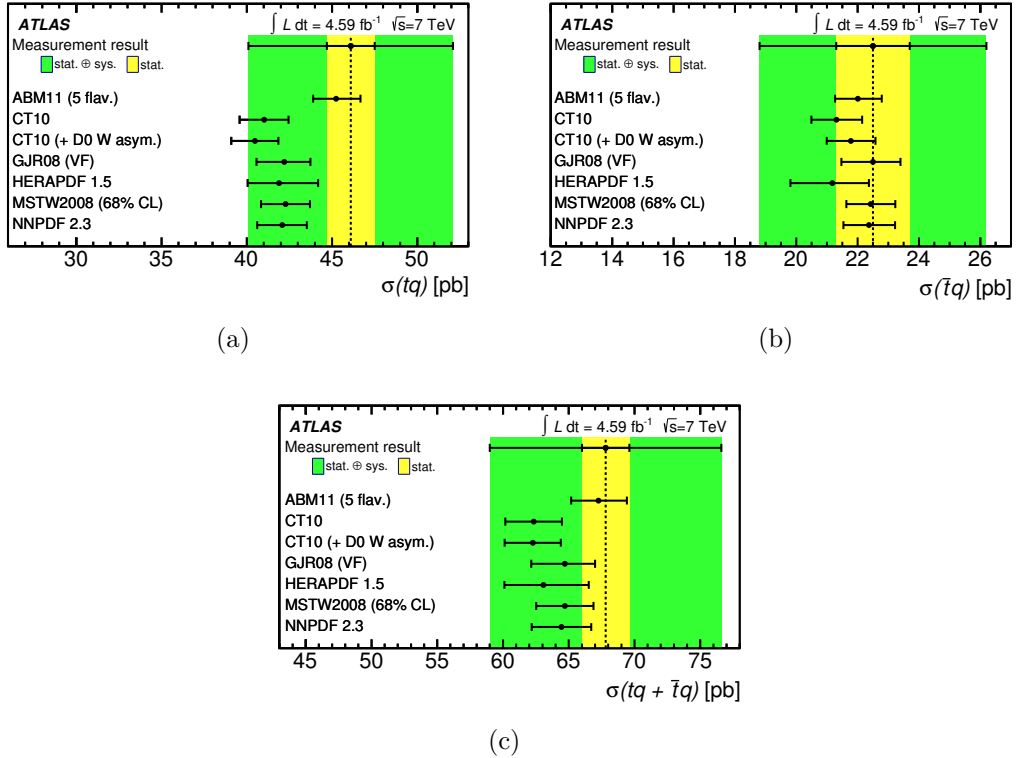


**Figure 5.19:** Comparison between observed and predicted values of (a)  $\sigma(tq)$ , (b)  $\sigma(\bar{t}q)$ , and (c)  $\sigma(tq + \bar{t}q)$  [174]. The predictions are calculated at NLO precision [62, 66] in the five-flavor scheme as described in Section 1.3.1. The dotted black line indicates the central value of the measurement. The combined statistical and systematic uncertainty of the measurement is shown in green, while the statistical uncertainty is represented by the yellow error band.

Currently, the results on  $\sigma(tq)$  and  $\sigma(\bar{t}q)$  are the only published results at  $\sqrt{s} = 7$  TeV achieving a total uncertainty of 12.4% on  $\sigma(tq)$  and 15.9% on  $\sigma(\bar{t}q)$ . The CMS experiment has presented a result on the combined inclusive cross section  $\sigma(tq + \bar{t}q)$  at  $\sqrt{s} = 7$  TeV [187]. The measurement is done using a dataset of  $1.17 \text{ fb}^{-1}$  ( $1.56 \text{ fb}^{-1}$ ) in the electron (muon) channel. Here, the results of three analysis methods, that use either the  $|\eta|$ -distribution of the light quark jet as discriminating variable or a multivariate discriminant, are combined to an inclusive cross section of  $\sigma(tq + \bar{t}q) = 67.2 \pm 3.7(\text{stat.}) \pm 4.8(\text{syst.}) \text{ pb}$ . This result is consistent with the result presented here and the NLO+NNLL prediction. The total uncertainty on the CMS measurement is 9.2% which is dominated by the signal modeling uncertainty and the uncertainty due to the  $W$ +jets background estimation. Differences to the presented analysis are the size of the JES uncertainty, that is less than 2% for the CMS measurement compared to 7.3% in the presented analysis, and the size of the PDF uncertainty, that is 1.3% instead of 3.2%. The PDF uncertainty in the CMS measurement is estimated differently by calculating the uncertainty of the CTEQ6 PDF set following the recommendation of the PDF group. In addition, the central value of the CT10 PDF set is evaluated. Then, the envelope of all predictions is taken as uncertainty. Comparisons with the NNPDF and MSTW2008 PDF sets are not performed. Due to these differences, the presented result on  $\sigma(tq + \bar{t}q)$  has a slightly worse precision of 12.4%.

### 5.4.2 Measurement of the cross-section ratio $R_t$

Now, the ratio of the top-quark and top-antiquark production  $R_t$  is determined to be:

$$\begin{aligned} R_t &= 2.04 \pm 0.13(\text{stat.}) \pm 0.12(\text{syst.}) \\ &= 2.04 \pm 0.18. \end{aligned}$$

By calculating the ratio of  $\sigma(tq)$  to  $\sigma(\bar{t}q)$ , systematic uncertainties, that affect the measurements of  $\sigma(tq)$  and  $\sigma(\bar{t}q)$  in the same way, cancel out for the cross-section ratio  $R_t$ . Thus, the systematic uncertainty of the measurement is much reduced compared to the inclusive cross-section results. The statistical uncertainties of the inclusive cross sections on the other hand add quadratically for the ratio. Therefore, the precision of  $R_t$  is driven by the statistical uncertainty on  $\sigma(\bar{t}q)$  of over 5%. Altogether, a precision of 8.7% is achieved for the measurement of  $R_t$ .

In Fig. 5.20 the measured value of  $R_t$  is compared to the NLO predictions obtained with different PDF sets. As for  $\sigma(tq)$ , an offset is observed for the ABM11 PDF set compared to the other predictions. The measurement of  $R_t$  is in agreement with all predictions. But with increasing precision, the measurement of  $R_t$  could provide a way to further constrain the involved PDFs.

$R_t$  has also been measured by the CMS experiment using  $19.7 \text{ fb}^{-1}$  of  $pp$ -collision data at  $\sqrt{s} = 8$  TeV [188]. Here,  $R_t$  is observed to be  $R_t = 1.95 \pm 0.10(\text{stat.}) \pm 0.19(\text{syst.})$  with a precision of 11.0%. While the statistical uncertainty is reduced compared to the presented measurement, the CMS experiment observes larger systematic uncertainties on their result in the background normalization, the signal

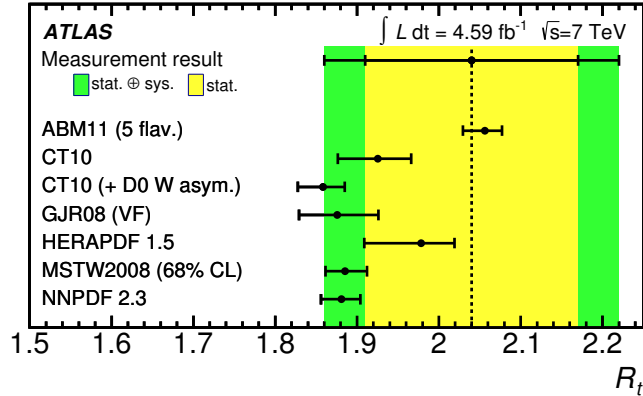


**Figure 5.20:** Comparison between observed and predicted values of  $R_t$ . The predictions are calculated at NLO precision [62, 66] in the five-flavor scheme as described in Section 1.3.1. The dotted black line indicates the central value of the measured value. The combined statistical and systematic uncertainty of the measurement is shown in green, while the statistical uncertainty is represented by the yellow error band.

modeling, and the PDFs. Again, the CMS result for  $R_t$  is consistent with the presented result and all the NLO predictions.

### 5.4.3 Cross-section dependence on the top-quark mass

The  $t$ -channel single top-quark cross sections are measured assuming a top-quark mass of  $m_t = 172.5$  GeV. The dependence of the cross-section measurements on  $m_t$  is evaluated by comparing signal models generated with  $m_t = 170$  GeV and  $m_t = 175$  GeV with the default signal model. Studies have shown, that changing the top-quark mass by  $\pm 2.5$  GeV does not cause a significant fluctuation in the kinematic shape of the signal templates generated with different top-quark masses. Therefore, the dependence of the measured cross sections on  $m_t$  is mainly due to acceptance effects. By changing the number of predicted events, the observed inclusive cross sections are determined for the two shifted mass points. To quantify the dependence, a quadratic function is determined, that relates the cross-section values calculated using the different acceptances for the signal model with  $m_t = 170$  GeV,  $m_t = 172.5$  GeV, and  $m_t = 175$  GeV. The quadratic function is given by:

$$\sigma_t = \sigma_t(172.5 \text{ GeV}) + p_1 \cdot \Delta m_t + p_2 \cdot \Delta m_t^2 \quad (5.5)$$

with  $\Delta m_t = m_t - 172.5$  GeV. The parameters  $p_1$  and  $p_2$  are calculated and are presented in Table 5.9 for  $\sigma(tq)$ ,  $\sigma(\bar{t}q)$  and  $\sigma(tq + \bar{t}q)$ . In Fig. 5.21 the three cross sections values and the function are shown for the case of  $\sigma(tq + \bar{t}q)$ . The cross-section ratio  $R_t$  is largely independent of the top-quark mass because the changes in  $\sigma(tq)$  and  $\sigma(\bar{t}q)$  cancel.

**Table 5.9:** Parametrization factors for the  $m_t$  dependence (see Equation 5.5) of  $\sigma(tq)$ ,  $\sigma(\bar{t}q)$  and  $\sigma(tq + \bar{t}q)$ .

	$p_1$ [pb/GeV]	$p_2$ [pb/ GeV <sup>2</sup> ]
$\sigma(tq + \bar{t}q)$	-0.46	-0.06
$\sigma(tq)$	-0.27	-0.04
$\sigma(\bar{t}q)$	-0.19	-0.02

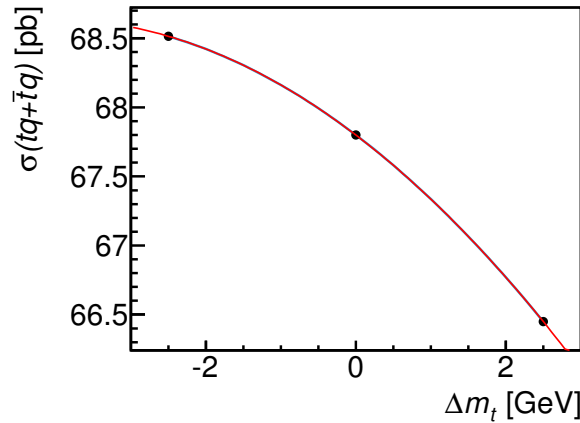


**Figure 5.21:**  $\sigma(tq + \bar{t}q)$  shown as a function of  $m_t$  evaluated at  $m_t = 170$  GeV and  $m_t = 175$  GeV.

#### 5.4.4 $|V_{tb}|$ extraction

Since  $\sigma(tq + \bar{t}q)$  is proportional to  $|V_{tb}|^2$ ,  $|V_{tb}|$  can be extracted from the measurement. The  $|V_{tb}|$  measurement is independent of assumptions about the number of quark generations and about the unitarity of the CKM matrix. The only assumptions required are, that  $|V_{tb}| \gg |V_{td}|, |V_{ts}|$ , that the branching ratio  $B(t \rightarrow Wb) \sim 1$ , and that the  $Wtb$  interaction is an SM-like left-handed weak coupling. The  $t\bar{t}$ -background rate is unaffected by a variation of  $|V_{tb}|$ , since the decay to a quark of a potentially existing higher generation are prohibited by kinematics. On the other hand, the rates of  $Wt$  and  $s$ -channel single-top quark production also scale with  $|V_{tb}|^2$ . Since their contributions are small in the signal region, the resulting variation of the total top-quark background yield is considered negligible.

The value of  $|V_{tb}|^2$  is extracted by dividing the measured value of  $\sigma(tq + \bar{t}q)$  by the prediction of the NLO+NNLL calculation [54]. The experimental and theoretical uncertainties are added in quadrature. The result obtained is

$$\begin{aligned} |V_{tb}| &= 1.02 \pm 0.01(\text{stat.}) \pm 0.06(\text{syst.}) \pm 0.02(\text{theo.})^{+0.01}_{-0.00}(m_t) \\ &= 1.02 \pm 0.07. \end{aligned}$$

A lower limit on  $|V_{tb}|$  is extracted in a Bayesian limit computation, assuming that the likelihood curve of  $|V_{tb}|^2$  has a Gaussian shape, centered at the measured value. This is shown in Fig. 5.22. A flat prior in  $|V_{tb}|^2$  is applied, being one in the interval

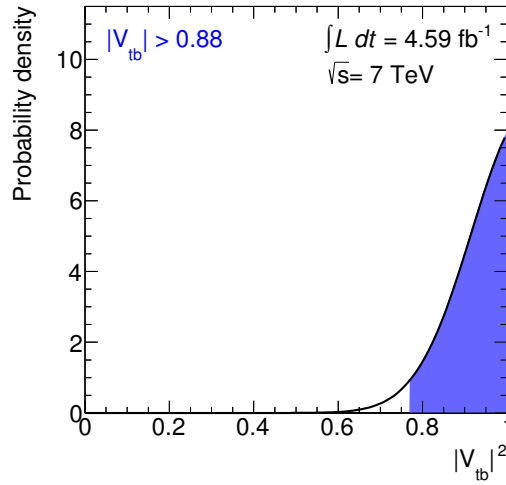


**Figure 5.22:** Probability-density function of the square of the CKM matrix element  $|V_{tb}|$ , assuming  $|V_{tb}| \leq 1$ . A lower limit is extracted,  $|V_{tb}|^2 > 0.77$  at the 95% CL (blue region), corresponding to a lower limit of  $|V_{tb}| > 0.88$ .

$[0, 1]$  and zero otherwise. The resulting lower limit is  $|V_{tb}| > 0.88$  at the 95% CL assuming  $|V_{tb}| \leq 1$ .

In an analogous manner,  $|V_{tb}|$  was extracted from the inclusive  $t$ -channel single top-quark cross-section measurement by the CMS experiment. Their most precise result is achieved by combining the cross-section measurements done at  $\sqrt{s} = 7$  TeV and at  $\sqrt{s} = 8$  TeV, described in Ref. [187] and Ref. [188], respectively. Thus,  $|V_{tb}|$  is measured to be  $|V_{tb}| = 0.998 \pm 0.041$ , and the corresponding lower limit is  $|V_{tb}| > 0.92$  at the 95% CL [188]. Both results, the CMS result as well as the result presented here, are consistent with the SM prediction of  $|V_{tb}| \approx 1$ .



# Chapter 6

## Differential cross-section measurements

The measurement of the differential cross sections of  $t$ -channel single top-quark production as a function of the transverse momentum of the top quark,  $p_T$ , as well as a function of the absolute value of the rapidity,  $|y|$ , is presented in this chapter. Both quantities are extracted from collision data for top quark and top antiquark separately.

All measurements are performed in a high-purity region, that is defined utilizing the NN discriminant in the 2-jet- $\ell^\pm$  channels. The background is estimated using the results from Chapter 5 and is subtracted from the data distribution. Then, the measured distributions are corrected for detector effects and selection efficiencies using an unfolding method. Several tests are performed to check the validity of the unfolding procedure. Finally, the results are presented including the impact of statistical and systematic uncertainties.

### 6.1 High-purity region

A highly pure sample of signal candidate-events containing sufficient statistics is necessary to perform a differential cross-section measurement. The 2-jet- $\ell^\pm$  SRs are chosen as a starting point for the search of a suitable high-purity region (HPR) as they have the largest signal fraction (shown in Section 4.2.3). To increase the signal purity in the 2-jet- $\ell^\pm$  SRs, the NN discriminant is used, since it is optimized to separate background events from signal events. Thus, the purity of signal events increases in the signal area of the NN close to one. By placing a cut on the NN discriminant  $o_{\text{NN}}$ , the background fraction is reduced without a significant decrease of signal candidate-events.

To choose a suitable cut threshold, the  $S/B$  distribution of  $o_{\text{NN}}$  is evaluated in the 2-jet- $\ell^+$  and 2-jet- $\ell^-$  channels, shown in Fig. 6.1. Here,  $S$  is the sum of predicted signal events and  $B$  the sum of predicted background events in the interval from each bin to the end of the distribution. It can be observed, that an  $S/B$  of approximately 2 can be achieved for the 2-jet- $\ell^+$  channel at a threshold of  $o_{\text{NN}} = 0.8$ . This threshold corresponds to an  $S/B \sim 1$  for the 2-jet- $\ell^-$  channel. Thus, the HPR is defined

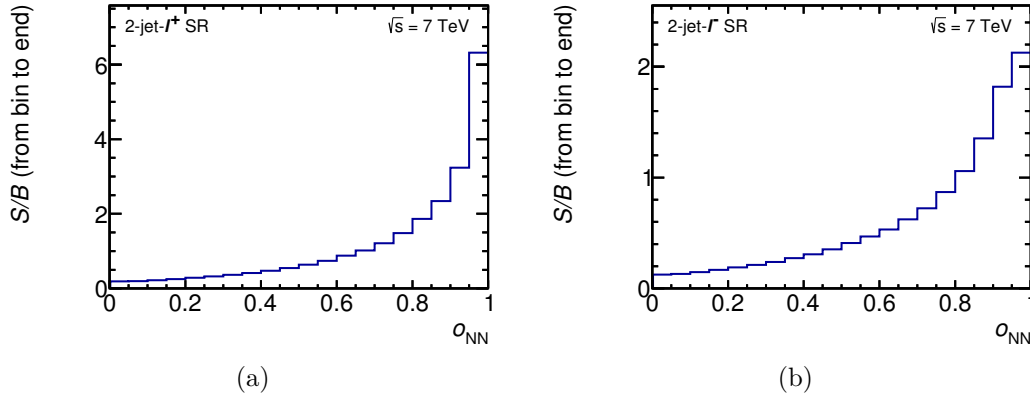


**Figure 6.1:** Distribution of the signal-over-background ratio,  $S/B$ , of the  $o_{\text{NN}}$  distribution in the (a) 2-jet- $\ell^+$  and (b) 2-jet- $\ell^-$  channels.  $S$  is the sum of predicted signal events from each bin to the end of the distribution and  $B$  is the sum of predicted background events from each bin to the end of the distribution.

exactly as the SR in the 2-jet- $\ell^+$  and 2-jet- $\ell^-$  channels including the additional requirement  $o_{\text{NN}} > 0.8$ .

The signal and background composition in the 2-jet- $\ell^+$  and 2-jet- $\ell^-$  HPR is given in the event yield in Table 6.1. All background processes except for  $W+c$  and multijet production are normalized with the fractions determined in the binned ML fit for the inclusive cross sections described in Section 5.2. The uncertainty on the expectation values is given by the normalization uncertainty of each process after the fit.  $W+c$  production is normalized to its theory prediction, and the multijet background is estimated with the jet-lepton method in the electron channel and the matrix method in the muon channel, as discussed in Section 4.2.2.

Since the sum of all backgrounds needs to be subtracted from the data distribution, it is necessary to determine the postfit normalization uncertainty of this sum. To evaluate the uncertainty of the background estimation, the same set of pseudo experiments, that is introduced in Section 5.3 to estimate the uncertainties on the measured inclusive cross-sections, is used. The  $\hat{\beta}$  distribution for the sum of all backgrounds is constructed by adding up the background estimators in each pseudo experiment. Thus, the correlations between all background processes are taken into account. Figure 6.2 shows the  $\hat{\beta}_{\text{background}}$  distribution for the 2-jet- $\ell^+$  and 2-jet- $\ell^-$  channels. The root-mean square is taken as the estimator of the uncertainty resulting into 13% uncertainty in the 2-jet- $\ell^+$  and 14% in the 2-jet- $\ell^-$  channel.

The general modeling of the HPR region is checked in the three most discriminating input variables for the 2-jet NN. The distributions are shown in Fig. 6.3 in the 2-jet- $\ell^+$  and 2-jet- $\ell^-$  HPR channels normalized to the fit results from Table 5.2. The data events are well described by the predicted compound model.

**Table 6.1:** Event yields for the 2-jet- $\ell^+$  and 2-jet- $\ell^-$  HPR channels. The expectation for the signal and background yields correspond to the result of the binned ML fit given in Table 5.2. The uncertainty of the expectations is the normalization uncertainty of each processes after the fit, as described in Sec. 5.3.

	2-jet- $\ell^+$ HPR	2-jet- $\ell^-$ HPR
$tq$	$1210 \pm 150$	$1.3 \pm 0.2$
$\bar{t}q$	$0.29 \pm 0.05$	$549 \pm 87$
$t\bar{t}, Wt, t\bar{b}, \bar{t}b$	$161 \pm 18$	$175 \pm 19$
$W^+ + b\bar{b}, c\bar{c}, \text{light jets}$	$250 \pm 48$	$0.35 \pm 0.07$
$W^- + b\bar{b}, c\bar{c}, \text{light jets}$	$0.7 \pm 0.2$	$166 \pm 40$
$W+c$	$110 \pm 26$	$125 \pm 30$
$Z+\text{jets}, \text{diboson}$	$15 \pm 10$	$11.4 \pm 6.8$
Multijet	$59 \pm 30$	$62 \pm 31$
Total background	$596 \pm 66$	$540 \pm 62$
Total expectation	$1810 \pm 160$	$1090 \pm 110$
Data	1813	1034

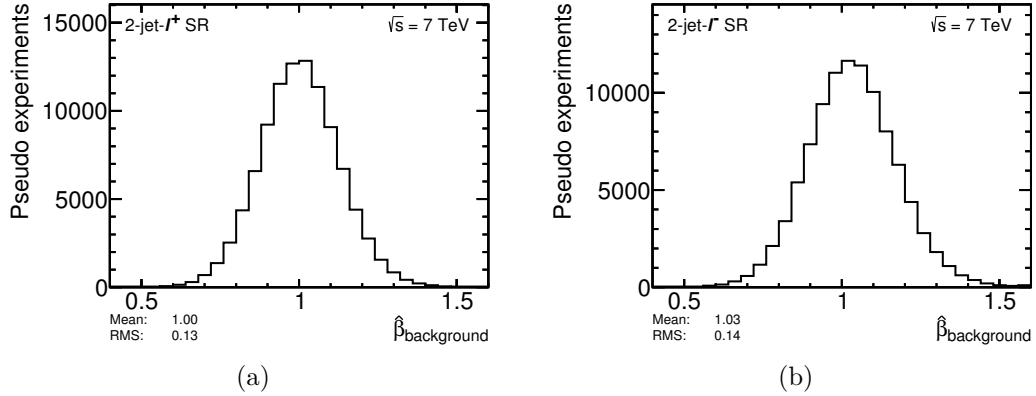


**Figure 6.2:** Distribution of  $\hat{\beta}_{\text{background}}$  for the sum of all backgrounds in the (a) 2-jet- $\ell^+$  and (b) 2-jet- $\ell^-$  channels, extracted from the corresponding set of pseudo experiments. All correlations between the uncertainties and the backgrounds are taken into account.

### 6.1.1 Measured distributions

The binning of the distributions for the differential cross-section measurements is chosen based on the following requirements:

- The experimental resolution of the reconstructed variable should be smaller than the bin width.
- At least 100 observed data events should be in each bin.

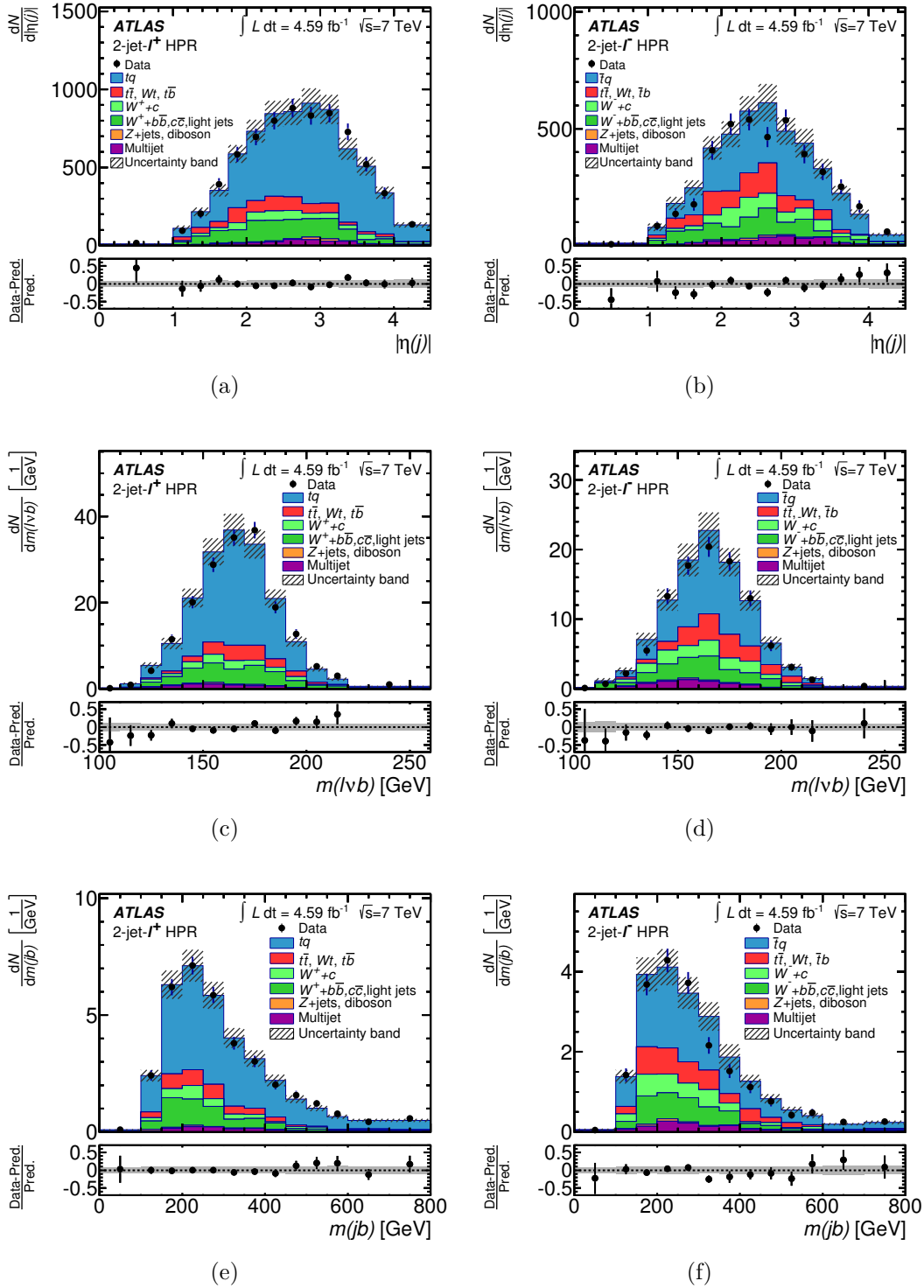


**Figure 6.3:** Distributions of the three most important discriminating variables in the 2-jet- $\ell^+$  and 2-jet- $\ell^-$  channels in the HPR normalized to the result of the binned ML fit [174]. Panels (a) and (b) show the absolute value of the pseudorapidity of the untagged jet  $|\eta(j)|$ , (c) and (d) the invariant mass of the reconstructed top quark  $m(\ell vb)$ , and (e) and (f) the invariant mass of the  $b$ -tagged and the untagged jet  $m(jb)$ . The last histogram bin includes overflows. The uncertainty band represents the normalization uncertainty of all processes after the fit and the Monte Carlo statistical uncertainty, added in quadrature. The relative difference between the observed and expected number of events in each bin is shown in the lower panels.

- The bin migration due to the top-quark reconstruction should be below 40% for each bin of the parton-level distribution.
- The same binning should be applied for the top-quark and top-antiquark distributions.

The resolution of each variable is defined as the RMS of a Gaussian fitted in the residual distribution of each variable. To investigate the dependence on the parton-level variable itself, the resolution is shown as a function of the corresponding parton-level variable in Fig. 6.4. Here, the binning of the parton-level variable is unrelated to the binning evaluation of this variable. The last bin width is increased to evaluate the resolution for large values of  $p_T$  or  $|y|$  with sufficient statistics of simulated events. The vertical error bars on the resolution correspond to the error on the RMS of the Gaussian.

In case of the  $p_T$  distribution of the top-quark, first the histogram borders have to be defined. All measured data events in the HPR fulfill  $p_T(\ell\nu b) < 500$  GeV. Thus, the distribution is shown from 0 GeV to 500 GeV. The last bin of the distribution is

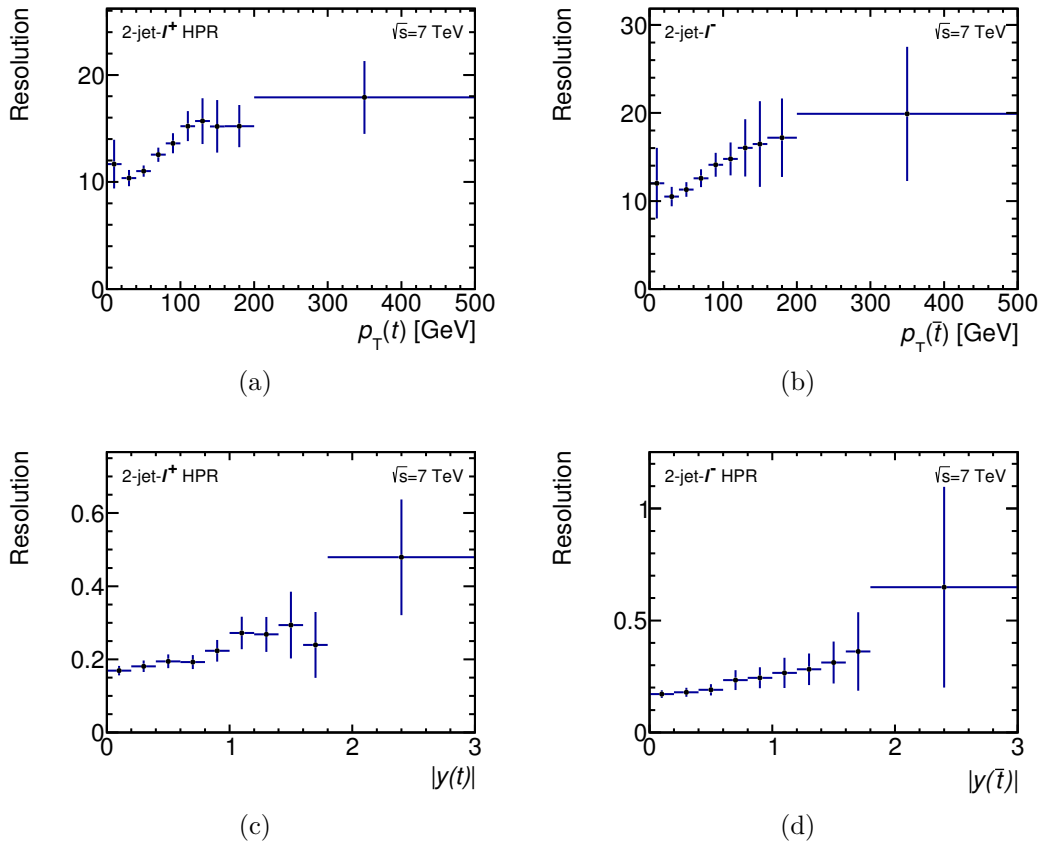


**Figure 6.4:** Resolution of  $p_T(t)$ ,  $p_T(\bar{t})$ ,  $|y(t)|$ , and  $|y(\bar{t})|$  as a function of the variable defined at the parton level, respectively. The vertical error bars correspond to the uncertainty on the resolution, while the horizontal error bar shows the width of the bin.

defined from 150 GeV to 500 GeV and the first bin from 0 GeV to 45 GeV to ensure a sufficient number of data events in each bin. In Fig. 6.4(a) and 6.4(b) the resolution is shown in several slices of  $p_T$  for the top quark and the top antiquark. The resolution is approximately 12 GeV, increasing to 25 GeV in the tails. The final bin sizes between 45 GeV and 150 GeV are chosen larger than 12 GeV to keep the migration between bins from the reconstruction level to the parton level below 40%. Thus, the final binning is chosen to be [0 GeV, 45 GeV, 75 GeV, 110 GeV, 150 GeV, 500 GeV]. The measured  $p_T$  distributions of the reconstructed top-quark in the HPR are shown in Fig. 6.5(a) and 6.5(b).

Due to the geometric coverage of the detector the range of the rapidity distribution is  $0 < |y(\ell\nu b)| < 3$ . Therefore, the histogram borders are set to 0 and 3. The last bin of the rapidity distribution is defined from 1.2 to 3, to fulfill the requirement on the data statistics. The resolution is shown in Fig. 6.4(c) as a function of  $|y(t)|$  and in Fig. 6.4(d) as a function of  $|y(\bar{t})|$ . It varies from 0.2 to 0.4 from central to forward rapidities. The first bin is chosen to have the minimal size allowed by the resolution of 0.2. All other bins are chosen to be larger due to the data statistics in the 2-jet- $\ell^-$  HPR channel and due to the migration. Thus, the final binning is [0, 0.2, 0.6, 1.2, 3]. The measured distributions of the reconstructed top-quark  $|y|$  in the HPR are shown in Fig. 6.5(c) and 6.5(d).

## 6.2 Extraction of differential cross sections

The measured kinematic properties of the reconstructed top-quark are distorted by detector effects and selection efficiencies. The correction of the measurements for these effects requires good understanding of the detector components involved in the detection and reconstruction of the measured distributions. A further challenge is the estimation of the uncertainties imposed by the measurement. Therefore, the correction of the variables to the parton level is part of the analysis.

First, the relation between the reconstructed distribution, as shown in Fig. 6.5, and the parton-level distribution is investigated. In the following, each bin of the reconstructed distribution is referred to by the index  $i$ , while each bin of the parton-level distribution is referred to by the index  $j$ . The measured data events in bin  $i$  can be expressed by:

$$N_i = \sum_j M_{ij} \cdot \epsilon_j \cdot \mathcal{L} \cdot \mathcal{B}(t \rightarrow \ell\nu b) \cdot d\sigma_j + B_i, \quad (6.1)$$

where  $N_i$  ( $B_i$ ) are the data (expected background) yields in each bin of the distribution,  $\mathcal{L}$  is the integrated luminosity of the data sample,  $\epsilon_j$  is the selection efficiency,  $d\sigma_j$  is the cross section in each parton-level bin  $j$ , and  $M_{ij}$  is the migration matrix.

The migration matrix accounts for the detector response and is defined as the probability to observe an event in bin  $i$  when its parton-level value is located in bin  $j$ . The migration matrix is built by relating the variables at reconstruction and parton level in selected simulated signal events. Figure 6.6 shows the migration matrices for the  $p_T$  and  $|y|$  of the top-quark and top-antiquark. It can be observed, that the selected parton-level top-quark located in a certain bin in the parton-level

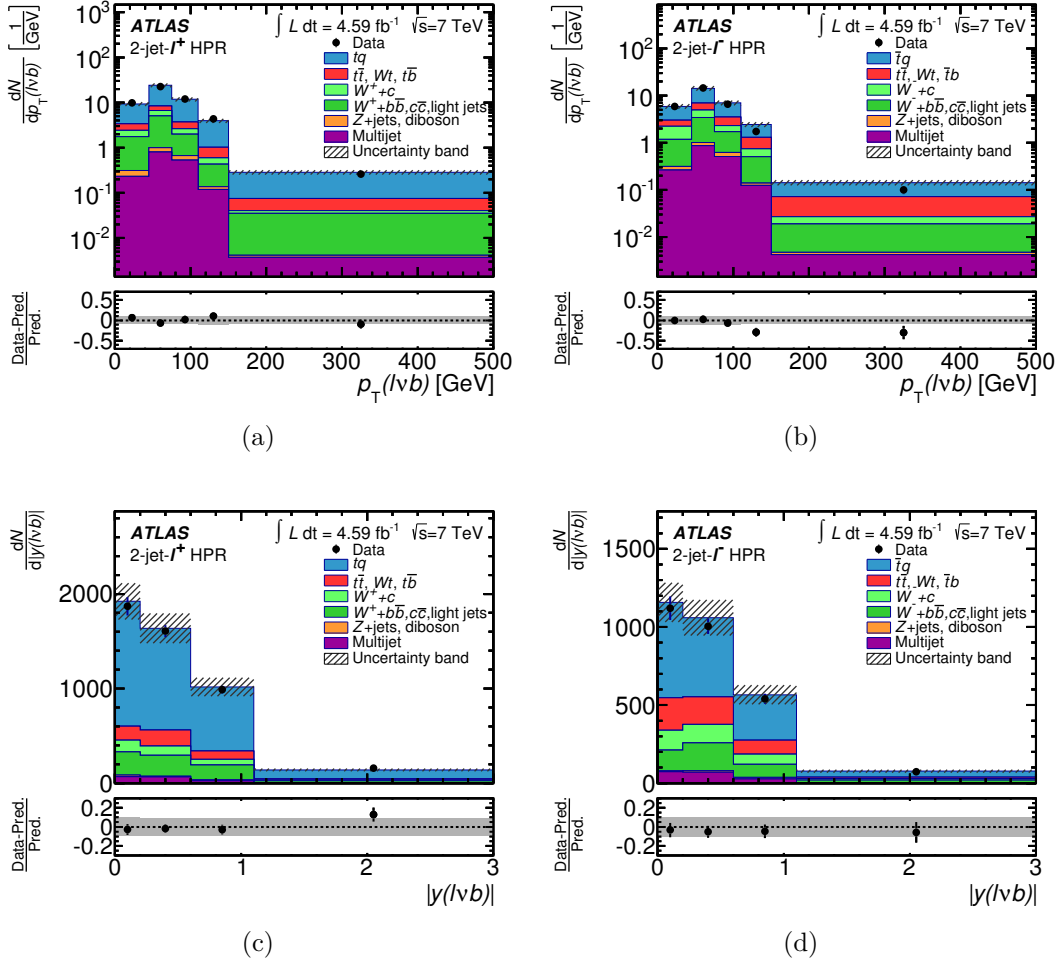


**Figure 6.5:** Measured distributions of (a) the top-quark  $p_T$ , (b) top-antiquark  $p_T$ , (c) top-quark  $|y|$ , and (d) top-antiquark  $|y|$  shown on reconstruction level in the HPR normalized to the result of the binned ML fit [174]. The uncertainty band represents the normalization uncertainty of all processes after the fit and the Monte Carlo statistical uncertainty, added in quadrature. The relative difference between the observed and expected number of events in each bin is shown in the lower panels.

distribution is reconstructed with a probability of 30-40% in a different bin. Thus, a significant amount of migration is present in the observables.

The selection efficiency  $\epsilon_j$  in each bin  $j$  of each variable is defined as the ratio of the parton-level yield before and after event selection and is evaluated in simulated signal events. The efficiencies are typically in the range of 1.0-2.2%. Distributions of  $\epsilon_j$  for each variable are given in Appendix B.1.

The cross section  $d\sigma_j$  in each parton-level bin  $j$  is connected to the differential cross section  $d\sigma/dX$  as a function of variable  $X$  via  $d\sigma_j = d\sigma/dX \cdot \Delta X_j$  where  $\Delta X_j$  is the width of bin  $j$  of variable  $X$ . Thus, the problem, that needs to be solved to

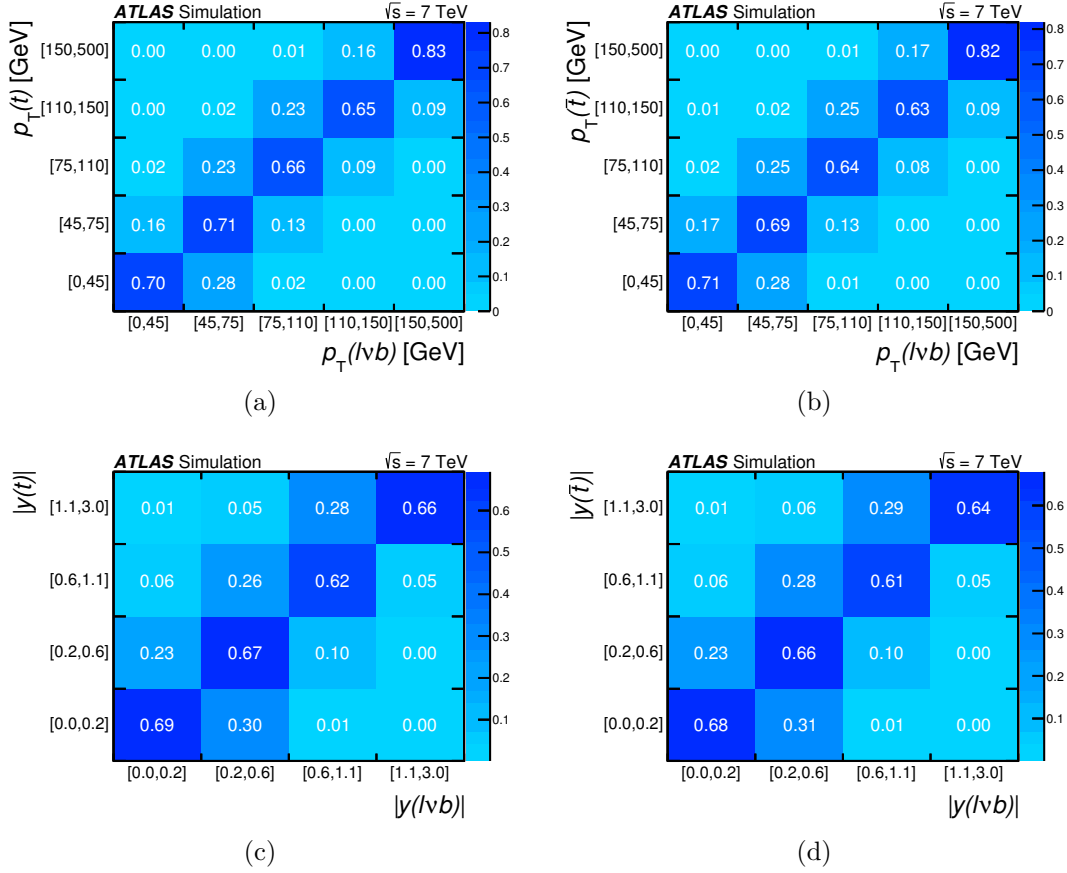


**Figure 6.6:** Migration matrices relating the parton level shown on the y axis and reconstruction level shown on the x axis for the (a) top-quark  $p_T$ , (b) top-antiquark  $p_T$ , (c) top-quark  $|y|$ , and (d) top-antiquark  $|y|$  distribution in selected events [174].

measure differential cross sections, is formulated in the following way:

$$\frac{d\sigma}{dX_j} = \frac{1}{\Delta X_j} \cdot \frac{\sum_i M_{ij}^{-1} \cdot (N_i - B_i)}{\epsilon_j \cdot \mathcal{L} \cdot \mathcal{B}(t \rightarrow \ell vb)}. \quad (6.2)$$

Equation 6.2 suggests three subsequent steps to determine the differential cross sections. First, the background contributions are subtracted from the measured data distribution. Then, the distribution is unfolded using the inverse of the migration matrix,  $M_{ij}^{-1}$ . Finally, the unfolded distribution is divided by the selection efficiency, the luminosity, the branching ratio, and the bin width. To determine the inverse of the migration matrix  $M_{ij}$ , a dedicated unfolding method is applied.

In Fig. 6.7 the kinematic properties of the top-quark are shown at parton level, selection level, and reconstruction level for simulated signal events. Parton level corresponds to the property of the top quark before any selection cuts are applied. The selection-level distributions show the distributions of the parton-level top-quark after the event selection, while the reconstruction-level distributions show the distributions of the reconstructed top quark. All distributions are normalized to unit area,

and thus show only the kinematic shape of the distributions. Comparing the parton-level distributions and the selection-level distributions, the acceptance effects due to the geometric coverage of the detector and the requirements of the event selection can be observed. Top quarks with low transverse momentum and large rapidity are less likely to be measured. The distortion by the detector response is visible, when the reconstruction-level distributions are compared to the selection-level distributions.

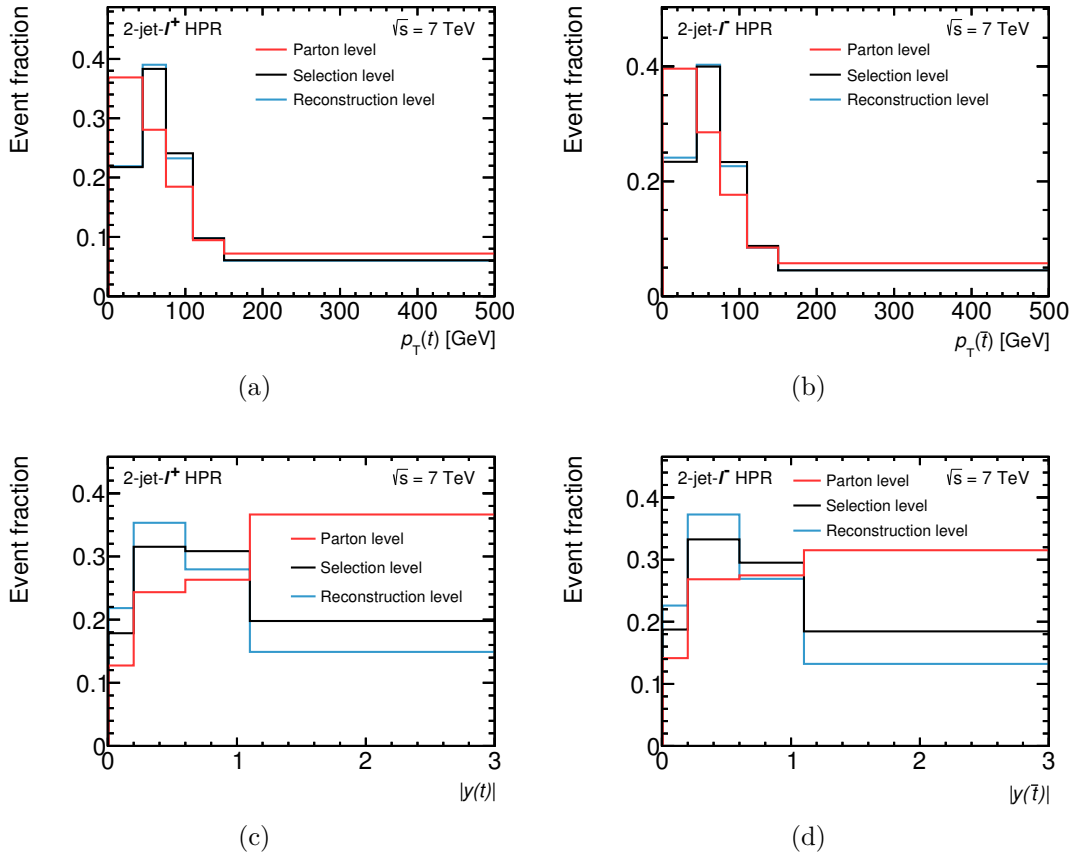


**Figure 6.7:** Comparison of the parton-level, selection-level, and reconstruction-level distributions for the (a) top-quark  $p_T$ , (b) top-antiquark  $p_T$ , (c) top-quark  $|y|$ , and (d) top-antiquark  $|y|$  using simulated signal events. The distributions are normalized to unit area.

## 6.2.1 Unfolding methods

Several methods are used in high-energy physics to unfold a reconstructed distribution. In the presented analysis an iterative Bayesian approach is used to unfold the distributions. The results obtained with the iterative Bayesian approach are cross-checked by deploying the simple bin-by-bin unfolding method and the singular value-decomposition (SVD) method. In the following all three methods are briefly described. The implementation of all methods in the program RooUnfold [189] (version 1.1.1) is used throughout the analysis.

### Iterative Bayesian unfolding method

An unfolding method based on Bayes' theorem was developed by G. D'Agostini and is fully described in Ref. [190]. The method is based on picturing the problem with an "effect"  $E$  and a "cause"  $C$ . The reconstructed measured events  $N_i$  in bin  $i$  correspond to the effects  $E_i$ , while the number of bins correspond to the number of effects  $n_E$ . In this analysis the cause  $C_j$  is represented by the number of predicted events of  $t$ -channel single top-quark events in each bin  $j$  of the parton-level distributions before any selection cuts. The bin number of the parton-level distribution corresponds to the number of causes  $n_C$ .

$E$  is well measured, but  $C$  cannot be measured. Thus,  $C$  is estimated as follows: The probability for an effect to originate from a definite cause,  $P(E_i, C_j)$ , can be estimated assuming knowledge of the migration matrix and the measurement efficiency and resolution which are determined using the MC signal simulation. Then, using Bayes theorem (shown in detail in Ref. [190]) the probability for cause  $C_j$  to produce an effect  $E_i$  can be written as:

$$P(C_j, E_i) = \frac{P(E_i, C_j) \cdot P_0(C_j)}{\sum_{k=1}^{n_C} P(E_i, C_k) \cdot P_0(C_k)} . \quad (6.3)$$

The term  $P_0(C_j)$  is an arbitrary initial distribution for the parton-level distribution,  $P(E_i, C_j)$  corresponds to the migration matrix, since it describes the probability for effect  $E_i$  to originate from cause  $C_j$ .

The estimation  $\hat{n}(C_j)$  of cause  $C_j$  is then given by:

$$\hat{n}(C_j) = \frac{1}{\epsilon_j} \sum_{i=1}^{n_E} n(E_i) \cdot P(C_j, E_i) , \quad (6.4)$$

where  $n(E_i)$  is the number of observed events and  $\epsilon_j$  is the selection efficiency for parton-level bin  $j$ . The final distribution for the parton-level distribution  $\hat{P}(C_j)$  is expressed by:

$$\hat{P}(C_j) = \frac{\hat{n}(C_j)}{\sum_{j=1}^{n_C} \hat{n}(C_j)} . \quad (6.5)$$

Final values for  $\hat{n}(C_j)$  and  $\hat{P}(C_j)$  are derived in an iterative way starting from the initial distribution  $P_0(C_j)$ . In RooUnfold the initial distribution is set to the parton-level distribution of the simulated sample. After each iteration,  $P_0(C_j)$  is

set to  $\hat{P}(C_j)$ . The result from the previous and the current iteration are compared with a  $\chi^2$  calculation. The iterations are stopped once the value of  $\chi^2$  is small enough. Thus, the number of iterations,  $n_{\text{iter}}$ , that corresponds to the regularization parameter of the Bayesian unfolding, can be determined.

A more stringent criterion to determine  $n_{\text{iter}}$  than the  $\chi^2$  calculation is to check the change in each bin content  $N_j$  after each iteration  $n_{\text{iter}}$  and to require this change to be smaller than 1%. This condition is formulated in the following equation for iteration  $l$ :

$$\Delta N_j = \frac{N_j(n_{\text{iter}} = l) - N_j(n_{\text{iter}} = l + 1)}{N_j(n_{\text{iter}} = l + 1)} < 1\% . \quad (6.6)$$

1000 pseudo experiments are used to investigate  $\Delta N_j$  for all distributions. The mean in the change of the bin content per iteration is used to determine  $\Delta N_j$ . As a result of these studies, the number of iterations is determined to six iterations for the top-quark  $p_T$  and five iterations for the top-quark rapidities.

An uncertainty is assigned on the determination of the number of iterations. The unfolded result is compared to the result retrieved from an iterative unfolding using  $n_{\text{iter}} + 1$  iterations for each distribution. The difference between both unfolded results is taken as uncertainty on the unfolding process.

### Bin-by-bin unfolding method

This simple method uses the ratio of the reconstructed predictions to the parton-level predictions and extracts correction factors for each bin of the distributions. Since no inter-bin migration is taken into account, this method is only useful when the measured values and the predicted values agree well. Otherwise, biases from the MC simulation model might occur. In this analysis, the bin-by-bin method is only used as a cross check.

### Singular value-decomposition method

The SVD method [191] is an extension of a simple matrix inversion. In the simple matrix inversion, a direct solution can lead to rapidly oscillating solutions due to numerical instabilities and finite statistics of both data and simulation samples. To avoid this behavior, an SVD of the migration matrix is performed. Thus, the matrix  $M$  can be rewritten as:

$$M = USV^T \quad (6.7)$$

where  $U$  and  $V$  are  $n \times n$  orthogonal matrices and  $S$  is an  $n \times n$  diagonal matrix. The inverted migration matrix can be written as:

$$M^{-1} = VS^{-1}U^T . \quad (6.8)$$

This transformation greatly simplifies the inversion process. Finding appropriate matrices for the decomposition is a non-trivial linear-algebra problem. Details of the determination of the inversion using SVD are given in Ref. [191]. The SVD is regularized by the parameter  $k$ , that is set to the number of bins of the respective distribution in the presented analysis. The SVD method is only used for cross checks in this thesis.

## 6.2.2 Tests of the unfolding process

Several checks are performed to validate the unfolding of each distribution and to verify, that the simulation does not bias the result. To test the consistency of the signal simulation, the signal-simulation sample is divided into two parts of equal size. The migration matrix is extracted from one part of the sample. The other part is used to extract the reconstructed distribution. Then, the reconstructed distribution is unfolded. For this check the resulting distribution is not divided by the selection efficiency. Then, the unfolded distribution is compared to the selected parton-level distribution of the second part of the simulated sample. This comparison is shown in Fig. 6.8. The selection-level distributions are retrieved by the unfolding process in all distributions.

Another check is performed to ensure, that the results are not biased towards the underlying simulated truth distribution. This check is done by altering the shape of the selection-level distributions in the signal simulation with different linear and parabola slopes. The altered selection-level distributions are recovered by unfolding the reconstructed distributions with the nominal migration matrix. The resulting distributions are not divided by the selection efficiency for this check. An example of this check for each distribution is given in Fig. 6.9. Here, a linear step function is applied to 21 equidistant bins of the  $p_T$  distribution of the selection-level top-quark, changing the event weight by multiplying with factors in the range of  $[1.0, 5.0]$ . Thus, also the integral of the distribution is changed. For the  $|y|$  distribution of the selection-level top-quark a linear step function is applied to 11 equidistant bins, changing the event weight by multiplying factors between  $[1.5, 0.5]$ . In each unfolded variable the altered selection-level distribution is recovered.

To ensure, that the iterative Bayesian unfolding gives reliable results, the unfolded result is compared to the result of the SVD unfolding method and the bin-by-bin unfolding method. The application of the SVD method has not been optimized, but the regularization parameter  $k$  is set to the number of bins for each distribution. The comparison of all methods is shown in Fig 6.10. All three distributions agree within the uncertainty in the data statistics.

## 6.2.3 Evaluation of uncertainties

In this section the propagation of the statistical and systematic uncertainties through the unfolding process is described. Each uncertainty is evaluated separately. The total uncertainty is then estimated by the quadratic sum of all uncertainties. In addition to the sources of systematic uncertainties described in Section 5.3.1 and the background normalization uncertainty described in Section 6.1, an uncertainty in the unfolding process itself is added, that is introduced in Section 6.2.1.

The statistical uncertainty on the unfolded result is estimated using pseudo experiments. The content of each bin in the measured data distribution is fluctuated with the Poisson distribution of the bin content in the pseudo experiments. The uncertainty in the size of the background MC samples is evaluated by fluctuating the bin contents of the background templates using a Gaussian distribution of a width corresponding to the bin error. In case of the signal MC sample the bins of

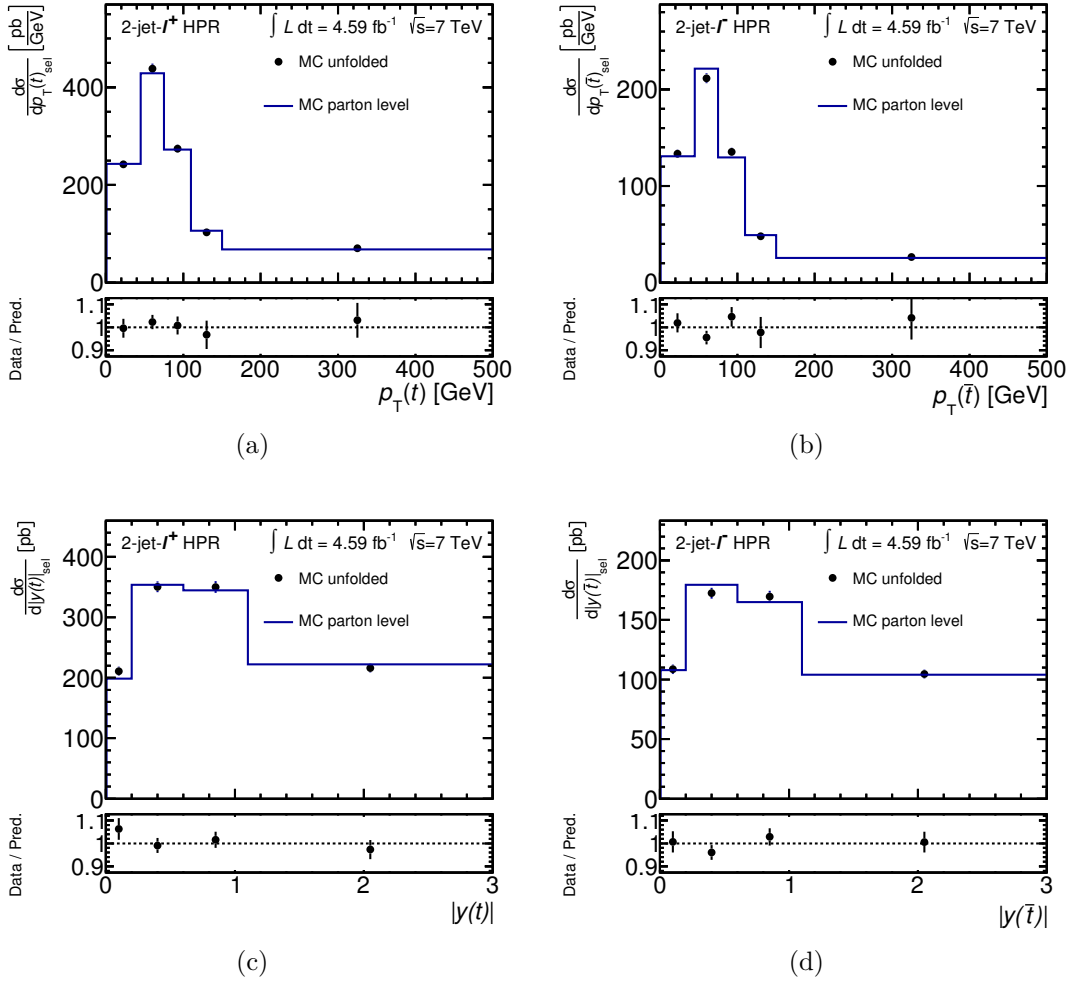


**Figure 6.8:** Demonstration of the consistency of the unfolding process by unfolding one half of the simulated signal sample while the migration matrix is derived with the other half. The unfolded differential cross sections on selection level as a function of (a)  $p_T(t)$ , (b)  $p_T(\bar{t})$ , (c)  $|y(t)|$ , and (d)  $|y(\bar{t})|$  are denoted with black points. Here, the error bars correspond to the uncertainty in the size of the simulated sample. In the lower panels, the ratio of the unfolded distribution over the selection-level distribution is shown.

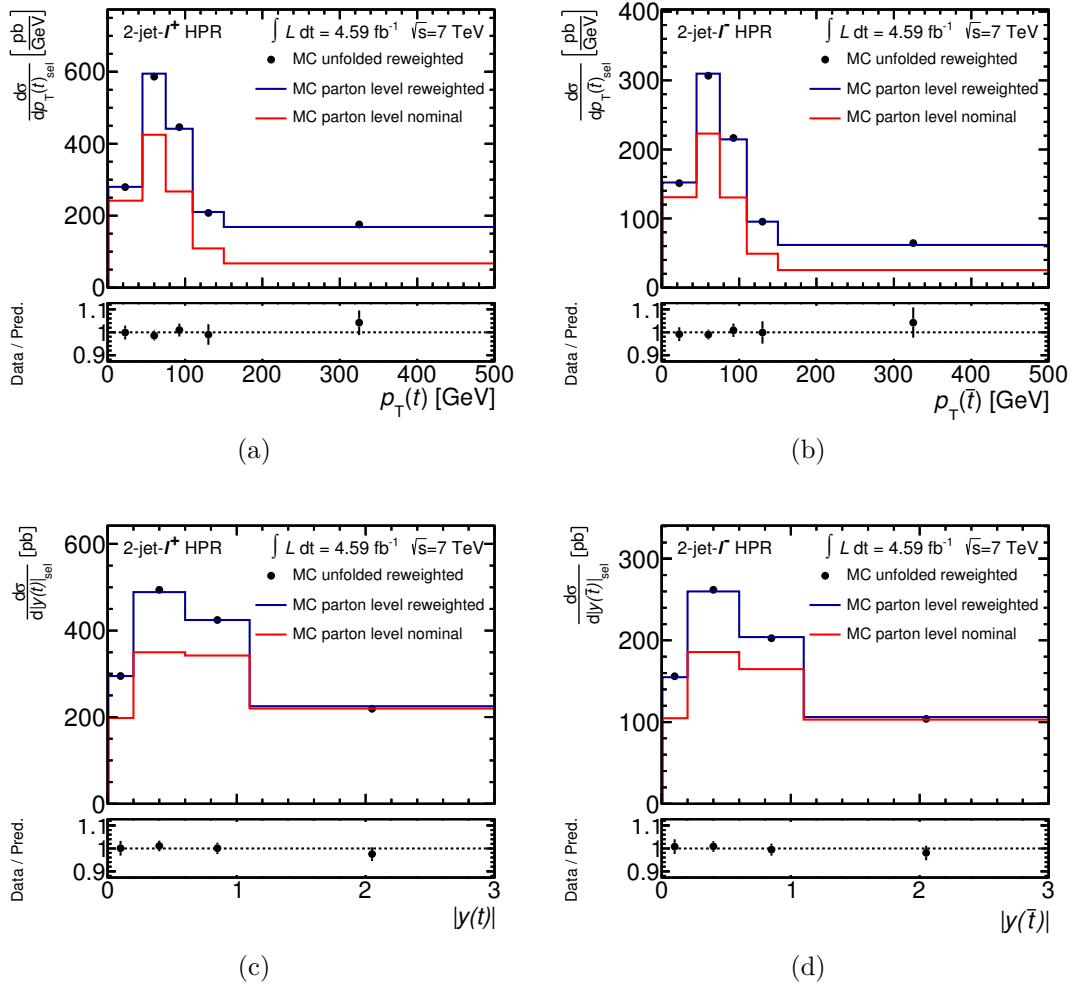


**Figure 6.9:** Test of the unfolding process by altering the parton-level distributions of the simulation after selection. The resulting reconstructed distributions are unfolded using the nominal migration matrix. In Panels (a) and (b) the  $p_T$  distribution is changed in 20% steps, while in Panels (c) and (d) the rapidity distribution is changed in 10% steps. In the lower panels, the ratio of the unfolded distribution over the altered selection-level distribution is shown. Each unfolding process recovers the altered selection-level distribution.

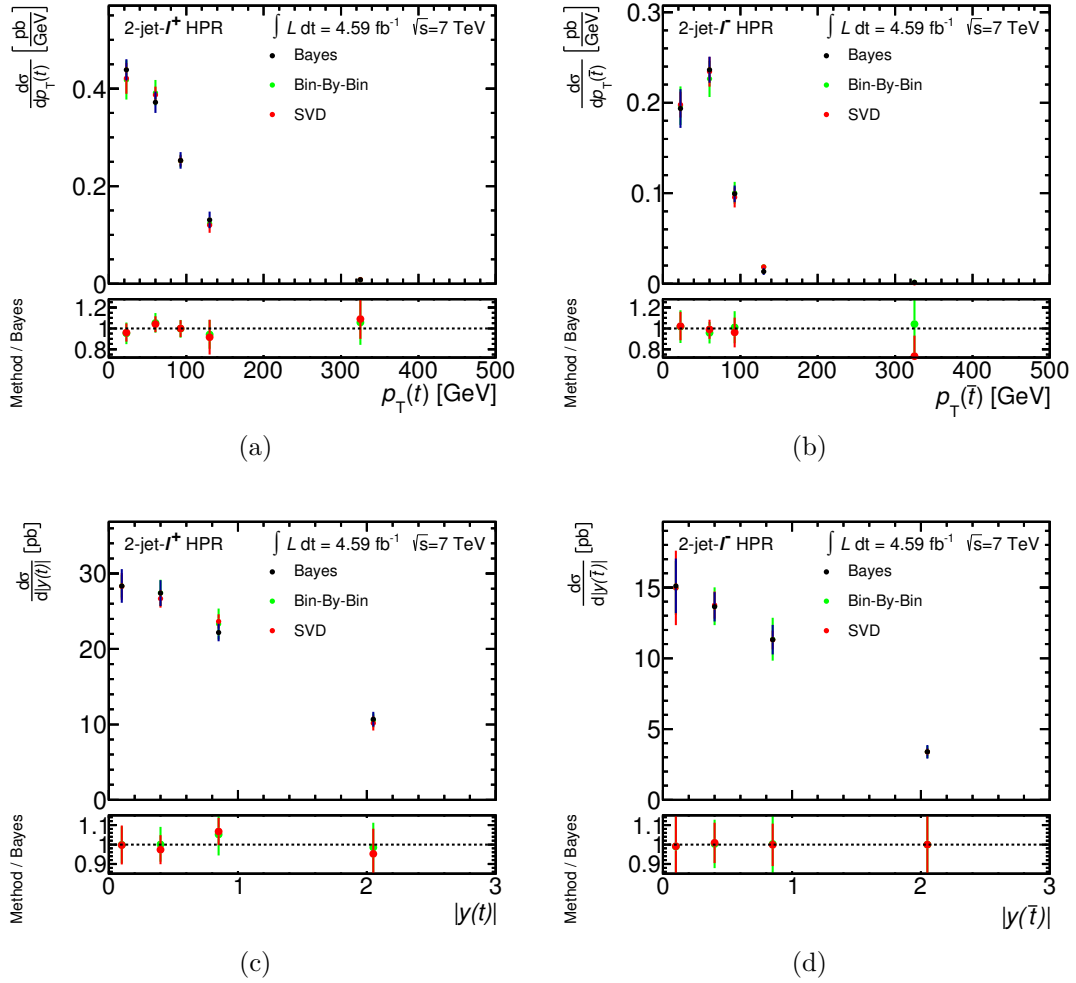


**Figure 6.10:** Comparison between the results of the Bayesian, SVD, and bin-by-bin unfolding methods for (a)  $p_T(t)$ , (b)  $p_T(\bar{t})$ , (c)  $|y(t)|$ , and (d)  $|y(\bar{t})|$ . The error bars represent the uncertainty in data statistics. In the lower panels, the ratio of the unfolded distribution over the unfolding distribution using the Bayesian method is shown.

the migration matrix and the selection efficiency are fluctuated analogously. In each pseudo experiment the background subtraction and the unfolding is performed using the respective fluctuated template. The root-mean square of the spread of results in each bin is taken as the estimator of the uncertainty.

The systematic uncertainties enter the analysis in several places. They affect the background yield, that is subtracted from the measured distribution. Thus, the input to the unfolding process changes. They also affect the migration matrix and the selection efficiency, that are estimated using the signal MC sample. Similar to Section 5.3 the impact of each systematic uncertainty is evaluated using shifted simulated samples. Here, the effect of each uncertainty is analyzed by propagating all shifts to the input of the unfolding process. Then, the unfolding is performed using always the nominal migration matrix and selection efficiency.

The impact of the systematic uncertainties on the background yield is estimated by subtracting the shifted background distributions from the measured data distribution. The resulting distribution is then unfolded, and the difference to the nominal result gives the uncertainty. To assign uncertainties on the signal modeling, the reconstructed distribution of the shifted sample is unfolded and then compared to the nominal simulated distribution on parton level. The relative difference between the shifted and the nominal distribution is applied as uncertainty on the measured result.

To reduce the impact of systematic uncertainties normalized differential cross sections  $1/\sigma \cdot (d\sigma/dX_j)$  are calculated by dividing the differential cross section by the total cross section evaluated by integrating over all bins. For both, the absolute and the normalized differential cross sections, all uncertainties are evaluated as described above.

Systematic uncertainties dominate over the statistical uncertainty in case of the absolute differential cross sections. Large uncertainties originate from the background normalization, the signal generator and parton shower uncertainty, the JES due to the uncertainty in the  $\eta$  intercalibration as well as the PDF uncertainties. Furthermore, a large uncertainty arises from the MC sample size. A detailed list of the contributions of different sources of systematic uncertainties in each bin of each distribution is shown in Appendix B.2 for  $d\sigma/dp_T(t)$ ,  $d\sigma/dp_T(\bar{t})$ ,  $d\sigma/d|y(t)|$ , and  $d\sigma/d|y(\bar{t})|$ . In the case of the normalized differential cross sections, some systematic uncertainties cancel. Thus, the measurement is dominated by the statistical uncertainty, the uncertainty due to the Monte Carlo sample size, and the uncertainty in the choice of the signal generator and parton shower. Details of the contribution of each systematic uncertainty in each bin of the normalized distributions are also given in Appendix B.2.

In summary, for the absolute differential cross-section measurements a precision of 15-25% is achieved in case of  $d\sigma/dp_T(t)$ , 18-74% in case of  $d\sigma/dp_T(\bar{t})$ , 12-15% in case of  $d\sigma/d|y(t)|$ , and 23-29% in case of  $d\sigma/d|y(\bar{t})|$ . The total uncertainty is reduced for the normalized differential cross-section measurements. Thus, the estimated uncertainty is 9-22% for  $1/\sigma d\sigma/dp_T(t)$ , 15-67% for  $1/\sigma d\sigma/dp_T(\bar{t})$ , 8.5-15% for  $1/\sigma d\sigma/d|y(t)|$ , and 17-19% for  $1/\sigma d\sigma/d|y(\bar{t})|$ .

## 6.3 Results

The absolute differential cross-section results are listed in Table 6.2 and the normalized results in Table 6.3 as a function of  $p_T$  and  $|y|$  of the top quark. A graphical representation of the results is shown in Fig. 6.11 for the absolute cross sections and in Fig. 6.12 for the normalized case. They are compared to NLO predictions calculated with MCFM using the MSTW2008 PDF set for all variables. Uncertainties on the predicted values include the uncertainty on the scale choice and the PDF. To compare the NLO prediction with the measurement,  $\chi^2$  values are computed [192] with HERAFitter [34, 193] taking into account the full correlation of the systematic and statistical uncertainties. The  $\chi^2$  values for the non-normalized differential cross sections are listed in Table 6.4.

Bin-wise correlation matrices for the statistical uncertainty are given in Appendix B.3 for the differential cross sections and the normalized differential cross sections.

Overall, good agreement is observed between the NLO predictions and the differential cross-section measurements. This is also supported by the  $\chi^2$  values listed in Table 6.4. A slight deviation is observed in the tail of the differential cross section as a function of the  $p_T(\bar{t})$ , but the deviation is not significant.

Large contributions to the uncertainties on the results arise from the limited size of the data and simulated samples which could be improved in future measurements. With large available statistics the signal purity of the HPR regions can be further increased. Thus, the uncertainty due to the background normalization could be reduced.

**Table 6.2:** Differential  $t$ -channel single top-quark production cross section as a function of  $p_{\text{T}}(t)$ ,  $p_{\text{T}}(\bar{t})$ ,  $|y(t)|$  and  $|y(\bar{t})|$  with the uncertainties for each bin given in percent.

$p_{\text{T}}(t)$ [GeV]	$\frac{d\sigma}{dp_{\text{T}}(t)}$ [ $-\frac{\text{fb}}{\text{GeV}}$ ]	total [%]	stat. [%]	syst. [%]
[0, 45]	$440 \pm 70$	$\pm 15$	$\pm 7.4$	$\pm 13$
[45, 75]	$370 \pm 60$	$\pm 16$	$\pm 6.5$	$\pm 14$
[75, 110]	$250 \pm 40$	$\pm 15$	$\pm 7.7$	$\pm 13$
[110, 150]	$133 \pm 27$	$\pm 20$	$\pm 12$	$\pm 16$
[150, 500]	$7.8 \pm 1.9$	$\pm 25$	$\pm 16$	$\pm 19$
$p_{\text{T}}(\bar{t})$ [GeV]	$\frac{d\sigma}{dp_{\text{T}}(\bar{t})}$ [ $-\frac{\text{fb}}{\text{GeV}}$ ]	total [%]	stat. [%]	syst. [%]
[0, 45]	$190 \pm 50$	$\pm 28$	$\pm 12$	$\pm 25$
[45, 75]	$230 \pm 40$	$\pm 18$	$\pm 8.2$	$\pm 17$
[75, 110]	$97 \pm 27$	$\pm 27$	$\pm 13$	$\pm 24$
[110, 150]	$13.0 \pm 9.7$	$\pm 74$	$\pm 26$	$\pm 70$
[150, 500]	$1.4 \pm 0.9$	$\pm 59$	$\pm 26$	$\pm 53$
$ y(t) $	$\frac{d\sigma}{d y(t) }$ [pb]	total [%]	stat. [%]	syst. [%]
[0, 0.2]	$28 \pm 4$	$\pm 15$	$\pm 9.0$	$\pm 12$
[0.2, 0.6]	$27.3 \pm 3.3$	$\pm 12$	$\pm 6.3$	$\pm 10$
[0.6, 1.1]	$22.1 \pm 3.0$	$\pm 14$	$\pm 7.5$	$\pm 11$
[1.1, 3.0]	$10.7 \pm 1.6$	$\pm 15$	$\pm 7.0$	$\pm 13$
$ y(\bar{t}) $	$\frac{d\sigma}{d y(\bar{t}) }$ [pb]	total [%]	stat. [%]	syst. [%]
[0, 0.2]	$15.0 \pm 3.4$	$\pm 23$	$\pm 13$	$\pm 18$
[0.2, 0.6]	$13.3 \pm 3.3$	$\pm 25$	$\pm 9.5$	$\pm 23$
[0.6, 1.1]	$11.2 \pm 2.6$	$\pm 23$	$\pm 11$	$\pm 20$
[1.1, 3.0]	$3.3 \pm 0.9$	$\pm 29$	$\pm 13$	$\pm 25$

**Table 6.3:** Normalized differential  $t$ -channel single top-quark production cross section as a function of  $p_{\text{T}}(t)$ ,  $p_{\text{T}}(\bar{t})$ ,  $|y(t)|$  and  $|y(\bar{t})|$  with the uncertainties for each bin given in percent.

$p_{\text{T}}(t)$ [GeV]	$\frac{1}{\sigma} \frac{d\sigma}{dp_{\text{T}}(t)} [\frac{10^{-3}}{\text{GeV}}]$	total [%]	stat. [%]	syst. [%]
[0, 45]	$9.2^{+0.8}_{-0.9}$	$^{+8.4}_{-9.4}$	$\pm 5.3$	$^{+6.5}_{-7.7}$
[45, 75]	$7.8 \pm 0.9$	$\pm 11$	$\pm 6.9$	$\pm 8.8$
[75, 110]	$5.3 \pm 0.8$	$\pm 15$	$\pm 8.0$	$\pm 13$
[110, 150]	$2.8 \pm 0.6$	$\pm 21$	$\pm 11$	$\pm 18$
[150, 500]	$0.16 \pm 0.04$	$\pm 22$	$\pm 15$	$\pm 16$
$p_{\text{T}}(\bar{t})$ [GeV]	$\frac{1}{\sigma} \frac{d\sigma}{dp_{\text{T}}(\bar{t})} [\frac{10^{-3}}{\text{GeV}}]$	total [%]	stat. [%]	syst. [%]
[0, 45]	$9.6 \pm 1.6$	$\pm 17$	$\pm 8.2$	$\pm 15$
[45, 75]	$11.6 \pm 1.8$	$\pm 15$	$\pm 8.8$	$\pm 12$
[75, 110]	$4.9 \pm 1.2$	$\pm 25$	$\pm 13$	$\pm 21$
[110, 150]	$0.7 \pm 0.4$	$^{+67}_{-61}$	$\pm 26$	$^{+62}_{-56}$
[150, 500]	$0.07 \pm 0.04$	$\pm 51$	$\pm 26$	$\pm 45$
$ y(t) $	$\frac{1}{\sigma} \frac{d\sigma}{d y(t) }$	total [%]	stat. [%]	syst. [%]
[0, 0.2]	$0.59 \pm 0.09$	$\pm 15$	$\pm 9.0$	$\pm 11$
[0.2, 0.6]	$0.57 \pm 0.05$	$\pm 9.0$	$\pm 6.4$	$\pm 6.3$
[0.6, 1.1]	$0.46 \pm 0.05$	$\pm 9.7$	$\pm 7.5$	$\pm 6.2$
[1.1, 3.0]	$0.223 \pm 0.019$	$\pm 8.5$	$\pm 4.9$	$\pm 6.9$
$ y(\bar{t}) $	$\frac{1}{\sigma} \frac{d\sigma}{d y(\bar{t}) }$	total [%]	stat. [%]	syst. [%]
[0, 0.2]	$0.75 \pm 0.14$	$\pm 19$	$\pm 13$	$\pm 13$
[0.2, 0.6]	$0.66 \pm 0.11$	$\pm 17$	$\pm 9.1$	$\pm 14$
[0.6, 1.1]	$0.555 \pm 0.095$	$\pm 17$	$\pm 11$	$\pm 13$
[1.1, 3.0]	$0.163 \pm 0.030$	$\pm 18$	$\pm 11$	$\pm 15$

**Table 6.4:** Comparison between the measured differential cross sections and the predictions from the NLO calculation using the MSTW2008 PDF set. For each variable and prediction a  $\chi^2$  value is calculated [192] with HERAFitter using the covariance matrix of each measured spectrum. The theory uncertainties of the predictions are treated as uncorrelated. The number of degrees of freedom (NDF) is equal to the number of bins in the measured spectrum.

	$\frac{d\sigma}{dp_{\text{T}}(t)}$	$\frac{d\sigma}{dp_{\text{T}}(\bar{t})}$	$\frac{d\sigma}{d y(t) }$	$\frac{d\sigma}{d y(\bar{t}) }$
$\chi^2/\text{NDF}$	7.55/5	4.68/5	6.30/4	0.32/4

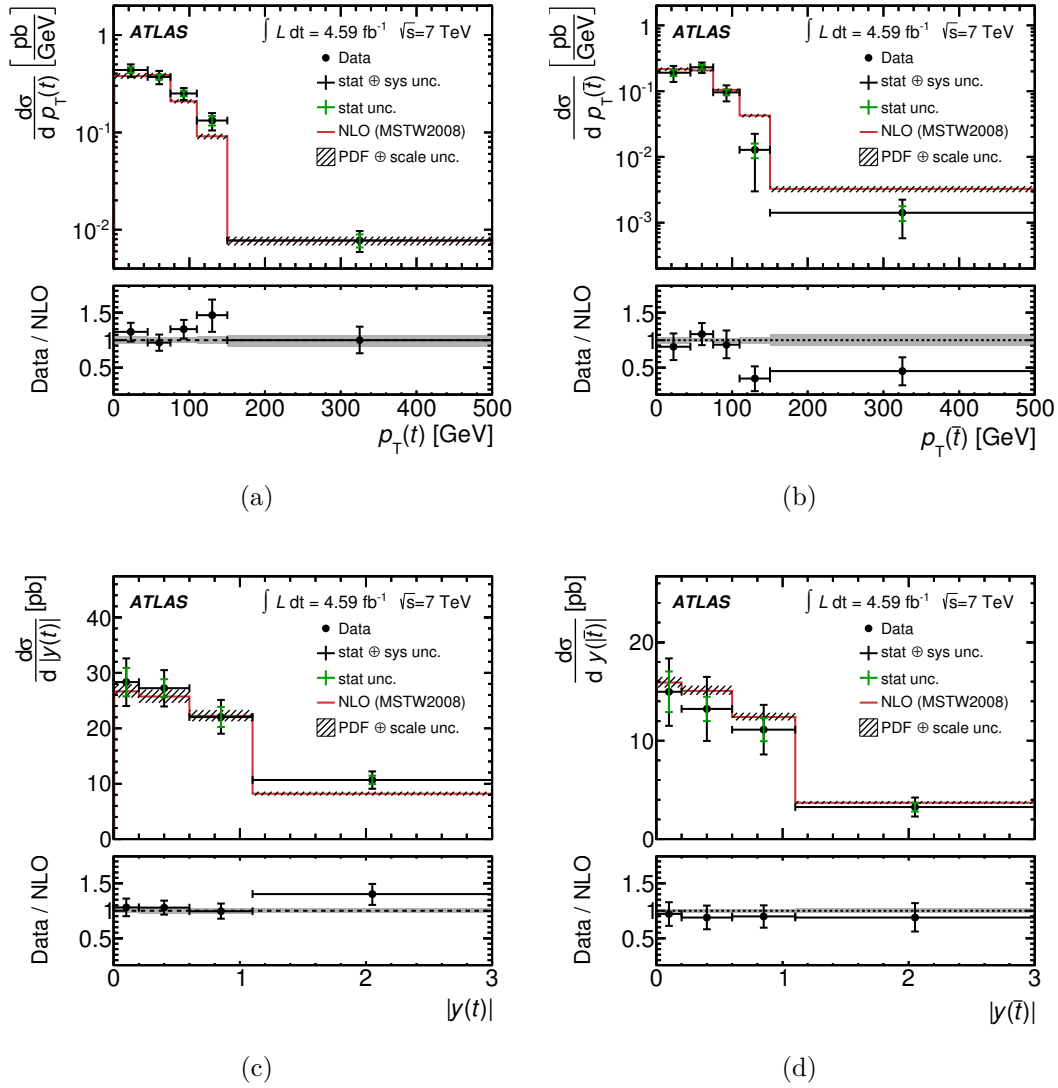


**Figure 6.11:** Differential cross section as a function of (a)  $p_T(t)$ , (b)  $p_T(\bar{t})$ , (c)  $|y(t)|$  and (d)  $|y(\bar{t})|$  [174]. The differential distributions are compared to the QCD NLO calculation. The black vertical error bars on the data points denote the total combined uncertainty, the green error bars denote the statistical uncertainty, while the red line denotes the theory predictions calculated at NLO using MCFM [65]. Uncertainties on the predicted values include the PDF and scale uncertainties. The horizontal error bars indicate the bin width.

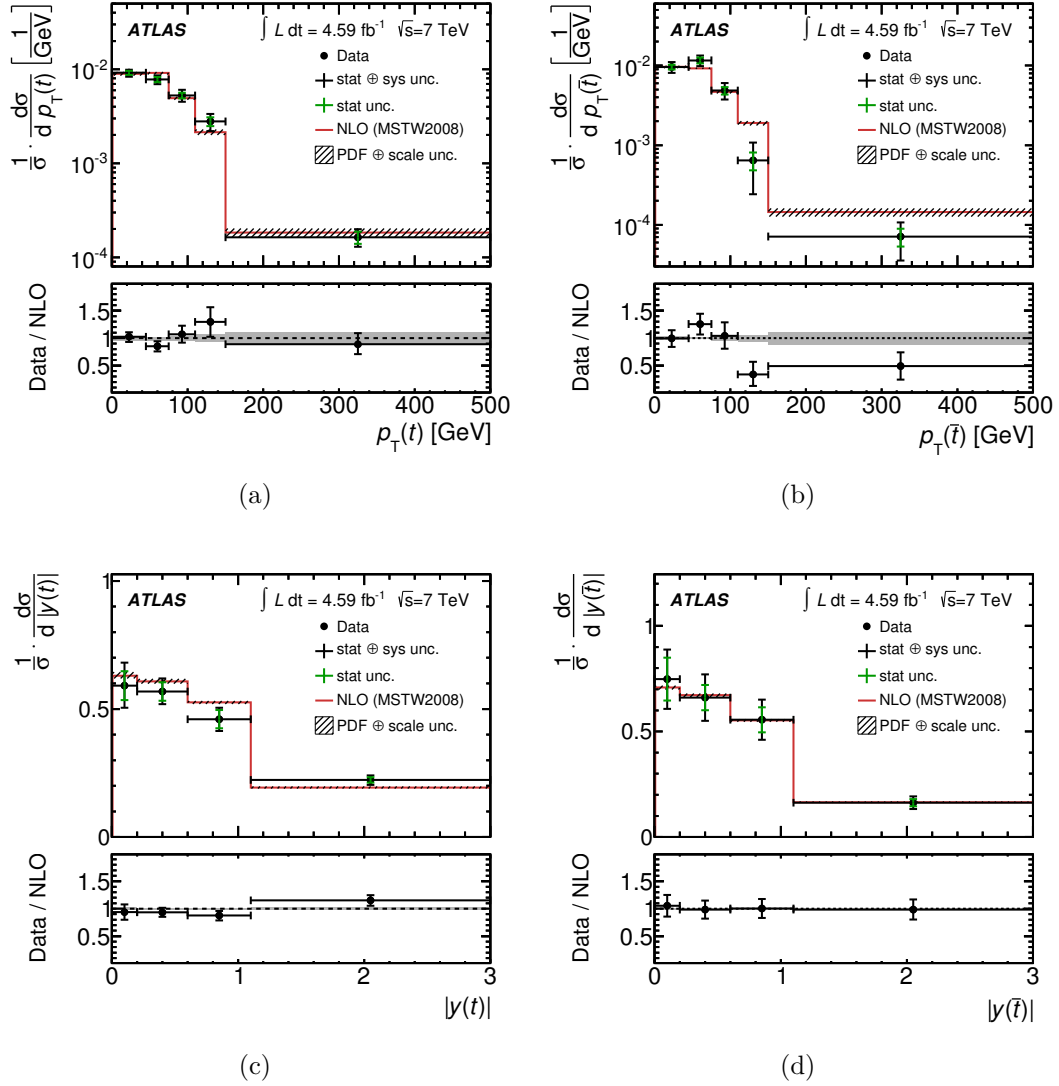


**Figure 6.12:** Normalized differential cross section as a function of (a)  $p_T(t)$ , (b)  $p_T(\bar{t})$ , (c)  $|y(t)|$  and (d)  $|y(\bar{t})|$  [174]. The normalized differential distributions are compared to the QCD NLO calculation. The black vertical error bars on the data points denote the total combined uncertainty, the green error bars denote the statistical uncertainty, while the red line denotes the theory predictions calculated at NLO using MCFM [65]. Uncertainties on the predicted values include the PDF and scale uncertainties. The horizontal error bars indicate the bin width.



# Chapter 7

## Conclusion

In the presented analysis, measurements of the inclusive and differential  $t$ -channel single top-quark production cross-sections are performed using  $4.59 \text{ fb}^{-1}$  of  $pp$ -collision data at  $\sqrt{s} = 7 \text{ TeV}$ , that was recorded by the ATLAS experiment during the 2011 data-taking period. By studying  $t$ -channel single top-quark production, one can gain insights on the electroweak interaction via the  $Wtb$  vertex and on the absolute value of the CKM matrix element  $|V_{tb}|$ . Furthermore, the ratio of the initial-state up-type and down-type quarks can be investigated via the ratio of the produced top quarks and top antiquarks. This value, called  $R_t$ , is then sensitive to the ratio of the  $u$ - and  $d$ -quark PDFs. Moreover, differential measurements of the singly produced top quark are important to validate the kinematic event modeling of  $t$ -channel single top-quark production.

The experimental signature of  $t$ -channel single top-quark candidate events features one isolated charged lepton (electron or muon), large values of missing transverse momentum, and two or three jets. One of the jets is required to be  $b$ -tagged. One of the challenges in the presented analysis is the extraction of signal events amongst a large number of background events. In the 2-jet signal region large background contributions arise equally from  $W$ +jets production and top-quark pair production, while the top-quark pair production dominates the background in the 3-jet signal region. First, a series of selection cuts are applied to the observed events, that were optimized in this analysis to suppress background contributions as much as possible while upholding a good signal-selection efficiency. This way, a signal fraction of about 13% is achieved in the 2-jet signal region and of about 5.4% in the 3-jet signal region. Then, neural networks are trained and used as discriminants in the analysis to separate signal and background events.

The strategy of the presented measurement of the inclusive  $t$ -channel single top-quark cross-section  $\sigma(tq + \bar{t}q)$  is based on the previous ATLAS measurement documented in Ref. [56] and [170] using  $1.04 \text{ fb}^{-1}$  of data. With respect to the previous analysis the precision of the measurement was much improved in this analysis. To reduce the uncertainty in the  $b$ -tagging efficiency correction factor, this factor is now included in the measurement. Thus, a large reduction of over 50% is achieved in this uncertainty contribution. Also, the signal modeling and its uncertainties were studied and changed in the context of this analysis. Furthermore, the uncertainty in

the jet-energy scale was investigated in detail. The resulting inclusive cross section is measured to be

$$\sigma(tq + \bar{t}q) = 68 \pm 2 \text{ (stat.)} \pm 8 \text{ (syst.) pb,}$$

which is consistent with the NLO+NNLL prediction. As a result of the performed optimizations the measurement has a total uncertainty of 12.4% which is about half of the uncertainty given in the previous ATLAS result. The largest remaining uncertainty with a contribution of 7.3% originates from the uncertainty in the modeling of the JES  $\eta$  intercalibration. The sensitivity of the measurement to this uncertainty originates from the most discriminating variable in the 2-jet signal region, the absolute value of pseudorapidity of the untagged jet. For large pseudorapidities, the modeling uncertainty increases due to the different predictions of the compared parton-shower models. If this modeling uncertainty is reduced, a higher precision for  $\sigma(tq + \bar{t}q)$  will be achieved.

Using the measurement of  $\sigma(tq + \bar{t}q)$ , the CKM matrix-element  $|V_{tb}|$  is extracted under the assumption  $|V_{tb}| \gg |V_{td}|, |V_{ts}|$ , resulting in  $|V_{tb}| = 1.02 \pm 0.07$ . Within the uncertainties, the value for  $|V_{tb}|$  is consistent with the prediction of  $|V_{tb}| \approx 1$ . A lower limit of  $|V_{tb}| > 0.88$  is set at the 95% CL assuming  $0 < |V_{tb}| < 1$ .

In the context of this thesis, the analysis was extended to measure the  $t$ -channel single top-quark cross section  $\sigma(tq)$  and top-antiquark cross section  $\sigma(\bar{t}q)$  as well as their ratio  $R_t$  for the first time. First preliminary results on these values were presented in Ref. [194]. In comparison to the preliminary results, all measurements were further optimized in this work. To improve the precision, the same strategies were applied as for the  $\sigma(tq + \bar{t}q)$  measurement. Furthermore, the  $W$ +jets background processes were evaluated taking the lepton-charge asymmetry in each process into account. Thus, the following results are observed:

$$\begin{aligned} \sigma(tq) &= 46 \pm 1 \text{ (stat.)} \pm 6 \text{ (syst.) pb,} \\ \sigma(\bar{t}q) &= 23 \pm 1 \text{ (stat.)} \pm 3 \text{ (syst.) pb} \quad \text{and} \\ R_t &= 2.04 \pm 0.13 \text{ (stat.)} \pm 0.12 \text{ (syst.).} \end{aligned}$$

Currently, the results on  $\sigma(tq)$  and  $\sigma(\bar{t}q)$  are the only published results at  $\sqrt{s} = 7$  TeV achieving a total uncertainty of 12.4% on  $\sigma(tq)$  and 15.9% on  $\sigma(\bar{t}q)$ . Here, the precision was improved by about 10% compared to the preliminary results. Both observed cross sections are consistent with the corresponding NLO+NNLL predictions. The cross-section ratio  $R_t$  is measured with a precision of 8.7%. Its uncertainty is dominated by the data statistic uncertainty. For the measurement of  $R_t$ , a result from the CMS experiment exists using  $pp$ -collision data at  $\sqrt{s} = 8$  TeV [188]. A precision of 11.0% is achieved for  $R_t$ . Thus, the result presented in this thesis is currently the most precise measurement of  $R_t$ . So far, the measurement of  $R_t$  is consistent with all predictions obtained with different PDF sets. But with increasing precision, the measurement of  $R_t$  has the possibility to further constrain the evaluated PDF sets.

The second part of this thesis is the measurement of the differential cross section of  $t$ -channel single top-quark production as a function of the transverse momentum and the rapidity of the top-quark and top-antiquark. The presented measurements

---

were performed for the very first time. Hence, a measurement strategy was developed and successfully executed. First, a high-purity signal region was constructed by placing a selection requirement on the NN discriminants in the 2-jet final state. This way, a signal-to-background ratio of two is achieved for the  $tq$  production and of one for the  $\bar{t}q$  production. Then, the measured  $p_T$  and  $|y|$  distributions are unfolded using an iterative Bayesian approach and subsequently corrected for the selection efficiency. Thus, a precision between 10% and 30% is achieved in most bins of the differential distributions. All measured differential cross sections are well described by the NLO prediction for the transverse momentum and rapidity of the parton-level top quark. Recently, a preliminary measurement of the differential cross section of the combined  $t$ -channel single top-quark and top-antiquark production as a function of the transverse momentum and the rapidity of the top-quark has been presented by the CMS experiment at  $\sqrt{s} = 8$  TeV [195]. These results are also in agreement with the corresponding NLO predictions.

In future measurements, the precision of the differential measurements can be improved by adding to the statistics of the dataset and the simulated compound model as well as by improving the purity of the signal region. Therefore, these measurements will probably be repeated at  $\sqrt{s} = 8$  TeV or even higher center-of-mass energies, where a larger dataset is available.



# Appendix A

## Additional material to Chapter 5

In this appendix additional material to the inclusive cross-section measurements and to the measurement of  $R_t$  is shown.

### A.1 Acceptance uncertainties

**Table A.1:** List of relative acceptance uncertainties for each process given in percent in the 2-jet- $\ell^+$  channel.

Source	$tq$ [%]	$t\bar{t}, Wt, t\bar{b}$ [%]	$W+c$ [%]	$W^++b\bar{b}, c\bar{c}$ , light jets [%]	$Z$ +jets, diboson [%]
JES statistical	+0.2 -0.1	-1.1 +1.3	+3.0 -1.3	+0.9 -1.7	-0.2 -1.4
JES detector	+0.3 -0.0	-0.9 +1.0	+2.8 -1.2	+0.9 -1.5	-0.8 -1.2
JES mixed det. and mod.	+0.3 +0.2	-0.3 +0.3	+1.6 -0.5	+0.1 -0.7	-0.8 -0.1
JES $\eta$ intercalibration	+1.0 -1.0	-2.3 +2.6	+3.3 -1.0	+2.3 -3.7	+2.9 -3.0
JES physics modeling	+0.2 +0.1	-2.0 +1.8	+3.3 -1.7	+1.3 -2.2	+1.9 -2.2
JES close-by jets	-0.1 +0.1	-1.7 +1.6	+2.4 -1.2	-0.6 -0.6	+0.8 -1.0
JES flavor composition	+0.2 +0.3	-1.0 +0.6	+9.2 -7.0	+2.5 -3.7	+5.1 -6.4
JES flavor response	+0.3 +0.2	-1.8 +1.4	+6.3 -3.6	+0.8 -1.7	+2.1 -3.9
$b$ -JES	+0.5 -0.1	-0.7 +0.3	+1.6 -0.2	+0.1 -0.8	+0.5 -0.4
JES pile-up	+0.3 +0.2	-0.3 -0.0	+0.3 +1.3	+0.2 -0.4	-1.0 -0.0
Jet energy resolution	-0.5 +0.5	+0.5 -0.5	+0.3 -0.3	+1.0 -1.0	+3.6 -3.6
Lepton efficiencies	+2.6 -2.6	+2.7 -2.6	+2.6 -2.6	+2.6 -2.6	+2.7 -2.7
Lepton reconstruction (MS)	+0.3 +0.1	+0.1 +0.2	+1.5 +1.4	+0.2 -0.2	-0.3 -0.9
Lepton reconstruction (ID)	+0.3 +0.1	+0.3 +0.1	+0.2 +0.3	+0.4 -0.1	-0.4 -0.3
Lepton energy scale	+0.3 +0.0	-0.3 +0.4	+0.9 +0.9	+0.6 -0.3	-0.3 -1.9
$b$ -tagging efficiency	+7.1 -7.2	+5.0 -5.7	+0.1 -0.1	+3.9 -4.0	+2.4 -2.6
$c$ -tagging efficiency	-0.0 +0.0	+0.0 -0.0	+12.7 -12.7	+1.8 -1.8	+3.6 -3.6
Mistag rate	+0.0 -0.0	+0.0 -0.0	+2.2 -2.2	+8.5 -8.5	+7.8 -7.8
$t\bar{t}$ generation	-	-0.3 +0.3	-	-	-
$W$ +jets shape variations	-	-	+0.2 +0.4	+0.4 +0.6	-
$E_T^{\text{miss}}$ cell-out softjet	+0.5 -0.1	+0.3 -0.6	+2.2 +0.1	+0.0 +0.3	-0.3 -1.6
$E_T^{\text{miss}}$ pile-up	+0.4 -0.0	+0.1 -0.4	+1.8 -0.3	+0.0 -0.1	-1.6 -0.6
Jet vertex fraction	+0.4 -0.6	+1.2 -1.1	+0.8 -0.8	+1.2 -1.0	+1.1 -1.0
PDF	+3.3 -3.3	+8.3 -7.7	-	-	-
$tq$ generator+parton shower	+2.6 -2.6	-	-	-	-
$t\bar{t}$ ISR/FSR	-	-3.3 +3.3	-	-	-
$tq$ scale variations	+2.7 -2.7	-	-	-	-

**Table A.2:** List of relative acceptance uncertainties for each process given in percent in the 2-jet- $\ell^-$  channel.

Source	$\bar{t}q$ [%]	$t\bar{t}, Wt, t\bar{b}$ [%]	$W+c$ [%]	$W^-+b\bar{b}, c\bar{c},$ light jets [%]	$Z$ +jets, diboson [%]
JES statistical	+0.6 -0.0	-1.3 +1.4	+2.0 -1.2	+1.4 -1.0	+1.0 -1.9
JES detector	+0.5 -0.1	-1.0 +1.2	+1.1 -1.0	+1.4 -0.9	+0.7 -1.1
JES mixed det. and mod.	+0.0 +0.2	-0.3 +0.4	+0.7 -0.4	+0.6 -0.3	+0.2 -0.3
JES $\eta$ intercalibration	+1.1 -1.0	-2.1 +3.2	+4.1 -3.4	+1.9 -1.8	+3.6 -3.2
JES physics modeling	-0.1 -0.1	-2.1 +2.5	+2.7 -2.7	+2.4 -1.6	+1.7 -2.4
JES close-by jets	+0.3 +0.3	-1.1 +2.0	+1.7 -1.3	-0.3 -0.5	-0.8 +1.7
JES flavor composition	-0.1 +0.3	-0.4 +1.1	+5.7 -6.1	+4.4 -2.7	+3.8 -5.5
JES flavor response	-0.1 +0.3	-1.8 +1.4	+3.0 -3.5	+3.2 -0.7	+2.4 -4.5
$b$ -JES	+0.4 -0.2	+0.1 +1.0	+0.4 -0.3	+1.4 -0.7	-0.2 +1.3
JES pile-up	-0.1 +0.2	+0.3 +0.5	+0.8 -0.7	-0.3 +0.3	+0.1 -0.2
Jet energy resolution	-0.6 +0.6	-0.5 +0.5	+1.7 -1.7	-0.3 +0.3	+4.2 -4.2
Lepton efficiencies	+2.6 -2.6	+2.6 -2.6	+2.6 -2.6	+2.6 -2.6	+2.7 -2.6
Lepton reconstruction (MS)	+0.1 +0.3	+0.4 +0.6	+0.5 -0.3	+0.5 -0.5	+0.3 -0.5
Lepton reconstruction (ID)	+0.1 +0.3	+0.6 +0.7	-0.3 +0.1	-0.6 +0.2	+0.7 +0.4
Lepton energy scale	+0.3 +0.1	+0.7 +0.1	+0.6 -1.1	+0.9 -0.4	+0.0 -1.7
$b$ -tagging efficiency	+6.9 -7.0	+5.0 -5.7	+0.1 -0.1	+3.7 -3.8	+2.4 -2.5
$c$ -tagging efficiency	-0.0 +0.0	+0.0 -0.0	+12.7 -12.7	+2.0 -2.0	+4.0 -4.0
Mistag rate	+0.0 -0.0	+0.1 -0.1	+2.2 -2.2	+8.6 -8.6	+8.4 -8.4
$t\bar{t}$ generation	-	-0.5 +0.5	-	-	-
$W$ +jets shape variations	-	-	+0.3 +0.5	+0.3 +0.6	-
$E_T^{\text{miss}}$ cell-out softjet	+0.2 +0.2	+0.5 +0.3	-0.1 -0.7	+1.1 -1.2	+1.9 +0.4
$E_T^{\text{miss}}$ pile-up	+0.1 +0.2	+0.4 +0.4	+0.7 -0.1	-0.4 -0.6	+0.6 +0.4
Jet vertex fraction	+0.4 -0.6	+1.2 -1.1	+0.8 -0.8	+1.4 -1.1	+1.1 -1.0
PDF	+5.4 -5.4	+5.0 -5.5	-	-	-
$tq$ generator+parton shower	+1.4 -1.4	-	-	-	-
$t\bar{t}$ ISR/FSR	-	-3.4 +3.4	-	-	-
$tq$ scale variations	+3.6 -3.6	-	-	-	-

**Table A.3:** List of relative acceptance uncertainties for each process given in percent in the 3-jet- $\ell$  channel.

Source	$tq + \bar{t}q$ [%]	$t\bar{t}, Wt, t\bar{b}$ [%]	$W+c$ [%]	$W+b\bar{b}, c\bar{c},$ light jets [%]	$Z$ +jets, diboson [%]
JES statistical	+1.0 -1.3	-0.2 +0.0	+3.2 -2.0	+1.1 -1.1	+2.4 -1.4
JES detector	+1.2 -1.2	-0.2 -0.1	+3.1 -1.5	+0.8 -0.8	+2.1 -1.0
JES mixed det. and mod.	+0.2 -0.1	-0.2 +0.1	+2.0 -0.6	-0.2 -0.2	+0.9 -0.4
JES $\eta$ intercalibration	+3.6 -3.7	-1.1 +0.4	+5.7 -3.6	+2.8 -3.3	+6.0 -3.0
JES physics modeling	+1.8 -1.7	-0.4 +0.1	+3.2 -3.3	+2.4 -1.7	+2.7 -2.1
JES close-by jets	+1.0 -1.2	-0.8 +0.2	+2.6 -1.3	+2.0 -0.6	+1.3 -1.2
JES flavor composition	+0.6 -0.6	-0.5 -0.1	+8.6 -9.2	+6.3 -5.0	+9.7 -6.8
JES flavor response	+0.5 -0.5	-0.7 +0.3	+5.1 -3.9	+3.1 -2.8	+5.4 -3.8
$b$ -JES	+1.4 -1.4	-0.2 -0.4	+0.4 +0.3	+1.2 -0.4	-0.1 -0.1
JES pile-up	+0.1 -0.1	-0.4 -0.1	+0.8 +0.8	-0.7 -0.1	-0.0 -0.0
Jet energy resolution	+0.2 -0.2	-0.6 +0.6	+4.0 -4.0	+2.3 -2.3	+6.4 -6.4
Lepton efficiencies	+2.6 -2.6	+2.6 -2.6	+2.7 -2.6	+2.6 -2.6	+2.7 -2.7
Lepton reconstruction (MS)	+0.2 +0.1	-0.1 +0.1	+0.5 +0.0	-0.2 -0.1	+1.3 +0.9
Lepton reconstruction (ID)	+0.2 +0.1	+0.1 +0.0	-0.4 +0.2	-0.5 -0.4	+0.8 +1.1
Lepton energy scale	+0.2 -0.4	+0.1 -0.3	+1.0 +0.7	-0.5 +0.1	+1.1 +0.1
$b$ -tagging efficiency	+2.5 -3.5	+2.5 -3.6	+0.2 -0.2	+4.1 -4.3	+3.2 -3.4
$c$ -tagging efficiency	-0.0 +0.0	-0.0 +0.0	+12.4 -12.4	+1.9 -1.9	+3.2 -3.2
Mistag rate	-0.0 +0.0	-0.0 +0.0	+4.1 -4.2	+7.6 -7.6	+8.0 -8.0
$t\bar{t}$ generation	-	+0.1 -0.1	-	-	-
$W$ +jets shape variations	-	-	+1.1 +0.1	+1.4 +0.2	-
$E_T^{\text{miss}}$ cell-out softjet	+0.4 +0.1	-0.2 -0.2	+1.6 +1.3	+0.3 +0.1	+0.9 +1.6
$E_T^{\text{miss}}$ pile-up	+0.3 +0.1	+0.2 -0.2	+1.9 +0.6	+0.5 -0.5	+0.6 +0.8
Jet vertex fraction	+0.7 -0.9	+1.2 -1.3	+1.3 -1.2	+1.4 -1.3	+1.5 -1.3
PDF	+3.6 -3.2	+8.3 -7.9	-	-	-
$tq$ generator+parton shower	+9.4 -9.4	-	-	-	-
$t\bar{t}$ ISR/FSR	-	-3.8 +3.8	-	-	-
$tq$ scale variations	+5.2 -5.2	-	-	-	-

**Table A.4:** List of relative acceptance uncertainties for each process given in percent in the 3-jet- $\ell^+$  channel.

Source	$tq$ [%]	$t\bar{t}, Wt, t\bar{b}$ [%]	$W+c$ [%]	$W^++b\bar{b}, c\bar{c},$ light jets [%]	$Z$ +jets, diboson [%]
JES statistical	+0.8 -1.5	-0.3 +0.1	+3.3 -3.0	+1.2 -1.2	+3.1 -1.5
JES detector	+1.0 -1.5	-0.3 -0.1	+3.6 -2.7	+0.8 -0.9	+2.7 -1.4
JES mixed det. and mod.	-0.0 -0.2	-0.1 +0.1	+1.9 -0.8	-0.5 -0.1	+1.2 -0.9
JES $\eta$ intercalibration	+3.4 -4.1	-0.9 +0.3	+5.9 -6.6	+2.8 -3.1	+6.0 -3.1
JES physics modeling	+1.5 -1.8	-0.3 +0.3	+4.0 -5.2	+2.1 -2.0	+3.0 -2.1
JES close-by jets	+0.9 -1.3	-0.8 +0.2	+4.1 -2.4	+1.6 -1.0	+1.4 -1.1
JES flavor composition	+0.7 -1.0	-0.4 -0.2	+8.4 -12.1	+5.8 -5.0	+9.2 -6.0
JES flavor response	+0.7 -0.9	-0.8 +0.3	+6.3 -6.1	+3.1 -2.7	+5.2 -3.5
$b$ -JES	+1.4 -1.7	-0.0 -0.3	-0.1 +0.3	+0.7 -0.8	+0.2 +0.2
JES pile-up	+0.2 -0.5	-0.3 -0.2	+0.6 -0.9	-0.5 +0.0	-0.2 -0.2
Jet energy resolution	-0.3 +0.3	-0.8 +0.8	+4.9 -4.9	+1.9 -1.9	+5.7 -5.7
Lepton efficiencies	+2.6 -2.6	+2.6 -2.6	+2.7 -2.6	+2.6 -2.6	+2.7 -2.7
Lepton reconstruction (MS)	+0.2 -0.1	-0.2 -0.1	+0.7 +0.2	-0.1 -0.2	+1.8 +0.9
Lepton reconstruction (ID)	+0.2 -0.1	+0.1 +0.1	-1.3 +0.5	-0.7 -0.2	+1.1 +1.8
Lepton energy scale	+0.1 -0.5	+0.2 -0.4	+2.0 +1.7	-0.7 -0.3	+0.7 +0.1
$b$ -tagging efficiency	+2.6 -3.6	+2.4 -3.5	+0.2 -0.2	+4.0 -4.2	+3.3 -3.5
$c$ -tagging efficiency	-0.0 +0.0	-0.1 +0.1	+12.4 -12.4	+1.9 -1.9	+3.3 -3.3
Mistag rate	-0.0 +0.0	-0.0 +0.0	+4.1 -4.1	+7.9 -8.0	+7.6 -7.6
$t\bar{t}$ generation	-	+0.1 -0.1	-	-	-
$W$ +jets shape variations	-	-	+1.0 +0.0	+1.6 +0.3	-
$E_T^{\text{miss}}$ cell-out softjet	+0.4 -0.2	-0.3 -0.2	+2.8 +1.6	-0.4 +0.2	+0.9 +1.8
$E_T^{\text{miss}}$ pile-up	+0.3 -0.1	+0.2 -0.4	+1.5 +1.1	-0.1 -0.3	-0.1 +1.6
Jet vertex fraction	+0.7 -0.9	+1.2 -1.3	+1.2 -1.2	+1.6 -1.4	+1.4 -1.3
PDF	+3.3 -3.3	+8.3 -7.9	-	-	-
$tq$ generator+parton shower	+7.1 -3.9	-	-	-	-
$t\bar{t}$ ISR/FSR	-	-3.9 +3.9	-	-	-
$tq$ scale variations	+5.2 -5.2	-	-	-	-

**Table A.5:** List of relative acceptance uncertainties for each process given in percent in the  $3\text{-jet-}\ell^-$  channel.

Source	$\bar{t}q$ [%]	$t\bar{t}, Wt, t\bar{b}$ [%]	$W+c$ [%]	$W^-+b\bar{b},c\bar{c},$ light jets [%]	$Z+\text{jets},$ diboson [%]
JES statistical	+1.5 -1.1	-0.0 -0.0	+3.1 -1.1	+0.9 -1.0	+1.6 -1.3
JES detector	+1.6 -0.7	-0.1 -0.1	+2.5 -0.5	+0.8 -0.6	+1.5 -0.7
JES mixed det. and mod.	+0.7 +0.1	-0.2 +0.1	+2.1 -0.4	+0.3 -0.3	+0.5 +0.1
JES $\eta$ intercalibration	+4.0 -2.8	-1.3 +0.5	+5.5 -0.9	+3.0 -3.7	+6.0 -2.9
JES physics modeling	+2.4 -1.5	-0.5 -0.0	+2.5 -1.6	+2.7 -1.2	+2.4 -2.1
JES close-by jets	+1.2 -1.1	-0.7 +0.3	+1.2 -0.3	+2.6 +0.0	+1.1 -1.3
JES flavor composition	+0.4 +0.1	-0.6 +0.0	+8.8 -6.5	+6.9 -5.0	+10.3 -7.6
JES flavor response	+0.4 +0.1	-0.7 +0.3	+3.9 -1.8	+3.1 -3.0	+5.5 -4.2
$b$ -JES	+1.3 -0.7	-0.4 -0.5	+0.9 +0.2	+1.8 +0.1	-0.3 -0.5
JES pile-up	+0.0 +0.5	-0.4 -0.0	+0.9 +2.4	-1.0 -0.4	+0.2 +0.1
Jet energy resolution	+1.2 -1.2	-0.3 +0.3	+3.2 -3.2	+3.0 -3.0	+7.1 -7.1
Lepton efficiencies	+2.6 -2.6	+2.6 -2.6	+2.7 -2.6	+2.6 -2.6	+2.7 -2.7
Lepton reconstruction (MS)	+0.3 +0.4	+0.0 +0.2	+0.4 -0.2	-0.2 +0.2	+0.7 +1.0
Lepton reconstruction (ID)	+0.3 +0.5	+0.0 -0.1	+0.5 -0.1	-0.1 -0.8	+0.4 +0.4
Lepton energy scale	+0.4 -0.0	+0.1 -0.2	+0.2 -0.2	-0.1 +0.6	+1.5 +0.0
$b$ -tagging efficiency	+2.3 -3.3	+2.6 -3.7	+0.1 -0.1	+4.1 -4.3	+3.1 -3.3
$c$ -tagging efficiency	-0.0 +0.0	-0.0 +0.0	+12.4 -12.4	+1.9 -1.9	+3.1 -3.1
Mistag rate	+0.0 -0.0	-0.0 +0.0	+4.2 -4.2	+7.1 -7.1	+8.3 -8.4
$t\bar{t}$ generation	-	+0.1 -0.1	-	-	-
$W$ +jets shape variations	-	-	+1.1 +0.1	+1.2 +0.1	-
$E_T^{\text{miss}}$ cell-out softjet	+0.6 +0.5	-0.1 -0.1	+0.6 +1.0	+1.3 +0.0	+0.9 +1.4
$E_T^{\text{miss}}$ pile-up	+0.3 +0.5	+0.1 -0.1	+2.4 +0.0	+1.5 -0.8	+1.4 -0.0
Jet vertex fraction	+0.7 -0.9	+1.2 -1.3	+1.3 -1.2	+1.2 -1.2	+1.5 -1.4
PDF	+7.0 -7.0	+8.4 -7.9	-	-	-
$tq$ generator+parton shower	+5.6 -5.6	-	-	-	-
$t\bar{t}$ ISR/FSR	-	-3.7 +3.7	-	-	-
$tq$ scale variations	+5.2 -5.2	-	-	-	-

**Table A.6:** List of relative acceptance uncertainties for each process given in percent in the 3-jet-2-tag channel.

Source	$tq + \bar{t}q$ [%]	$t\bar{t}, Wt, t\bar{b}$ [%]	$W+c$ [%]	$W+b\bar{b}, c\bar{c}$ , light jets [%]	$Z$ +jets, diboson [%]
JES statistical	+0.2 -1.2	-0.2 +0.1	-3.2 +15.3	+1.4 -1.5	+0.8 -1.1
JES detector	+0.5 -1.6	+0.1 -0.0	-3.2 +0.0	+0.9 -0.7	+0.7 -0.1
JES mixed det. and mod.	+0.5 -0.7	-0.1 +0.1	-3.2 +0.0	+0.4 -1.1	+0.0 -0.1
JES $\eta$ intercalibration	+1.7 -1.8	-1.0 +1.2	-1.1 +17.2	-1.5 -2.0	-1.5 -0.2
JES physics modeling	+1.5 -1.8	-0.3 +0.0	+1.1 +15.3	+2.5 -0.9	+1.7 -2.3
JES close-by jets	-0.3 -0.9	-0.4 +0.8	-2.0 +1.5	+0.4 -1.8	-3.4 -0.9
JES flavor composition	-0.8 -0.2	-0.8 +0.9	-1.4 +17.0	-0.3 -0.5	+4.9 -5.1
JES flavor response	-0.8 -0.3	-1.4 +1.3	-0.8 +16.5	+0.1 +0.6	+1.2 -5.1
$b$ -JES	+1.1 -2.4	+1.1 -0.7	-2.0 +1.5	+3.2 -4.4	+1.1 -6.1
JES pile-up	-0.7 -0.6	-0.3 +0.4	-2.7 +1.5	-1.4 -1.9	-3.0 -1.0
Jet energy resolution	-0.7 +0.7	-0.8 +0.8	+0.4 -0.4	+0.9 -0.9	+7.2 -7.2
Lepton efficiencies	+2.6 -2.6	+2.6 -2.6	+3.0 -3.0	+2.6 -2.6	+2.7 -2.7
Lepton reconstruction (MS)	-0.2 -0.8	+0.2 -0.2	-2.6 -2.0	-1.2 -1.0	-3.0 -1.5
Lepton reconstruction (ID)	-0.2 -0.8	+0.2 -0.0	+2.3 -2.0	-0.4 -1.8	-3.3 -0.5
Lepton energy scale	-0.5 -0.5	-0.1 -0.2	+0.1 +2.3	+0.1 -0.7	+2.0 -1.8
$b$ -tagging efficiency	+18.3 -16.7	+18.3 -16.7	-	+16.6 -15.2	+13.2 -12.3
$c$ -tagging efficiency	+0.1 -0.1	+0.4 -0.4	+16.6 -15.8	+1.8 -1.7	+2.0 -2.0
Mistag rate	+0.4 -0.4	+0.3 -0.3	+19.5 -19.5	+3.4 -3.0	+9.7 -8.2
$t\bar{t}$ generation	-	+2.9 -2.9	-	-	-
$W$ +jets shape variations	-	-	-0.1 -0.5	+1.5 +0.3	-
$E_T^{\text{miss}}$ cell-out softjet	-0.0 -1.2	+0.0 +0.4	-2.0 -2.8	-3.5 +0.6	+0.4 -0.7
$E_T^{\text{miss}}$ pile-up	-0.1 -0.8	+0.3 +0.2	+0.1 -0.6	-1.8 +0.6	-4.5 -0.5
Jet vertex fraction	+0.6 -0.9	+1.1 -1.2	+1.3 -1.3	+1.2 -1.2	+2.4 -1.7
PDF	-	+8.3 -7.9	-	-	-
$tq$ generator+parton shower	+11.4 -11.4	-	-	-	-
$t\bar{t}$ ISR/FSR	-	-8.2 +8.2	-	-	-
$tq$ scale variations	+7.2 -7.2	-	-	-	-



# Appendix B

## Additional material to Chapter 6

In this appendix additional material to the differential cross-section measurements is shown.

### B.1 Selection efficiency in the HPR

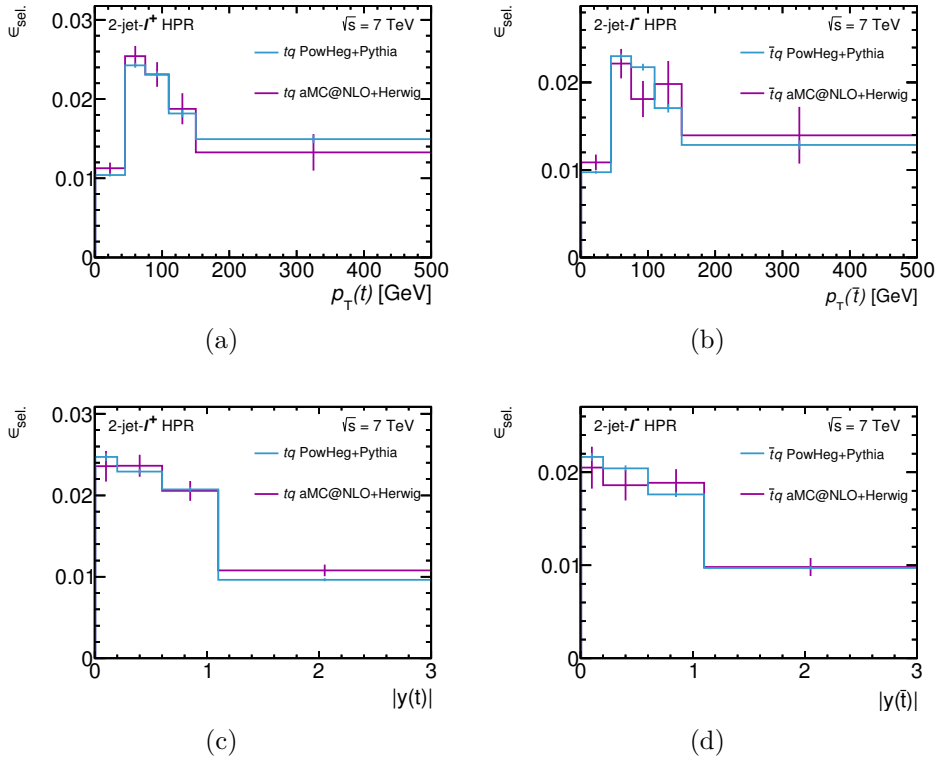


**Figure B.1:** Selection efficiencies in each bin of the (a) top-quark  $p_T$ , (b) top-antiquark  $p_T$ , (c) top-quark  $|y|$ , and (d) top-antiquark  $|y|$  distribution. The selection efficiency  $\epsilon_j$  in each bin  $j$  of each variable is defined as the ratio of the parton-level yield before and after event selection and is evaluated using simulation.

## B.2 Detailed list of uncertainties

**Table B.1:** Detailed list of the contribution of each source of uncertainty to the total relative uncertainty on the measured  $\frac{d\sigma}{dp_T(t)}$  distribution given in percent for each bin. The list includes only those uncertainties that contribute with more than 1%. The following uncertainties contribute to the total uncertainty with less than 1% to each bin content: JES detector, JES statistical, JES physics modeling, JES mixed detector and modeling, JES close-by jets, JES pile-up, JES flavor composition, JES flavor response, jet vertex fraction,  $b/\bar{b}$  acceptance,  $E_T^{\text{miss}}$  modeling,  $W$  +jets shape variation, and  $t\bar{t}$  generator.

$\frac{d\sigma}{dp_T(t)}$	$p_T(t)$ bins [GeV]				
	[0, 45]	[45, 75]	[75, 110]	[110, 150]	[150, 500]
Data statistical	$\pm 7.4$	$\pm 6.5$	$\pm 7.7$	$\pm 12$	$\pm 16$
Monte Carlo statistical	$\pm 5.5$	$\pm 5.3$	$\pm 4.8$	$\pm 6.0$	$\pm 9.4$
Background normalization	$\pm 6.1$	$\pm 7.5$	$\pm 5.2$	$\pm 3.0$	$\pm 5.2$
JES $\eta$ intercalibration	$< 1$	$^{+2.6}_{-1.3}$	$^{+3.4}_{-1.9}$	$< 1$	$^{+9.0}_{-4.2}$
$b$ -JES	$< 1$	$^{+1.2}_{-2.3}$	$< 1$	$\pm 1.6$	$< 1$
Jet energy resolution	$\pm 1.0$	$\pm 2.4$	$\pm 2.3$	$\pm 3.0$	$< 1$
$b$ -tagging efficiency	$\pm 3.0$	$\pm 3.1$	$\pm 3.3$	$\pm 3.6$	$\pm 6.2$
$c$ -tagging efficiency	$\pm 1.3$	$\pm 1.5$	$< 1$	$< 1$	$< 1$
Mistag rate	$\pm 2.0$	$\pm 1.9$	$< 1$	$< 1$	$\pm 1.2$
Lepton uncertainties	$\pm 2.6$	$\pm 2.6$	$\pm 2.6$	$\pm 2.6$	$\pm 2.6$
PDF	$\pm 3.0$	$\pm 1.8$	$\pm 2.3$	$\pm 2.8$	$\pm 2.4$
$tq$ generator + parton shower	$\pm 6.8$	$\pm 8.2$	$\mp 7.9$	$\mp 12$	$^{+9.2}_{-9.7}$
$tq$ scale variation	$\pm 2.8$	$< 1$	$\pm 3.7$	$< 1$	$^{+6.0}_{-6.4}$
Unfolding	$\pm 1.3$	$\pm 1.4$	$< 1$	$< 1$	$< 1$
Luminosity	$\pm 1.8$	$\pm 1.8$	$\pm 1.8$	$\pm 1.8$	$\pm 1.8$
Total systematic	$\pm 13$	$\pm 14$	$\pm 13$	$\pm 16$	$\pm 19$
Total	$\pm 15$	$\pm 16$	$\pm 15$	$\pm 20$	$\pm 25$

**Table B.2:** Detailed list of the contribution of each source of uncertainty to the total relative uncertainty on the measured  $\frac{d\sigma}{dp_T(\bar{t})}$  distribution given in percent for each bin. The list includes only those uncertainties that contribute with more than 1%. The following uncertainties contribute to the total uncertainty with less than 1% to each bin content: JES detector, JES statistical, JES physics modeling, JES mixed detector and modeling, JES close-by jets, JES pile-up, JES flavor composition, JES flavor response,  $b$ -JES, jet vertex fraction, mistag rate,  $b/\bar{b}$  acceptance,  $E_T^{\text{miss}}$  modeling,  $W$  +jets shape variation, and  $t\bar{t}$  generator.

$\frac{d\sigma}{dp_T(\bar{t})}$	$p_T(\bar{t})$ bins [GeV]				
	[0, 45]	[45, 75]	[75, 110]	[110, 150]	[150, 500]
Data statistical	$\pm 12$	$\pm 8.2$	$\pm 13$	$\pm 26$	$\pm 26$
Monte Carlo statistical	$\pm 12$	$\pm 9.1$	$\pm 14$	$\pm 28$	$\pm 28$
Background normalization	$\pm 14$	$\pm 11$	$\pm 16$	$\pm 48$	$\pm 33$
JES $\eta$ intercalibration	$-9.0$ $+8.7$	$+1.9$ $-3.7$	$+4.9$ $-1.3$	$+15$ $-13$	$< 1$
Jet energy resolution	$\pm 1.0$	$\pm 2.2$	$\pm 3.4$	$< 1$	$\pm 3.0$
$b$ -tagging efficiency	$\pm 3.0$	$\pm 3.1$	$\pm 3.2$	$\pm 3.6$	$\pm 5.9$
$c$ -tagging efficiency	$\pm 5.6$	$\pm 2.0$	$\pm 2.2$	$\pm 10$	$\pm 5.9$
Lepton uncertainties	$\pm 2.6$	$\pm 2.6$	$\pm 2.6$	$\pm 2.6$	$\pm 2.7$
PDF	$\pm 3.8$	$\pm 4.3$	$\pm 5.3$	$\pm 7.2$	$\pm 8.2$
$tq$ generator + parton shower	$\pm 12.2$	$< 1$	$\mp 9.6$	$\pm 11$	$< 1$
$tq$ scale variation	$\pm 3.1$	$< 1$	$\pm 3.2$	$\pm 1.9$	$\pm 5.9$
Unfolding	$< 1$	$< 1$	$< 1$	$\pm 6.9$	$\pm 2.6$
Luminosity	$\pm 1.8$	$\pm 1.8$	$\pm 1.8$	$\pm 1.8$	$\pm 1.8$
Total systematic	$\pm 25$	$\pm 17$	$\pm 24$	$\pm 70$	$\pm 53$
Total	$\pm 27$	$\pm 18$	$\pm 27$	$\pm 74$	$\pm 59$

**Table B.3:** Detailed list of the contribution of each source of uncertainty to the total relative uncertainty on the measured  $\frac{d\sigma}{d|y(t)|}$  distribution given in percent for each bin. The list includes only those uncertainties that contribute with more than 1%. The following uncertainties contribute to the total uncertainty with less than 1% to each bin content: JES detector, JES statistical, JES physics modeling, JES mixed detector and modeling, JES close-by jets, JES pile-up, JES flavor composition, JES flavor response, jet vertex fraction,  $b/\bar{b}$  acceptance,  $E_T^{\text{miss}}$  modeling,  $W$ +jets shape variation,  $t\bar{t}$  generator,  $t\bar{t}$  ISR/FSR, and unfolding.

$\frac{d\sigma}{d y(t) }$	$ y(t) $ bins			
	[0, 0.2]	[0.2, 0.6]	[0.6, 1.1]	[1.1, 3.0]
Data statistical	$\pm 9.0$	$\pm 6.3$	$\pm 7.5$	$\pm 7.1$
Monte Carlo statistical	$\pm 5.9$	$\pm 4.8$	$\pm 5.0$	$\pm 4.4$
Background normalization	$\pm 5.3$	$\pm 6.5$	$\pm 6.7$	$\pm 4.7$
JES $\eta$ intercalibration	$^{+1.7}_{-0.6}$	$< 1$	$^{+1.7}_{-0.4}$	$< 1$
b-JES	$^{+1.1}_{-1.7}$	$< 1$	$^{+1.1}_{+0.2}$	$< 1$
Jet energy resolution	$\pm 3.2$	$\pm 1.7$	$< 1$	$\pm 3.1$
$b$ -tagging efficiency	$\pm 3.3$	$\pm 3.4$	$\pm 3.4$	$\pm 3.2$
$c$ -tagging efficiency	$\pm 1.3$	$\pm 1.2$	$\pm 1.2$	$\pm 1.0$
Mistag rate	$< 1$	$\pm 1.3$	$\pm 2.0$	$\pm 1.4$
Lepton uncertainties	$\pm 2.6$	$\pm 2.7$	$\pm 2.6$	$\pm 2.5$
PDF	$\pm 3.6$	$\pm 3.6$	$\pm 2.8$	$\pm 2.8$
$tq$ generator + parton shower	$\mp 5.7$	$\pm 0.8$	$\pm 4.0$	$\pm 8.7$
$tq$ scale variation	$\pm 3.5$	$< 1$	$\pm 2.6$	$\pm 4.7$
Luminosity	$\pm 1.8$	$\pm 1.8$	$\pm 1.8$	$\pm 1.8$
Total systematic	$\pm 12$	$\pm 10$	$\pm 11$	$\pm 14$
Total	$\pm 15$	$\pm 12$	$\pm 14$	$\pm 15$

**Table B.4:** Detailed list of the contribution of each source of uncertainty to the total relative uncertainty on the measured  $\frac{d\sigma}{d|y(\bar{t})|}$  distribution given in percent for each bin. The list includes only those uncertainties that contribute with more than 1%. The following uncertainties contribute to the total uncertainty with less than 1% to each bin content: JES detector, JES statistical, JES physics modeling, JES mixed detector and modeling, JES close-by jets, JES pile-up, JES flavor composition, JES flavor response, b-JES, jet vertex fraction,  $b/\bar{b}$  acceptance, mistag rate,  $E_{\text{T}}^{\text{miss}}$  modeling,  $W$  +jets shape variation,  $t\bar{t}$  generator,  $t\bar{t}$  ISR/FSR, and unfolding.

$\frac{d\sigma}{d y(\bar{t}) }$	$ y(\bar{t}) $ bins			
	[0, 0.2]	[0.2, 0.6]	[0.6, 1.1]	[1.1, 3.0]
Data statistical	$\pm 13$	$\pm 9.5$	$\pm 11$	$\pm 13$
Monte Carlo statistical	$\pm 11$	$\pm 12$	$\pm 11$	$\pm 17$
Background normalization	$\pm 11$	$\pm 16$	$\pm 13$	$\pm 15$
JES $\eta$ intercalibration	$< 1$	$^{+1.0}_{-1.8}$	$< 1$	$^{+2.3}_{-0.9}$
Jet energy resolution	$\pm 2.3$	$\pm 2.2$	$\pm 1.0$	$\pm 3.2$
$b$ -tagging efficiency	$\pm 3.4$	$\pm 3.3$	$\pm 3.2$	$\pm 3.2$
$c$ -tagging efficiency	$\pm 2.5$	$\pm 3.6$	$\pm 2.9$	$\pm 4.0$
Lepton uncertainties	$\pm 2.7$	$\pm 2.7$	$\pm 2.6$	$\pm 2.4$
PDF	$\pm 6.0$	$\pm 5.3$	$\pm 4.4$	$\pm 4.1$
$tq$ generator + parton shower	$\pm 1.0$	$\mp 5.6$	$\pm 6.6$	$\pm 6.2$
$tq$ scale variation	$\pm 2.1$	$\pm 2.6$	$\pm 1.6$	$\pm 4.3$
Luminosity	$\pm 1.8$	$\pm 1.8$	$\pm 1.8$	$\pm 1.8$
Total systematic	$\pm 18$	$\pm 23$	$\pm 20$	$\pm 25$
Total	$\pm 23$	$\pm 25$	$\pm 23$	$\pm 29$

**Table B.5:** Detailed list of the contribution of each source of uncertainty to the total relative uncertainty on the measured  $\frac{1}{\sigma} \frac{d\sigma}{dp_T(t)}$  distribution given in percent for each bin. The list includes only those uncertainties that contribute with more than 1%. The JES  $\eta$  intercalibration uncertainty has a sign switch from the first to the second bin. For the  $tq$  generator + parton shower uncertainty a sign switch is denoted with  $\mp$ . The following uncertainties contribute to the total uncertainty with less than 1% to each bin content: JES detector, JES statistical, JES physics modeling, JES mixed detector and modeling, JES close-by jets, JES pile-up, JES flavor composition, JES flavor response,  $b$ -JES, jet vertex fraction,  $b/\bar{b}$  acceptance,  $c$ -tagging efficiency,  $E_T^{\text{miss}}$  modeling, lepton uncertainties,  $W$ +jets shape variation, and  $t\bar{t}$  generator.

$\frac{1}{\sigma} \frac{d\sigma}{dp_T(t)}$	$p_T(t)$ bins [GeV]				
	[0, 45]	[45, 75]	[75, 110]	[110, 150]	[150, 500]
Source					
Data statistical	$\pm 5.3$	$\pm 6.9$	$\pm 8.0$	$\pm 11$	$\pm 15$
Monte Carlo statistical	$\pm 4.2$	$\pm 5.5$	$\pm 5.2$	$\pm 6.2$	$\pm 9.3$
Background normalization	$< 1$	$\pm 1.7$	$< 1$	$\pm 3.0$	$< 1$
JES $\eta$ intercalibration	$-4.7$ $+1.5$	$+3.5$ $-2.3$	$+4.1$ $-0.8$	$< 1$	$+9.6$ $-3.1$
Jet energy resolution	$< 1$	$< 1$	$< 1$	$\mp 1.4$	$\pm 2.7$
$b$ -tagging efficiency	$< 1$	$< 1$	$< 1$	$< 1$	$\pm 2.8$
Mistag rate	$< 1$	$< 1$	$< 1$	$\pm 1.0$	$< 1$
$tq$ generator + parton shower	$\pm 3.9$	$\pm 5.4$	$\mp 11$	$\mp 14$	$\pm 6.9$
$tq$ scale variation	$< 1$	$\mp 1.8$	$\pm 1.3$	$\mp 2.7$	$+4.4$ $-5.1$
Unfolding	$< 1$	$\pm 1.7$	$< 1$	$< 1$	$\pm 1.1$
Total systematic	$+6.5$ $-7.7$	$\pm 8.8$	$\pm 13$	$\pm 18$	$\pm 16$
Total	$+8.4$ $-9.4$	$\pm 11$	$\pm 15$	$\pm 21$	$\pm 22$

**Table B.6:** Detailed list of the contribution of each source of uncertainty to the total relative uncertainty on the measured  $\frac{1}{\sigma} \frac{d\sigma}{dp_T(\bar{t})}$  distribution given in percent for each bin. The list includes only those uncertainties that contribute with more than 1%. Sign switches within one uncertainty are denoted with  $\mp$  and  $\pm$ . The following uncertainties contribute to the total uncertainty with less than 1% to each bin content: JES detector, JES statistical, JES physics modeling, JES mixed detector and modeling, JES close-by jets, JES pile-up, JES flavor composition, JES flavor response,  $b$ -JES, jet vertex fraction,  $b/\bar{b}$  acceptance, mistag rate,  $E_T^{\text{miss}}$  modeling, lepton uncertainties,  $W$  +jets shape variation, and  $t\bar{t}$  generator.

$\frac{1}{\sigma} \frac{d\sigma}{dp_T(\bar{t})}$	$p_T(\bar{t})$ bins [GeV]				
	[0, 45]	[45, 75]	[75, 110]	[110, 150]	[150, 500]
Data statistical	$\pm 8.2$	$\pm 8.8$	$\pm 13$	$\pm 26$	$\pm 26$
Monte Carlo statistical	$\pm 8.7$	$\pm 9.6$	$\pm 14$	$\pm 28$	$\pm 27$
Background normalization	$< 1$	$\pm 4.5$	$\pm 1.8$	$\pm 39$	$\pm 22$
JES $\eta$ intercalibration	$-7.5$ $+6.7$	$+3.8$ $-5.3$	$+6.9$ $-3.1$	$+17$ $-9.9$	$< 1$
Jet energy resolution	$< 1$	$< 1$	$\mp 1.6$	$\pm 1.8$	$\mp 1.2$
$b$ -tagging efficiency	$< 1$	$< 1$	$< 1$	$< 1$	$+2.4$ $-2.8$
$c$ -tagging efficiency	$\mp 1.8$	$\pm 2.0$	$\pm 1.7$	$-6.2$ $+5.9$	$\mp 2.0$
PDF	$< 1$	$< 1$	$< 1$	$\pm 2.5$	$\pm 3.6$
$tq$ generator + parton shower	$+7.7$ $-8.2$	$-3.6$ $+3.7$	$-13$ $+14$	$+6.4$ $-7.0$	$-4.2$ $+4.5$
$tq$ scale variation	$\pm 1.3$	$\mp 3.0$	$\pm 1.4$	$\mp 1.8$	$\pm 5.1$
Unfolding	$< 1$	$< 1$	$< 1$	$\pm 6.7$	$\pm 2.8$
Total systematic	$\pm 15$	$\pm 13$	$\pm 21$	$+62$ $-56$	$\pm 45$
Total	$\pm 17$	$\pm 15$	$\pm 25$	$+67$ $-61$	$\pm 52$

**Table B.7:** Detailed list of the contribution of each source of uncertainty to the total relative uncertainty on the measured  $\frac{1}{\sigma} \frac{d\sigma}{d|y(t)|}$  distribution given in percent for each bin. The list includes only those uncertainties that contribute with more than 1%. Sign switches within one uncertainty are denoted with  $\mp$  and  $\pm$ . The following uncertainties contribute to the total uncertainty with less than 1% to each bin content: JES detector, JES statistical, JES physics modeling, JES mixed detector and modeling, JES close-by jets, JES pile-up, JES flavor composition, JES flavor response, b-JES, jet vertex fraction,  $b/\bar{b}$  acceptance, b-tagging efficiency, c-tagging efficiency, mistag rate,  $E_T^{\text{miss}}$  modeling, lepton uncertainties,  $W$ +jets shape variation,  $t\bar{t}$  generator,  $t\bar{t}$  ISR/FSR, and unfolding.

$\frac{1}{\sigma} \frac{d\sigma}{d y(t) }$	$ y(t) $ bins			
	[0, 0.2]	[0.2, 0.6]	[0.6, 1.1]	[1.1, 3.0]
Data statistical	$\pm 9.0$	$\pm 6.4$	$\pm 7.5$	$\pm 5.0$
Monte Carlo statistical	$\pm 5.9$	$\pm 4.8$	$\pm 4.9$	$\pm 3.2$
Background normalization	$< 1$	$< 1$	$\pm 1.1$	$\pm 1.0$
JES $\eta$ intercalibration	+1.6 -1.5	-0.5 +2.3	+1.4 -1.5	$< 1$
Jet energy resolution	$\pm 1.2$	$< 1$	$\mp 1.6$	$\pm 1.0$
PDF	$\pm 1.7$	$\pm 1.8$	$< 1$	$\pm 2.3$
$tq$ generator + parton shower	-9.0 +9.8	-2.8 +3.0	$< 1$	+4.8 -5.2
$tq$ scale variation	$< 1$	$< 1$	$< 1$	$\pm 1.5$
Total systematic	$\pm 11$	$\pm 6.3$	$\pm 6.2$	$\pm 6.9$
Total	$\pm 15$	$\pm 9.0$	$\pm 9.7$	$\pm 8.5$

**Table B.8:** Detailed list of the contribution of each source of uncertainty to the total relative uncertainty on the measured  $\frac{1}{\sigma} \frac{d\sigma}{d|y(\bar{t})|}$  distribution given in percent for each bin. The list includes only those uncertainties that contribute with more than 1%. Sign switches within one uncertainty are denoted with  $\mp$  and  $\pm$ . The following uncertainties contribute to the total uncertainty with less than 1% to each bin content: JES detector, JES statistical, JES physics modeling, JES mixed detector and modeling, JES close-by jets, JES pile-up, JES flavor composition, JES flavor response,  $b$ -JES, jet energy resolution, jet vertex fraction,  $b/\bar{b}$  acceptance,  $b$ -tagging efficiency,  $c$ -tagging efficiency, mistag rate,  $E_T^{\text{miss}}$  modeling, lepton uncertainties,  $W$  +jets shape variation,  $t\bar{t}$  generator,  $t\bar{t}$  ISR/FSR, and unfolding.

$\frac{1}{\sigma} \frac{d\sigma}{d y(\bar{t}) }$	$ y(\bar{t}) $ bins			
	[0, 0.2]	[0.2, 0.6]	[0.6, 1.1]	[1.1, 3.0]
Data statistical	$\pm 13$	$\pm 9.1$	$\pm 11$	$\pm 11$
Monte Carlo statistical	$\pm 12$	$\pm 11$	$\pm 12$	$\pm 14$
Background normalization	$\pm 3.4$	$\pm 2.4$	$\pm 1.1$	$< 1$
JES $\eta$ intercalibration	$< 1$	$^{+0.5}_{-1.9}$	$< 1$	$^{+1.5}_{-0.8}$
PDF	$\pm 1.6$	$\pm 1.0$	$< 1$	$\pm 1.8$
$tq$ generator + parton shower	$\mp 1.4$	$^{-7.8}_{+8.2}$	$^{+4.0}_{-4.3}$	$^{+3.8}_{-3.9}$
$tq$ scale variation	$\pm 1.9$	$< 1$	$< 1$	$< 1$
Total systematic	$\pm 13$	$\pm 14$	$\pm 13$	$\pm 15$
Total	$\pm 19$	$\pm 17$	$\pm 17$	$\pm 18$

### B.3 Correlation matrices

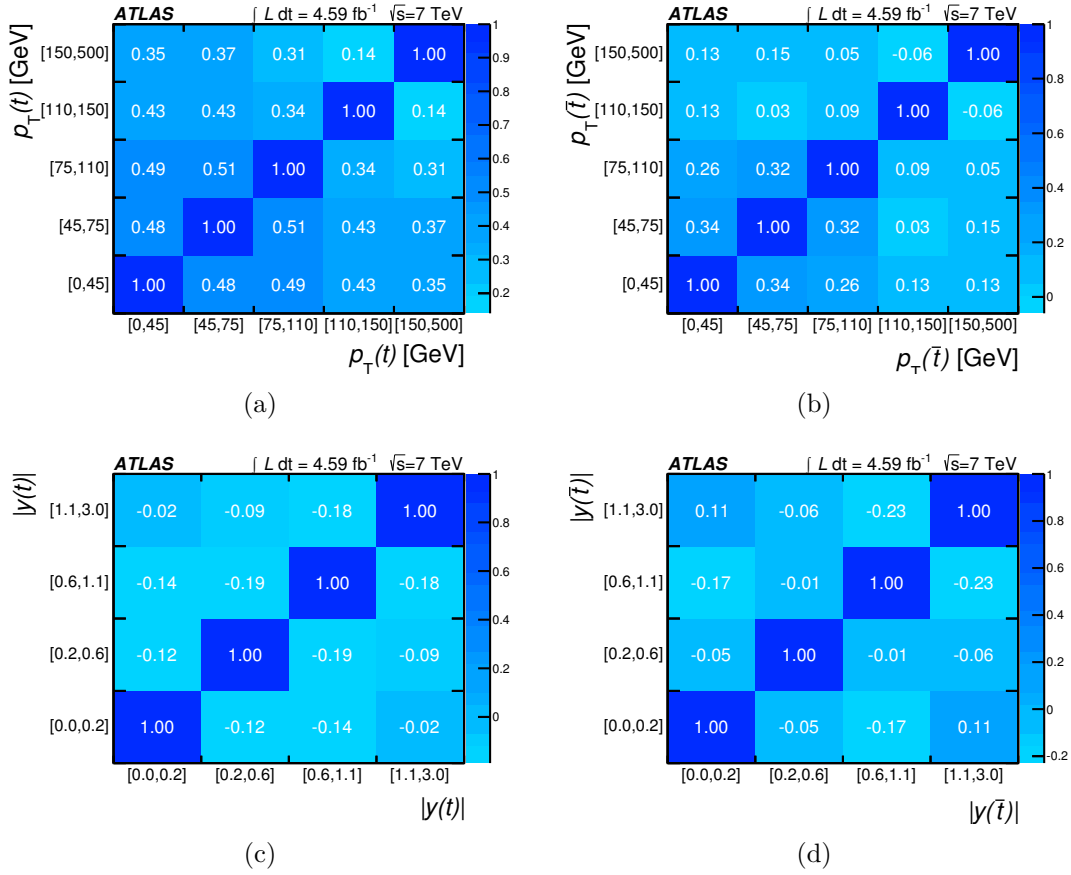


**Figure B.2:** Statistical correlation matrices for the differential cross section as a function of (a)  $p_T(t)$ , (b)  $p_T(\bar{t})$ , (c)  $|y(t)|$  and (d)  $|y(\bar{t})|$  [174].

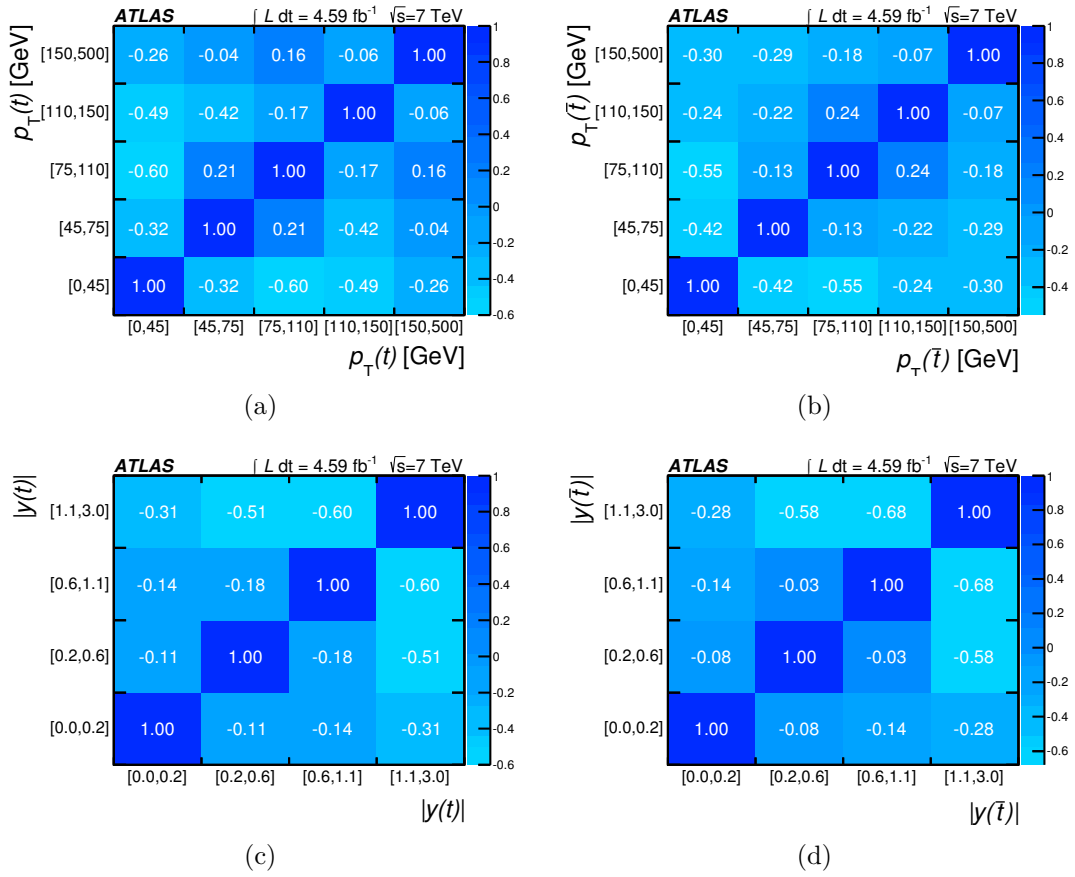


**Figure B.3:** Statistical correlation matrices for the normalized differential cross section as a function of (a)  $p_T(t)$ , (b)  $p_T(\bar{t})$ , (c)  $|y(t)|$  and (d)  $|y(\bar{t})|$  [174].



# List of Figures

1.1	All fundamental particles and their interactions in the SM. . . . .	3
1.2	Handedness of fermions. . . . .	5
1.3	Mixing of quark flavors in the charged-current weak interaction. . . . .	5
1.4	QCD-improved parton model. . . . .	8
1.5	Examples for LO and NLO Feynman diagrams. . . . .	9
1.6	The DGLAP splitting functions. . . . .	10
1.7	$x$ - $Q^2$ kinematic plane of the LHC collision data. . . . .	12
1.8	CT10 PDF sets at three different $Q^2$ . . . . .	13
1.9	Possible decay modes of the top quark . . . . .	15
1.10	Top-quark pair production at leading order in $pp$ collision. . . . .	16
1.11	Single top-quark production in the $t$ -channel production mode at lowest order in $pp$ collision. . . . .	17
1.12	Single top-quark production in the $s$ - and $Wt$ -channel at lowest order in $pp$ collision. . . . .	17
1.13	Shape comparison in $p_T$ and $\eta$ of the 4FS and 5FS calculation of the spectator $b$ -quark at NLO precision. . . . .	20
1.14	LO Feynman diagrams for the single top-quark and top-antiquark in the $t$ -channel mode. . . . .	20
1.15	Momentum fraction for the $u$ quarks and $d$ quarks in $t$ -channel single top-quark events. . . . .	21
1.16	Calculated values for $\sigma(tq)$ , $\sigma(\bar{t}q)$ , $\sigma(tq+\bar{t}q)$ , and $R_t$ for different NLO PDF sets in the 5FS. . . . .	23
1.17	Spin correlation between top-quark production and top-quark decay. . . . .	25
1.18	$tq$ and $t\bar{q}$ production in FCNC-channels at lowest order in $pp$ collision. . . . .	27
2.1	The accelerator complex at CERN. . . . .	30
2.2	Peak instantaneous luminosity per fill of the LHC during the 2011 data-taking period. . . . .	31
2.3	Average number of interactions per bunch crossing in $pp$ collisions during 2011. . . . .	32
2.4	Cut-away view of the complete ATLAS detector. . . . .	33
2.5	Cut-away view of the ATLAS Inner Detector. . . . .	35
2.6	Cut-away view of the ATLAS calorimeter system. . . . .	38
2.7	Total integrated luminosity of $\sqrt{s} = 7$ TeV $pp$ collision delivered to the ATLAS detector during 2011. . . . .	42

3.1	General structure of a hard proton-proton collision. . . . .	46
3.2	Illustration of the track parameterization. . . . .	50
3.3	Residual distributions of kinematic properties of the reconstructed leptons in simulated $t$ -channel single top-quark signal events. . . . .	53
3.4	Average response of simulated jets and influence of different in-situ calibrations as a function of $p_T^{\text{jet}}$ . . . . .	56
3.5	Relative jet response as a function of the jet pseudorapidity. . . . .	57
3.6	Residual distributions of reconstructed jets and $E_T^{\text{miss}}$ in simulated $t$ -channel single top-quark signal events. . . . .	59
3.7	Schematic of a $b$ -hadron decay. . . . .	60
3.8	Light quark jet and $c$ -quark jet rejection as a function of the $b$ -tag efficiency for several $b$ -tagger. . . . .	61
3.9	$b$ -tagging efficiency and calibration for the JetFitterCombNNc tagger. . . . .	62
4.1	Comparison of top-quark properties at parton level for several MC signal generators. . . . .	66
4.2	Comparison of jet properties at particle level for several MC signal generators. . . . .	68
4.3	Comparison of the $n_{\text{jet}}$ distribution at particle level for several MC signal generators. . . . .	69
4.4	Examples for top-quark background events. . . . .	70
4.5	Examples for $W$ +jets background events. . . . .	71
4.6	Examples for background events from $Z$ +jets and diboson production. . . . .	73
4.7	Examples for QCD multijet events. . . . .	75
4.8	Illustration of selection cuts. . . . .	79
4.9	$E_T^{\text{miss}}$ distributions normalized to the fit result in the central $e^+$ and $e^-$ signal regions. . . . .	81
4.10	Topology of a three-layer feed-forward neural network. . . . .	85
4.11	Comparison of the first set of kinematic distributions normalized to unit area in the 2-jet- $\ell$ channel. . . . .	89
4.12	Comparison of the second set of kinematic distributions normalized to unit area in the 2-jet- $\ell$ channel. . . . .	90
4.13	Comparison of the $E_T^{\text{miss}}$ distribution normalized to unit area in the 2-jet- $\ell$ channel. . . . .	91
4.14	Comparison of the first set of kinematic distributions normalized to unit area in the 3-jet- $\ell$ channel. . . . .	92
4.15	Comparison of the second set of kinematic distributions normalized to unit area in the 3-jet- $\ell$ channel. . . . .	93
4.16	Distributions of $ \eta(j) $ , $m(\ell\nu b)$ , and $m(jb)$ in the 2-jet- $\ell^+$ and 2-jet- $\ell^-$ channels in the CR. . . . .	95
4.17	Distributions of $m_T(\ell E_T^{\text{miss}})$ , $\eta(\ell\nu)$ , and $m(\ell b)$ in the 2-jet- $\ell^+$ and 2-jet- $\ell^-$ channels in the CR. . . . .	96
4.18	Distributions of $\Delta R(\ell, j)$ , $\Delta R(t, j)$ , and $H_T$ in the 2-jet- $\ell^+$ and 2-jet- $\ell^-$ channels in the CR. . . . .	97

4.19	Distributions of $\Delta p_{\text{T}}(\ell\nu b, j)$ , $\eta(b)$ , and $\Delta p_{\text{T}}(\ell, j)$ in the 2-jet- $\ell^+$ and 2-jet- $\ell^-$ channels in the CR. . . . .	98
4.20	Distribution of $E_{\text{T}}^{\text{miss}}$ in the 2-jet- $\ell^+$ and 2-jet- $\ell^-$ channels in the CR. . . . .	99
4.21	Distributions of $ \Delta y(j_1, j_2) $ , $m(j_2 j_3)$ , and $m(\ell\nu b)$ in the 3-jet- $\ell^+$ and 3-jet- $\ell^-$ channels in the CR. . . . .	100
4.22	Distributions of $m_{\text{T}}(\ell E_{\text{T}}^{\text{miss}})$ , $\Sigma\eta(j_i)$ , and $m(j_1 j_2)$ in the 3-jet- $\ell^+$ and 3-jet- $\ell^-$ channels in the CR. . . . .	101
4.23	Distributions of $H_{\text{T}}$ , $\cos\theta(\ell, j)_{\ell\nu b, \text{r.f.}}$ , and $\eta(\ell\nu)$ in the 3-jet- $\ell^+$ and 3-jet- $\ell^-$ channels in the CR. . . . .	102
4.24	Distributions of $m(\ell b)$ and $p_{\text{T}}(\ell\nu b)$ in the 3-jet- $\ell^+$ and 3-jet- $\ell^-$ channels in the CR. . . . .	103
4.25	Over-training check of the training for the NN discriminants in the 2-jet- $\ell$ SR and 3-jet- $\ell$ SR. . . . .	106
4.26	Template-shape distributions of the NN discriminants in the 2-jet SR and 3-jet SR. . . . .	106
4.27	Distributions of NN discriminants in the CR in the 2-jet- $\ell^+$ , the 2-jet- $\ell^-$ , the 2-jet- $\ell$ , the 3-jet- $\ell^+$ , the 3-jet- $\ell^-$ and the 3-jet- $\ell$ channels. . . . .	107
5.1	Distribution of the estimated scale factor $\hat{\beta}_{tq+\bar{t}q}^s$ for the $t$ -channel signal process. . . . .	112
5.2	NN discriminant distributions normalized to the fit results. . . . .	115
5.3	Distributions of $ \eta(j) $ , $m(\ell\nu b)$ , and $m(jb)$ in the 2-jet- $\ell^+$ and 2-jet- $\ell^-$ channels in the SR. . . . .	116
5.4	Distributions of $m_{\text{T}}(\ell E_{\text{T}}^{\text{miss}})$ , $\eta(\ell\nu)$ , and $m(\ell b)$ in the 2-jet- $\ell^+$ and 2-jet- $\ell^-$ channels in the SR. . . . .	117
5.5	Distributions of $\Delta R(\ell, j)$ , $\Delta R(\ell\nu b, j)$ , and $H_{\text{T}}$ in the 2-jet- $\ell^+$ and 2-jet- $\ell^-$ channels in the SR. . . . .	118
5.6	Distributions of $\Delta p_{\text{T}}(\ell\nu b, j)$ , $\eta(b)$ , and $\Delta p_{\text{T}}(\ell, j)$ in the 2-jet- $\ell^+$ and 2-jet- $\ell^-$ channels in the SR. . . . .	119
5.7	Distribution of $E_{\text{T}}^{\text{miss}}$ in the 2-jet- $\ell^+$ and 2-jet- $\ell^-$ channels in the SR. . . . .	120
5.8	Distributions of $ \Delta y(j_1, j_2) $ , $m(j_2 j_3)$ , and $m(\ell\nu b)$ in the 3-jet- $\ell^+$ and 3-jet- $\ell^-$ channels in the SR. . . . .	121
5.9	Distributions of $m_{\text{T}}(\ell E_{\text{T}}^{\text{miss}})$ , $\Sigma\eta(j_i)$ , and $m(j_1 j_2)$ in the 3-jet- $\ell^+$ and 3-jet- $\ell^-$ channels in the SR. . . . .	122
5.10	Distributions of $H_{\text{T}}$ , $\cos\theta(\ell, j)_{\ell\nu b, \text{r.f.}}$ , and $\eta(\ell\nu)$ in the 3-jet- $\ell^+$ and 3-jet- $\ell^-$ channels in the SR. . . . .	123
5.11	Distributions of $m(\ell b)$ and $p_{\text{T}}(\ell\nu b)$ in the 3-jet- $\ell^+$ and 3-jet- $\ell^-$ channels in the SR. . . . .	124
5.12	Fractional JES systematic uncertainty as a function of jet $p_{\text{T}}$ and $\eta$ for the uncertainty on the in-situ calibration. . . . .	126
5.13	Fractional JES systematic uncertainty as a function of jet $p_{\text{T}}$ and $\eta$ for the total uncertainty. . . . .	127
5.14	Determination of the PDF acceptance uncertainty using three different PDF sets for the signal process. . . . .	130

5.15	Shape variations of the NN discriminant for the JES variation due to the $\eta$ -intercalibration modeling in the 2-jet- $\ell$ channel. . . . .	133
5.16	Shape variations of the NN discriminant for the JES variation due to the $\eta$ -intercalibration modeling in the 3-jet- $\ell$ channel. . . . .	134
5.17	Profile distributions to test the effect of the fit of the $b$ -tagging efficiency. . . . .	138
5.18	Residual distribution of $\delta^{b\text{-tag}}$ for the binned ML fits. . . . .	138
5.19	Comparison between observed and predicted values of $\sigma(tq)$ , $\sigma(\bar{t}q)$ , and $\sigma(tq + \bar{t}q)$ . . . . .	139
5.20	Comparison between observed and predicted values of $R_t$ . . . . .	141
5.21	$\sigma(tq + \bar{t}q)$ as a function of $m_t$ . . . . .	142
5.22	Probability-density function of the square of the CKM matrix element $ V_{tb} $ , assuming $ V_{tb}  \leq 1$ . . . . .	143
6.1	Distribution of the signal-over-background ratio of the $o_{\text{NN}}$ distribution in the 2-jet- $\ell^+$ and 2-jet- $\ell^-$ channels. . . . .	146
6.2	Distribution of $\hat{\beta}_{\text{background}}$ for the sum of all backgrounds in the 2-jet- $\ell^+$ and 2-jet- $\ell^-$ channels. . . . .	147
6.3	Distributions of $ \eta(j) $ , $m(\ell\nu b)$ , and $m(jb)$ in the 2-jet- $\ell^+$ and 2-jet- $\ell^-$ channels in the HPR. . . . .	148
6.4	Resolution of $p_{\text{T}}(t)$ , $p_{\text{T}}(\bar{t})$ , $ y(t) $ , and $ y(\bar{t}) $ as a function of the variable defined at the parton level, respectively. . . . .	149
6.5	Measured distributions of $p_{\text{T}}(t)$ , $p_{\text{T}}(\bar{t})$ , $ y(t) $ , and $ y(\bar{t}) $ shown in the HPR. . . . .	151
6.6	Migration matrices relating the parton level and reconstruction level in selected events. . . . .	152
6.7	Comparison of the parton-level, selection-level, and reconstruction-level distributions. . . . .	153
6.8	Consistency test of the unfolding process using half of the signal simulation. . . . .	157
6.9	Test of the unfolding process using altered distributions at selection level. . . . .	158
6.10	Crosscheck of the unfolding process using different unfolding method. . . . .	159
6.11	Differential cross section as a function of $p_{\text{T}}(t)$ , $p_{\text{T}}(\bar{t})$ , $ y(t) $ and $ y(\bar{t}) $ . . . . .	164
6.12	Normalized differential cross section as a function of $p_{\text{T}}(t)$ , $p_{\text{T}}(\bar{t})$ , $ y(t) $ and $ y(\bar{t}) $ . . . . .	165
B.1	Selection efficiencies in each bin of the transverse momentum and the absolute value of the rapidity for the top-quark and top-antiquark. . . . .	179
B.2	Statistical correlation matrices for the differential cross section as a function of $p_{\text{T}}(t)$ , $p_{\text{T}}(\bar{t})$ , $ y(t) $ and $ y(\bar{t}) $ . . . . .	188
B.3	Statistical correlation matrices for the normalized differential cross section as a function of $p_{\text{T}}(t)$ , $p_{\text{T}}(\bar{t})$ , $ y(t) $ and $ y(\bar{t}) $ . . . . .	189

# List of Tables

1.1	Properties of elementary fermions. . . . .	2
1.2	List of the PDF sets used in this thesis. . . . .	14
1.3	Calculated $\sigma(tq)$ values for different NLO PDF sets in the 5FS. . . . .	22
1.4	Calculated $\sigma(\bar{t}q)$ values for different NLO PDF sets in the 5FS. . . . .	22
1.5	Calculated $R_t$ values for different NLO PDF sets in the 5FS . . . . .	23
2.1	Comparison of LHC parameters between the design values and the values during operation in 2011. . . . .	31
2.2	General performance goals of the ATLAS detector. . . . .	34
2.3	Segmentation of the all-good 2011 $pp$ -collision dataset. . . . .	43
4.1	Overview of MC simulated samples. . . . .	74
4.2	Overview of special MC simulated samples used for the evaluation of systematic uncertainties. . . . .	75
4.3	Jet-lepton identification criteria. . . . .	76
4.4	Multijet background estimation in the the $e$ +jets final states. . . . .	80
4.5	Multijet background estimation in the the $\mu$ +jets final states. . . . .	82
4.6	Event yield of all analysis channels in the signal region. . . . .	83
4.7	Event yield of all analysis channels in the control region. . . . .	83
4.8	Composition of the training samples for the NNs. . . . .	104
4.9	Ranking of the NN input variables in the 2-jet and 3-jet channels. . . . .	105
5.1	Gaussian constraints for the background rates. . . . .	112
5.2	Estimators of the parameters of the likelihood function of the fit for $\sigma(tq)$ and $\sigma(\bar{t}q)$ . . . . .	113
5.3	Estimators of the parameters of the likelihood function of the fit for $\sigma(tq + \bar{t}q)$ . . . . .	114
5.4	Estimators of the parameters of the likelihood function for different fit scenarios. . . . .	120
5.5	Relative uncertainties on the theoretical cross-sections for the background processes. . . . .	130
5.6	List of relative acceptance uncertainties for each process in the 2-jet- $\ell$ channel. . . . .	132
5.7	Detailed list of contributions to the total uncertainty on the measured values of $\sigma(tq)$ , $\sigma(\bar{t}q)$ , $R_t$ , and $\sigma(tq + \bar{t}q)$ . . . . .	136

5.8	Evaluation of acceptance and template-shape uncertainties for the most important sources of uncertainties. . . . .	137
5.9	Parametrization factors for the $m_t$ dependence of $\sigma(tq)$ , $\sigma(\bar{t}q)$ and $\sigma(tq + \bar{t}q)$ . . . . .	142
6.1	Event yields for the 2-jet- $\ell^+$ and 2-jet- $\ell^-$ HPR channels. . . . .	147
6.2	Results for the differential cross sections as a function of $p_T(t)$ , $p_T(\bar{t})$ , $ y(t) $ and $ y(\bar{t}) $ . . . . .	162
6.3	Results for the normalized differential cross sections as a function of $p_T(t)$ , $p_T(\bar{t})$ , $ y(t) $ and $ y(\bar{t}) $ . . . . .	163
6.4	$\chi^2$ value for the measured differential cross sections compared to the NLO predictions. . . . .	163
A.1	List of relative acceptance uncertainties in the 2-jet- $\ell^+$ channel. . . . .	172
A.2	List of relative acceptance uncertainties in the 2-jet- $\ell^-$ channel. . . . .	173
A.3	List of relative acceptance uncertainties in the 3-jet- $\ell$ channel. . . . .	174
A.4	List of relative acceptance uncertainties in the 3-jet- $\ell^+$ channel. . . . .	175
A.5	List of relative acceptance uncertainties in the 3-jet- $\ell^-$ channel. . . . .	176
A.6	List of relative acceptance uncertainties in the 3-jet-2-tag channel. . . . .	177
B.1	Contribution of each source of uncertainty to the total relative uncertainty on the measured $\frac{d\sigma}{dp_T(t)}$ distribution. . . . .	180
B.2	Contribution of each source of uncertainty to the total relative uncertainty on the measured $\frac{d\sigma}{dp_T(\bar{t})}$ distribution. . . . .	181
B.3	Contribution of each source of uncertainty to the total relative uncertainty on the measured $\frac{d\sigma}{d y(t) }$ distribution. . . . .	182
B.4	Contribution of each source of uncertainty to the total relative uncertainty on the measured $\frac{d\sigma}{d y(\bar{t}) }$ distribution. . . . .	183
B.5	Contribution of each source of uncertainty to the total relative uncertainty on the measured $\frac{1}{\sigma} \frac{d\sigma}{dp_T(t)}$ distribution. . . . .	184
B.6	Contribution of each source of uncertainty to the total relative uncertainty on the measured $\frac{1}{\sigma} \frac{d\sigma}{dp_T(\bar{t})}$ distribution. . . . .	185
B.7	Contribution of each source of uncertainty to the total relative uncertainty on the measured $\frac{1}{\sigma} \frac{d\sigma}{d y(t) }$ distribution. . . . .	186
B.8	Contribution of each source of uncertainty to the total relative uncertainty on the measured $\frac{1}{\sigma} \frac{d\sigma}{d y(\bar{t}) }$ distribution. . . . .	187

# Bibliography

- [1] F. Abe et al. “Observation of top quark production in  $\bar{p}p$  collisions”. *Phys. Rev. Lett.* 74 (1995), pp. 2626–2631. arXiv:hep-ex/9503002 [hep-ex].
- [2] S. Abachi et al. “Observation of the top quark”. *Phys. Rev. Lett.* 74 (1995), pp. 2632–2637. arXiv:hep-ex/9503003 [hep-ex].
- [3] ATLAS Collaboration, CDF Collaboration, CMS Collaboration, and DØ Collaboration. *First combination of Tevatron and LHC measurements of the top-quark mass*. Tech. rep. ATLAS-CONF-2014-008. CDF-NOTE-11071. CMS-PAS-TOP-13-014. D0-NOTE-6416. CERN, Fermilab, Mar. 2014. arXiv:1403.4427 [hep-ex].
- [4] T. A. Aaltonen et al. “First Observation of Electroweak Single Top Quark Production”. *Phys. Rev. Lett.* 103 (2009), p. 092002. arXiv:0903.0885 [hep-ex].
- [5] V. M. Abazov et al. “Observation of Single Top Quark Production”. *Phys. Rev. Lett.* 103 (2009), p. 092001. arXiv:0903.0850 [hep-ex].
- [6] S. L. Glashow. “Partial Symmetries of Weak Interactions”. *Nucl. Phys.* 22 (1961), pp. 579–588.
- [7] S. Weinberg. “A Model of Leptons”. *Phys. Rev. Lett.* 19 (1967), pp. 1264–1266.
- [8] A. Salam. “Weak and Electromagnetic Interactions”. *Conf. Proc.* C680519 (1968), pp. 367–377.
- [9] M. Y. Han and Y. Nambu. “Three Triplet Model with Double  $SU(3)$  Symmetry”. *Phys. Rev.* 139 (1965), B1006–B1010.
- [10] O. W. Greenberg. “Spin and Unitary Spin Independence in a Paraquark Model of Baryons and Mesons”. *Phys. Rev. Lett.* 13 (1964), pp. 598–602.
- [11] D. Griffiths. *Introduction to Elementary Particles*. Weinheim, Germany: WILEY-VCH, 2008. ISBN: 3527406018.
- [12] J. Beringer et al. “Review of Particle Physics (RPP)”. *Phys. Rev.* D86 (2012), p. 010001.
- [13] The English Wikipedia Project. *Elementary Particle Interactions*. [http://upload.wikimedia.org/wikipedia/commons/4/4c/Elementary\\_particle\\_interactions.svg](http://upload.wikimedia.org/wikipedia/commons/4/4c/Elementary_particle_interactions.svg). Apr. 2013.

- [14] D. J. Gross and F. Wilczek. “Asymptotically Free Gauge Theories. I”. *Phys. Rev. D* 8 (1973), pp. 3633–3652.
- [15] H. D. Politzer. “Asymptotic Freedom: An Approach to Strong Interactions”. *Phys. Rept.* 14 (1974), pp. 129–180.
- [16] C. S. Wu, E. Ambler, R. W. Hayward, D. D. Hoppes, and R. P. Hudson. “Experimental Test of Parity Conservation in Beta Decay”. *Phys. Rev.* 105 (1957), pp. 1413–1414.
- [17] N. Cabibbo. “Unitary Symmetry and Leptonic Decays”. *Phys. Rev. Lett.* 10 (1963), pp. 531–533.
- [18] S. L. Glashow, J. Iliopoulos, and L. Maiani. “Weak Interactions with Lepton-Hadron Symmetry”. *Phys. Rev. D* 2 (1970), pp. 1285–1292.
- [19] M. Kobayashi and T. Maskawa. “CP Violation in the Renormalizable Theory of Weak Interaction”. *Prog. Theor. Phys.* 49 (1973), pp. 652–657.
- [20] J. H. Christenson, J. W. Cronin, V. L. Fitch, and R. Turlay. “Evidence for the  $2\pi$  Decay of the  $K_2^0$  Meson”. *Phys. Rev. Lett.* 13 (1964), pp. 138–140.
- [21] P. W. Higgs. “Broken Symmetries and the Masses of Gauge Bosons”. *Phys. Rev. Lett.* 13 (1964), pp. 508–509.
- [22] F. Englert and R. Brout. “Broken Symmetry and the Mass of Gauge Vector Mesons”. *Phys. Rev. Lett.* 13 (1964), pp. 321–323.
- [23] ATLAS Collaboration. “Observation of a new particle in the search for the Standard Model Higgs boson with the ATLAS detector at the LHC”. *Phys. Lett. B* 716 (2012), pp. 1–29. arXiv:1207.7214 [hep-ex].
- [24] CMS Collaboration. “Observation of a new boson at a mass of 125 GeV with the CMS experiment at the LHC”. *Phys. Lett. B* 716 (2012), pp. 30–61. arXiv:1207.7235 [hep-ex].
- [25] ATLAS Collaboration. “Measurement of the Higgs boson mass from the  $H \rightarrow \gamma\gamma$  and  $H \rightarrow ZZ^* \rightarrow 4\ell$  channels with the ATLAS detector using 25 fb<sup>-1</sup> of  $pp$  collision data”. *Phys. Rev. D* 90.5 (2014), p. 052004. arXiv:1406.3827 [hep-ex].
- [26] R. Devenish and A. Cooper-Sarkar. *Deep Inelastic Scattering*. Oxford, Great Britain: Oxford University Press, 2004.
- [27] J. C. Collins, D. E. Soper, and G. F. Sterman. “Factorization of Hard Processes in QCD”. *Adv. Ser. Direct. High Energy Phys.* 5 (1988), pp. 1–91. arXiv:hep-ph/0409313 [hep-ph].
- [28] R. P. Feynman. “Space-Time Approach to Quantum Electrodynamics”. *Phys. Rev.* 76 (1949), pp. 769–789.
- [29] W. A. Bardeen, A. J. Buras, D. W. Duke, and T. Muta. “Deep Inelastic Scattering Beyond the Leading Order in Asymptotically Free Gauge Theories”. *Phys. Rev. D* 18 (1978), p. 3998.

- [30] Y. L. Dokshitzer. “Calculation of the Structure Functions for Deep Inelastic Scattering and  $e^+e^-$  Annihilation by Perturbation Theory in Quantum Chromodynamics.” *Sov. Phys. JETP* 46 (1977), pp. 641–653.
- [31] V. N. Gribov and L. N. Lipatov. “Deep inelastic  $ep$  scattering in perturbation theory”. *Sov. J. Nucl. Phys.* 15 (1972), pp. 438–450.
- [32] G. Altarelli and G. Parisi. “Asymptotic Freedom in Parton Language”. *Nucl. Phys.* B126 (1977), p. 298.
- [33] W. J. Stirling. *7 TeV LHC  $x$ ,  $Q^2$  parton kinematics*. <http://www.hep.ph.ic.ac.uk/~wstirling/plots/lhcgrid7.eps>. Private communication. 2014.
- [34] F. D. Aaron et al. “Combined Measurement and QCD Analysis of the Inclusive  $e^\pm p$  Scattering Cross Sections at HERA”. *J. High Energy Phys.* 1001 (2010), p. 109. arXiv:0911.0884 [hep-ex].
- [35] H.-L. Lai et al. “New parton distributions for collider physics”. *Phys. Rev.* D82 (2010), p. 074024. arXiv:1007.2241 [hep-ph].
- [36] M. Gluck, P. Jimenez-Delgado, and E. Reya. “Dynamical parton distributions of the nucleon and very small- $x$  physics”. *Eur. Phys. J. C* 53 (2008), pp. 355–366. arXiv:0709.0614 [hep-ph].
- [37] S. Alekhin, J. Blumlein, S. Klein, and S. Moch. “The 3, 4, and 5-flavor NNLO Parton from Deep-Inelastic-Scattering Data and at Hadron Colliders”. *Phys. Rev.* D81 (2010), p. 014032. arXiv:0908.2766 [hep-ph].
- [38] A. D. Martin, W. J. Stirling, R. S. Thorne, and G. Watt. “Parton distributions for the LHC”. *Eur. Phys. J. C* 63 (2009), pp. 189–285. arXiv:0901.0002 [hep-ph].
- [39] R. D. Ball et al. “Impact of Heavy Quark Masses on Parton Distributions and LHC Phenomenology”. *Nucl. Phys.* B849 (2011), pp. 296–363. arXiv:1101.1300 [hep-ph].
- [40] R. D. Ball et al. “Parton distributions with LHC data”. *Nucl. Phys.* B867 (2013), pp. 244–289. arXiv:1207.1303 [hep-ph].
- [41] S. Herb et al. “Observation of a Dimuon Resonance at 9.5 GeV in 400 GeV Proton-Nucleus Collisions”. *Phys. Rev. Lett.* 39 (1977), pp. 252–255.
- [42] J. H. Kuhn. “Theory of top quark production and decay.” In: *The top quark and the electroweak interaction. Proceedings, 23rd Summer Institute on Particle Physics, Stanford, USA, July 10-21, 1995*. 1996, pp. 1–64. arXiv:hep-ph/9707321 [hep-ph].
- [43] I. I. Y. Bigi, Y. L. Dokshitzer, V. A. Khoze, J. H. Kuhn, and P. M. Zerwas. “Production and Decay Properties of Ultraheavy Quarks”. *Phys. Lett.* B181 (1986), p. 157.
- [44] M. Cacciari, M. Czakon, M. Mangano, A. Mitov, and P. Nason. “Top-pair production at hadron colliders with next-to-next-to-leading logarithmic soft-gluon resummation”. *Phys. Lett.* B710 (2012), pp. 612–622. arXiv:1111.5869 [hep-ph].

- [45] P. Baernreuther, M. Czakon, and A. Mitov. “Percent Level Precision Physics at the Tevatron: First Genuine NNLO QCD Corrections to  $q\bar{q} \rightarrow t\bar{t} + X$ ”. *Phys. Rev. Lett.* 109 (2012), p. 132001. arXiv:1204.5201 [hep-ph].
- [46] M. Czakon and A. Mitov. “NNLO corrections to top-pair production at hadron colliders: the all-fermionic scattering channels”. *J. High Energy Phys.* 1212 (2012), p. 054. arXiv:1207.0236 [hep-ph].
- [47] M. Czakon and A. Mitov. “NNLO corrections to top pair production at hadron colliders: the quark-gluon reaction”. *J. High Energy Phys.* 1301 (2013), p. 080. arXiv:1210.6832 [hep-ph].
- [48] M. Czakon, P. Fiedler, and A. Mitov. “Total Top-Quark Pair-Production Cross Section at Hadron Colliders Through  $\mathcal{O}(\alpha_S^4)$ ”. *Phys. Rev. Lett.* 110.25 (2013), p. 252004. arXiv:1303.6254 [hep-ph].
- [49] M. Czakon and A. Mitov. “Top++: A Program for the Calculation of the Top-Pair Cross-Section at Hadron Colliders”. *Comput. Phys. Commun.* 185 (2011), p. 2930. arXiv:1112.5675 [hep-ph].
- [50] A. D. Martin, W. J. Stirling, R. S. Thorne, and G. Watt. “Uncertainties on  $\alpha(S)$  in global PDF analyses and implications for predicted hadronic cross sections”. *Eur. Phys. J. C* 64 (2009), pp. 653–680. arXiv:0905.3531 [hep-ph].
- [51] M. Botje et al. *The PDF4LHC Working Group Interim Recommendations*. Tech. rep. Jan. 2011. arXiv:1101.0538 [hep-ph].
- [52] J. Gao et al. “The CT10 NNLO Global Analysis of QCD”. *Phys. Rev.* D89 (2014), p. 033009. arXiv:1302.6246 [hep-ph].
- [53] ATLAS Collaboration. “Measurement of the  $t\bar{t}$  production cross-section using  $e\mu$  events with  $b$ -tagged jets in  $pp$  collisions at  $\sqrt{s} = 7$  and 8 TeV with the ATLAS detector”. *Eur. Phys. J. C* 74.10 (2014), p. 3109. arXiv:1406.5375 [hep-ex].
- [54] N. Kidonakis. “Next-to-next-to-leading-order collinear and soft gluon corrections for  $t$ -channel single top quark production”. *Phys. Rev.* D83 (2011), p. 091503. arXiv:1103.2792 [hep-ph].
- [55] M. Brucherseifer, F. Caola, and K. Melnikov. “On the NNLO QCD corrections to single-top production at the LHC”. (2014). arXiv:1404.7116 [hep-ph].
- [56] ATLAS Collaboration. “Measurement of the  $t$ -channel single top-quark production cross section in  $pp$  collisions at  $\sqrt{s} = 7$  TeV with the ATLAS detector”. *Phys. Lett.* B717 (2012), pp. 330–350. arXiv:1205.3130 [hep-ex].
- [57] N. Kidonakis. “NNLL resummation for  $s$ -channel single top quark production”. *Phys. Rev.* D81 (2010), p. 054028. arXiv:1001.5034 [hep-ph].
- [58] T. A. Aaltonen et al. “Observation of  $s$ -channel production of single top quarks at the Tevatron”. *Phys. Rev. Lett.* 112 (2014), p. 231803. arXiv:1402.5126 [hep-ex].

- [59] N. Kidonakis. “Two-loop soft anomalous dimensions for single top quark associated production with a  $W^-$  or  $H^-$ ”. *Phys. Rev.* D82 (2010), p. 054018. arXiv:1005.4451 [hep-ph].
- [60] S. Chatrchyan et al. “Observation of the associated production of a single top quark and a  $W$  boson in  $pp$  collisions at  $\sqrt{s} = 8$  TeV”. *Phys. Rev. Lett.* 112 (2014), p. 231802. arXiv:1401.2942 [hep-ex].
- [61] V. M. Abazov et al. “Evidence for  $s$ -channel single top quark production in  $p\bar{p}$  collisions at  $\sqrt{s} = 1.96$  TeV”. *Phys. Lett.* B726 (2013), pp. 656–664. arXiv:1307.0731 [hep-ex].
- [62] J. M. Campbell, R. Frederix, F. Maltoni, and F. Tramontano. “Next-to-Leading-Order Predictions for  $t$ -Channel Single-Top Production at Hadron Colliders”. *Phys. Rev. Lett.* 102 (2009), p. 182003. arXiv:0903.0005 [hep-ph].
- [63] J. M. Campbell, R. Frederix, F. Maltoni, and F. Tramontano. “NLO predictions for  $t$ -channel production of single top and fourth generation quarks at hadron colliders”. *J. High Energy Phys.* 0910 (2009), p. 042. arXiv:0907.3933 [hep-ph].
- [64] F. Maltoni, G. Ridolfi, and M. Ubiali. “ $b$ -initiated processes at the LHC: a reappraisal”. *J. High Energy Phys.* 1207 (2012), p. 022. arXiv:1203.6393 [hep-ph].
- [65] J. M. Campbell and R. K. Ellis. “MCFM for the Tevatron and the LHC”. *Nucl. Phys. Proc. Suppl.* 205-206 (2010), pp. 10–15. arXiv:1007.3492 [hep-ph].
- [66] P. Kant et al. “HATHOR for single top-quark production: Updated predictions and uncertainty estimates for single top-quark production in hadronic collisions”. (2014). arXiv:1406.4403 [hep-ph].
- [67] M. R. Whalley, D. Bourilkov, and R. C. Group. “The Les Houches accord PDFs (LHAPDF) and LHAGLUE”. In: *HERA and the LHC: A Workshop on the implications of HERA for LHC physics. Proceedings, Part B.* 2005, pp. 575–581. arXiv:hep-ph/0508110 [hep-ph].
- [68] A. Quadt. “Top quark physics at hadron colliders”. *Eur. Phys. J. C* 48 (2006), pp. 835–1000.
- [69] V. M. Abazov et al. “Precision measurement of the ratio  $B(t \rightarrow Wb)/B(t \rightarrow Wq)$  and Extraction of  $V_{tb}$ ”. *Phys. Rev. Lett.* 107 (2011), p. 121802. arXiv:1106.5436 [hep-ex].
- [70] T. Aaltonen et al. “Measurement of  $R = \mathcal{B}(t \rightarrow Wb)/\mathcal{B}(t \rightarrow Wq)$  in Top-quark-pair Decays using Lepton+jets Events and the Full CDF Run II Data set”. *Phys. Rev.* D87 (2013), p. 111101. arXiv:1303.6142 [hep-ex].
- [71] CMS Collaboration. “Measurement of the ratio  $B(t \rightarrow Wb)/B(t \rightarrow Wq)$  in  $pp$  collisions at  $\sqrt{s} = 8$  TeV”. *Phys. Lett.* B736 (2014), p. 33. arXiv:1404.2292 [hep-ex].

- [72] W. Wagner. “Direct Measurements of  $V_{tb}$ ”. In: *CKM unitarity triangle. Proceedings, 6th International Workshop, CKM 2010, Warwick, UK, September 6-10, 2010*. 2011. arXiv:1101.4235 [hep-ex].
- [73] H. Lacker et al. “Model-independent extraction of  $|V_{tq}|$  matrix elements from top-quark measurements at hadron colliders”. *Eur. Phys. J. C* 72 (2012), p. 2048. arXiv:1202.4694 [hep-ph].
- [74] N. Kidonakis. “Top-quark transverse-momentum distributions in  $t$ -channel single-top production”. *Phys. Rev. D* 88 (2013), p. 031504. arXiv:1306.3592 [hep-ph].
- [75] R. Schwienhorst, C.-P. Yuan, C. Mueller, and Q.-H. Cao. “Single top quark production and decay in the  $t$ -channel at next-to-leading order at the LHC”. *Phys. Rev. D* 83 (2011), p. 034019. arXiv:1012.5132 [hep-ph].
- [76] P. Falgari, F. Giannuzzi, P. Mellor, and A. Signer. “Off-shell effects for  $t$ -channel and  $s$ -channel single-top production at NLO in QCD”. *Phys. Rev. D* 83 (2011), p. 094013. arXiv:1102.5267 [hep-ph].
- [77] R. Frederix, E. Re, and P. Torrielli. “Single-top  $t$ -channel hadroproduction in the four-flavour scheme with POWHEG and aMC@NLO”. *J. High Energy Phys.* 1209 (2012), p. 130. arXiv:1207.5391 [hep-ph].
- [78] W. Wagner. “Top quark physics in hadron collisions”. *Rept. Prog. Phys.* 68 (2005), pp. 2409–2494. arXiv:hep-ph/0507207 [hep-ph].
- [79] G. Mahlon and S. J. Parke. “Single top quark production at the LHC: Understanding spin”. *Phys. Lett. B* 476 (2000), pp. 323–330. arXiv:hep-ph/9912458 [hep-ph].
- [80] T. M. P. Tait and C.-P. Yuan. “Single top quark production as a window to physics beyond the standard model”. *Phys. Rev. D* 63 (2000), p. 014018. arXiv:hep-ph/0007298 [hep-ph].
- [81] C. Gerber et al. *Tevatron-for-LHC Report: Top and Electroweak Physics*. Tech. rep. FERMILAB-CONF-07-052-E-T. Batavia IL, USA: Fermilab, May 2007. arXiv:0705.3251 [hep-ph].
- [82] J. Alwall et al. “Is  $V_{tb} \simeq 1$ ?” *Eur. Phys. J. C* 49 (2007), pp. 791–801. arXiv:hep-ph/0607115 [hep-ph].
- [83] O. Eberhardt, A. Lenz, and J. Rohrwild. “Less space for a new family of fermions”. *Phys. Rev. D* 82 (2010), p. 095006. arXiv:1005.3505 [hep-ph].
- [84] O. Eberhardt, A. Lenz, A. Menzel, U. Nierste, and M. Wiebusch. “Status of the fourth fermion generation before ICHEP2012: Higgs data and electroweak precision observables”. *Phys. Rev. D* 86 (2012), p. 074014. arXiv:1207.0438 [hep-ph].
- [85] O. Cakir, I. T. Cakir, A. Senol, and A. T. Tasci. “Anomalous single production of fourth family up type quark associated with neutral gauge bosons at the LHC”. *J. Phys. G* 39 (2012), p. 055005. arXiv:1106.6059 [hep-ph].

- [86] J. A. Aguilar-Saavedra. “Single top quark production at LHC with anomalous  $Wtb$  couplings”. *Nucl. Phys.* B804 (2008), pp. 160–192. arXiv:0803.3810 [hep-ph].
- [87] R. Coimbra, A. Onofre, R. Santos, and M. Won. “METop - a generator for single top production via FCNC interactions”. *Eur. Phys. J. C* 72 (2012), p. 2222. arXiv:1207.7026 [hep-ph].
- [88] L. Evans and P. Bryant. “LHC Machine”. *J. Inst.* 3 (2008), S08001.
- [89] ATLAS Collaboration. “The ATLAS Experiment at the CERN Large Hadron Collider”. *J. Inst.* 3 (2008), S08003.
- [90] CMS Collaboration. “The CMS experiment at the CERN LHC”. *J. Inst.* 3 (2008), S08004.
- [91] LHCb Collaboration. “The LHCb Detector at the LHC”. *J. Inst.* 3 (2008), S08005.
- [92] ALICE Collaboration. “The ALICE experiment at the CERN LHC”. *J. Inst.* 3 (2008), S08002.
- [93] TOTEM Collaboration. “The TOTEM experiment at the CERN Large Hadron Collider”. *J. Inst.* 3 (2008), S08007.
- [94] LHCf Collaboration. “The LHCf detector at the CERN Large Hadron Collider”. *J. Inst.* 3 (2008), S08006.
- [95] MoEDAL Collaboration. *Technical Design Report of the MoEDAL Experiment*. Tech. rep. CERN-LHCC-2009-006. Geneva, Switzerland: CERN, June 2009. URL: <http://cds.cern.ch/record/1181486>.
- [96] M. Barnes et al. *The PS complex as proton pre-injector for the LHC: design and implementation report*. Geneva, Switzerland: CERN, 2000. ISBN: 9290831634.
- [97] M. Benedikt et al. “The PS complex produces the nominal LHC beam”. In: *Particle accelerator. Proceedings, 7th European Conference, EPAC 2000, Vienna, Austria, June 26-30, 2000. Vol. 1-3*. CERN-PS-2000-039-OP. July 2000. URL: <http://cds.cern.ch/record/452081>.
- [98] P. Collier et al. *The SPS as injector for LHC: Conceptual design*. CERN-SL-97-007-DI. Geneva, Switzerland: CERN, Mar. 1997. URL: <http://cds.cern.ch/record/322782>.
- [99] Forthommel. *Map of the CERN accelerator complex*. <http://upload.wikimedia.org/wikipedia/commons/b/ba/Cern-accelerator-complex.svg>. May 2011.
- [100] J. Haffner. *The CERN accelerator complex. Complexe des accélérateurs du CERN*. ©CERN. Oct. 2013. URL: <https://cds.cern.ch/record/1621894>.
- [101] ATLAS Collaboration. *Peak Luminosity per day in 2011*. <https://atlas.web.cern.ch/Atlas/GROUPS/DATAPREPARATION/PublicPlots/2011/DataSummary/figs/peakLumiByFill.eps>. 2011.

- [102] ATLAS Collaboration. *Performance of the ATLAS Inner Detector Track and Vertex Reconstruction in the High Pile-Up LHC Environment*. Tech. rep. ATLAS-CONF-2012-042. Geneva: CERN, Mar. 2012. URL: <http://cds.cern.ch/record/1435196>.
- [103] ATLAS Collaboration. *Number of Interactions per Crossing*. [https://twiki.cern.ch/twiki/pub/AtlasPublic/LuminosityPublicResults/mu\\_2011-2\\_1.eps](https://twiki.cern.ch/twiki/pub/AtlasPublic/LuminosityPublicResults/mu_2011-2_1.eps). 2011.
- [104] G. Aad et al. “ATLAS pixel detector electronics and sensors”. *J. Inst.* 3 (2008), P07007.
- [105] ATLAS Collaboration. *Alignment of the ATLAS Inner Detector Tracking System with 2010 LHC proton-proton collisions at  $\sqrt{s} = 7$  TeV*. Tech. rep. ATLAS-CONF-2011-012. Geneva, Switzerland, Mar. 2011. URL: <http://cds.cern.ch/record/1334582>.
- [106] ATLAS Collaboration. *RMS of residuals as a function of track incident angle (Collision data)*. [https://twiki.cern.ch/twiki/pub/AtlasPublic/PixelPublicResults/res\\_RMS\\_phi\\_repro\\_MC.eps](https://twiki.cern.ch/twiki/pub/AtlasPublic/PixelPublicResults/res_RMS_phi_repro_MC.eps). Mar. 2011.
- [107] ATLAS Collaboration. *Data Quality Information for 2011 Data*. <https://atlas.web.cern.ch/Atlas/GROUPS/DATAPREPARATION/PublicPlots/DQ/atlas-dq-eff-pp2011-At0M-.png>. 2011.
- [108] ATLAS Collaboration. “Readiness of the ATLAS Tile Calorimeter for LHC collisions”. *Eur. Phys. J. C* 70 (2010), pp. 1193–1236. arXiv:1007.5423 [physics.ins-det].
- [109] ATLAS Collaboration. *MDT resolution plots*. Tech. rep. ATLAS-PLOT-MUON-2011-006. Oct. 2011. URL: <http://atlas.web.cern.ch/Atlas/GROUPS/MUON/PLOTS/ATLAS-PLOT-MUON-2011-006/>.
- [110] ATLAS Collaboration. “Improved luminosity determination in  $pp$  collisions at  $\sqrt{s} = 7$  TeV using the ATLAS detector at the LHC”. *Eur. Phys. J. C* 73 (2013), p. 2518. arXiv:1302.4393 [hep-ex].
- [111] V. Cindro et al. “The ATLAS beam conditions monitor”. *J. Inst.* 3 (2008), P02004.
- [112] S. van der Meer. *Calibration of the Effective Beam Height in the ISR*. Tech. rep. CERN-ISR-PO-68-31. ISR-PO-68-31. Geneva, Switzerland: CERN, 1968.
- [113] U. Amaldi et al. “The Real Part of the Forward Proton Proton Scattering Amplitude Measured at the CERN Intersecting Storage Rings”. *Phys. Lett.* B66 (1977), p. 390.
- [114] ATLAS Collaboration. “Electron reconstruction and identification efficiency measurements with the ATLAS detector using the 2011 LHC proton-proton collision data”. *Eur. Phys. J. C* 74 (2014), p. 2941. arXiv:1404.2240 [hep-ex].

- [115] P. Jenni, M. Nessi, M. Nordberg, and K. Smith. *ATLAS high-level trigger, data-acquisition and controls: Technical Design Report*. Technical Design Report ATLAS. Geneva: CERN, 2003.
- [116] ATLAS Collaboration. *Total Integrated Luminosity in 2011*. <https://atlas.web.cern.ch/Atlas/GROUPS/DATAPREPARATION/PublicPlots/2011/DataSummary/figs/sumLumiByDay.eps>. 2011.
- [117] M. L. Mangano and T. J. Stelzer. “Tools for the simulation of hard hadronic collisions”. *Ann. Rev. Nucl. Part. Sci.* 55 (2005), pp. 555–588.
- [118] A. Buckley et al. “General-purpose event generators for LHC physics”. *Phys. Rept.* 504 (2011), pp. 145–233. arXiv:1101.2599 [hep-ph].
- [119] B. Andersson. *The Lund model*. Cambridge Monographs on Particle Physics, Nuclear Physics and Cosmology (Book 7). Cambridge, Great Britain: Cambridge University Press, 1998. ISBN: 0521420946.
- [120] D. Amati and G. Veneziano. “Preconfinement as a Property of Perturbative QCD”. *Phys. Lett.* B83 (1979), p. 87.
- [121] S. Catani, F. Krauss, R. Kuhn, and B. R. Webber. “QCD matrix elements + parton showers”. *J. High Energy Phys.* 0111 (2001), p. 063. arXiv:hep-ph/0109231 [hep-ph].
- [122] J. Alwall et al. “Comparative study of various algorithms for the merging of parton showers and matrix elements in hadronic collisions”. *Eur. Phys. J. C* 53 (2008), pp. 473–500. arXiv:0706.2569 [hep-ph].
- [123] P. Nason. “A New method for combining NLO QCD with shower Monte Carlo algorithms”. *J. High Energy Phys.* 0411 (2004), p. 040. arXiv:hep-ph/0409146 [hep-ph].
- [124] S. Frixione, P. Nason, and C. Oleari. “Matching NLO QCD computations with Parton Shower simulations: the POWHEG method”. *J. High Energy Phys.* 0711 (2007), p. 070. arXiv:0709.2092 [hep-ph].
- [125] S. Alioli, P. Nason, C. Oleari, and E. Re. “A general framework for implementing NLO calculations in shower Monte Carlo programs: the POWHEG BOX”. *J. High Energy Phys.* 1006 (2010), p. 043. arXiv:1002.2581 [hep-ph].
- [126] J. Alwall et al. “The automated computation of tree-level and next-to-leading order differential cross sections, and their matching to parton shower simulations”. *J. High Energy Phys.* 1407 (2014), p. 079. arXiv:1405.0301 [hep-ph].
- [127] S. Frixione and B. R. Webber. “Matching NLO QCD computations and parton shower simulations”. *J. High Energy Phys.* 0206 (2002), p. 029. arXiv:hep-ph/0204244 [hep-ph].
- [128] B. P. Kersevan and E. Richter-Was. “The Monte Carlo event generator AcerMC versions 2.0 to 3.8 with interfaces to PYTHIA 6.4, HERWIG 6.5 and ARIADNE 4.1”. *Comput. Phys. Commun.* 184 (2013), pp. 919–985. arXiv:hep-ph/0405247 [hep-ph].

- [129] T. Stelzer and W. F. Long. “Automatic generation of tree level helicity amplitudes”. *Comput. Phys. Commun.* 81 (1994), pp. 357–371. arXiv:hep-ph/9401258 [hep-ph].
- [130] B. P. Kersevan and I. Hinchliffe. “A Consistent prescription for the production involving massive quarks in hadron collisions”. *J. High Energy Phys.* 0609 (2006), p. 033. arXiv:hep-ph/0603068 [hep-ph].
- [131] M. A. G. Aivazis, J. C. Collins, F. I. Olness, and K. Tung. “Leptoproduction of heavy quarks. 2. A Unified QCD formulation of charged and neutral current processes from fixed target to collider energies”. *Phys. Rev.* D50 (1994), pp. 3102–3118. arXiv:hep-ph/9312319 [hep-ph].
- [132] M. L. Mangano, M. Moretti, F. Piccinini, R. Pittau, and A. D. Polosa. “ALPGEN, a generator for hard multiparton processes in hadronic collisions”. *J. High Energy Phys.* 0307 (2003), p. 001. arXiv:hep-ph/0206293 [hep-ph].
- [133] T. Sjostrand, S. Mrenna, and P. Z. Skands. “PYTHIA 6.4 Physics and Manual”. *J. High Energy Phys.* 0605 (2006), p. 026. arXiv:hep-ph/0603175 [hep-ph].
- [134] P. Z. Skands. “Tuning Monte Carlo Generators: The Perugia Tunes”. *Phys. Rev.* D82 (2010), p. 074018. arXiv:1005.3457 [hep-ph].
- [135] G. Corcella et al. “HERWIG 6: An Event generator for hadron emission reactions with interfering gluons (including supersymmetric processes)”. *J. High Energy Phys.* 0101 (2001), p. 010. arXiv:hep-ph/0011363 [hep-ph].
- [136] J. M. Butterworth, J. R. Forshaw, and M. H. Seymour. “Multiparton interactions in photoproduction at HERA”. *Z. Phys.* C72 (1996), pp. 637–646. arXiv:hep-ph/9601371 [hep-ph].
- [137] ATLAS Collaboration. *New ATLAS event generator tunes to 2010 data*. Tech. rep. ATL-PHYS-PUB-2011-008. Geneva, Switzerland: CERN, Apr. 2011. URL: <http://cds.cern.ch/record/1345343>.
- [138] GEANT4 Collaboration. “GEANT4: A Simulation toolkit”. *Nucl. Instrum. Meth.* A506 (2003), pp. 250–303.
- [139] ATLAS Collaboration. “The ATLAS Simulation Infrastructure”. *Eur. Phys. J. C* 70 (2010), pp. 823–874. arXiv:1005.4568 [physics.ins-det].
- [140] T. Cornelissen et al. *Concepts, Design and Implementation of the ATLAS New Tracking (NEWT)*. Tech. rep. ATL-SOFT-PUB-2007-007. Geneva, Switzerland: CERN, Mar. 2007. URL: <http://cds.cern.ch/record/1020106>.
- [141] R. E. Kalman. “A New Approach to Linear Filtering and Prediction Problems”. *J. Fluids Eng.* 82.1 (1960), pp. 35–45.
- [142] R. Fruhwirth. “Application of Kalman filtering to track and vertex fitting”. *Nucl. Instrum. Meth.* A262 (1987), pp. 444–450.

- [143] M. Limper, S. Bentvelsen, and A. P. Colijn. “Track and vertex reconstruction in the ATLAS inner detector”. Presented on 12 Oct 2009. PhD thesis. Amsterdam, Netherlands: Amsterdam U., 2009. URL: <http://cds.cern.ch/record/1202457>.
- [144] G. Piacquadio, K. Prokofiev, and A. Wildauer. “Primary vertex reconstruction in the ATLAS experiment at LHC”. *J. Phys. Conf. Ser.* 119 (2008), p. 032033.
- [145] R. Fruhwirth, W. Waltenberger, and P. Vanlaer. “Adaptive vertex fitting”. *J. Phys.* G34 (2007), N343.
- [146] ATLAS Collaboration. *Performance of primary vertex reconstruction in proton-proton collisions at  $\sqrt{s} = 7$  TeV in the ATLAS experiment*. Tech. rep. ATLAS-CONF-2010-069. Geneva, Switzerland: CERN, July 2010. URL: <http://cds.cern.ch/record/1281344>.
- [147] ATLAS Collaboration. “Electron performance measurements with the ATLAS detector using the 2010 LHC proton-proton collision data”. *Eur. Phys. J. C* 72 (2012), p. 1909. arXiv:1110.3174 [hep-ex].
- [148] ATLAS Collaboration. “Electron and photon energy calibration with the ATLAS detector using LHC Run 1 data”. *Eur. Phys. J. C* 74.10 (2014), p. 3071. arXiv:1407.5063 [hep-ex].
- [149] ATLAS Collaboration. “Muon reconstruction efficiency and momentum resolution of the ATLAS experiment in proton-proton collisions at  $\sqrt{s}=7$  TeV in 2010”. *Eur. Phys. J. C* 74.9 (2014), p. 3034. arXiv:1404.4562 [hep-ex].
- [150] W. Lampl et al. *Calorimeter Clustering Algorithms: Description and Performance*. Tech. rep. ATL-LARG-PUB-2008-002. Geneva, Switzerland: CERN, Apr. 2008. URL: <http://cds.cern.ch/record/1099735>.
- [151] ATLAS Collaboration. *Pile-up corrections for jets from proton-proton collisions at  $\sqrt{s} = 7$  TeV in ATLAS in 2011*. Tech. rep. ATLAS-CONF-2012-064. Geneva, Switzerland: CERN, July 2012. URL: <http://cds.cern.ch/record/1459529>.
- [152] ATLAS Collaboration. “Jet energy measurement with the ATLAS detector in proton-proton collisions at  $\sqrt{s} = 7$  TeV”. *Eur. Phys. J. C* 73 (2013), p. 2304. arXiv:1112.6426 [hep-ex].
- [153] M. Cacciari, G. P. Salam, and G. Soyez. “The Anti- $k_t$  jet clustering algorithm”. *J. High Energy Phys.* 0804 (2008), p. 063. arXiv:0802.1189 [hep-ph].
- [154] ATLAS Collaboration. “Jet energy measurement and its systematic uncertainty in proton-proton collisions at  $\sqrt{s} = 7$  TeV with the ATLAS detector”. *Eur. Phys. J. C* 75.1 (2015), p. 17. arXiv:1406.0076 [hep-ex].
- [155] M. Bahr et al. “Herwig++ Physics and Manual”. *Eur. Phys. J. C* 58 (2008), pp. 639–707. arXiv:0803.0883 [hep-ph].

- [156] M. Cacciari, G. P. Salam, and G. Soyez. “FastJet User Manual”. *Eur. Phys. J. C* 72 (2012), p. 1896. arXiv:1111.6097 [hep-ph].
- [157] ATLAS Collaboration. *Expected Performance of the ATLAS Experiment - Detector, Trigger and Physics*. Geneva, Switzerland: CERN, 2009. ISBN: 9789290833215. arXiv:0901.0512 [hep-ex].
- [158] ATLAS Collaboration. *Commissioning of the ATLAS high-performance  $b$ -tagging algorithms in the 7 TeV collision data*. Tech. rep. ATLAS-CONF-2011-102. Geneva, Switzerland: CERN, July 2011. URL: <http://cds.cern.ch/record/1369219>.
- [159] G. Piacquadio and C. Weiser. “A new inclusive secondary vertex algorithm for  $b$ -jet tagging in ATLAS”. *J. Phys. Conf. Ser.* 119 (2008), p. 032032.
- [160] ATLAS Collaboration. *Measurement of the  $b$ -tag Efficiency in a Sample of Jets Containing Muons with 5 fb<sup>-1</sup> of Data from the ATLAS Detector*. Tech. rep. ATLAS-CONF-2012-043. Geneva, Switzerland: CERN, Mar. 2012. URL: <http://cds.cern.ch/record/1435197>.
- [161] P. Tepel and W. Wagner. “Performance studies of  $b$ -tagging algorithms for single top-quark analyses with the ATLAS detector at  $\sqrt{s} = 7$  TeV”. Presented 25 Sep 2012. MA thesis. Wuppertal, Germany: Wuppertal U., Sept. 2012. URL: <https://cds.cern.ch/record/1565499>.
- [162] ATLAS Collaboration. “Performance of Missing Transverse Momentum Reconstruction in Proton-Proton Collisions at 7 TeV with ATLAS”. *Eur. Phys. J. C* 72 (2012), p. 1844. arXiv:1108.5602 [hep-ex].
- [163] T. Chwalek, T. Müller, and W. Wagner. “Measurement of the  $W$  boson helicity in top-antitop quark events with the CDF II experiment”. MA thesis. Karlsruhe, Germany: Karlsruhe U., Oct. 2006. URL: <http://ekp-invenio.physik.uni-karlsruhe.de/record/44857>.
- [164] P. Sturm, T. Mueller, and W. Wagner. “Studies for the Measurement of Single-Top-Quark-Events with the CMS-Experiment”. Presented on 17 Mar 2008. MA thesis. Karlsruhe, Germany: Karlsruhe U., Mar. 2008. URL: <https://cds.cern.ch/record/1311220>.
- [165] A. Sherstnev and R. S. Thorne. “Parton Distributions for LO Generators”. *Eur. Phys. J. C* 55 (2008), pp. 553–575.
- [166] J. Pumplin et al. “New generation of parton distributions with uncertainties from global QCD analysis”. *J. High Energy Phys.* 0207 (2002), p. 012. arXiv:hep-ph/0201195 [hep-ph].
- [167] C. Anastasiou, L. J. Dixon, K. Melnikov, and F. Petriello. “High precision QCD at hadron colliders: Electroweak gauge boson rapidity distributions at NNLO”. *Phys. Rev. D* 69 (2004), p. 094008.
- [168] W. J. Stirling and E. Vryonidou. “Charm production in association with an electroweak gauge boson at the LHC”. *Phys. Rev. Lett.* 109 (2012), p. 082002. arXiv:1203.6781 [hep-ph].

- [169] ATLAS Collaboration. “Measurement of the production of a  $W$  boson in association with a charm quark in  $pp$  collisions at  $\sqrt{s} = 7$  TeV with the ATLAS detector”. *J. High Energy Phys.* 1405 (2014), p. 068. arXiv:1402.6263 [hep-ex].
- [170] P. Sturm and W. Wagner. “Measurement of the  $t$ -Channel Single Top-Quark Production Cross-Section with the ATLAS Detector at  $\sqrt{s} = 7$  TeV”. Presented 01 June 2012. PhD thesis. Wuppertal, Germany: Wuppertal U., Nov. 2012. URL: <http://elpub.bib.uni-wuppertal.de/edocs/dokumente/fbc/physik/diss2012/sturm>.
- [171] S. Catani, M. Dittmar, D. E. Soper, W. J. Stirling, S. Tapprogge, et al. “QCD”. In: *1999 CERN Workshop on standard model physics (and more) at the LHC, CERN, Geneva, Switzerland, 25-26 May: Proceedings*. 2000, pp. 1–116. arXiv:hep-ph/0005025 [hep-ph].
- [172] ATLAS Collaboration. “Measurement of the top quark pair production cross-section with ATLAS in the single lepton channel”. *Phys. Lett.* B711 (2012), pp. 244–263. arXiv:1201.1889 [hep-ex].
- [173] H.-C. Lee and S. C. M. Bentvelsen. “Single Top Quark Production at the LHC: Data Processing and Cross Section Measurement”. Presented 29 Oct. 2013. PhD thesis. Amsterdam, Netherlands: Amsterdam U., 2013. URL: <http://cds.cern.ch/record/1609057>.
- [174] ATLAS Collaboration. “Comprehensive measurements of  $t$ -channel single top-quark production cross sections at  $\sqrt{s} = 7$  TeV with the ATLAS detector”. *Phys. Rev.* D90.11 (2014), p. 112006. arXiv:1406.7844 [hep-ex].
- [175] M. Feindt. “A Neural Bayesian Estimator for Conditional Probability Densities”. (2004). arXiv:physics/0402093 [physics.data-an].
- [176] M. Feindt and U. Kerzel. “The NeuroBayes neural network package”. *Nucl. Instrum. Meth.* A559 (2006), pp. 190–194.
- [177] G. Cowan. *Statistical Data Analysis*. Oxford, United Kingdom: Oxford University Press, 1998. ISBN: 0198501552.
- [178] F. James and M. Roos. “Minuit: A System for Function Minimization and Analysis of the Parameter Errors and Correlations”. *Comput. Phys. Commun.* 10 (1975), pp. 343–367.
- [179] G. Sartisohn and W. Wagner. “Higgs Boson Search in the  $H \rightarrow WW^{(*)} \rightarrow l\nu l\nu$  Channel using Neural Networks with the ATLAS Detector at 7 TeV”. Presented 08 May 2012. PhD thesis. Wuppertal, Germany: Wuppertal U., Mar. 2012. URL: <http://elpub.bib.uni-wuppertal.de/servlets/DocumentServlet?id=2837>.
- [180] ATLAS Collaboration. “Jet energy resolution in proton-proton collisions at  $\sqrt{s} = 7$  TeV recorded in 2010 with the ATLAS detector”. *Eur. Phys. J. C* 73 (2013), p. 2306. arXiv:1210.6210 [hep-ex].

- [181] ATLAS Collaboration. *b-jet tagging calibration on c-jets containing  $D^{*+}$  mesons*. Tech. rep. ATLAS-CONF-2012-039. Geneva, Switzerland: CERN, Mar. 2012. URL: <https://cds.cern.ch/record/1435193>.
- [182] ATLAS Collaboration. *Measurement of the Mistag Rate with  $5 \text{ fb}^{-1}$  of Data Collected by the ATLAS Detector*. Tech. rep. ATLAS-CONF-2012-040. Geneva, Switzerland: CERN, Mar. 2012. URL: <http://cds.cern.ch/record/1435194>.
- [183] ATLAS Collaboration. “Measurement of the muon reconstruction performance of the ATLAS detector using 2011 and 2012 LHC proton-proton collision data”. *Eur. Phys. J. C* 74.11 (2014), p. 3130. arXiv:1407.3935 [hep-ex].
- [184] ATLAS Collaboration. “Measurement of  $t\bar{t}$  production with a veto on additional central jet activity in  $pp$  collisions at  $\sqrt{s} = 7 \text{ TeV}$  using the ATLAS detector”. *Eur. Phys. J. C* 72 (2012), p. 2043. arXiv:1203.5015 [hep-ex].
- [185] A. Roe and A. Quadt. “Measurement of the Top Quark Pair Production Cross Section and Simultaneous Extraction of the  $W$  Heavy Flavor Fraction at  $\sqrt{s} = 7 \text{ TeV}$  with the ATLAS Detector at the LHC”. Presented 22 March 2012. PhD thesis. Göttingen, Germany: Göttingen U., Apr. 2012. URL: <https://ediss.uni-goettingen.de/handle/11858/00-1735-0000-000D-F082-7>.
- [186] S. Frixione, F. Stoeckli, P. Torrielli, B. R. Webber, and C. D. White. *The MC@NLO 4.0 Event Generator*. Tech. rep. CAVENDISH-HEP-10-12. CERN-PH-TH-2010-216. IPPP-10-62. DCPT-10-124. Oct. 2010. arXiv:1010.0819 [hep-ph].
- [187] CMS Collaboration. “Measurement of the single-top-quark  $t$ -channel cross section in  $pp$  collisions at  $\sqrt{s} = 7 \text{ TeV}$ ”. *J. High Energy Phys.* 1212 (2012), p. 035. arXiv:1209.4533 [hep-ex].
- [188] CMS Collaboration. “Measurement of the  $t$ -channel single-top-quark production cross section and of the  $|V_{tb}|$  CKM matrix element in  $pp$  collisions at  $\sqrt{s} = 8 \text{ TeV}$ ”. *J. High Energy Phys.* 1406 (2014), p. 090. arXiv:1403.7366 [hep-ex].
- [189] T. Adye. “Unfolding algorithms and tests using RooUnfold”. In: *PHYSTAT 2011 Workshop on Statistical Issues Related to Discovery Claims in Search Experiments and Unfolding, CERN, Geneva, Switzerland, 17 - 20 Jan 2011*. 2011, pp. 313–318. arXiv:1105.1160 [physics.data-an].
- [190] G. D’Agostini. “A Multidimensional unfolding method based on Bayes’ theorem”. *Nucl. Instrum. Meth.* A362 (1995), pp. 487–498.
- [191] A. Hocker and V. Kartvelishvili. “SVD approach to data unfolding”. *Nucl. Instrum. Meth.* A372 (1996), pp. 469–481. arXiv:hep-ph/9509307 [hep-ph].
- [192] V. Radescu. Private communication. June 5, 2014.

- 
- [193] F. D. Aaron et al. “A Precision Measurement of the Inclusive ep Scattering Cross Section at HERA”. *Eur. Phys. J. C* 64 (2009), pp. 561–587. arXiv:0904.3513 [hep-ex].
- [194] ATLAS Collaboration. *Measurement of the  $t$ -channel single top-quark and top-antiquark production cross-sections and their ratio in  $pp$  collisions at  $\sqrt{s} = 7$  TeV*. Tech. rep. ATLAS-CONF-2012-056. Geneva, Switzerland: CERN, June 2012. URL: <http://cds.cern.ch/record/1453783>.
- [195] CMS Collaboration. *Single top  $t$ -channel differential cross section at 8 TeV*. Tech. rep. CMS-PAS-TOP-14-004. Geneva, Switzerland: CERN, Oct. 2014. URL: <http://cds.cern.ch/record/1956681>.



# Danksagung

Ich möchte mich ganz herzlich bei Prof. Dr. Wolfgang Wagner bedanken für die exzellente Betreuung meiner Promotion und die vier Jahre guter Zusammenarbeit. Er hatte immer ein offenes Ohr für Probleme jeglicher Art. Ganz besonders möchte ich mich für die zwei Jahre CERN-Aufenthalt bedanken, in denen mich sowohl wissenschaftlich als auch persönlich weiterentwickeln konnte.

Auch möchte ich mich bei Dr. Tancredi Carli dafür bedanken, dass er sich bereit erklärt hat, Zweitgutachter dieser Arbeit zu sein, und für seine langjährige Unterstützung dieser Analyse in der ATLAS-Top-Physik Gruppe.

Großer Dank gebührt auch Dr. Dominic Hirschbühl für seine stets konstruktive Kritik und große Hilfsbereitschaft rund um die Uhr. Diese Eigenschaften hat er auch bei dem Korrekturlesen dieser Arbeit wieder unter Beweis gestellt. Vielen Dank dafür!

Bei Dr. Georg Sartisohn und Dr. Philipp Sturm möchte ich mich sehr für die tolle Aufnahme in die Doktorandengruppe, die vielen praktischen und persönlichen Ratschläge, und die spontanen Korrekturlese-Einsätze bedanken. Dr. Simon Köhlmann möchte ich für die vielen hilfreichen und unterstützenden Gespräche danken.

Phillipp Tepel und Arwa Bannoura danke ich für die nette Aufnahme in das Wuppertaler Büro, die tolle Atmosphäre und die guten Gespräche sowie die gute Kaffeemaschine im Büro.

Besondere Anerkennung gilt Dr. Torsten Harenberg für seine oft nächtlichen Einsätze um die Analysen bis zu den ATLAS-Abgabefristen fertigzustellen und für die große Unterstützung in alle Computing Fragen. Auch möchte ich mich bei der ganzen Wuppertaler ATLAS Gruppe für die schöne Zeit und den festen Zusammenhalt in insgesamt sieben Jahren bedanken.

I would like to thank the ATLAS single-top group for the nice working atmosphere and the great support for this analysis throughout the three years.

Jacob Finkenrath, Mirco Tischler, Franziska Szeibert, Daniel Bindig und Christian Riegel danke ich für viele gute gemeinsame Stunden Entspannung mit einer Flasche Bier sowie der netten Wiederaufnahme in Wuppertal nach zwei Jahren Abwesenheit. Tatjana, Sascha, Otto und Paul für viele gute Stunden rund ums CERN und am See. Jens danke ich für die viele Geduld und das viele Reisen: Danke, dass du da warst!

Am meisten möchte ich jedoch meiner Familie danken. Ihr habt mich immer unterstützt und ermutigt, und endlose Stunden Erzählungen über Physik ertragen in all den Jahren.